Effect of die design on extensional viscosity determination from entrance pressure drop measurements

Bc. Jiří Juračka

Master's thesis
2024

Tomas Bata University in Zlín
Faculty of Technology

Univerzita Tomáše Bati ve Zlíně
Fakulta technologická
Ústav výrobního inženýrství

Akademický rok: 2023/2024

ZADÁNÍ DIPLOMOVÉ PRÁCE

(projektu, uměleckého díla, uměleckého výkonu)

Jméno a příjmení:	**Bc. Jiří Juračka**
Osobní číslo:	**T22373**
Studijní program:	**N0788A270008 Konstrukce nástrojů**
Forma studia:	**Prezenční**
Téma práce:	**Vliv konstrukce vytlačovacích hlav na stanovení tahové viskozity z měření vstupní tlakové ztráty**

Zásady pro vypracování

1. Vypracujte literární studii na dané téma.
2. Ohodnoťte vliv konstrukce vytlačovacích hlav na stanovení tahové viskozity polymerních tavenin s využitím vysokotlakého kapilárního reometru při různých teplotách, deformacích a deformačních rychlostech.
3. Porovnejte naměřená data s nezávislými měřeními provedenými pomocí metody EVF a Sentmanatova elongačního reometru a naměřená data popište vhodnou konstituční rovnicí.

Forma zpracování diplomové práce: **tištěná/elektronická**
Jazyk zpracování: **Angličtina**

Seznam doporučené literatury:

1. J. Drabek, M. Zatloukal, Measurement and modeling of uniaxial and planar extensional viscosities for linear isotactic polypropylenes, *Physics of Fluids* 35(1), 013105 (2023).
2. Y.H. Wen, C.C. Wang, G.S. Cyue, R.H. Kuo, C.H. Hsu, R.Y. Chang, Extensional rheology of linear and branched polymer melts in fast converging flows, *Rheologica Acta*, 62(4), 183-204 (2023).
3. A.Y. Malkin, A.I. Isayev, *Rheology: concepts, methods, and applications*, 4th ed. (ChemTec Publishing, Toronto 2022).
4. P. Carreau, D. De Kee, R. P. Chhabra, *Rheology of polymeric systems: principles and applications*, 2nd ed. (Hanser, Munich 2021).
5. J.M. Dealy, D.J. Read, R.G. Larson, *Structure and rheology of molten polymers: from structure to flow behavior and back again*, 2nd ed. (Hanser, Munich 2018).
6. C.W. Macosko, *Rheology: principles, measurements, and applications* (Wiley, New York 1994).

Vedoucí diplomové práce: **prof. Ing. Martin Zatloukal, Ph.D., DSc.**
Ústav inženýrství polymerů

Datum zadání diplomové práce: **2. ledna 2024**
Termín odevzdání diplomové práce: **10. května 2024**

L.S.

prof. Ing. Roman Čermák, Ph.D. v.r.
děkan

doc. Ing. Martin Bednařík, Ph.D. v.r.
ředitel ústavu

Ve Zlíně dne 27. února 2024

PROHLÁŠENÍ AUTORA
DIPLOMOVÉ PRÁCE

Beru na vědomí, že:

- diplomová práce bude uložena v elektronické podobě v univerzitním informačním systému a dostupná k nahlédnutí;
- na moji diplomovou práci se plně vztahuje zákon č. 121/2000 Sb. o právu autorském, o právech souvisejících s právem autorským a o změně některých zákonů (autorský zákon) ve znění pozdějších právních předpisů, zejm. § 35 odst. 3;
- podle § 60 odst. 1 autorského zákona má Univerzita Tomáše Bati ve Zlíně právo na uzavření licenční smlouvy o užití školního díla v rozsahu § 12 odst. 4 autorského zákona;
- podle § 60 odst. 2 a 3 autorského zákona mohu užít své dílo – diplomovou práci nebo poskytnout licenci k jejímu využití jen s předchozím písemným souhlasem Univerzity Tomáše Bati ve Zlíně, která je oprávněna v takovém případě ode mne požadovat přiměřený příspěvek na úhradu nákladů, které byly Univerzitou Tomáše Bati ve Zlíně na vytvoření díla vynaloženy (až do jejich skutečné výše);
- pokud bylo k vypracování diplomové práce využito softwaru poskytnutého Univerzitou Tomáše Bati ve Zlíně nebo jinými subjekty pouze ke studijním a výzkumným účelům (tj. k nekomerčnímu využití), nelze výsledky diplomové práce využít ke komerčním účelům;
- pokud je výstupem diplomové práce jakýkoliv softwarový produkt, považují se za součást práce rovněž i zdrojové kódy, popř. soubory, ze kterých se projekt skládá. Neodevzdání této součásti může být důvodem k neobhájení práce.

Prohlašuji,

- že jsem na diplomové práci pracoval samostatně a použitou literaturu jsem citoval. V případě publikace výsledků budu uveden jako spoluautor.
- že odevzdaná verze diplomové práce a verze elektronická nahraná do IS/STAG jsou obsahově totožné.

Ve Zlíně dne:

Jméno a příjmení studenta:

……………………………..
podpis studenta

ABSTRAKT

Diplomová práce se zabývá experimentálním výzkumem vlivu konstrukce kapilárních hlav na velikost vstupní tlakové ztráty pro stanovení jednoosé tahové viskozity polymerních tavenin pomocí vysokotlaké kapilární reometrie. Testy byly provedeny pro dva odlišné polymery při různých teplotách, deformacích a deformačních rychlostech se specifickým důrazem na pochopení vlivu kontrakčního poměru (dosahovaného změnou průměru válce při zachování konstantního průměru kapilár o prakticky nulové délce) na generovanou vstupní tlakovou ztrátu taveniny rozvětveného nízkohustotního polyethylenu. Jednoosá tahová viskozita byla stanovena jak podle Gibsonovy a původní Cogswellovy metody, tak pomocí modifikované Cogswellovy metody navržené Padmanabhanem, které byly porovnány s nezávislými měřeními provedenými pomocí metody EVF a Sentmanatova elongačního reometru. Následně byly testovány celkem čtyři pokročilé konstituční rovnice pro pochopení jejich schopnosti popsat smykovou viskozitu a nemonotónní průběh jednoosé tahové viskozity.

Klíčová slova: Tok náhlou kontrakcí, Vstupní tlaková ztráta, Kontrakční poměr, Jednoosá tahová viskozita, Konstituční rovnice.

ABSTRACT

This Master's thesis deals with the experimental research on the effects of the capillary dies design on the entrance pressure drop for the determination of the uniaxial extensional viscosity of polymer melts using high-pressure capillary rheometry. The tests were carried out for two different polymers at different temperatures, strains and strain rates with a specific emphasis on understanding the effect of the contraction ratio (achieved by changing the diameter of the barellu while maintaining a constant diameter of capillaries of practically zero length) on the generated entrance pressure drop of the branched low density polyethylene melt. Uniaxial extensional viscosity was determined by both Gibson's and the original Cogswell method, and the modified Cogswell method proposed by Padmanabhan, which were compared with independent measurements made using the EVF method and the Sentmanat extensional rheometer. Subsequently, four different advanced constitutive equations were tested to understand their ability to describe the shear viscosity and the non-monotonic character of the uniaxial extensional viscosity.

Keywords: Flow through abrupt contractions, Entrance pressure drop, Contraction ratio, Uniaxial extensional viscosity, Constitutive equations.

ACKNOWLEDGEMENTS

From the bottom of my heart, I would like to thank everyone who supported me during my studies. Especially to my family and loved ones, to whom we are very grateful.

Significantly and above all, I would like to thank the supervisor of my Master’s thesis, prof. Ing. Martin Zatloukal, Ph.D. DSc., for his endless patience, help, and support in completing the individual phases of this thesis. Furthermore, for the incredible amount of information provided and initiation into the fascinating scientific field of Rheology. I appreciate it very much, and there are probably no words of thanks to express it.

I also thank all the academic staff of the Faculty of Technology for providing valuable and interesting information.

Other thanks go to Dr. Sylvie Vervoort from the Dow Chemical Company, for providing the molecular characteristics of the LDPE material.

The Grant Agency of the Czech Republic (Grant No. 24-11442S) is also to be thanked for financial support.

The author also wishes to thank NETZSCH Gerätebau GmbH for providing the Rosand RH10 capillary rheometer.

I hereby declare that the print version of my Master's thesis and the electronic version of my thesis deposited in the IS/STAG system are identical.

CONTENTS

INTRODUCTION

Rheology is an interdisciplinary science discipline that describes the deformation and flow of matter with non-standard complex behavior, which can range from the ideal viscous behavior of liquids to the ideal elastic behavior of solids. Rheology is important in describing and predicting the flow behavior of the polymer being processed and eliminating flow instabilities [1], designing and optimizing the production process [2] [3], and controlling or differentiating individual polymer lots [4][5]. The knowledge and laws of rheology are not only used in the processing of polymer melts, suspensions [6], solutions [7], or emulsions [8] but also in the processing and description behavior of various foods [9], coatings [10], cosmetics [11] and many other matters with complex behavior [12].

Viscosity is a fundamental rheological property characterizing the degree of resistance of a polymer material to applied external loads or the resistance of the polymer to flow during processing. Depending on the type of flow, which is standardly divided into shear and extensional, shear and extensional viscosity can be defined. During industrial processing, the polymer is usually subjected to a combination of shear and extensional flows. Extensional viscosity is usually neglected due to its imprecise experimental determination, simplified modeling and simulation of manufacturing processes [13][14][15].

However, for a better understanding of the macromolecular structure of polymers, optimization of process settings, design of production equipment, and prediction of unstable flow, accurate knowledge of extensional viscosity is essential, especially for technologies where extensional flow is dominant. These include blow molding, injection molding, extrusion, and coextrusion processes (especially for dies with converging flow channels), rolling, foaming, and fiber production.

Although there are several experimental methods for determining extensional viscosity [16][17][18][19], only one of them allows the determination of extensional viscosity at high extensional strain rates, which occur in a wide range of manufacturing processes such as melt blown or injection molding. An undeniable advantage of this measurement technique is the possibility to evaluate both high-viscosity [20] and low-viscosity [21] polymer systems. This method is based on the entrance pressure drop measurements during the flow of polymer melts by abrupt contraction using a capillary rheometer [22][23]. Since this is not a homogeneous extensional flow and the extensional viscosity cannot be obtained directly, some "approximation" techniques [24][25][26] have been developed to obtain the extensional viscosity from the measured values.

The simplest way to obtain the entrance pressure drop as accurately as possible is to use an orifice die (a die having virtually zero length). However, several influences negatively affect entrance pressure drop measurements, which are connected with the die design when followed concerning correct functionality, manufacturability, rigidity, and easy assembly or disassembly.

Many publications have discussed these influences and methods of their possible elimination. The last studies in this area have focused on the problem of filling the exit region of an orifice die; some of the authors who have made improvements to the design of commercial orifice die have been Kim and Dealy [27][28] and Zatloukal and Musil [29]. However, another important and many authors underestimated effect in measuring entrance pressure drop is emphasized by Rajagopalan [30] in his numerical study. He says that it is not always guaranteed that the contraction flow occurs in a steady state. Whether the melt reaches a steady state is primarily determined by the polymer material and the magnitude of the melt's total deformation during the contraction flow.

To achieve steady-state values of extensional stresses, it is necessary to design a flow channel geometry that can influence the time and nature of polymer melt extension, such that the total strain at a given deformation rate is sufficiently high at the entrance region of the die orifice.

The primary purpose of this work is therefore to investigate the effect of die design on extensional viscosity determination from entrance pressure drop measurements, to evaluate different techniques relating entrance pressure drop to extensional viscosity, and to compare the obtained data with experimental data obtained by other relevant experimental techniques.

I. THEORY

1 INTRODUCTION TO POLYMER MELT RHEOLOGY

At the Third Plasticity Symposium in December 1928 [31], it was decided that due to the need to characterize the non-standard behavior of newly emerging complex matters [16][32], it is necessary to establish the society to deal with these problems (the future Society of Rheology was officially established in 1929). This conference thus formally give rise to a new interdisciplinary science that combines the foundations of physics, chemistry, materials engineering, and other branches of science [19]. At the suggestion of Prof. Bingham, a colloidal chemist who had long been involved in plastic flow [23], the name "Rheology" [33][34] (the root "Rheo" means flow in Greek) [19] was assigned to this branch of science, which studies deformation and flow of matter.

Rheology has not been concerned with the study of electron flow and heat flow since its inception [35], nor with purely hydrodynamic, aerodynamic, or problems associated with classical elasticity theory because they were sufficiently addressed in separate branches of physics [35][36][37]. The flow behavior of polymeric materials is one of the main areas of interest for Rheologists.

1.1 A short review of Continuum Mechanics

The main subject of rheology is the study of how the flow properties of matter are influenced by their structure (composition) or temperature and pressure [3][38]. Furthermore, investigate and develop relationships between the applied stress (state), the resulting deformation/strain (geometry change), and the deformation/strain rate (kinematics) of the loaded material at a given point [38]. The mathematical formulation of such relationships is called the constitutive equation (see Chapter 4) [16][19].

The following subsections will briefly discuss basic rheological parameters and relationships using continuum mechanics (where a continuum is a matter, a body with a continuous medium [39]). These parameters are detailed in publications such as [3][16][19][35] [38][40][41].

1.1.1 Stress (Stress Tensor)

Stress is a physical quantity of continuum mechanics that characterizes the state of the continuum and is induced by external forces [42]. However, this is not the case for heterogeneous materials (e.g., filled polymers, blends) where residual or thermal stresses may be generated [19]. Stresses can also be defined as the interaction of one part of a continuous medium between adjacent ones utilizing internal forces [16][38][42].

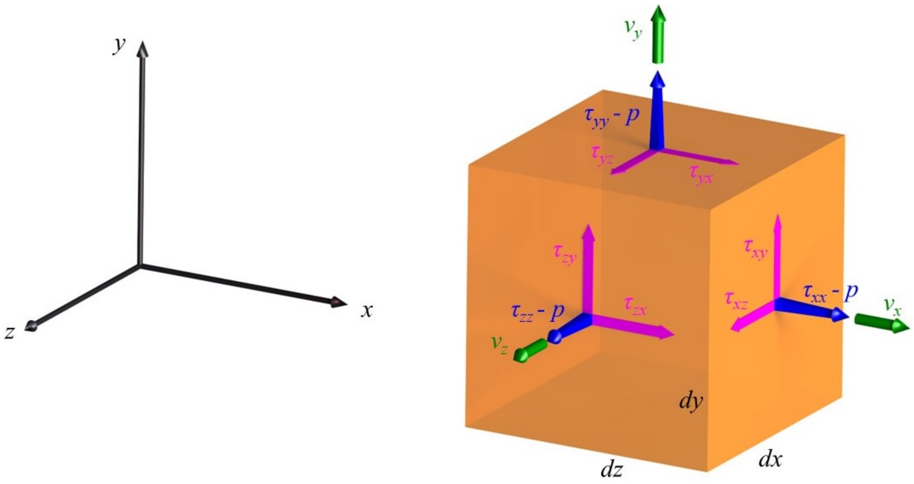

Figure 1 Stress components and velocity vectors of a cubic material element *dx dy dz* in the Cartesian coordinate system (*x, y, z*) (adapted from [2][3][41][43])

From the visualization shown (Fig. 1), it can be concluded that stress is a second-order tensor quantity that describes the stress state of a solid with up to nine stress components, three normal $(\tau_{xx}, \tau_{yy}, \tau_{zz})$ and six shear $(\tau_{xy}, \tau_{yx}, \tau_{xz}, \tau_{zx}, \tau_{zy}, \tau_{yz})$. Each stress component has two indices, the first indicating the direction of the normal to the surface on which the stress is applied and the second indicating the direction of its application [19]. The total stress tensor $\underline{\underline{\sigma}}$ with the standard continuum mechanics convention (normal stress τ_{xx} is positive and pressure p is negative) [16][19], according to the following equation:

$$\underline{\underline{\sigma}} = \begin{pmatrix} \tau_{xx} - p & \tau_{xy} & \tau_{xz} \\ \tau_{yx} & \tau_{yy} - p & \tau_{yz} \\ \tau_{zx} & \tau_{zy} & \tau_{zz} - p \end{pmatrix}, \tag{1}$$

where p is the isotropic pressure (for incompressible materials, which practically include polymer melts, the pressure p is a constant) [44]. The tensor $\underline{\underline{\sigma}}$ is so-called symmetric since its matrix is symmetric along the main diagonal. If the indexes of the stress components (e.g., $xy \Longrightarrow yx$) are exchanged, their values do not change (combined shear stress $\tau_{xy} = \tau_{yx}$). Hence, due to symmetry, tensor $\underline{\underline{\sigma}}$ can be expressed by only six independent components [38][35]. The matrix notation of stress (Eq.1) without the presence of pressure p is called an extra stress tensor $\underline{\underline{\tau}}$ [45].

1.1.2 Deformation (Strain Tensor)

Deformation (strain) is a change in the shape of a body in space caused by an external force in which the distance of individual points within the body changes [16][19]. Volumetric changes in the shape of a solid can also be expressed by the extension ratio λ_{ER}, which indicates by what proportion the solid has been extended [19].

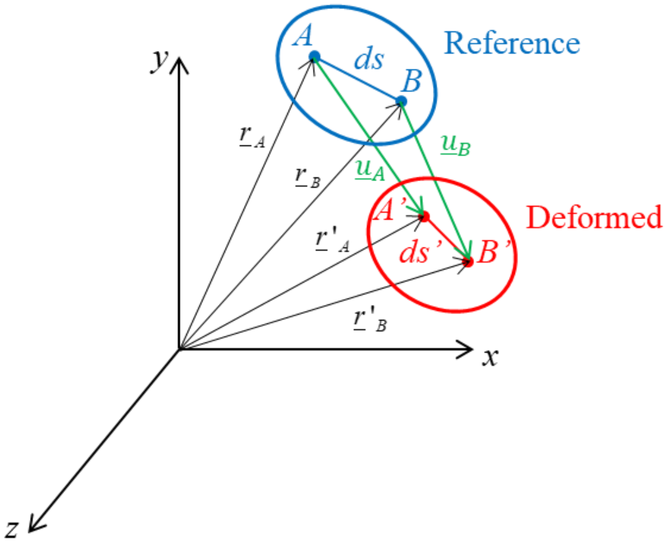

Figure 2 Visualization of deformation, displacement of two arbitrary points A and B (characterized by radius vector $\underline{r}_A$, $\underline{r}_B$) of the body to the new position A' and B' (characterized by radius vector $\underline{r}'_A$, $\underline{r}'_B$), and the change of the infinitesimally small distances ds to ds' between them (adapted from [19])

Fig. 2 shows the infinitesimal distances ds of two arbitrary points of the unloaded body A and B. After strain, these points move to new positions A' and B' with their new again infinitesimal distance ds' [19][38]. The following equation gives the scalar deformation ε sometimes called as “engineering strain”

$$\varepsilon = \frac{ds - ds'}{ds}. \tag{2}$$

However, the strain as a measure of the change in distance between points A and B can, like the stress (see Section 1.1), be written in tensor form (coordinates x, y, z) with six independent strain components $\underline{\underline{\varepsilon}}$

$$\underline{\underline{\varepsilon}} = \frac{1}{2}\left(\frac{\partial u_i}{\partial x_j} + \frac{\partial u_j}{\partial x_i}\right) + \frac{1}{2}\left(\frac{\partial u_x}{\partial x_i}\frac{\partial u_x}{\partial x_j} + \frac{\partial u_y}{\partial x_i}\frac{\partial u_y}{\partial x_j} + \frac{\partial u_z}{\partial x_i}\frac{\partial u_z}{\partial x_j}\right), \tag{3}$$

where the values u_i and u_j (where $i, j = x, y, z$) represent the components (projections) of the displacement vector $\underline{u}$ ($\underline{u}_A$ or $\underline{u}_B$), which can be defined as the movement of point A (or B) to its new position A' (or B') [19]. At small deformations (<< 1), it is possible to simplify (Eq. 3) by linearizing it and obtaining only the derivative term (the first right-hand term in Eq. 3) [42]. Such a tensor is called the small or infinitesimal deformation tensor $\underline{\underline{d}}$

$$\underline{\underline{d}} = \begin{pmatrix} \frac{\partial u_x}{\partial x} & \frac{1}{2}\left(\frac{\partial u_x}{\partial y} + \frac{\partial u_y}{\partial x}\right) & \frac{1}{2}\left(\frac{\partial u_x}{\partial z} + \frac{\partial u_z}{\partial x}\right) \\ \frac{1}{2}\left(\frac{\partial u_y}{\partial x} + \frac{\partial u_x}{\partial y}\right) & \frac{\partial u_y}{\partial y} & \frac{1}{2}\left(\frac{\partial u_y}{\partial z} + \frac{\partial u_z}{\partial y}\right) \\ \frac{1}{2}\left(\frac{\partial u_z}{\partial x} + \frac{\partial u_x}{\partial z}\right) & \frac{1}{2}\left(\frac{\partial u_z}{\partial y} + \frac{\partial u_y}{\partial z}\right) & \frac{\partial u_z}{\partial z} \end{pmatrix}, \tag{4}$$

where, the first row of the symmetric tensor represents the components of small deformation in the x axis direction, the second in the y direction, and the third in the z direction. On the main diagonal are the components of tensile (normal) deformation, and the other components describe the change in angle (shear deformation) [19].

From a quantitative point of view, the deformation can be detected using the gradient of the relative displacement $\underline{\underline{g}}$, sometimes also referred to as $\underline{\nabla}\underline{u}$ ($\underline{\nabla}$ is the nabla operator that expresses the maximum change of the given quantity). The $\underline{\underline{g}}$ is a non-symmetric tensor quantity that nine dimensionless components can describe [16][19][38]

$$\left(\underline{\nabla}\underline{u}\right) = \underline{\underline{g}} = \frac{1}{2}\left(\frac{\partial u_i}{\partial x_j} + \frac{\partial u_j}{\partial x_i}\right) + \frac{1}{2}\left(\frac{\partial u_i}{\partial x_j} - \frac{\partial u_j}{\partial x_i}\right). \tag{5}$$

The (Eq. 5) shows that the gradient of the relative displacement is composed of two parts: the deformation $\underline{\underline{d}}$ and the rotation $\underline{\underline{\theta}}$

$$\underline{\underline{g}} = \underline{\underline{d}} + \underline{\underline{\theta}}. \tag{6}$$

The tensor rotation $\underline{\underline{\theta}}$ is again a second-order tensor quantity that describes the rotation of infinitesimal volumes inside a body [19].

1.1.3 Deformation rate (Deformation Rate Tensor)

The strain rate describes the kinematics (motion) of the loaded body. In Fig. 1, a cubic material element *dx dy dz* can be observed in the Cartesian coordinate system (x, y, z) whose motion is characterized by the velocity vector components $\underline{v}$ (v_x, v_y, v_z) [2][40].

The maximum change in the velocity vector $\underline{v}$ in a given direction is determined by the velocity gradient $\underline{\underline{L}}$, sometimes also called $\underline{\nabla}\,\underline{v}$ [16]. It is about a second-order tensor quantity that can be expressed using the time derivative of the gradient of the relative displacement $\underline{\underline{g}}$ (Eq. 5) [19][35][40]

$$\left(\underline{\nabla}\,\underline{v}\right)=\underline{\underline{L}}=\frac{\partial v_i}{\partial x_j}=\frac{\partial}{\partial x_j}\frac{\partial u_i}{\partial t}=\frac{\partial}{\partial t}\left(\frac{\partial u_i}{\partial x_j}\right)=\left(\frac{\partial \underline{\underline{g}}}{\partial t}\right). \tag{7}$$

For completeness, the transposed velocity gradient $\underline{\underline{L}}^T$ [35] is as follows:

$$\left(\underline{\nabla}\,\underline{v}\right)^T=\underline{\underline{L}}^T=\frac{\partial v_j}{\partial x_i}. \tag{8}$$

As well as the relative position gradient $\underline{\underline{g}}$, the velocity gradient $\underline{\underline{L}}$ is a second-order tensor quantity described by the nine-component:

$$\underline{\underline{L}}=\frac{1}{2}\left(\frac{\partial v_i}{\partial x_j}+\frac{\partial v_j}{\partial x_i}\right)+\frac{1}{2}\left(\frac{\partial v_i}{\partial x_j}-\frac{\partial v_j}{\partial x_i}\right). \tag{9}$$

The tensor $\underline{\underline{L}}$ consists of two parts: a symmetric strain rate tensor $\underline{\underline{D}}$, and an unsymmetrical rotation tensor $\underline{\underline{W}}$

$$\underline{\underline{L}}=\underline{\underline{D}}+\underline{\underline{W}}. \tag{10}$$

The symmetric strain rate tensor, $\underline{\underline{D}}$, for small deformations, characterizes the changes in the shape of the body at a given point [19] and is indicative of the intensity and type of polymer flow

$$\underline{\underline{D}}=\begin{pmatrix} \dfrac{\partial v_x}{\partial x} & \dfrac{1}{2}\left(\dfrac{\partial v_x}{\partial y}+\dfrac{\partial v_y}{\partial x}\right) & \dfrac{1}{2}\left(\dfrac{\partial v_x}{\partial z}+\dfrac{\partial v_z}{\partial x}\right) \\ \dfrac{1}{2}\left(\dfrac{\partial v_y}{\partial x}+\dfrac{\partial v_x}{\partial y}\right) & \dfrac{\partial v_y}{\partial y} & \dfrac{1}{2}\left(\dfrac{\partial v_y}{\partial z}+\dfrac{\partial v_z}{\partial y}\right) \\ \dfrac{1}{2}\left(\dfrac{\partial v_z}{\partial x}+\dfrac{\partial v_x}{\partial z}\right) & \dfrac{1}{2}\left(\dfrac{\partial v_z}{\partial y}+\dfrac{\partial v_y}{\partial z}\right) & \dfrac{\partial v_z}{\partial z} \end{pmatrix}, \tag{11}$$

the main diagonal contains the tensile strain rate components (see Section 2.1), and the other position are the shear strain rate components (see Section 2.2) [2][40].

1.2 The Deborah (De) and Weissenberg (Wi) numbers

The Deborah number (*De*) is a dimensionless quantity and one of the important parameters of rheology [16][35][46]. It serves to provide information about the effect of time on the change in shape (deformation) or flow of a particular material [47] and, therefore the characterization of the behavior of matters [12][48]. The *De* was defined by Marcus Rainer based on a biblical hymn (psalm) sung by the prophetess Deborah after her victory over the Philistines: “The mountains flowed before the Lord” (Judges 5:5) [34]. It is important to note here that Rainer used this exact passage from the 1611 King James Version of the Bible. There are many publications and analyses that address the question of whether the translation of the archaic Hebrew passage used is correct. There are tens of other translations which, for example, instead of “the mountains flowed,” say “the mountains trembled before the Lord,” [49]. This passage's illustration (Fig. 3) is given in the original archaic Hebrew.

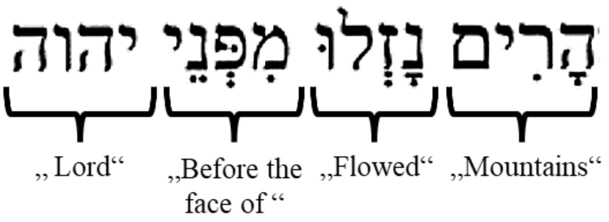

Figure 3 The original text of the passage in Biblical Hebrew. It is read from right to left (adapted from [49])

The publication [49] discusses in detail the correctness of the translation used by Rainer and compares different translations and opinions. The conclusion of the paper [49] is that the translation used by Rainer is grammatically correct, but not in the complete same sense.

The passage (Fig. 3) inspired Rainer, and he realized that from the perspective of the infinite observation time of God, "the mountains flow", although, from the perspective of mortal man's time, they appear rigid [34][50]. Deborah's number, *De*, can thus be defined by the following equation:

$$\mathrm{De} = \frac{\lambda}{\Theta}. \tag{12}$$

Relaxation time λ is a material parameter that characterizes the stress relaxation after deformation or flow [18][46] and characteristic flow time Θ is always tied to the process [16][48].

In addition to *De*, another dimensionless quantity, the Weissenberg number (*Wi*), can be used to characterize the viscoelastic behavior, which can be defined for steady shear as follows:

$$\mathrm{Wi} = \lambda \dot{\gamma}, \tag{13}$$

where λ is the characteristic time scale and $\dot{\gamma}$ is the characteristic shear strain rate [48][51].

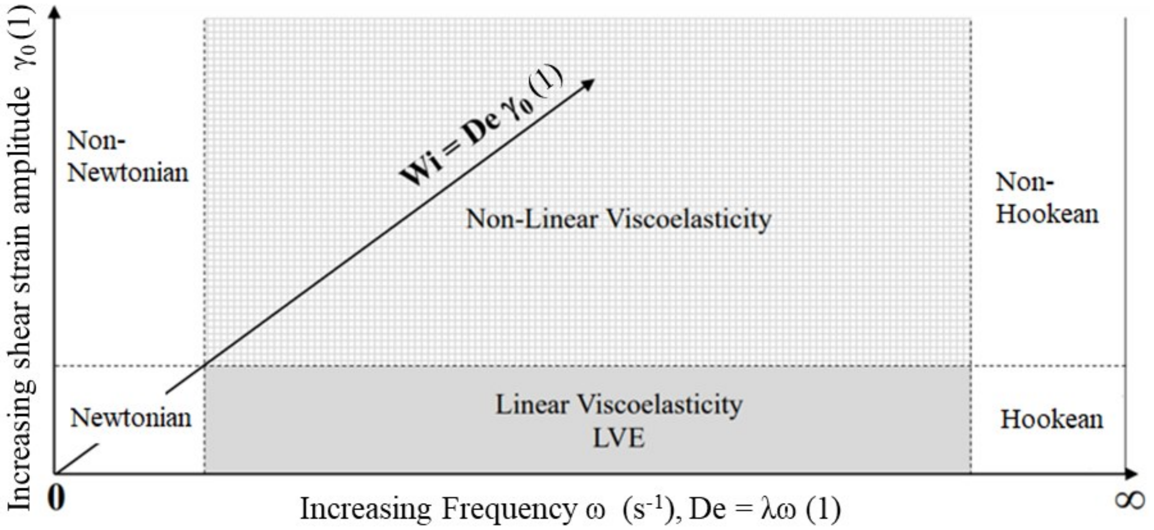

Figure 4 Distribution of the flow/deformation behavior of matter using Pipkin map, with the use of dimensionless quantities Deborah's number *De* and Weissenberg's number *Wi* (adapted from [52])

Although according to *De* the behavior of matter appears to be Newtonian, the magnitude of the applied deformation also influences its behavior. At high shear strains $\dot{\gamma}$, this behavior is nonlinearly viscoelastic, as illustrated by the Pipkin map (Fig. 4), which separates the behavior of matter in this view for “oscillatory steady-state shear flows” [46]. As can be seen from Fig. 4, the *Wi* can be expressed as the ratio of two strain rates when considering shear steady-state flow. If $\mathrm{Wi} \gg 1$, it is a nonlinear viscoelastic behavior, conversely, when $\mathrm{Wi} \ll 1$ the behavior is linearly viscoelastic [51][52].

From the above, it is possible to conclude that the viscoelastic behavior of the investigated matter is not only determined by the time aspect (defined by *De*) but also by the deformation aspect (defined by *Wi*).

2 SHEAR AND EXTENSION FLOW (BASIC FLOWS)

Shear and extensional flows are among the basic (standard) flows in polymeric materials' rheological measurements and manufacturing processes [18]. In most processing processes, polymer flow is composed of a combination of shear and extensional; mostly, one type dominates and thus controls the flow [44].

2.1 Shear flow

Shear flow is the most discussed flow across rheology and is considered the easiest flow to achieve in laboratory measurements [18][53]. The shear flow or shear deformation of a unit melt element considered from an incompressible material is demonstrated in Fig. 5 [44][45].

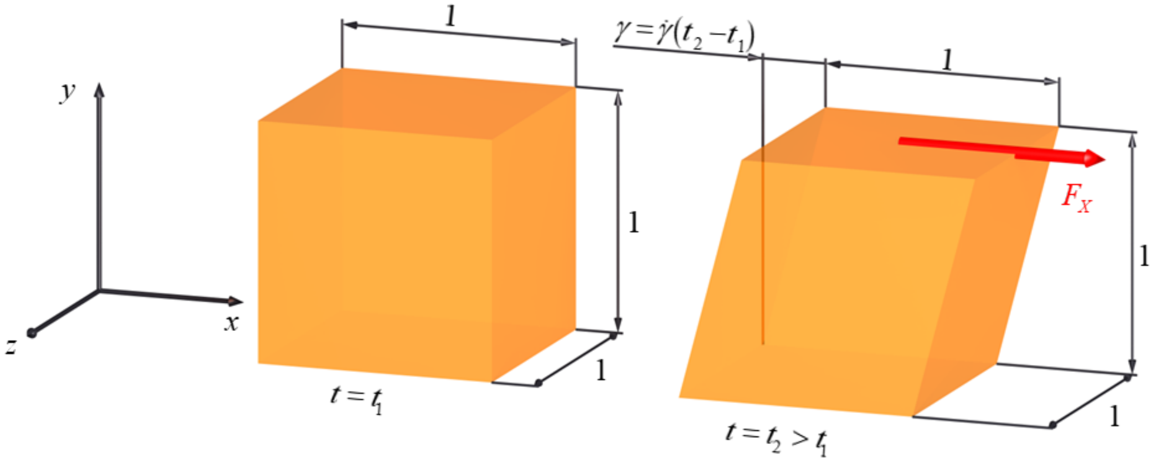

Figure 5 Schematic definition of shear flow/deformation of a melt element starting at time t_1 and ending at time t_2 caused by force (F_x) action in the x-axis at neglecting the rotation of the element (adapted from [41][43][44])

The deformation of an element (Fig. 5) is caused by an unknown load starting at time t_1 (when the body is at rest) and ending at time t_2. The resulting angle that is clamped between the edge of the deformed element and the y-axis is referred to as the shear strain γ [41][45] and is mathematically written as follows:

$$\gamma=\dot{\gamma}\left(t_2-t_1\right), \tag{14}$$

where $\dot{\gamma}$ is the rate of shear deformation (shear rate), and the bracket (t_2-t_1) characterizes the time interval over which the deformation occurs [3].

A simple shear flow of a melt element is generally defined and labeled according to Fig.5. Its characteristic feature is a constant melt velocity in the direction of the streamline (x-axis

Fig. 5), and a change of this velocity in one direction perpendicular to it (y-axis Fig. 5). An axis with no change in velocity is referred to as neutral (z-axis Fig. 5) [3][18].

The velocity profile for simple shear flow according to the above convention can be given as follows:

$$v_x = \dot{\gamma} y,\ v_y = 0,\ v_z = 0, \tag{15}$$

where $\dot{\gamma}$ can be a constant or time-dependent $\dot{\gamma}(t)$ (oscillatory shear flow [52]) [45]. If the $\dot{\gamma}$ is time-independent in shear flow, one can speak of a so-called steady, simple shear flow for which the stress responses are time-independent [37] (see Section 2.1.1).

For a steady, simple shear flow, the general tensor of the strain rate $\underline{\underline{D}}$ (Eq. 11) can be transformed into the following form based on the velocity field given above (Eq. 15)

$$\underline{\underline{D}} = \begin{pmatrix} 0 & \frac{\dot{\gamma}}{2} & 0 \\ \frac{\dot{\gamma}}{2} & 0 & 0 \\ 0 & 0 & 0 \end{pmatrix}. \tag{16}$$

The total stress tensor $\underline{\underline{\sigma}}$, for an incompressible polymer melt can again be adapted from the general form $\underline{\underline{\sigma}}$ (Eq. 1) for steady, simple shear flow to the following form:

$$\underline{\underline{\sigma}} = \begin{pmatrix} \tau_{xx} - p & \tau_{xy} & 0 \\ \tau_{yx} & \tau_{yy} - p & 0 \\ 0 & 0 & \tau_{zz} - p \end{pmatrix}. \tag{17}$$

During the shear flow of viscoelastic liquids such as polymer melts, normal stress components are generated. There are two normal stress differences: first, N_1 and second N_2, [18] defined as follows:

$$N_1 = (\tau_{xx} - p) - (\tau_{yy} - p) = \tau_{xx} - \tau_{yy}, \tag{18}$$

$$N_2 = (\tau_{yy} - p) - (\tau_{zz} - p) = \tau_{yy} - \tau_{zz}. \tag{19}$$

The N_1 usually achieve higher positive values. On the contrary N_2 takes negative values and reaches smaller values than N_1 (about 5 to 30 % of the magnitude of N_1) [16]. Thus, in a typical shear flow measurement, three nonzero stress quantities (sometimes referred to as extra stresses) are detected: the shear stress $\left(\tau_{xy} = \tau_{yx}, \text{ see Section 1.1}\right)$ and the first N_1 and second N_2 normal stress differences [18].

2.1.1 Material functions for steady shear flow

For a complete characterization of the steady shear flows of the measured polymer material, three dependencies of the material function on the constant shear rate ($\dot{\gamma}$ = const.) are needed. These functions are sometimes also referred to as viscometric functions (see Section 2.1.2) [54].

These functions include the dependence of shear viscosity on shear rate $\dot{\gamma}$, which at low $\dot{\gamma}$ is directly proportional to $\dot{\gamma}$ and is referred to as "zero shear rate (Newtonian) viscosity" η_0 [38] defined as:

$$\tau_{xy} = \eta\dot{\gamma}\,. \tag{20}$$

Others are the dependence of N_1 and N_2 on the shear strain rate $\dot{\gamma}$. Since N_1 and N_2 are directly proportional to the second-order shear rate $\left(\dot{\gamma}^2\right)$ these quantities are expressed by the so-called normal stress difference coefficients (first ψ_1 and second ψ_2) [46]

$$\psi_1(\dot{\gamma}) = \frac{N_1}{\dot{\gamma}^2}\,, \tag{21}$$

$$\psi_2(\dot{\gamma}) = \frac{N_2}{\dot{\gamma}^2}\,. \tag{22}$$

For completeness, the results from the measurements of transient shear viscosity growth on time $\eta^+(\dot{\gamma},t)$ at constant $\dot{\gamma}$ (startup test - shear viscosity growth) [38][54] and also the transient first normal stress difference coefficient $\psi_1(\dot{\gamma},t)$ [55] will be presented as the example. These measurements [54] for PS within shear strain rate range $\dot{\gamma}$ (0.5 - 452) s^{-1} and 180 °C (these values were time and temperature shifted from the values of $\dot{\gamma}$ (0.2 - 47.16) s^{-1} and temperature 160 °C) are provided in Figs. 6, 7. From Fig. 6 it can be generally inferred that as $\dot{\gamma}$ increases, the time taken for the shear viscosity to stabilize decreases, furthermore significant overshoot and slight undershoot can be observed as $\dot{\gamma}$ increases [54][55]. The next figure (Fig. 7) shows the corresponding steady-state values of η and ψ_1. These data were also compared with the numerical prediction of the DEIA model, as can be seen in Fig. 7, which was the subject of the discussed work [55].

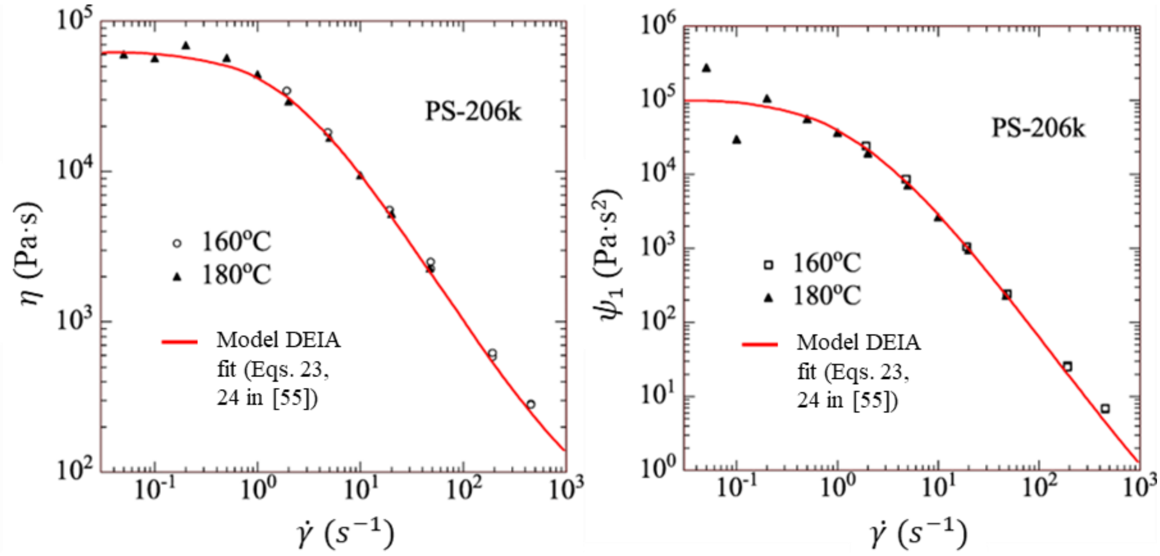

Figure 6 Shear stress growth coefficient $\eta^{+}(\dot{\gamma},t)$ and first normal stress growth coefficient $\psi_{1}(t)$ versus time *t* for PS melt at 180 °C with DEIA model predictions (taken from [55])

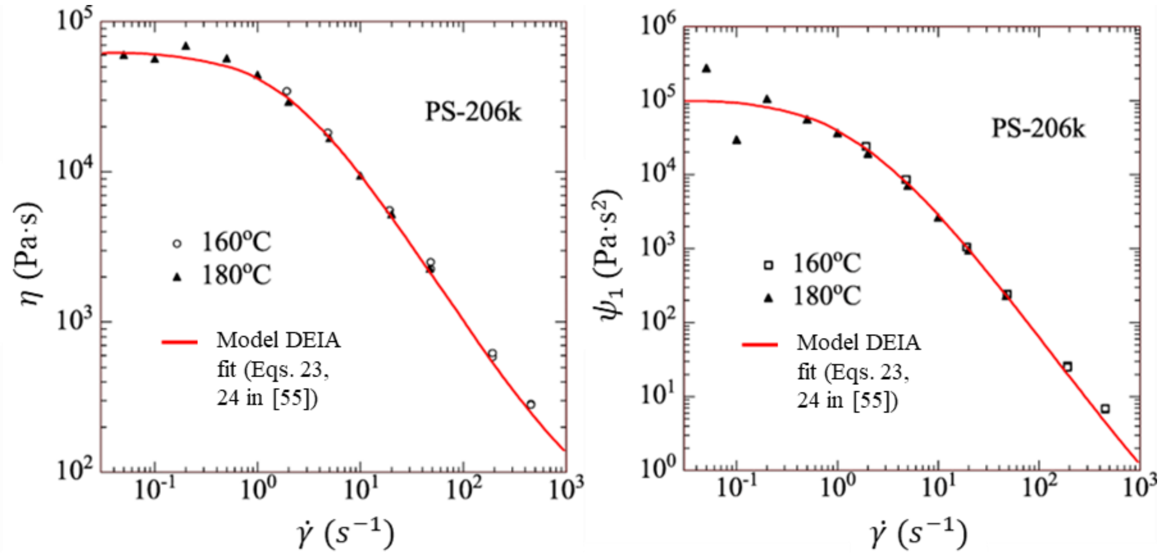

Figure 7 Steady-state shear viscosity η and steady-state first normal stress coefficient ψ_{1} versus shear rate for PS melt at 180 °C (square symbols shift data from 160 °C to 180 °C) with DEIA model prediction (taken from [55])

2.1.2 Types of Steady Simple Shear flows

The steady shear flows of the processed or measured polymer material can generally be divided into two basic flow types according to the generation mode. These are drag and pressure driven flow [3][16][53] or their combination, which can occur, e.g., in polymer melt flow inside a screw extruder or melt blown technology [2][56][50].

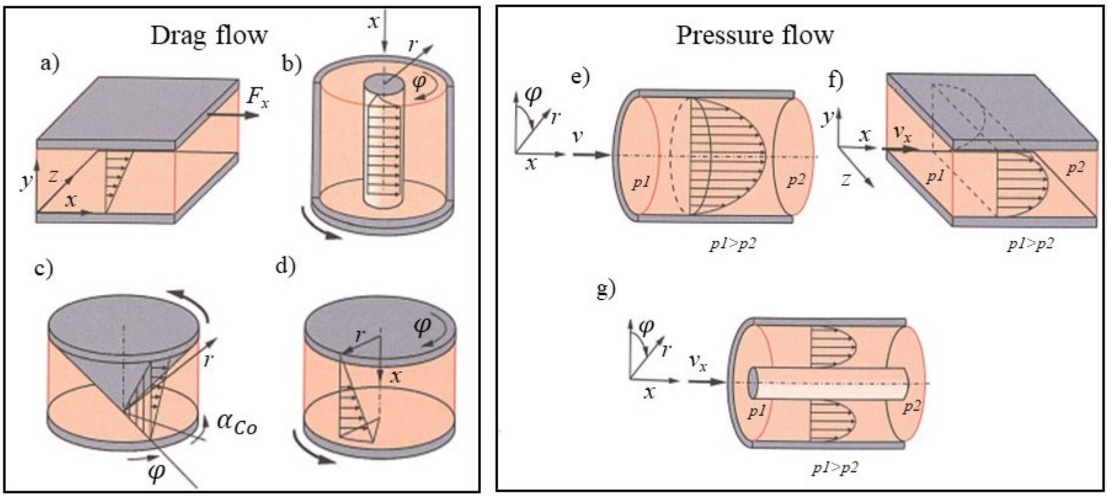

Figure 8 The steady shear flows in the simplest flow domains (adapted from [3]). Drag flow: a) between parallel plane, b) between coaxial cylinder, c) between cone a plane, d) parallel disk flow. Pressure driven flow: e) cylinder channel, f) between two parallel planes, g) annular channel

Drag flow occurs when the polymer material is sheared between two surfaces, one moving and the other is permanently stationary. The Fig. 8a-d shows the drag flows in the basic (simplest) geometries together with the velocity profiles (possible wall slip is not considered) [3][53]. In this type of flow, homogeneous deformation occurs, which means that all flow lines have the same shear strain rate $\dot{\gamma}$, and the resulting shear stress τ does not depend on the position in the flow domain (if the flow conditions assumed to be isothermal) [53].

In the case of pressure-derived flow (pressure flow), the polymer material starts to flow due to the pressure difference along the length of the closed channel. The Fig. 8d-g shows pressure flows in simple flow geometries together with velocity profiles (again, possible wall slip is not considered) [3][53]. For pressure gradient-induced flow, inhomogeneous deformation occurs, with each flow line having a different shear strain rate, which is most prominent at the wall and most minor in the middle of the flow domain [53].

It is essential to mention that both types of steady shear flow, i.e., homogeneous (drag flow) and non-homogeneous (pressure flow), are classified as viscometric flows. Their behavior is determined by the three material or viscometric functions mentioned above (Section 2.1.1) [3][53]. Methods for the experimental determination of these functions are generally described in publications such as [16][17][19][46].

2.2 Extensional flow

In pure extensional or elongation flows, the melt element is stretched in the streamline's longitudinal direction without shear components (shear-free flow). The velocities (distances) of the melt particles on the same streamline change only in the direction of flow during extensional flow [53].

Knowledge of extensional flows is important for many polymer material processing processes. Further, they can also provide information about the branching of long polymer chains that shear measurements cannot reveal [14][38]. Typically (basic), three steady-state extensional flows are distinguished: uniaxial, biaxial, and planar extensional flow.

Extensional flows are characterized by large extensional deformations (strain) ε, which can be determined for the "1D cases" (typical for direct stretching, e.g., FSR see Section 2.2.5) along the general length *l* using the following differential equation:

$$d\varepsilon = \frac{1}{l} dl . \tag{23}$$

Solving this differential equation gives the following equation:

$$\varepsilon_H = \int_{l_0}^{l} d\varepsilon \frac{1}{l} dl = \ln\left(\frac{l}{l_0}\right) = \ln \lambda_{ER} , \tag{24}$$

where l_0 is the original length of the element, and *l* is the length after deformation, ε_H is the so-called Hencky strain (total extensional strain), which is widely used for large extensional deformations, polymer melts, and rubber materials, λ_{ER} is the extension ratio (mentioned already in Section 1.1.2) [17][57].

Figs. 9 -11 show basic steady-state extensional flows. In these cases, the incompressible melt element is deformed in the time interval $(t_2 - t_1)$, similar to shear (where t_1 is the beginning and t_2 is the end). The resulting total Hencky deformation ε_H can be expressed using the following equation:

$$\varepsilon_H = \dot{\varepsilon}(t_2 - t_1), \tag{25}$$

where $\dot{\varepsilon}$ is the rate of extensional deformation (extensional rate) [44], sometimes also referred to as the Hencky strain rate $\dot{\varepsilon}_H$ (in this thesis, will be $\dot{\varepsilon}_H = \dot{\varepsilon}$) [19][57].

In general, the velocity field for different steady-state extensional flows can be described using the convention in the Cartesian coordinate system (*x*, *y*, *z*) introduced by

Meissner et al. [58], which uses the parameter m [16][17][59]. According to the following equation:

$$v_x = \dot{\varepsilon}x,\ v_y = \dot{\varepsilon}my,\ v_z = -\dot{\varepsilon}(1+m)z\,. \tag{26}$$

2.2.1 Uniaxial Extensional Flow

Uniaxial flow is the simplest steady-state extensional flow, in which the melt element is stretched (by the force F_x) in one direction only (x-axis direction) and contracted in the other two directions (y and z directions), as can be seen in Fig. 9. The visualization also beautifully demonstrates the change in distance or velocity of two adjacent material particles [60].

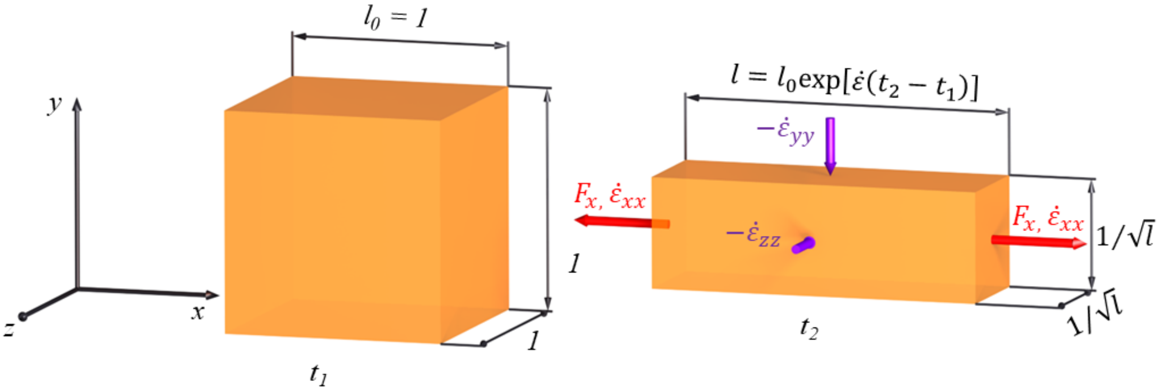

Figure 9 Uniaxial extensional flow of polymer melt element (adapted from [43][60])

According to the above convention for uniaxial extensional flow, the parameter $m = -0.5$ [16][45]. Then, the general velocity field (Eq. 26) for uniaxial extensional flow can be overwritten as follows:

$$v_x = \dot{\varepsilon}x,\ v_y = -\frac{1}{2}\dot{\varepsilon}y,\ v_z = -\frac{1}{2}\dot{\varepsilon}z\,. \tag{27}$$

The uniaxial extensional rate tensor $\underline{\underline{D}}$ can be expressed after modifying the general relation (Eq. 11) as follows:

$$\underline{\underline{D}} = \begin{pmatrix} \dot{\varepsilon} & 0 & 0 \\ 0 & -\frac{1}{2}\dot{\varepsilon} & 0 \\ 0 & 0 & -\frac{1}{2}\dot{\varepsilon} \end{pmatrix}. \tag{28}$$

The above matrix (Eq. 28) shows the validity of the law of conservation of volume since the sum of the diagonal components of the uniaxial extensional flow is zero. The positive components demonstrate the stretching of the melting element in a given direction. Negative components, on the other hand, show shrinkage of the material in a given direction. This is also true for other steady extensional flows [45].

The general total tensor stress $\underline{\underline{\sigma}}$ form (Eq. 1) for all basic extensional flows can be given as follows:

$$\underline{\underline{\sigma}} = \begin{pmatrix} \tau_{xx} - p & 0 & 0 \\ 0 & \tau_{yy} - p & 0 \\ 0 & 0 & \tau_{zz} - p \end{pmatrix}. \tag{29}$$

In the case of uniaxial extensional flow, there is only one non-zero normal stress difference, which is the uniaxial extensional stress $\sigma_{E,U}$

$$\sigma_{E,U} = (\tau_{xx} - p) - (\tau_{yy} - p) = (\tau_{xx} - p) - (\tau_{zz} - p) = \tau_{xx} - \tau_{yy} = \tau_{xx} - \tau_{zz}\,. \tag{30}$$

For steady-state extensional flows, the main property or material parameter is the extensional viscosity η_E, which expresses the resistance of the liquid against to the applied extensional flow [14][61][16]. Uniaxial extensional viscosity $\eta_{E,U}$ can be determined from the following equation:

$$\eta_{E,U} = \frac{\sigma_{E,U}}{\dot{\varepsilon}} = \frac{\tau_{xx} - \tau_{yy}}{\dot{\varepsilon}}\,. \tag{31}$$

Based on his groundbreaking work in this area, Trouton derived a ratio that relates the zero shear rate (Newtonian) viscosity η_0 to the extensional viscosity η_E [16]. For polymer melts, this ratio applies, but only at low extensional strain rates $\dot{\varepsilon}$ [62]. For uniaxial extensional flow, the Trouton ratio (*Tr*) can be written as follows:

$$\eta_{E,U} = 3\eta_0\,. \tag{32}$$

2.2.2 Biaxial Extensional Flow

In the biaxial steady-state extensional flow, the melt element (seen in Fig. 10) is stretched in two directions (*x*, *y*), and in the third direction (*z*), it is contracted.

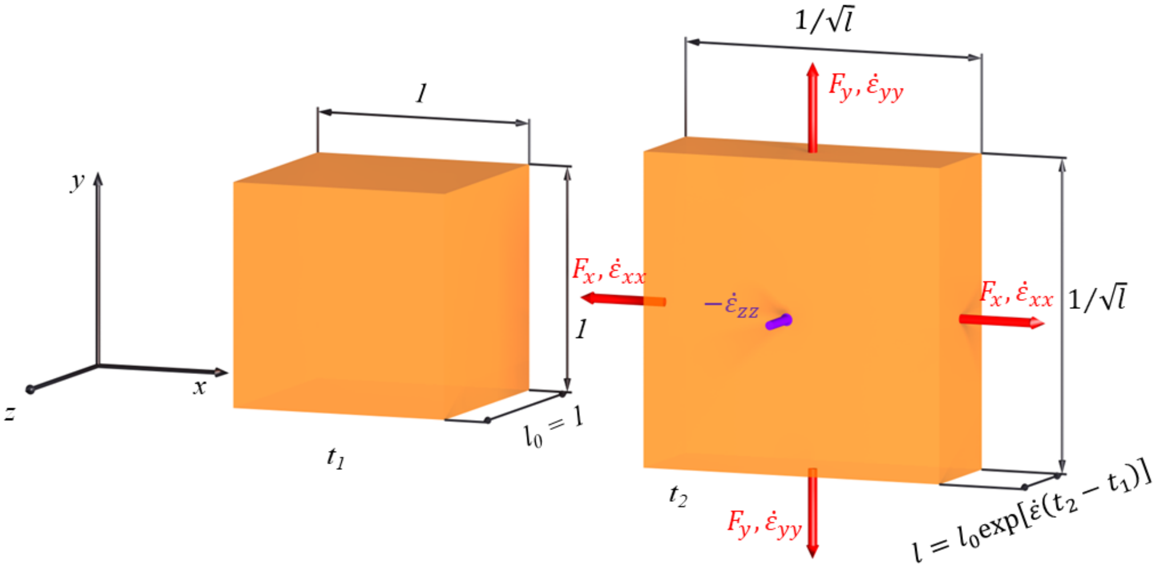

Figure 10 Biaxial extensional flow of melt element (adapted from [43][60])

The velocity field for biaxial extensional flow can be modified from Eq. 26, provided that the parameter $m = 1$, as follows:

$$v_x = \dot{\varepsilon}x,\ v_y = \dot{\varepsilon}y,\ v_z = -2\dot{\varepsilon}z\,. \tag{33}$$

Then, the deformation rate tensor $\underline{\underline{D}}$ for the biaxial extensional flow can be given as

$$\underline{\underline{D}} = \begin{pmatrix} \dot{\varepsilon} & 0 & 0 \\ 0 & \dot{\varepsilon} & 0 \\ 0 & 0 & -2\dot{\varepsilon} \end{pmatrix}. \tag{34}$$

Again, the biaxial extensional flow has only one non-zero normal stress difference, which can be considered biaxial extensional stress, identical to Eq. 30 $(\sigma_{E,U} = \sigma_{E,B})$ [45]. The same is true for the biaxial extensional viscosity, which is identical to Eq. 31

$$\eta_{E,B} = \frac{\sigma_{E,B}}{\dot{\varepsilon}} = \frac{\tau_{xx} - \tau_{yy}}{\dot{\varepsilon}}\,. \tag{35}$$

However, the *Tr* for biaxial extensional flow takes different value [62]:

$$\eta_{E,B} = 6\eta_0\,. \tag{36}$$

2.2.3 Planar Extensional Flow

Planar extensional flow is shown in Fig. 11. In this flow, the melt element is stretched in one direction (x-axis), in one other direction, the deformation is prevented (y-axis), and in the last direction (z-axis), shrinkage occurs [16][59][62].

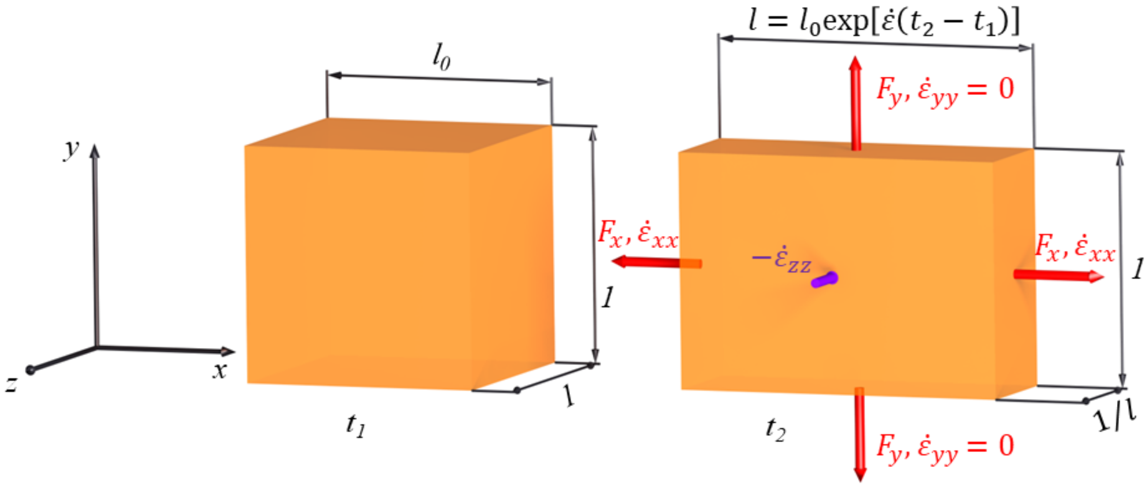

*The force F_y prevents the deformation in the direction of the y-axis

Figure 11 Planar extensional flow of melt element (taken from [43][60])

For a planar extensional flow, the parameter m = 0, and the velocity field (Eq. 26) of this flow can be given as follows:

$$v_x = \dot{\varepsilon}x,\ \ v_y = 0,\ \ v_z = -\dot{\varepsilon}z\,. \tag{37}$$

Then, the strain rate tensor $\underline{\underline{D}}$ for planar extensional flow corresponds to the following equation:

$$\underline{\underline{D}} = \begin{pmatrix} \dot{\varepsilon} & 0 & 0 \\ 0 & 0 & 0 \\ 0 & 0 & -\dot{\varepsilon} \end{pmatrix}. \tag{38}$$

However, unlike uniaxial extension, for planar extensional flow, both normal stress differences will take on non-zero values [16], and hence there can be two planar extensional stresses $\sigma_{E,P1}, \sigma_{E,P2}$

$$\sigma_{E,P1} = \left(\tau_{xx} - p\right) - \left(\tau_{zz} - p\right) = \tau_{xx} - \tau_{zz}\,, \tag{39}$$

$$\sigma_{E,P1} = \left(\tau_{yy} - p\right) - \left(\tau_{zz} - p\right) = \tau_{yy} - \tau_{zz}\,. \tag{40}$$

The planar flow is the only one that has two material functions since it has two different viscosity values. The first planar extensional viscosity $\eta_{E,P1}$ is given as

$$\eta_{E,P1} = \frac{\sigma_{E,P1}}{\dot{\varepsilon}} = \frac{\tau_{xx} - \tau_{zz}}{\dot{\varepsilon}}, \tag{41}$$

and the Trouton ratio *Tr* for this viscosity is as follows:

$$\eta_{E,P1} = 4\eta_0 . \tag{42}$$

The second planar extensional viscosity $\eta_{E,P2}$ is given as follow:

$$\eta_{E,P2} = \frac{\sigma_{E,P2}}{\dot{\varepsilon}} = \frac{\tau_{yy} - \tau_{zz}}{\dot{\varepsilon}}, \tag{43}$$

and it follows from the above that *Tr* for $\eta_{E,P2}$ will be given by the equation [62]

$$\eta_{E,P2} = 2\eta_0 . \tag{44}$$

2.2.4 Fundamental properties of steady uniaxial extensional flows

Fig.12 shows the time dependence of the uniaxial extensional viscosity $\eta_E^+(\dot{\varepsilon},t)$ and shear transient viscosity $\eta^+(\dot{\gamma},t)$ of branched LDPE at 150 °C, and the same range (shear $\dot{\gamma}$ and extensional $\dot{\varepsilon}$) rate (0.001 – 10) s^{-1}.

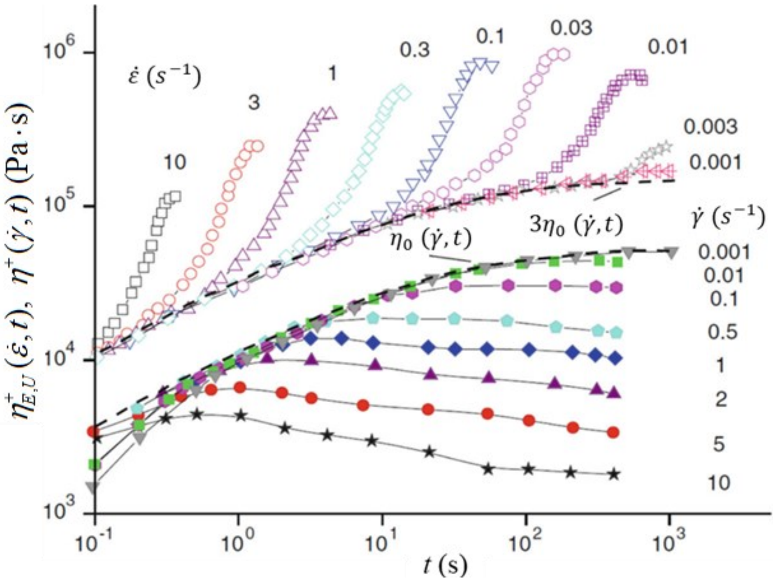

Figure 12 Time-dependent uniaxial extensional viscosity $\eta_E^+(\dot{\varepsilon},t)$ and shear viscosity $\eta^+(\dot{\gamma},t)$ for LDPE at 150 °C at various shear rates $\dot{\gamma}$ and extensional strain rates $\dot{\varepsilon}$ with linear viscoelastic envelope (dashed line) for extensional $\eta_{E,0}(\dot{\varepsilon},t) = 3\eta_0(\dot{\gamma},t)$ and shear $\eta_0(\dot{\gamma},t)$ viscosities (taken from [17])

The measured time-dependent transient shear viscosity data are consistent with the assumptions already described (Section. 2.1.1). The uniaxial extensional viscosity $\eta_E^+(\dot{\varepsilon},t)$

dependence obtained at constant $\dot{\varepsilon}$ where the curves steeply increase with time, shows a different behavior [17][63].Transient $\eta_E^+(\dot{\varepsilon},t)$ can also be described numerically, based on knowledge of the relaxation spectrum [46][64], using a generalized Maxwell's model [61] via the following equation:

$$\eta_E^+(\dot{\varepsilon},t)=\sum_{i=1}^{\infty}G_i\lambda_i\left[\frac{3}{(1-2\dot{\varepsilon}\lambda_i)(1+\dot{\varepsilon}\lambda_i)}-\frac{2}{(1-2\dot{\varepsilon}\lambda_i)}\exp^{\frac{-t}{\lambda_i}(1-2\dot{\varepsilon}\lambda_i)}-\right.$$
$$\left.-\frac{1}{1+\dot{\varepsilon}\lambda_i}\exp^{\frac{-t}{\lambda_i}(1-2\dot{\varepsilon}\lambda_i)}\right], \qquad (45)$$

where G_i and λ_i are the relaxation modulus and time in a particular "*i*" relaxation mode [65]. Fig. 12 also shows the validation of Trouton's ratio *Tr* for uniaxial extensional flow (Eq. 32). The viscosity curves at low strain rates ($\dot{\varepsilon}=\dot{\gamma}=0.001$ s^{-1}) essentially represent the so-called linear viscoelastic envelope, which can also be defined as a "short-term region of higher strain rate curves" [63]. The linear viscoelastic envelope equations for the transient extensional $\eta_{E,0}(\dot{\varepsilon},t)$ and shear $\eta_0(\dot{\gamma},t)$ viscosities can be obtained from Eq. 45.

If the extensional strain rate trends to zero $(\dot{\varepsilon}\to 0)$, the equation for determining the linear viscoelastic envelope $\eta_{E,0}(\dot{\varepsilon},t)$ can be rewritten into the following form:

$$\lim_{\dot{\varepsilon}\to\infty}\eta_E^+(\dot{\varepsilon},t)=3\cdot\sum_{i=1}^{\infty}G_i\lambda_i\left[1-\exp^{\frac{-t}{\lambda_i}}\right]=\eta_E^+(\dot{\varepsilon},t), \qquad (46)$$

and for linear viscoelastic envelope $\eta_0(\dot{\gamma},t)$ [65]

$$\lim_{\dot{\varepsilon}\to\infty}\eta_0^+(\dot{\gamma},t)=\sum_{i=1}^{\infty}G_i\lambda_i\left[1-\exp^{\frac{-t}{\lambda_i}}\right]=\eta_0^+(\dot{\gamma},t). \qquad (47)$$

An important conclusion shown in Fig. 12 is that the increase and subsequent steady state of the $\eta_{E,U}$ occurs only after a certain time period, which can also be characterized by the magnitude of the maximum Hencky strain ε_H [17]. The value of ε_H required to obtain a steady state depends mainly on the nature of the polymer melt (Fig. 13) and its ability to exhibit strain hardening [17][53]. The effect of strain hardening typically increases with increasing rate $\dot{\varepsilon}$ [66] and benefits the uniform/homogeneous deformation of the polymer melt during extensional flow. But it does not occur in all polymer materials such as e.g., linear PP (Polypropylene) [53][63]. However, it has a strong influence on low-density polyethylene (LDPE) having a high degree of branching and long branches [66].

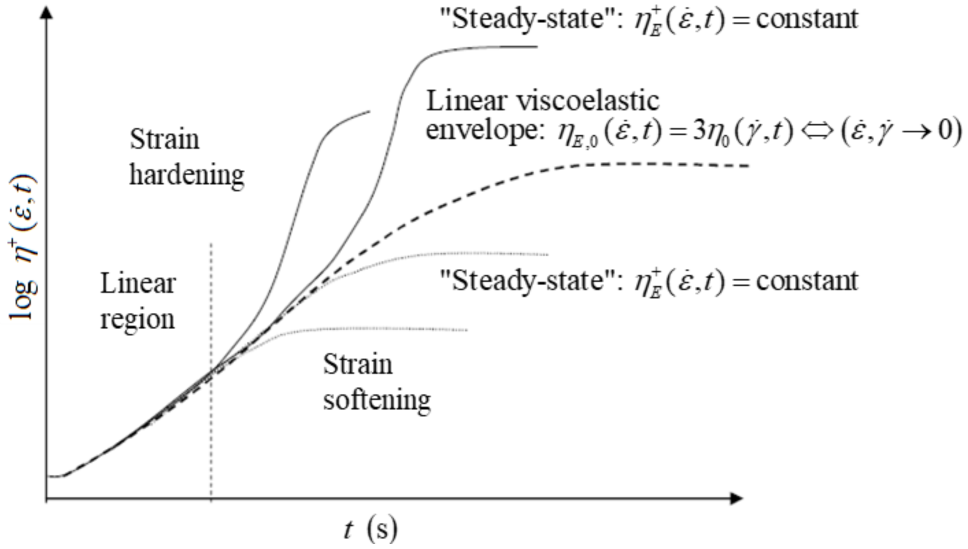

Figure 13 Transient uniaxial viscosity $\eta_E^+(\dot{\varepsilon},t)$ defined for different polymer melt behavior at one applied constant extensional strain rate $\dot{\varepsilon}$ (taken from [60])

Fig. 14 shows the uniaxial extensional stress $\sigma_{E,U}$ as a function of ε_H for a particular LDPE material, and $\dot{\varepsilon}$. Stress $\sigma_{E,U}$ reaches steady-state values as late at $\varepsilon_H \approx 5$. From these steady-state values, it is possible to construct a plot of the dependence of extensional viscosity on extensional rate, as demonstrated in Fig. 15 [60].

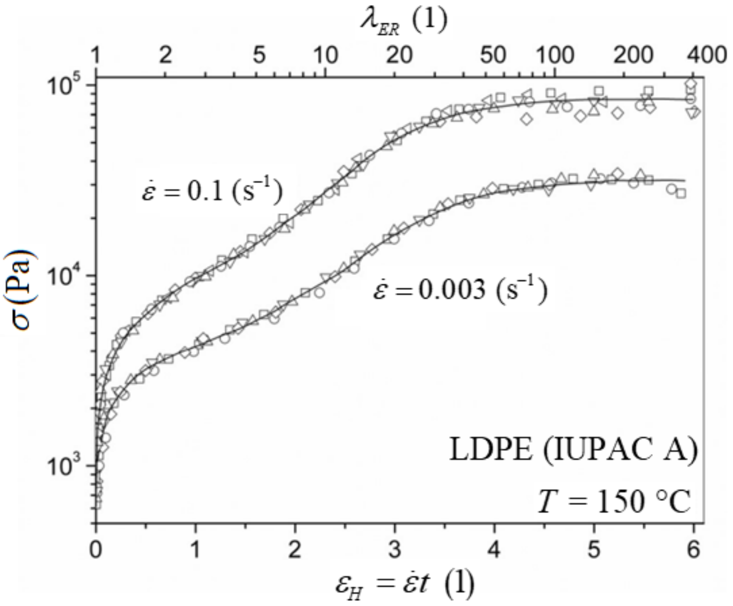

Figure 14 Extensional stress σ as function of Hencky strain ε_H at two constant extensional strain rates $\dot{\varepsilon}$ for LDPE at 150ºC. Here λ_{ER} is the stretching ratio (taken from [67])

The accuracy of determining the steady-state value from extensional viscosity plotted as a function of time or ε_H is still widely debated [38][67]. This only confirms the fact that the determination of extensional viscosity η_E is very challenging compared to shear viscosity [46].

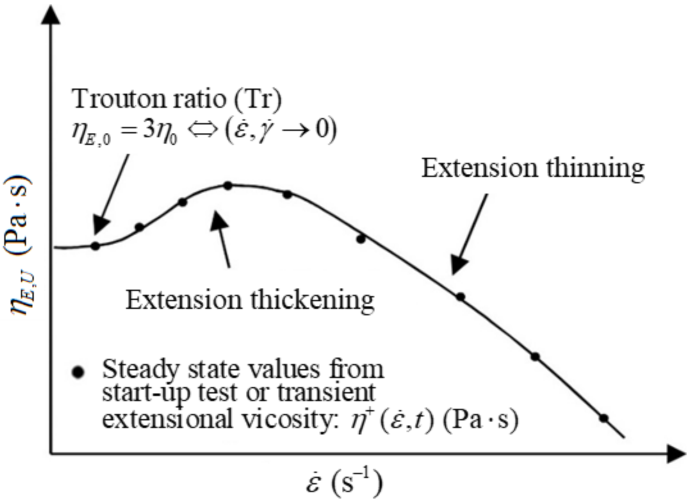

Figure 15 Typical extensional viscosity $\eta_{E,U}$ versus extensional rate $\dot{\varepsilon}$ curve for an extension-thickening polymer (taken from [60])

Typical uniaxial extensional viscosity $\eta_{E,U}$ versus the extensional strain rate $\dot{\varepsilon}$ is provided in Fig. 15. However, if the very wide extensional strain rate range is considered even for linear polymer melts (see Fig. 16), there are other interesting points.

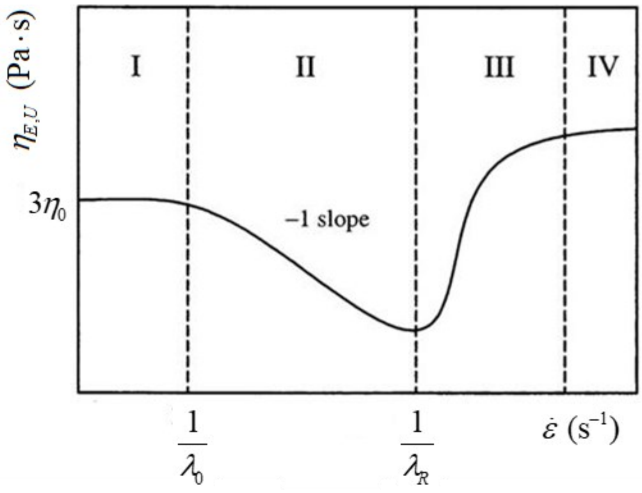

Figure 16 Prediction of the steady-state uniaxial extensional viscosity $\eta_{E,U}$ vs. extensional strain rate $\dot{\varepsilon}$ for linear, monodisperse polymer melt according to the standard Doi-Edwards model (taken from [68])

The dependence shown (Fig. 16) is predicted using the Doi-Edwards model [46] and can be divided into four regions (I. – IV.). In region (I.), the equilibrium state between entanglement formation and breakdown occurs – extensional viscosity is constant. In region II. i.e. at sufficiently high $\dot{\varepsilon}$ values, extensional viscosity suddenly decreases as entanglements breakdown becomes more dominant than formation. The beginning of this transition from viscous to pseudoplastic behavior is defined by the inverse of the macroscopic relaxation time $1/\lambda_0$. The plotted dependence curve takes its local minimum at the reciprocal Rouse time $1/\lambda_R$ and beyond that in the region (III.) a strain hardening ($\dot{\varepsilon} > 1/\lambda_R$, [66] or Rouse-Weissenberg numbers for extensional flow $W_{iR} > \dot{\varepsilon}\lambda_R$ [68][69]) occurs, where the macromolecules are completely free of entanglements. There is a stretching of the backbone of the macromolecules alone, increasing extensional viscosity $\eta_{E,U}$. In the last region (IV.) the maximum stretching of the chains occurs, and the viscosity is again constant $\eta_{E,U\infty}$. The viscosity value in this region often takes higher values than the initial viscosity, defined by the Trouten ratio T_r.

The conclusions of experimental studies do not always confirm the agreement with the Doi - Edwards prediction and show its non-universality [68][69][70].

The Rouse reorientation (or stretch) time λ_R [64], is the time from which macromolecules move in a completely unentangled state. It is twice the Rouse stress relaxation time $\lambda_{RS}\left(\lambda_R = 2\lambda_{RS}\right)$ and can be expressed by the equation:

$$\lambda_R = \frac{12M\eta_0(M)}{\pi^2 \rho R_G T}\left(\frac{M_c}{M}\right)^{a_M - 1}, \tag{48}$$

where M is the molecular weight, M_c is the critical molecular weight [46], R_G is the state gas constant ($R_G = 8.314\ \mathrm{J \cdot K^{-1} \cdot mol^{-1}}$), T is the thermodynamic temperature, ρ is the density of the polymer under investigation, and a_M is an exponent whose value depends on the molecular weight ($M \le M_C$, so $a_M = 1$ when $M \ge M_C$ je $a_M = 3{,}4$ for linear polymers) [66].

2.2.5 Experimental techniques for the determination of extensional viscosity

Many experimental techniques allow the measurement of extensional viscosities η_E, but they have own limitations, and also their commercial availability is somewhat limited

[17][63]. The biggest problem that must be tackled when finding steady-state values at given extensional rate $\dot{\varepsilon}$ is to keep a uniform deformation of the sample under investigation [19][63] and for such a long time that it can reach steady-state values (Figs. 13,14) [67]. The severity of this problem increases with increasing $\dot{\varepsilon}$.

According to the literature [71], the experimental methods for extensional viscosity measurements can be distinguished into pressure-, boundary- and capillarity-driven ("boundary-, capillarity- and pressure-driven" [71]) according the way in which the extensional flow is generated (Fig. 17).

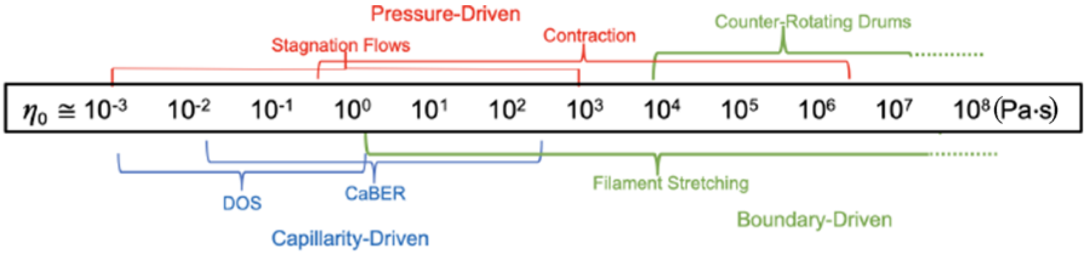

Figure 17 Shear (Newtonian) viscosity η_0 ranges of currently available extensional rheometers (taken from [71])

In capillarity-driven rheometers, an initial cylindrical polymer sample is stretched to form a liquid bridge between two parallel plates, thus creating a uniaxial extensional flow, which is unstable and thins and disintegrates due to capillary forces (Fig. 17) [72]. The most known commercially used capillarity-driven rheometer is the Capillary Breakup Extensional Rheometry (CaBER) [72][73], which allows the determination of extensional viscosity for polymer solutions with low viscosity (up to $\eta_0 = 7 \cdot 10^{-2}$ Pa·s), such as printing inks [72].

According to Fig. 17, experimental methods driven by free boundary include two experimental device concepts: Counter-Rotating Drums (CRD) and Filament Stretching (FSR). “With appropriate control schemes and analyses, they can measure true transient extensional viscosity $\eta_E^+(\dot{\varepsilon},t)$” [71]. The following is a short review of the essential facilities of this group of experimental techniques.

The simplest way to achieve extensional flow is by stretching the polymer sample. However, these classical tensile tests present some problems [17], particularly in the actual clamping of the sample and the influence of gravitational forces during the measurement [18].

Meissner [58], was the first to overcome these problems to some extent. From his concept of counter-running drums, many other experimental methods and devices evolved. His last modified device was commercialized under the name Rheometric Melt Extensional rheometer (RME) [46][63]. In Fig. 18, the RME is illustrated with grooved metal belts to reduce the slippage of the specimen during horizontal stretching. Buckling and degradation of the polymer sample are prevented by a bed of inert gas flowing over the porous worktable [17][76]. For RME, it is advantageous that the total extensional is not limited by the machine size, allowing measurements up to ε_H = 7 [76].

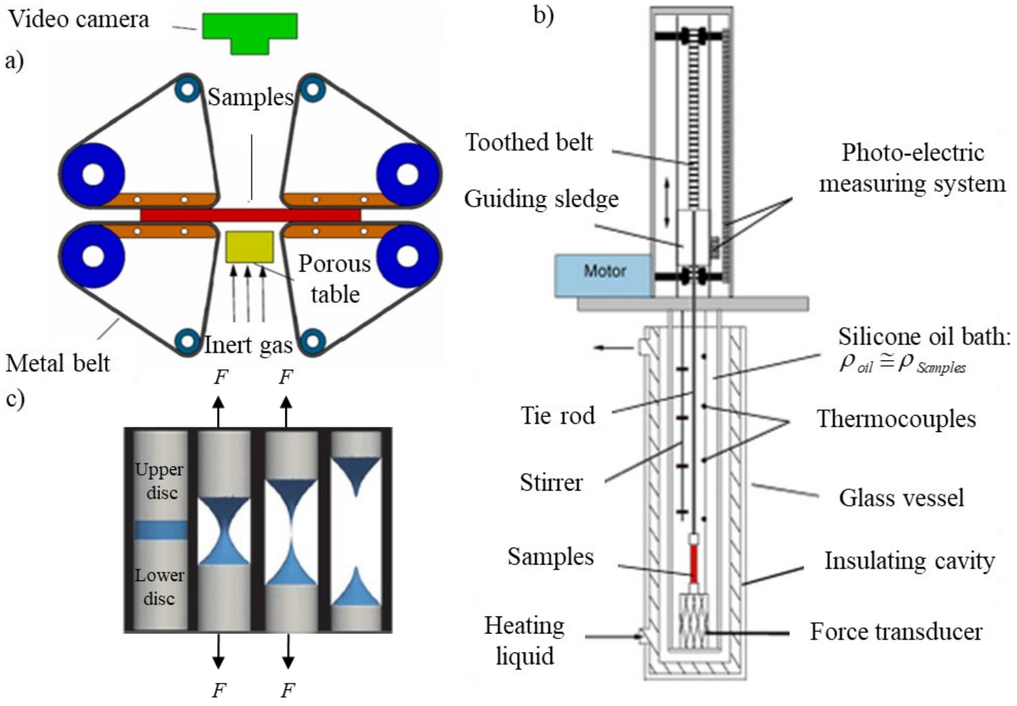

Figure 18 Different designs and methods for determining extensional viscosities η_E
a) Rheometric Melt Extensional rheometer (RME) [17][74], b) Münstedt Tensile Rheometer (MTR) [17][75], c) A scheme of the method for measuring deformability of a liquid droplet in extension [19]

Methods using Meissner's original concept include a miniaturized modification of the Meissner Extensional Rheometry Accessory (MERA), which consists of two pairs of counter-rotating drums and can be placed in the heated chamber of commercial rotational rheometers [77]. As well as another fiber-windup experimental device [78] based on which the currently most widely used and accurate extensional rheometers: Sentmanat Extensional Rheometer (SER) and Extensional Viscosity Fixture (EVF) [77] (see Chapter 8).

For the Münstedt Tensile Rheometer (MTR), the initial problems are solved by a different approach. During the measurement, the samples are immersed in a liquid that prevents them from buckling (silicone oil) and stretched in the vertical direction (Fig. 18b). The samples are glued to metal clips, which can cause difficulties. A disadvantage may be that the size of the device limits the overall extensional of the sample (ε_H = 4) [17][77]. The transient $\eta_E^+(\dot{\varepsilon},t)$ data obtained from the discussed device are shown in Fig. 12.

Table 1 Extensional rheometers overview (adapted from [18][74])

Feature (reference)	Meissner´s metal belt clamping rheometer RME ([17][46][76])	Münstedt Tensile Rheometer MTR ([17][18][46])	Capillary Rheometer ([47][53][61])	Sentmanat Extension Rheometer ([46][80])
Type of extensional	Uniaxial or planar	Uniaxial	Uniaxial or planar	Uniaxial
Sample	Polymer Film	Cylinder	Granules	Polymer strip
Sample size	< 2 g, requires careful preparation and loading	10 g, care must be taken to minimalize end effects	40 g minimum	5 – 200 mg
Flow stability	Can be unstable at high rates	Subject to gravity, tension and air currents	Unstable at very high rates	Stable up to $\dot{\varepsilon}$ < 20 s^{-1}
Viscosity range	High viscosity	High viscosity	Both low and high viscosities	> 10 000 Pa·s (zero shear rate viscosity η_0)
Restriction of gravity force	Silicone oil	Inter gas cushion	None	Geometry of the sample and its clamping
Homogenous	Could be, with care	No, at the end	No – mixed shear and extensional flow	Yes – truly uniform extensional deformation
Pressure effect	None	None	Yes – compressibility of melt in the reservoir could cause difficulties	None
Extensional rates $\dot{\varepsilon}$ (s^{-1})	Maximum extensional rate is limited by the ability to maintain the sample in steady flow; $\dot{\varepsilon} = \langle 10^{-3}; 10^{0} \rangle$	Maximum rates depend on clamp speeds; $\dot{\varepsilon} = \langle 10^{-3}; 5 \rangle$	High and low rates possible; $\dot{\varepsilon} = \langle 10^{0}; 10^{6} \rangle$	Maximum recommended extensional; $\dot{\varepsilon} = \langle 10^{-2}; 20 \rangle$

The third and final group of pressure-driven methods, which includes particularly the experimental method of tenting extensional properties using contraction or entrance flows in the form of entrance pressure drop measurements on a capillary rheometer, is the main focus of this thesis and will be discussed in a separate Chapter 3. Another device in which the extensional flow is pressure-driven is the Cross-Slot Extensional Rheometer (CSER).

It is based on a stress-optical measurement at the stagnation point of the flow and can be used to detect the planar extensional viscosity $\eta_{E,P}$ at a steady state [79].

The summary Table 1 presents parameters and other information for selected extensional rheometers. It is important to note that the experimental methods and equipment discussed herein that allow for the measurement of extensional properties of polymeric materials do not include all existing and used methods. The above experimental methods and devices and many others are reviewed in more detail, e.g., [16][17][18][19][46][53][77].

3 ENTRANCE PRESSURE DROP MEASUREMENTS IN A CAPILLARY RHEOMETER

According to the conclusions of Section 2.2.5 and the summary Table 1, various experimental methods can be used to determine the extensional viscosity (η_E), each with its limitations. However, for measurements at high extensional rates $\dot{\varepsilon}$ and a large range of polymer viscosities, only measuring the entrance pressure drop Δp_{entr} in contraction flows of capillary rheometers is suitable (see Table 1). This method is widely used despite several pitfalls and simplifications, some of which will be presented in this chapter.

Due to its versatility, capillary rheometry is frequently used in both industrial and academic settings. Capillary rheometers can have different designs, and a whole range of rheological properties can be determined using them [16][19][47][53][81].

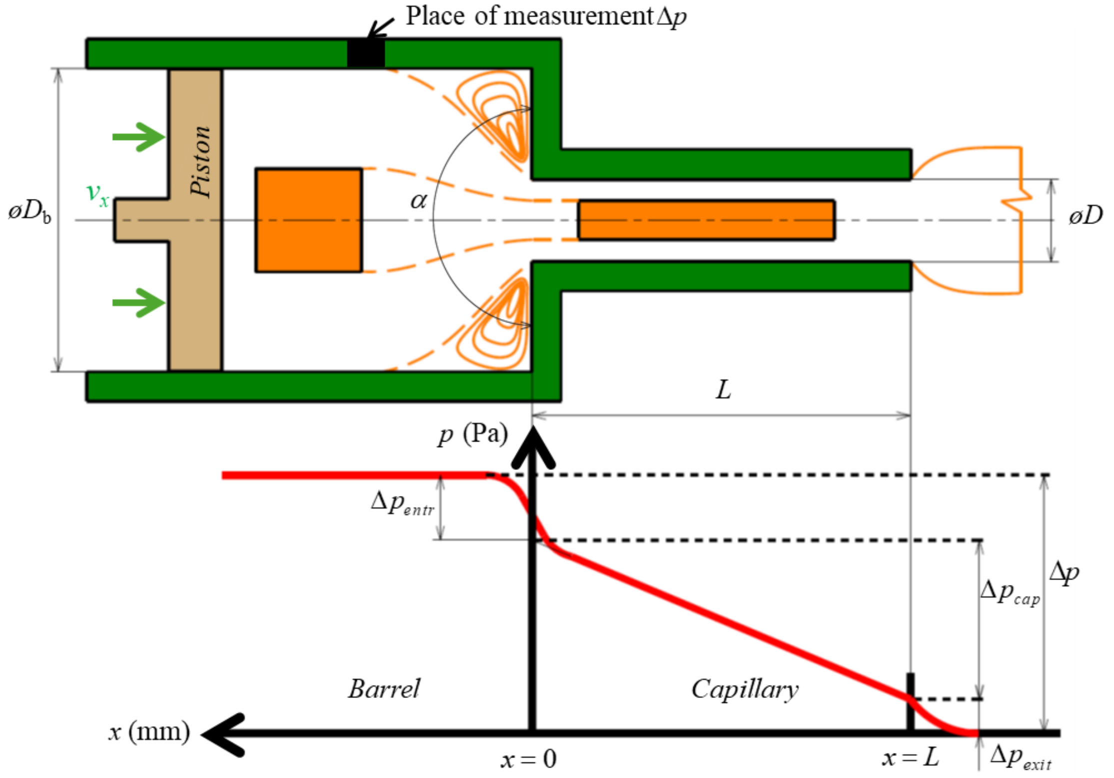

Figure 19 Schematic representation the contraction flow (i.e., flow from a wide barrel with diameter D_b through entry contraction angle α into a narrow capillary with length L and diameter D). Here the piston is moving by velocity v_x, the deformation of the melting element is visualized as an orange element), and pressure development along the axis of symmetry is provided at the bottom (adapted from [13][23])

The principle of contraction flow on which capillary rheometers are based, is shown in Fig. 19. It can be seen that the flow of polymer melt, generated by the movement of the piston or the compressed gas [38], is forced to flow from the wide barrel into the narrow capillary die through the so-called entry angle of contraction α (full wall-to-wall angle Fig. 19). This transition is accompanied by a pronounced pressure drops, which is graphically shown as a function of pressure versus flow channel length (*z*-axis) in Fig. 19. The total pressure drop Δp can also be affected by the flow between the piston and the barrel. This flow may appear, above all in low-viscosity polymers or using high pressure. It can be reduced using special piston tips (shown Fig. 20) made of PEEK [82].

The total pressure drop, Δp, can be determined using the measured pressure inside the wide barrel and is composed of three components

$$\Delta p = \Delta p_{cap} + \Delta p_{end} = \Delta p_{cap} + \Delta p_{exit} + \Delta p_{entr} \tag{49}$$

where Δp_{cap} is the capillary pressure drop, Δp_{end} is end pressure drop, Δp_{exit} is the exit pressure drop, and Δp_{entr} is the entrance pressure drop. The pressure drop in the capillary, Δp_{cap}, is caused by the shear flow of the melt along the length of the capillary. Its magnitude is determined by the shear viscosity η of the polymer being measured [38][53]. The sum of the entrance Δp_{entr} and the exit Δp_{exit} pressure drop is referred to as the end pressure drop Δp_{end} (end effects) since Δp_{exit} reaches small values ($\Delta p_{\mathrm{entr}} >> \Delta p_{\mathrm{exit}}$), it is usually neglected as here, and the detected value Δp_{entr} coincides with Δp_{end}. The exit pressure drop Δp_{exit} is associated with the elasticity of the melt. Thus the first normal stress difference N_1 [13] becomes measurable at higher shear stresses (τ_{xy} > 25 kPa) with the help of special measuring equipment (slit die) [16] [53][81].

Given the focus of this work, the focus of interest is the entrance pressure drop, Δp_{end}, which is associated with strong stretching of the melt in the flow direction because of its strong acceleration during contraction. The difficulties are mainly caused by the inhomogeneity of the extensional flow with the non-constant extensional rate $\dot{\varepsilon}$ [14][83][84]. Using Δp_{entr} and other quantities, it is possible to obtain an "approximate" value for the extensional viscosity η_E using approximation analyses [13][18], a minor presentation and comparison of which is given in Section 3.3.

The key is therefore to obtain the most accurate value of the entrance pressure drop Δp_{entr} which, of course, brings the complications already outlined. There are two concepts for experimental measurements performed on a capillary rheometer to obtain the value of the entrance pressure drop, Δp_{entr}. This is an extrapolation based on the Bagley plot analysis or by direct measurement using a "zero-length" capillary die, referred to as an orifice die.

3.1 Bagley's concept

To obtain the entrance pressure drop Δp_{entr} using the method originally proposed by Bagley, the total pressure drop Δp is measured on at least two or more capillary dies of identical diameter D but different length L to diameter D ratios (L/D) [53] [85]. There are also certain recommendations on how much and which L/D ratios to choose [86]. For example, an arrangement of two capillary dies allows a capillary device used in this thesis, whose working part is shown in Fig. 20.

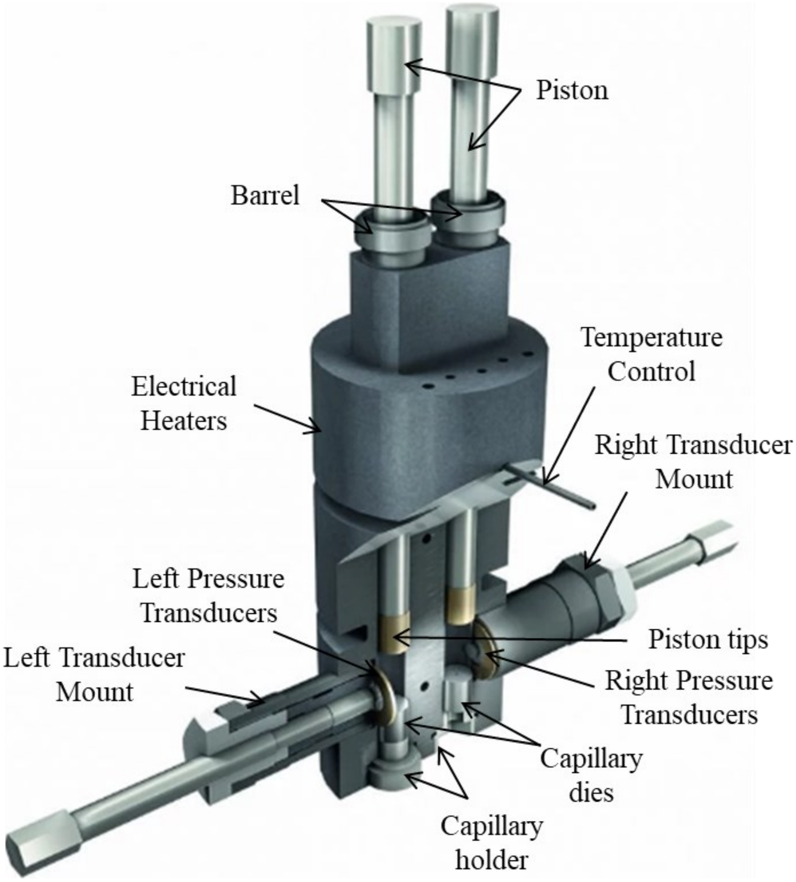

Figure 20 Example of the arrangement of the working part of a twin-bore capillary rheometer (adapted from [87])

The measured values of the total pressure drop Δp are plotted as a function of the L/D ratio of the capillary dies and extrapolated to the zero value of the L/D ratio [85]. The entrance pressure drop Δp_{entr} is subtracted from the vertical pressure axis of the Bagley plot.

The major disadvantage of this concept is that the entrance pressure drop Δp_{entr} is found as an indirectly measured quantity obtained by extrapolation, which is not always linear (Fig. 21b) [14][88], leading to inaccuracy [27][85]. The origin of the nonlinearity is attributed to viscous heating, the pressure dependence of the melt viscosity, or wall slip

[27][88][89]. The Bagley plot is also used to correct the measured shear quantities, where the pressure drop in the capillary Δp_{cap} must be found to calculate the corrected shear stress $\tau_{xy,\mathrm{corr}}$ (see Section 8.1, Eq.). Fig. 21a shows the results obtained from the experimental determination of Bagley plots using an Instron capillary rheometer at 150 °C over the range of apparent shear rates $\dot{\gamma}_{APP}$ (from 8.2 to 82 s^{-1}) for Linear metallocene PE (LmPE3), whose parameters are reported in [27]. It can be seen in Fig. 21b that when using a long capillary die (L/D = 40), it is no longer possible to use linear interleaving to describe all the data, but second-order polynomials must be used [27]. The entrance pressure drop Δp_{entr} was determined in two ways, resulting in two sets of experimental data.

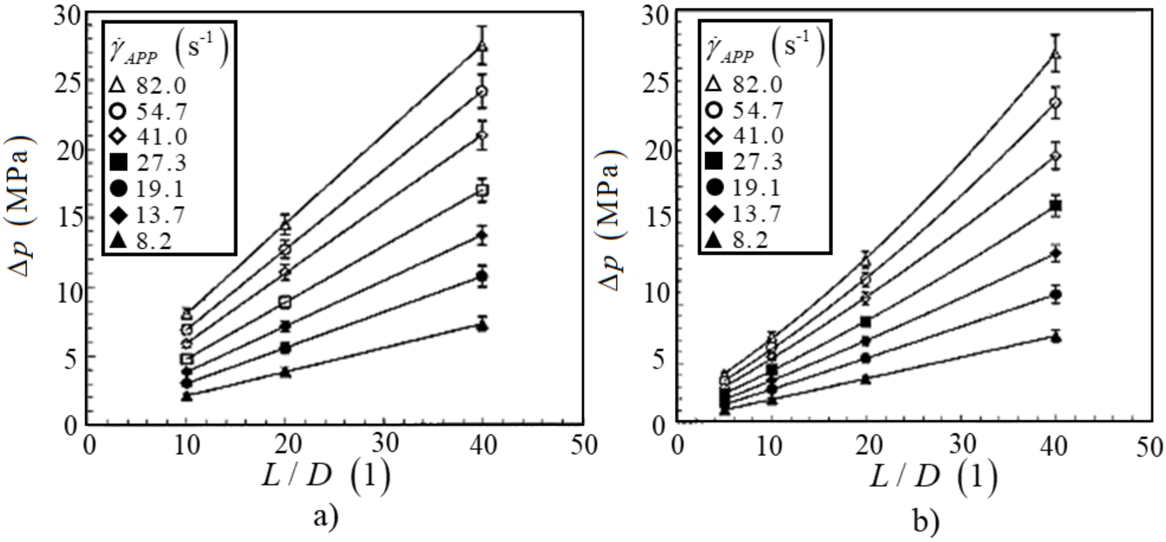

Figure 21 Bagley plots (capillary die with D = 0.762 mm, entry angle α = 90°) for LmPE3 at 150 °C (adapted from [27]). a) points are fitted linearly with a straight line, b) the points are fitted with a second-order polynomial

3.2 Orifice die

Experimental measurements using an orifice die provide a direct measurement of the entrance pressure drop (Δp_{entr}). As with the Bagley plot, the Δp_{end} is obtained [88] and the Δp_{exit} is again neglected for the same reasons. A significant advantage over the previous concept is that it requires fewer measurements to obtain results. Only the measurement using one orifice die, and one longer capillary die is sufficient [85].

Some studies have found that the geometry of the flow channel has the greatest influence on the accuracy of the entrance pressure drop Δp_{entr} measurements, as different die designs give different results [88]. The geometry of the orifice die flow channel is defined by the following parameters, i.e. the shape of the exit region/underside die, the ratio L/D, the entry angle of the contraction flow, and the contraction ratio [16][27]. Each of these parameters affects the accuracy of the measured Δp_{entr}.

3.2.1 Effect of filling underside of the die

A badly designed underside part of the orifice die (exit region) can cause the outgoing melt to stick to the walls of this part and subsequently fill the exit region. This is problematic as it causes an overestimation of the measured entrance pressure drop Δp_{entr}. Therefore, it is necessary to modify the exit region so that this does not occur while meeting other requirements for its functionality and optimal lifetime [27][88]. In the next section, case studies of authors who have dealt with this issue will be presented.

Mitsoulis, Hatzikiriakos, et al. (1996, 1998)

Mitsoulis, Hatzikiriakos, et al. [90][91] have conducted both experimental and numerical studies on the entrance pressure drop Δp_{entr} during contraction flows. In their two studies, they used two types of LLDPEs. In the first paper, only conventional LLDPE (Dowlex 2049) was used [90], and in the second paper, the measurements were extended to include metallocene type (mLLDPE) [91]. Experimental measurements were performed on an Instron capillary rheometer using a standard barrel (see Table 3). The first dataset was acquired through a Bagley plot labeled as "Free extrudate" while the second dataset was obtained using an orifice die labeled as "Filled expansion". The design of the die is illustrated in Fig. 22a.

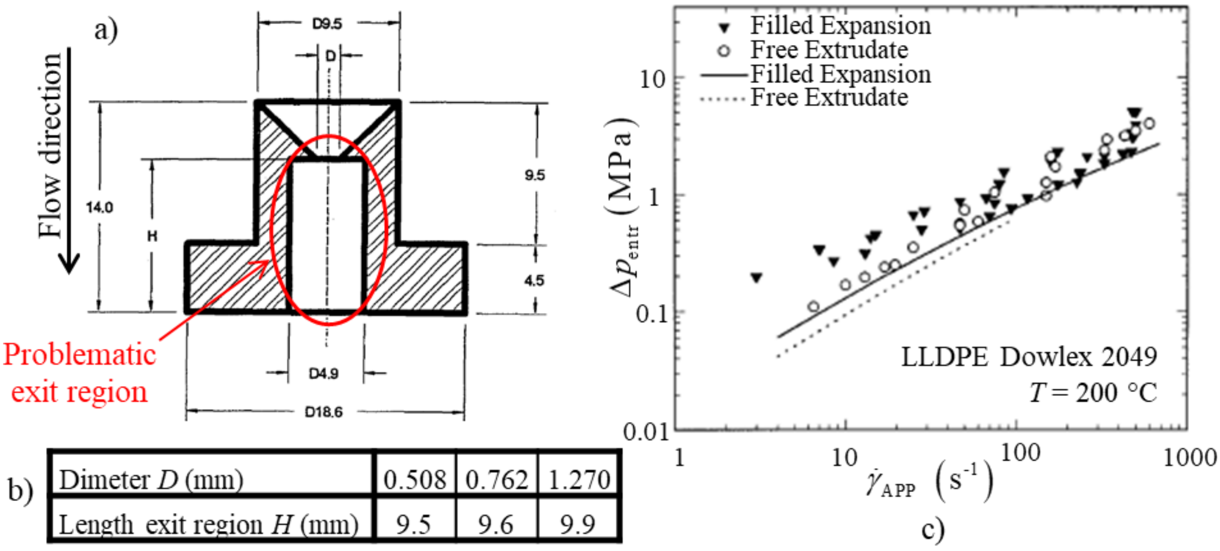

Dimeter D (mm)	0.508	0.762	1.270
Length exit region H (mm)	9.5	9.6	9.9

Figure 22 a) The geometry of the orifice dies used in the experiment with the entrance angle α = 90°, and b) Die dimensions, c) Differently obtained values of entrance pressure drop Δp_{entr} depending on the apparent shear rate $\dot{\gamma}_{\mathrm{APP}}$ (adapted from [91])

The entrance pressure drop data Δp_{entr} from both methods were plotted against the apparent shear rate $\dot{\gamma}_{\mathrm{APP}}$ and were also compared with the K-BKZ model [91], as shown in Fig. 22c. It can be seen that filling the exit region of the orifice die overestimates the entrance pressure drop Δp_{entr}, but data from both methods obtained at a high apparent shear rate $\dot{\gamma}_{\mathrm{APP}}$ becomes very similar [90][91].

Kim and Dealy (2001)

Kim and Dealy [27] follow the work of Mitsoulis and Hatzikiriakos et al. [90][91] and attempt to solve the problematic filling of the exit region by modifying the geometry of the orifice die. The modified orifice die (Fig. 23b) features an expansion section with a diameter approximately two to four times larger than the original design (Fig. 23a). The orifice die dimensions for both the old (Fig. 23a) and new (Fig. 23b) designs are $D_{\mathrm{b}} = 9.525$ mm (barrel diameter), $D = 1.270$ (orifice diameter), and $\alpha = 90°$ (entry angle). Measurements were again performed on an Instron capillary rheometer (standard barrel diameter $D_{\mathrm{b}} = 9.525$ mm and length $L_{\mathrm{b}} = 400$ mm [28]) for two polymer melts again LLDPE, mLLDPE at 150 °C. Material parameters and additional information can be found in [27][28].

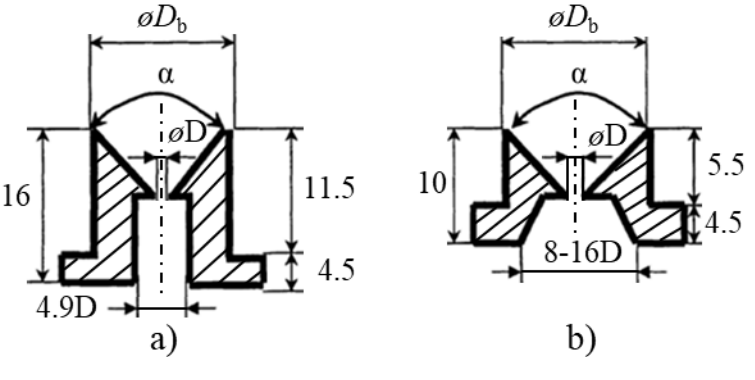

Figure 23 Schematic views cross-section of the orifice die used
a) standard (old) design, b) modified (new) design (taken from [27])

Fig. 24 shows the dependence of the measured entrance pressure drop Δp_{entr} on the apparent shear rate $\dot{\gamma}_{\mathrm{APP}}$. It can be seen that the gradual filling of the exit region in the old orifice die design (Fig. 23a) started already at low $\dot{\gamma}_{\mathrm{APP}}$. While in the new concept, the filling of the exit region did not occur in the whole range of $\dot{\gamma}_{\mathrm{APP}}$. The Δp_{entr} measured using the new concept was 50 % lower than that of the old orifice die, which was burdened by the error due to exit region filling. Δp_{entr} data from the modified orifice die (Fig.23b) were also compared with data obtained from the Bagley plot, and it was found that when the Bagley plot was linearly interleaved, the data from the two methods showed a significant agreement [27].

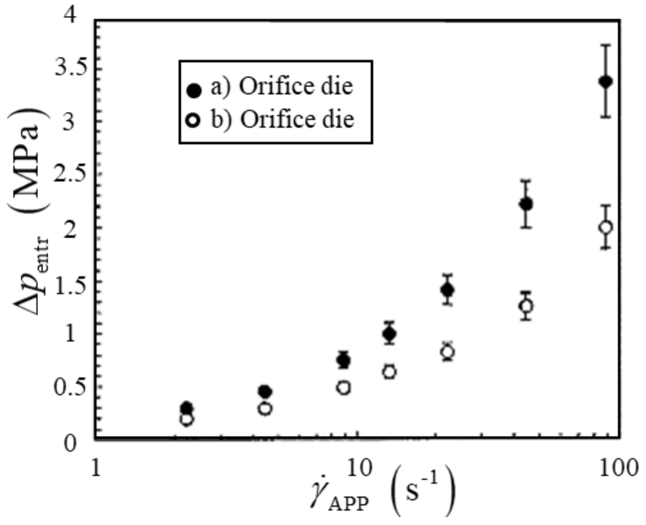

Figure 24 Entrance pressure drop Δp_{entr} versus apparent shear rate $\dot{\gamma}_{\mathrm{APP}}$ obtained from measurements on old orifice die (a) and new orifice die (b) LLDPE at 150 °C with die orifice $D = 1.270$ mm (with ($L/D = 0.5$) and entry angle $\alpha = 90°$ (taken from [27])

Aho and Syrjälä (2006) and Sunder and Goettfert (2001)

Aho and Syrjälä, in several papers [85][88][89], use the same orifice die (Fig. 25) as Sunder and Goettfert [86], who performed experimental measurements to determine the accuracy of the obtained entrance pressure drop Δp_{entr}. Aho and Syrjälä [85], performed verification experimental measurements on the orifice die visualized in Fig. 25.

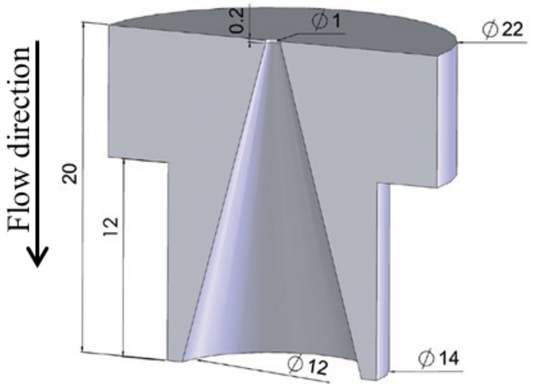

Figure 25 Schematic view cross-section of the Göttfert orifice die used, dimensions in mm (taken from [88])

Aho and Syrjälä [85] compared the entrance pressure drop Δp_{entr} with values obtained using a Bagley plot and measurements made with the orifice die visualized in Fig. 25. Measurements were conducted using a Göttfert Rheograph 6000 capillary rheometer with two polymer melts: LDPE (Lupolen 1840 H) and PS (Polystyrene 143E). The material parameters and experimental procedure details can be found in the referenced work [85][88].

The results of Δp_{entr} obtained from both methods were again plotted against the apparent shear rate $\dot{\gamma}_{\mathrm{APP}}$, as shown in Fig. 26 for the PS. However, the PS showed a significant difference of 143.82 %. This shows that the used design of the exit region of the orifice die (Fig. 26), is indeed inappropriate. During the measurement, this region fills up and thus significantly affects the Δp_{entr} [85].

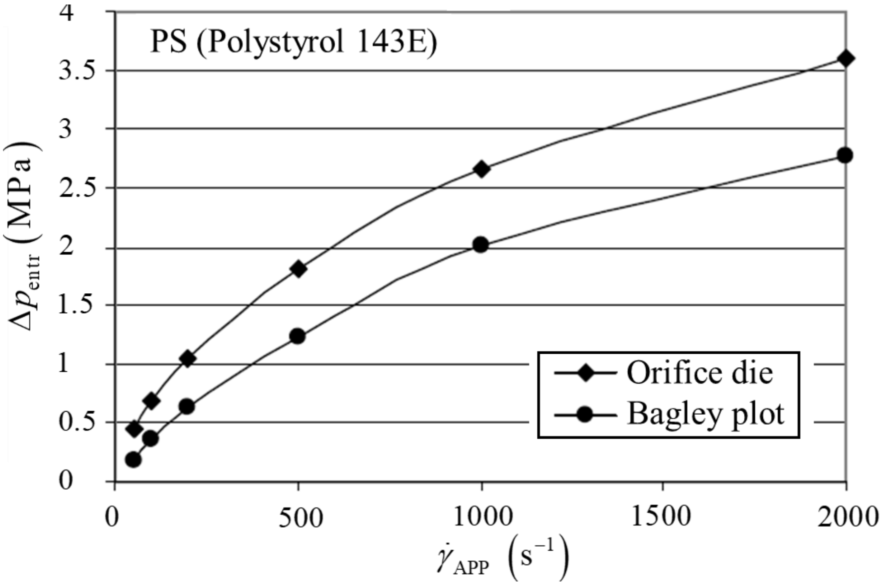

Figure 26 Comparing courses of entrance pressure drop Δp_{entr} on the apparent shear rate $\dot{\gamma}_{\mathrm{APP}}$ for PS using Bagely plot and Göttfert orifice die (taken from [85])

Zatloukal and Musil (2009)

Zatloukal and Musil [29][43] were others who addressed the problem of the "narrow orifice downstream" filling of the standard orifice die design (Figure 27b).

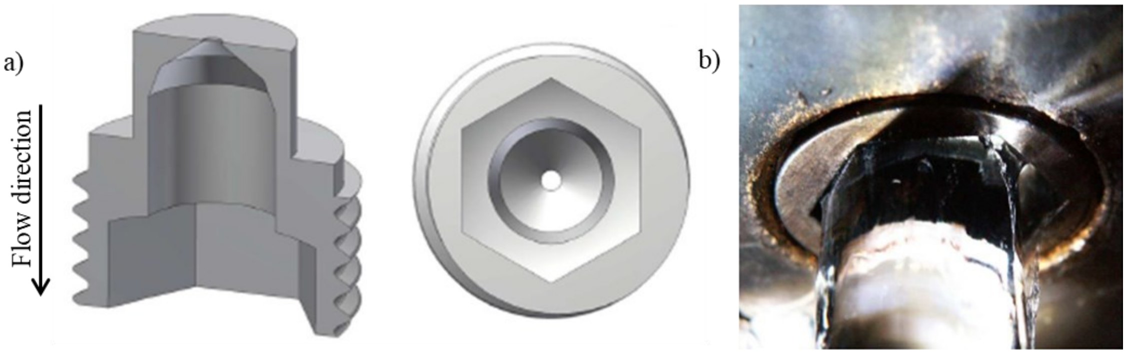

Figure 27 a) The geometry of an old orifice die with a narrow exit region, b) a detailed view of the orifice downstream region during measurements (taken from [29])

To eliminate this source of inaccuracy, the authors analyzed the polymer melt flow during contraction theoretically and experimentally. The theoretical design consisted of flow simulation through FEM analyses to verify the effect of filling the narrow space of the standard orifice die design (Fig. 27a). Based on the findings, the authors created a new orifice die design (which they also patented [92]) which is shown in Fig. 28a with a contraction entry angle of $\alpha = 180°$. The new die has a very open downstream region comprising a diverging channel section and four mounting holes (assembly requires a special wrench).The underside of the new orifice die, thus modified, eliminates the occurrence of the described inaccuracy since the melt does not touch the wall exit region (Fig. 28b) even at high flow rates.

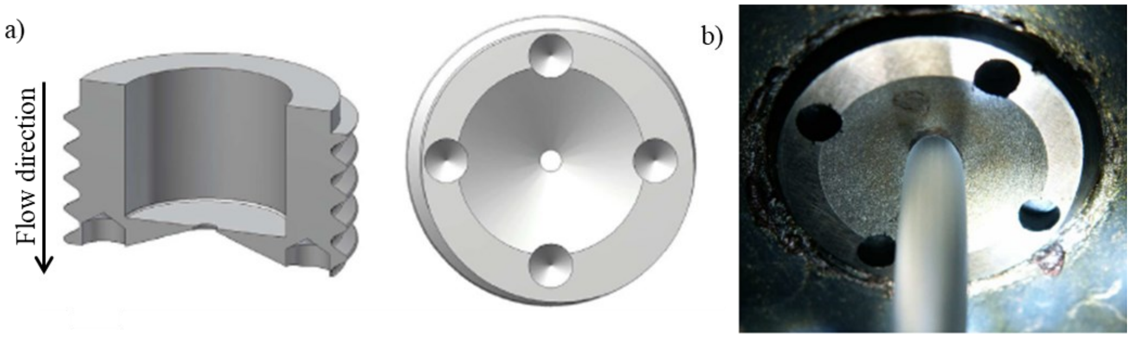

Figure 28 a) The geometry of a novel orifice die, b) a detailed view of the orifice downstream region during measurements (taken from [29])

In addition, the open downstream exit region is advantageous for exploring unsteady flow. Furthermore, orifice dies with an entry angle smaller than $\alpha < 180°$ were also designed [92], as well as rectangular dies for measuring planar extensional viscosity [59][93].

3.2.2 Effect of L/D ratio

The ratio of hole length (L) to diameter (D) is a parameter that affects the measured values of the entrance pressure drop (Δp_{entr}). Many authors have not addressed the close-to-zero range of the ($L/D \approx 0$) ratio.

The work of Kelly [94], who, among other things, performed important experimental measurements on an online rheometer, which he compared with off-line measurements on a twin-bore Rosand RH7-2 capillary rheometer. He used six orifice dies with the same diameter $D = 1$ mm and lengths L ranging from 0.1 to 1 mm (see Table 2 for exact lengths) and another drilled capillary die with an exact length $L = 2.0$ mm. Orifice die, were made in the form of tungsten carbide inserts with an outer diameter of 15 mm (which is the same as the barrel diameter D_b of the capillary rheometer). Measurements were conducted on RH7-2 using a 16 x 1 mm long capillary and the specified orifice dies for various PE materials

(LLDPE, LDPE, HDPE) at a temperature of 200 °C. The properties of these materials are provided in [94].

Table 2 Dimensions of the orifice dies used by Kelly (adapted from [94])

Capillary Diameter *D* (mm)	Capillary Length *L* (mm)
1	0,12
1	0,20
1	0,37
1	0,48
1	0,75
1	0,98

Fig. 29 shows the relationship between the entrance pressure drop Δp_{entr} and the *L/D* ratio for LLDPE material at 200 °C in the range of apparent shear rate $\dot{\gamma}_{APP}$ (50 – 2500) s^{-1}. From this, it can be roughly observed that when using an orifice with an *L/D* ratio up to 0.2, Δp_{entr} is constant over the whole range of $\dot{\gamma}_{APP}$ used. Above this value, there is a slight change in Δp_{entr} up to a value of ratio $L/D = 0.48$, from which the dependence has a linearly increasing character over the whole range of $\dot{\gamma}_{APP}$.

Kelly [94] further found that the data measured on the RH7 capillary rheometer showed the same trends as the corresponding data obtained on the online rheometer used by him.

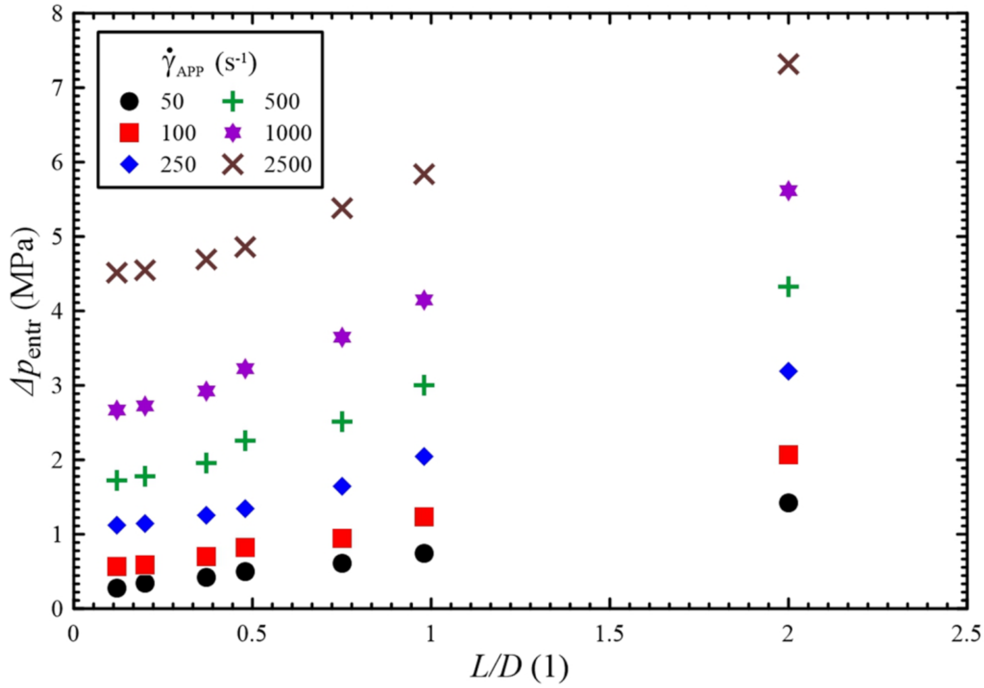

Figure 29 The dependence of the entrance pressure drop Δp_{entr} on the *L/D* ratio at different apparent shear rate values $\dot{\gamma}_{\mathrm{APP}}$ for LLDPE at 200 °C on RH7-2 (Adapted from [94])

The paper by Zatloukal et al. [95] discusses numerical modeling, including the influence of the *L/D* ratio orifice die on the apparent entrance viscosity η_{entr}, which was defined as

$$\eta_{entr} = \frac{\Delta p_{entr}}{\dot{\gamma}_{APP}}, \tag{50}$$

where Δp_{entr} is the entrance pressure drop and $\dot{\gamma}_{APP}$ is the apparent shear rate. For many applications, introducing this quantity can provide more accurate, better, or more general results than using Δp_{entr} to $\dot{\gamma}_{\mathrm{APP}}$ dependence. In particular, for the assessment of Newtonian behavior at low $\dot{\gamma}_{\mathrm{APP}}$, since the dependence of η_{entr} on $\dot{\gamma}_{\mathrm{APP}}$ shows a plateau [95]. The benefits of introducing this variable are also exploited in [96].

In the described work [95], the FEM simulation of polymer melt flow was performed on an axisymmetric die geometry with an abrupt contraction angle (α = 180°), a die diameter D = 1 mm, and a barrel diameter D_{b} = 15 mm. For the orifice die used in the numerical modeling (Fig. 30), it was assumed that the polymer melt would flow as a free beam and not stick to the underside of the die. Another premise is that the melt will not swell after exiting the orifice die, and therefore, the free surface boundary conditions were replaced by a wall with zero friction.

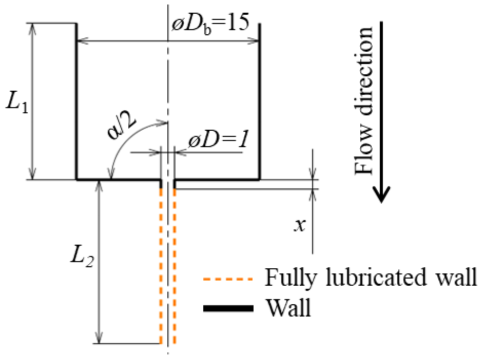

Figure 30 Schematic representation of orifice die used for numerical flow analyses, where x is orifice length in mm ($x \in \langle 0;0.3 \rangle$) and $L_1 = L_2$ = 12.75 mm, entry angle α = 180 °C. Dimensions are in mm, and the schema is not to scale (adapted from [95])

The relationship between the apparent entrance viscosity η_{entr} and the *L/D* ratio (from 0 to 0.3) and the apparent shear rate $\dot{\gamma}_{\mathrm{APP}}$ obtained from the numerical simulation on the orifice die is shown in Fig. 31. It pertains to the material referred to as M1 in the paper [95], which exhibits strain hardening. The plotted data were fitted with a suitable model (see [95]). At low $\dot{\gamma}_{\mathrm{APP}}$, the material exhibits a plateau, which transitions to a peak at higher values due to strain hardening, followed by a subsequent decrease. As the *L/D* ratio increases, the display of strain hardening becomes more limited as the entrance viscosity η_{ENT} increases with increasing *L/D* ratio at low and intermediate $\dot{\gamma}_{\mathrm{APP}}$. At high $\dot{\gamma}_{\mathrm{APP}}$, variation of the *L/D* ratio has no longer significant effect on η_{entr} (which is not the case for material not exhibiting strain hardening [95]). These statements have also been experimentally verified for LDPE material [86]. Based on these findings, a length correction was derived to calculate the extensional viscosity for different approximation methods (see Section 4.3).

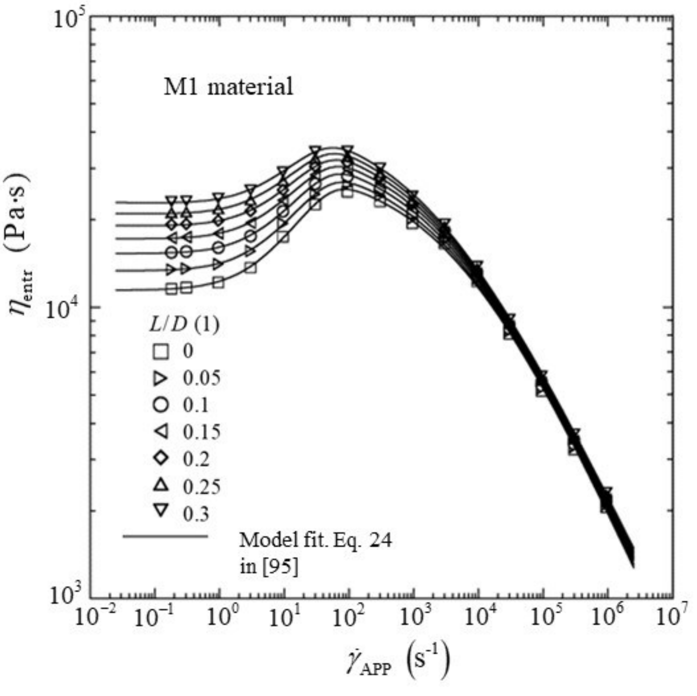

Figure 31 Predicted course of apparent entrance viscosity η_{entr} on apparent shear rate $\dot{\gamma}_{APP}$ for different *L/D* orifice die ratio for strain hardening material M1, fitted by a simple model (taken from [95])

3.2.3 Effect of the contraction entry angle

Entrance pressure drop Δp_{entr} can be further influenced by the magnitude of the contraction entry angle α (Fig. 19) [23][28][97] (in some publications, it is related to the axis of symmetry of the flow, so that half the angle, $\alpha/2$, is used [14][26], which is not used here). The entry angle α has the greatest influence on the shear fraction size in inhomogeneous contraction flow [26]. Shear flow occurs during contraction due to the melt's zero velocity on the channel's wall [71].

Mitsoulis and Hatzikiriakos [97] conducted a numerical and experimental study to investigate the effect of entry angle α on the magnitude of Δp_{entr}. Experimental measurements were performed on an Instron capillary rheometer with branched PP at

200 °C using six orifice dies with different entry angles (10°, 15°, 30°, 60°, 90° and 150°) [97] based on a modified design by Kim and Dealy [27] (Fig. 23b).

From Fig. 32, it can be concluded that the inlet angle has a negligible effect on the detected entrance pressure drop Δp_{entr}. Furthermore, it can be observed that up to the entry angle size α = 90°, Δp_{entr} decreases, after which it does not change significantly. This is evidenced by Fig. 34b, which shows the course of the dependence of the Δp_{entr} on the changing value of the entrance angle α at several low apparent shear rates $\dot{\gamma}_{APP}$ (ranging from 23.4 to 703 s^{-1}). According to the publication [97], the values of entry angle α > 90° no longer vary, and therefore their dependence was not plotted.

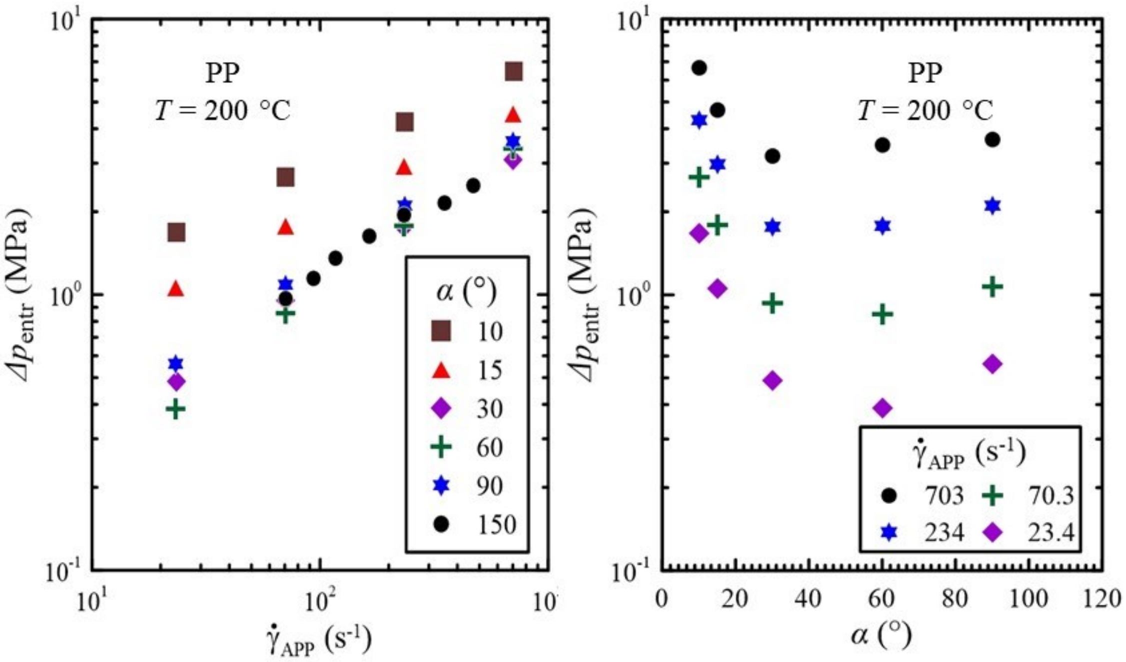

Figure 32 Effect of entry angle α of contraction on entrance pressure drop Δp_{entr} for branched PP at 200 °C (adapted from [97]). a) Comparison of the course of entrance pressure drop on apparent shear rate for different entry angles, b) Comparison of the course of the entrance pressure drop at the entry angle α for different apparent shear rate values $\dot{\gamma}_{APP}$

Another measurement investigating α effect was performed by Gibson [26] on a 4 mm diameter orifice die (D) with different entry angles (15°, 30°, 90°, 120°, 150°, and 180°). The PA 6.6 (ICI Maranyl 690) was filled with 50 % glass fiber and the measurement was performed on an instrumented injection molding machine at 285 °C [26]. Unlike the previous study, the author used a higher range $\dot{\gamma}_{APP}$ (1,000 - 10,000) s^{-1}, and the measurement was performed in the entire range of possible entry angles α.

Compared to the previous one, Gibson (based on Fig. 33) states that Δp_{entr} for the material and temperature used has an increasing character with the size of the entry angle α but is not as pronounced at lower $\dot{\gamma}_{APP}$ (Fig. 33, $\dot{\gamma}_{APP} = 1000\ \mathrm{s}^{-1}$). The measured data have also been compared by numerical prediction [26], which roughly matches them for the range of $\dot{\gamma}_{APP}$ used.

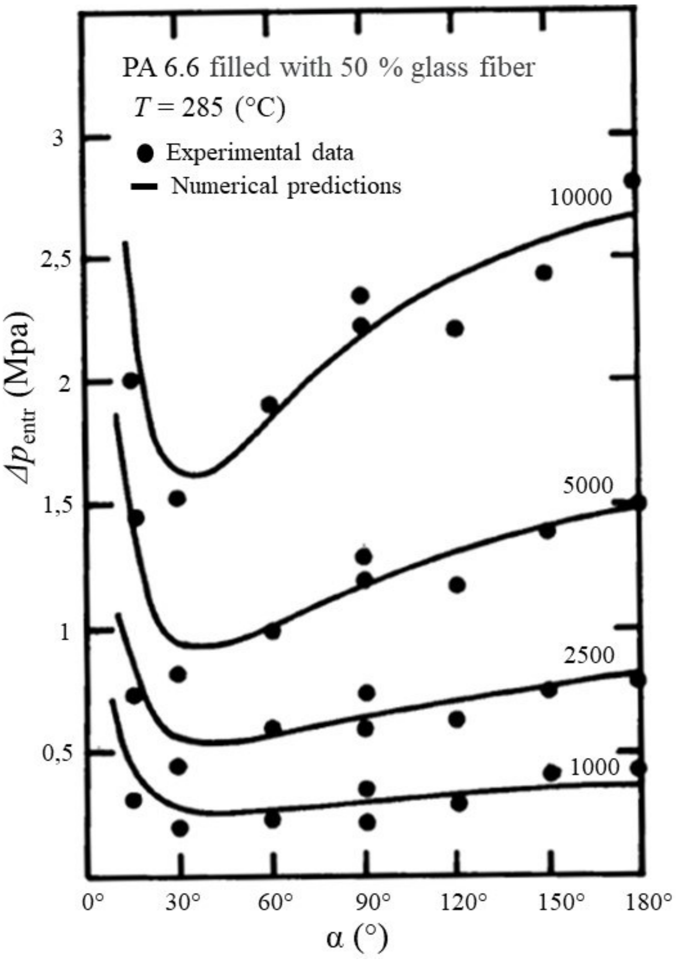

Figure 33 Experimental and numerical predictions for entrance pressure drop Δp_{entr} versus entry angle α at different apparent shear rates $\dot{\gamma}_{APP}$ (adapted from [26])

In conclusion, when using an orifice die with a small entry angle ($\alpha < 90°$), shear will be the dominant factor in the contraction flow, and the detected values of the entrance pressure drop Δp_{entr} will be affected by the error [28][97]. It is also shown in [97] that at abrupt contractions (i.e. when $\alpha = 180°$), Δp_{entr} is strongly dependent on the extensional viscosity η_E and gives the most accurate values of Δp_{entr}. Conversely, at a smaller entry angles α, the flow appears to be more stable with increasing flow rate [1][28][71]. Of course, it should be kept in mind that the above conclusions depend on the material used and the boundary conditions of the measurements.

3.2.4 Effect of contraction ratio (Effect of Hencky strain)

The total Hencky strain ε_H that the melt undergoes during contraction flow cannot be exactly quantified analytically because of its non-uniformity in the flow direction and the non-constant extensional rate $\dot{\varepsilon}$ [28][71][84].

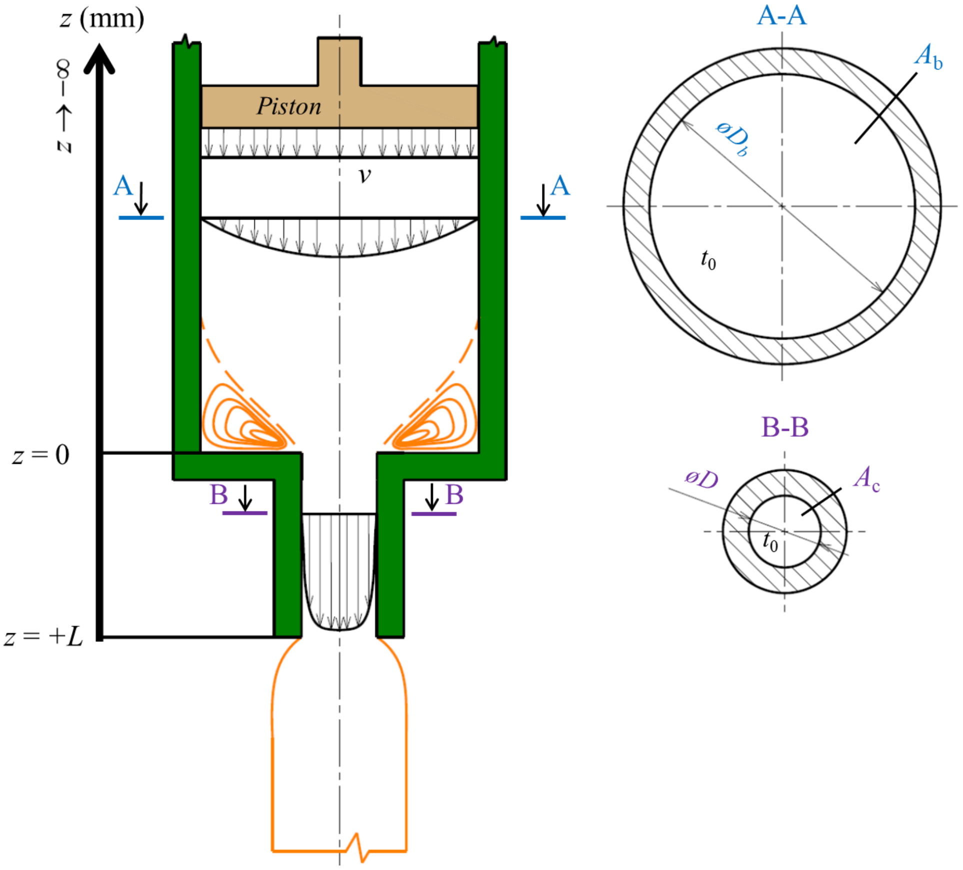

Figure 34 Schematic representation of the kinematics of polymer melts during contraction flow. The melt flows at a constant volume flow rate Q in the direction of the positive z-axis in a cross-sectional area of a barrel A_b with a mean velocity value $v_{z,b}$ at time t_0 into a narrow capillary of cross-sectional area A_c with an mean velocity value $v_{z,c}$ at time t_0 (based on information from [97])

However, it is possible to approximate the ε_H by a single value derived from the kinematics of the sudden contraction flow (as opposed to the relation of Section 2.2). This is shown schematically in Fig. 34, where the melt flows at a constant volume flow rate Q (determined using the piston velocity v). The melt moves in a wide barrel and a narrow capillary with a mean values velocity of $v_{z,b}$ and $v_{z,c}$, respectively. The Hencky strain ε_H faced by the polymer melt can be formulated using the following equation:

$$\varepsilon_H = \int_0^{t_0} \dot{\varepsilon} \cdot dt \, . \tag{51}$$

Extensional strain rate $\dot{\varepsilon}$ can then be represented as the change in velocity in the direction of the central axis

$$\varepsilon_H = \int_0^{t_0} \frac{dv_z}{dz} dt = \int_{v_{z,b}(z\to-\infty)}^{v_{z,c}(z=L)} \frac{1}{v_z} dv_z = \ln v_{z,c} - \ln v_{z,b} = \ln \frac{v_{z,c}}{v_{z,b}} = \ln \frac{\frac{Q}{A_c}}{\frac{Q}{A_b}} = \ln\left(\frac{A_b}{A_c}\right). \tag{52}$$

Thus, after integration, a simple equation can be defined to approximate the maximum limit of the ε_H to which the melt is subject during contraction flow [28] [71][97]. For the circular geometry provided in the Fig. 34, the final equation can still be modified into the following form:

$$\varepsilon_H = 2\ln\left(\frac{D_b}{D}\right) = 2\ln\left(C_R\right), \tag{53}$$

where D_b is the barrel diameter, D is the capillary diameter and C_R is contraction ratio [28].

Rajagopalan [30], in a follow-up paper to (Mitsoulis and Hatzikiriakos et al. [91]), discussed numerical predictions of contraction flow using Phan-Thien-Tanner (PTT) model in one mode. All details and the relations used are given in the original paper [30].

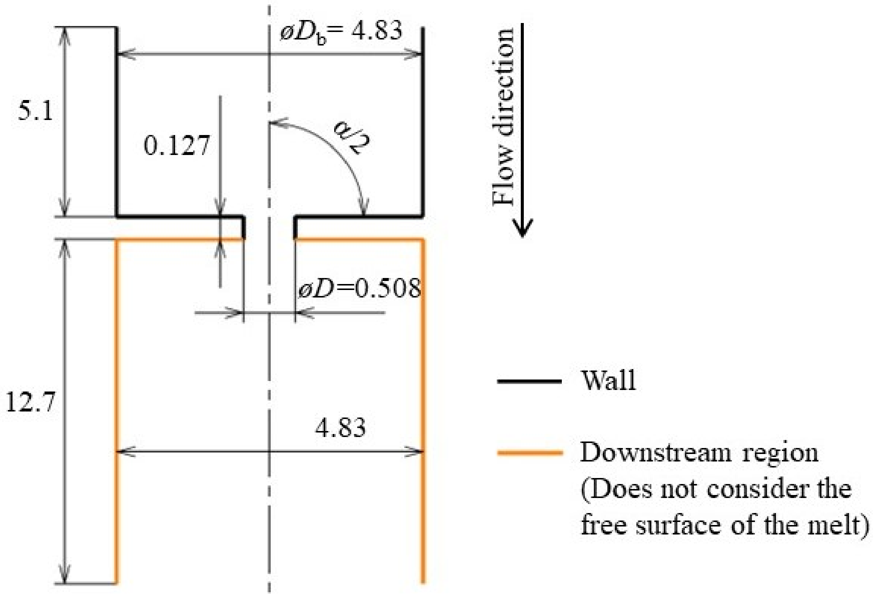

Figure 35 Schematic representation of orifice die geometry with abrupt contraction (α = 180°) used for numerical prediction in the described study, ratio $L/D \cong 0.25$ mm, all dimensions are in mm, and the schema is not to scale (adapted from [30])

Among other things, the present work addresses whether, in contraction flows (Fig. 35), the residence time (or Hencky strain ε_H) is large enough for the uniaxial extensional viscosity to reach a steady state (Chapter 2). Fig. 36 shows the $\eta_{E,U}$ versus at the extension rate $\dot{\varepsilon}$ for the linear (Fig. 36a) and exponential (Fig. 36b) forms of the PTT model, which depends highly on the material extensional parameter ε_{PTT}. In Fig. 36c, the dependence of the extensional viscosity growth for extensional rate $\dot{\varepsilon} = 10\ \mathrm{s}^{-1}$ (vertical red lines in Fig. 36a,b) on the ε_H, according to Eq. 53. The vertical line gives the value $\varepsilon_H = 4.5$ (Fig. 36c), which was obtained in the numerical simulation in the geometry used (Fig. 37) [30]. It can be seen that the linear form (ε_{PTT} = 0.05) of the PTT model needs a much larger transformation than the exponential form (ε_{PTT} = 0.05) for the uniaxial extensional viscosity $\eta_{E,U}$ to reach the equilibrium state.

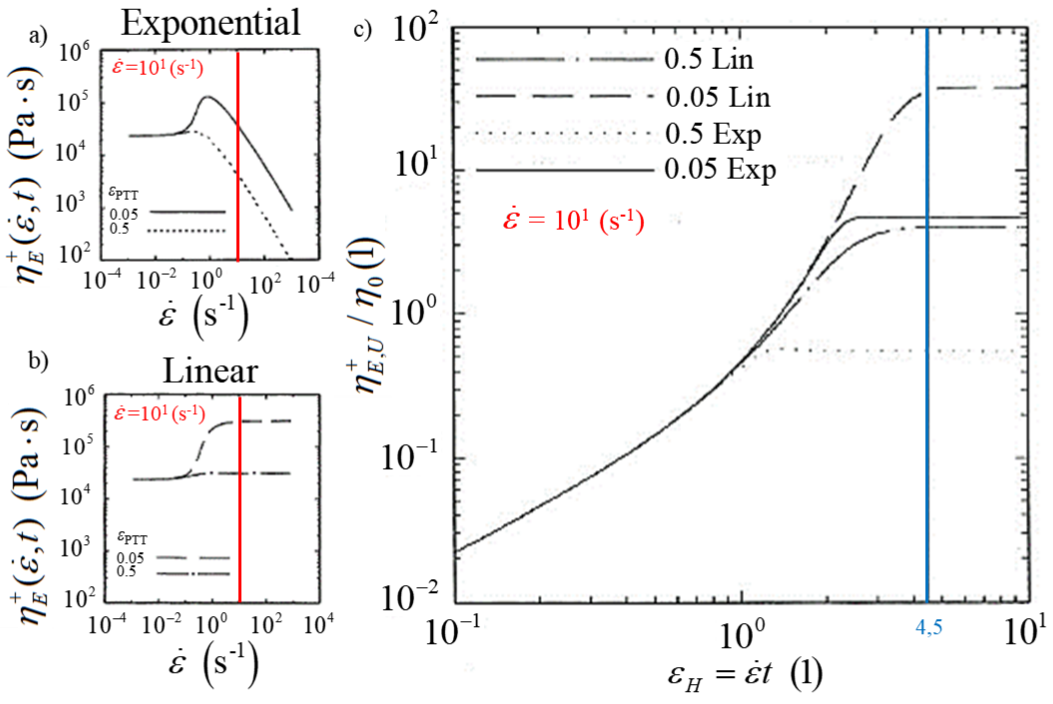

Figure 36 Comparison of the numerical courses of uniaxial extensional viscosity $\eta_{E,U}$ on extensional rate $\varepsilon^{\cdot}$ with different values of parameter ε_{PTT}, for: a) linear and b) exponential form of the PTT model, c) Courses of growing extensional viscosity $\eta_{E,U}$ (related to shear zero viscosity η_0) at extensional rate $\dot{\varepsilon}$ = 10 s^{-1} (red line) at the magnitude of extensional Hencky strain ε_H for different ε_{PTT} parameters and model forms (linear and exponential), the vertical line (blue line) indicates the used deformation (adapted from [30])

Therefore, follows from the above that the magnitude of the total deformation ε_H during the stretching of the melt element in the contraction flow determines whether $\eta_{E,U}$ reaches the equilibrium state or not. The magnitude of total strain depends on both the contraction ratio ($C_R = D_b/D$, see Eq. 53) and the material properties of the melt under investigation (such as strain hardening). The contraction ratio is therefore another parameter that can introduce significant inaccuracies when measuring extensional properties using entrance pressure drop Δp_{entr} measurements in contraction flows.

Kim and Dealy [28] experimentally investigated the effect of the contraction ratio on measured the entrance pressure drop Δp_{entr}. They performed measurements on an Instron capillary rheometer with two barrels: standard and large (see Table 3). Δp_{entr} was measured using modified orifice dies (Fig. 23b) with different diameters and thus different contraction ratios (or ε_H), as shown in Table 3. The authors [28] investigated the effect of the contraction ratio for five PE melts. Two branched metallocene types (B-mPE-1, B-mPE-3), a linear (L-mPE-3), and two linear conventional high-density types (HDPE-1, HDPE-3). The parameters of the materials used to give are in the discussed paper [28]. The courses of the dependence of the entrance pressure drop Δp_{entr} on the apparent shear rate $\dot{\gamma}_{APP}$ and the varying contraction ratio (or ε_H) are shown in Fig. 37a,b.

Table 3 Dimensions of the orifice die parameters used corresponding to (Fig. 23b) (adapted from [28])

Orifice diameter D (mm)	Contraction ratio $C_R = D_b/D$ (1)	Entrance angle α (°)	Hencky Strain ε_H (1) (Eq. 53)	Barrel D_b (mm)
0.762	12.5	180	5.05	Standard barrel D_b = 9,525
0.381	25.0	180	6.44	
0.254	37.5	180	7.25	
1.270	16.0	180	5.55	Large barrel D_b = 20,350
0.762	26.7	180	6.57	
0.508	40.1	180	7.38	

The sample dependences shown in Fig. 37a are obtained from measurements using a standard barrel and three orifice dies with entry angle α =180° for the material L-mPE-3 at 150 °C. As the contraction ratio increases, the entrance pressure drop Δp_{entr} decreases, and this trend has been observed for other materials [28]. However, when using large barrels (with almost the same contraction ratio), the dependences showed an opposite trend again for all materials. This can be seen in Fig. 37b for the B-mPE-3 material at 150 °C. This trend is consistent with Rajagopalan's numerical prediction [30] since as ε_H increases, Δp_{entr} also increases. However, the authors do not explain these different trends in their paper.

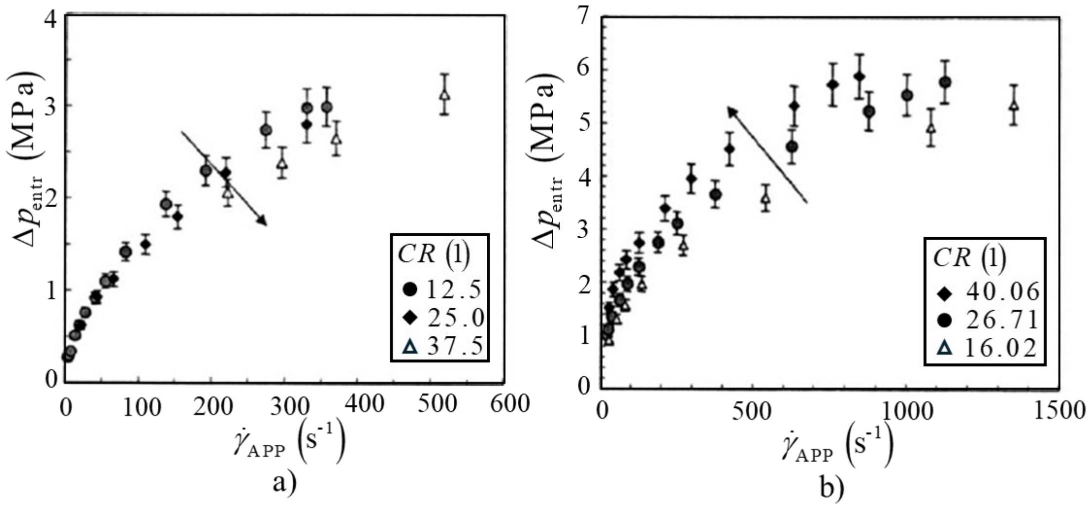

Figure 37 Course of dependence of entrance pressure drop Δp_{entr} vs. apparent shear rate $\dot{\gamma}_{APP}$ and Contraction ratio C_R with α = 180° at 150 °C. a) L-mPE-3 and standard barrel, b) H-mPE-3 and large barrel (taken from [28])

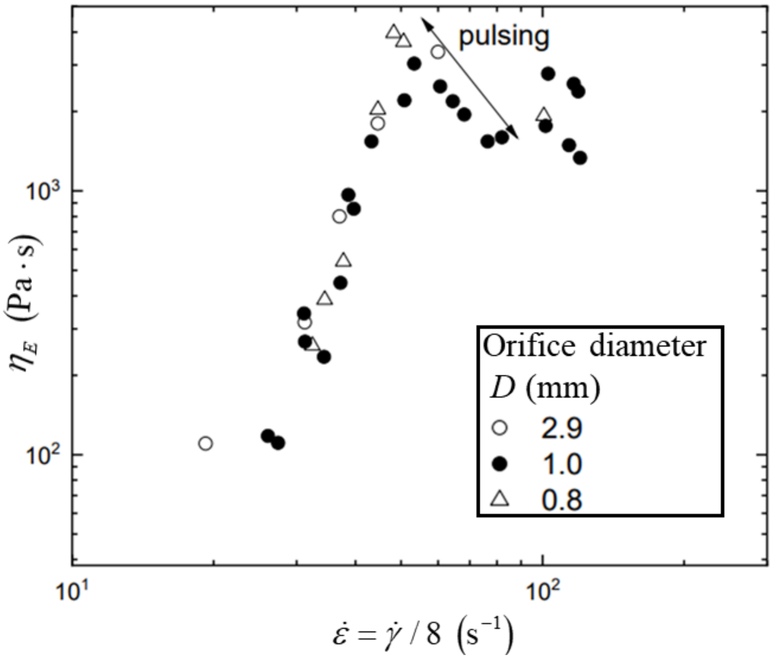

Figure 38 The course of the dependence of the uniaxial extensional viscosity $\eta_{E,U}$ on the apparent extensional rate $\dot{\varepsilon}$ for the Boger liquid at 20 °C (Adapted from [71][98])

In another interesting experimental measurement, reminded in [71], the extensional viscosity η_E of the Boger fluid in a contraction flow is determined using the Cogswell technique. As shown in Fig. 38, it can be seen that there is no significant change in the dependence of the extension viscosity on extension rate $\dot{\varepsilon}$ with changing the orifice die diameter (i.e. with changed contraction ratio C_R) [71]. This can be attributed to the fact that the Boger liquid is a polymer solution. It consists of high molecular weight polyisobutylene with a polybutene solvent and kerosene [71][98] and therefore shows a strong increase of extensional viscosity with increasing $\dot{\varepsilon}$. Thus, it can be speculated that the discussed effect cannot be observed since steady-state values of η_E already occur at low Hencky strains ε_H, and no change occurs as the contraction ratio increases, since η_E is already at a steady state.

3.3 Effect of the Approximation Technique on Calculating Extensional Viscosity

Based on the measured entrance pressure drop Δp_{entr} and other parameters such as apparent shear rate $\dot{\gamma}_{APP}$ and correction shear stress $\tau_{xy,\mathrm{corr}}$, several "approximation" techniques have been developed [99] to evaluate the extensional viscosity η_E and extension rate $\dot{\varepsilon}$. These are mainly the three most widely used (basic) techniques proposed first by Cogswell [24], then by Binding [25], and Gibson [26]. All these analyses, for example, neglect the effect of the elasticity of polymer melts (N_1 effect). However, there is also a model (Binding (N_1)) proposed by Binding [100], which accounts for the N_1 effect. This model has been experimentally tested in [84].

Because of the different premises used when deriving the basic methods, extensional viscosity η_E and extension rate $\dot{\varepsilon}$ may give different results. Therefore, another influence on the accuracy of the extensional parameters is the type of method used. To compare the capability and suitability of techniques, a number of both experimental measurements and numerical simulations have been performed for different materials and under different conditions, [29][30][95][101].

Laun and Schuch [101] performed comparative measurements of extensional viscosity for three polyolefins melts (two branched LDPEs and linear HDPE) obtained from entrance pressure drop measurements (using orifice die [71]) at contraction flow calculated by Cogswell analysis, Filament Stretching (FR), and Rotary Clamping (CR). The measured and evaluated data are shown in Fig. 40. It can be observed from these data that the data obtained by Cogswell analysis match reasonably well with those obtained by other techniques (FR, CR) at higher extensional rate $\dot{\varepsilon}$ for branched PE (LDPE 6, LDPE 9), which is not true for linear PE (HDPE 3). The under oscillation shown at intermediate values of $\dot{\varepsilon}$ is because the Cogswell technique (but also Binding, Gibson [95][102]) fails to predict the correct value of the Trouton ratio (*Tr*) at low $\dot{\varepsilon}$.

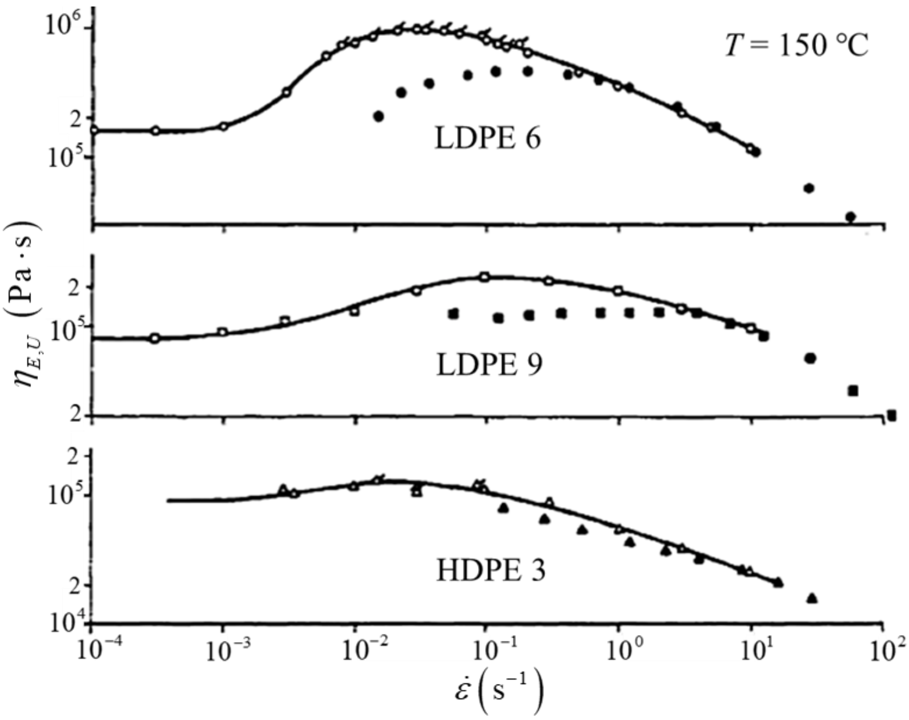

Figure 39 Comparison of the dependence of uniaxial extensional viscosity $\eta_{E,U}$ on extensional rate $\dot{\varepsilon}$ obtained from filament stretching (unfilled dashed symbols), rotational clamping (unfilled symbols) and from entrance pressure drop Δp_{entr} calculated using Cogswell analysis (filled symbols), (taken from [101])

This problem was theoretically and experimentally investigated in the above-discussed work by Zatloukal et al. [95]. Where the truth of this statement was verified by a numerical simulation performed on the orifice die (Fig. 31). The values of the *Tr* obtained by the authors for basic techniques are shown in Table 4, where the entrance viscosity (according to the Eq. 50) is related to twice the zero shear rate (Newtonian) viscosity $(\eta_{ENT,0} / 2\eta_0)$ [35][102]. This ratio for Newtonian fluids is calculated as 0.575 in the publication [35][95].

Table 4 Calculation of the Trouton ratio for different methods (adapted from [95])

Technique	Calculation relation *Tr* used in the publication [95][102]	Trouton ratio *Tr* (1)
Cogswell	$Tr = \frac{9}{2}\left(\frac{\eta_{ENT,0}}{2\eta_0}\right)^2$	1.49
Binding	$Tr = \frac{27}{8}\left(\frac{\eta_{ENT,0}}{2\eta_0}\right)^2$	1.94
*Gibson	$Tr = \frac{96}{3\pi + 8}\frac{\eta_{ENT,0}}{2\eta_0} - \frac{512}{\pi^4 (3\pi + 8)}$	2.87

* For Gibson model, the premise is that $(D / D_b)^3 \approx 0$ (where D_b is the diameter of the barrel and *D* is the diameter orifice die) [95].

Based on the verification of the above problem, Zatloukal et al. proposed “effective entry length correction $(L/D)_{Tr}$” [95] which can be used to obtain more accurate results of approximation techniques in the low extensional rate $\dot{\varepsilon}$ region (Newtonian behavior plateau). In Table 5, specific $(L/D)_{Tr}$ for different computational techniques of extension viscosity were found.

Table 5 A suggested orifice die $(L/D)_{Tr}$ ratios for different approximation methods (adapted from [95])

Approximation method	Cogswell	Binding	Gibson
$(L/D)_{Tr}$ (1)	0.1208	0.1839	0.0122

Zatloukal and Musil [29] deal, among other things, with comparing differently obtained uniaxial extensional viscosity. They compare the results based on the corrected (using $(L/D)_{Tr}$ correction) and uncorrected approximation techniques with the uniaxial extensional viscosity obtained from SER measurements. Experimental measurement of the entrance pressure drop Δp_{entr}, from which the uniaxial viscosity was calculated according to the authors, was performed on a twin bore capillary rheometer RH7-2 for three polyolefins melts. A novel orifice die design with an entry angle α = 180° was used during the measurements (Fig. 28a).

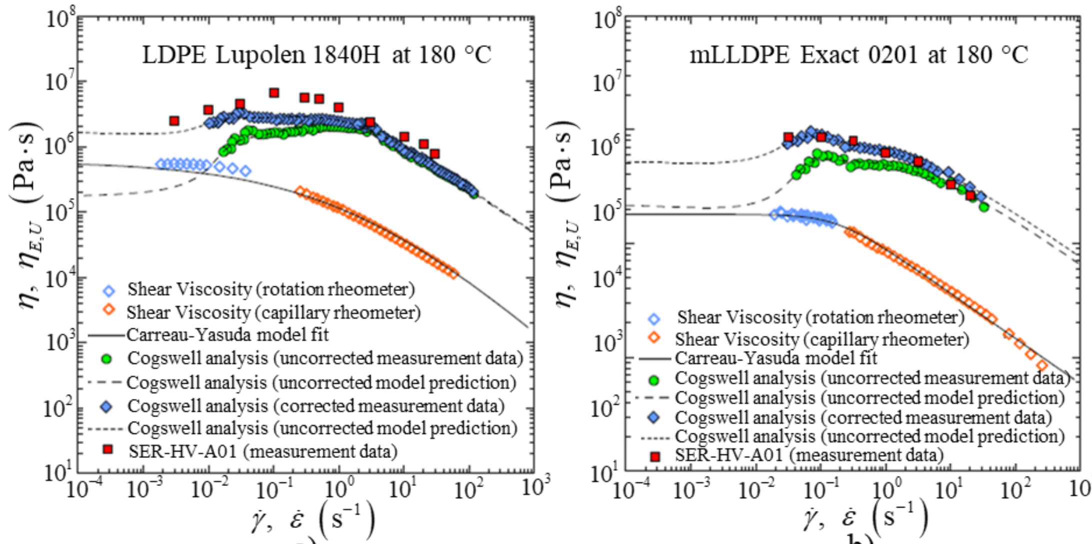

a) b)

Figure 40 Shear η and uniaxial extensional $\eta_{E,U}$ viscosity versus shear $\dot{\gamma}$ and extensional strain $\dot{\varepsilon}$ rate determined using corrected and uncorrected data for Cogswell approximation analyses (Adapted from [29]). a) LDPE, b) mLLDPE

For the branched LDPE polymer Lupolen 1840H, the authors found that the results from the Cogswell analysis are in most agreement with the measurements obtained from SER (Fig. 40a). On the contrary, the results of the Binding analysis showed good agreement with the measured data only at low extensional rates, and Gibson's underestimated the measured data for the LDPE. Cogswell analysis, however, is unable, due to the large strain hardening of the material, to effectively describe the region at intermediate values of $\dot{\varepsilon}$. The authors give a strain hardening condition $\eta_{E,U\max}/3\eta_0 < 2$ (where $\eta_{E,U\max}$ is the maximum uniaxial extensional viscosity and η_0 is the zero shear rate viscosity), i.e. when the condition is satisfied, the Cogswell analysis gives more accurate results (for LDPE Lupolen 1840H, the ratio is equal to $\eta_{E,U\max}/3\eta_0 = 3$).

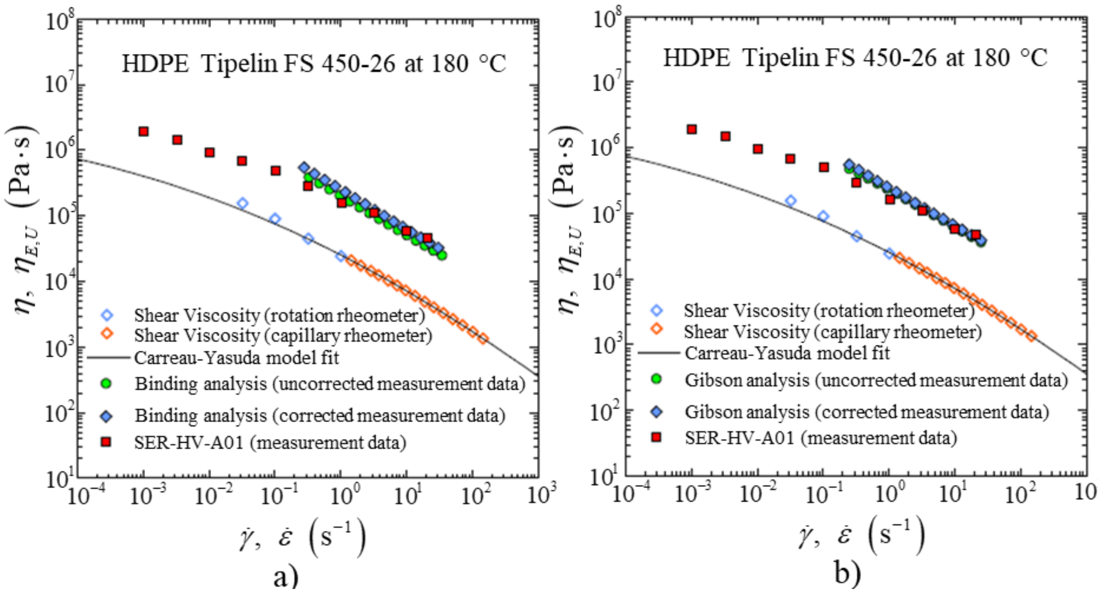

Figure 41 Shear η and uniaxial extensional $\eta_{E,U}$ viscosity versus shear $\dot{\gamma}$ and extensional $\dot{\varepsilon}$ rate determined by various techniques and comparison of corrected and uncorrected measured data of approximation analyses (Adapted from [29]). a) Binding method, b) Gibson method

This is proved on the polymer material with small level of branches, mLLDPE Exact 0201 (Fig. 40b) with low level of the strain hardening ($\eta_{E,U\max}/3\eta_0$ = 1.6) for which the uniaxial extensional viscosity data from SER are consistent with the uniaxial extensional viscosity obtained from Cogswell analysis. On the other hand, the results from the Cogswell technique do not match the SER measurements for the linear HDPE Tipelin FS 450-26. However, the Binding and Gibson analysis provided good agreement over the entire range of extensional strain rates $\dot{\varepsilon}$ as shown in Fig. 41ab.

The conclusions provided in [29] are consistent with other experimental and numerical studies such as, e.g. [30][84]. Other works using the corrections described above for approximation analyses to deduce extensional viscosity from the entrance pressure drop measurements include, for example [14].

4 CONSTITUTIVE EQUATIONS OF POLYMER MELTS

Constitutive equations (CE) are mathematical tools that allow obtaining information about stresses during the flow/deformation of polymer materials [103]. Together with the equations of conservation of mass, energy, and momentum [3][40], they theoretically explain the behavior of polymer melts in various flow situations, and thus are widely used in the design of equipment and optimization of the production process [104]. The ideal solution would be a CE that describes the full Pipkin map (Fig. 4). However, such a model would be computationally very complex and time-consuming in any computation. For these reasons, emphasis is placed on using CEs that are simple and additionally precise to describe the issue at hand [105]. More detailed descriptions of CEs for polymer melts can be found, e.g., in [41][46][61][106].

4.1 Models for non-Newtonian fluids

Generalized Newtonian fluid (GNF) constitutive equations are classified as one of the simplest models in which the viscosity η is not constant but depends on the strain rate tensor $\underline{\underline{D}}$ (Eq. 11) or sometimes the temperature T [18]. The first models of this kind can provide steady shear viscosity values with sufficient accuracy, but they cannot predict elastic behavior or any time dependence [107]. These models include the Power law model, Carreau-model, Cross model, and others [61]. Subsequently, models were also proposed that gave good results for uniaxial extensional viscosity $\eta_{E,U}$ using the second $\left(II_{\underline{\underline{D}}}\right)$ and third $\left(III_{\underline{\underline{D}}}\right)$ invariants of the strain rate tensor $\underline{\underline{D}}$. However, these models failed to separate uniaxial $\eta_{E,U}$ and planar $\eta_{E,P}$ extensional viscosities (because $III_{\underline{\underline{D}}} = 0,$ see Table 6) [107].

According to [107], many authors have tried to find a mechanism to distinguish between different types of extensional viscosity. However, this was only succeeded by Yao [105] [108], who, based on the idea of previous authors [107][108], introduced the objective velocity gradient tensor $\underline{\underline{\bar{L}}} = \underline{\underline{D}} + \underline{\underline{\bar{W}}}$ (where $\underline{\underline{\bar{W}}}$ objective vorticity tensor [108][109]). Zatloukal [109] also uses this new tensor in his formulation of modified GNF model. The introduction of this variable eliminates fluid rotation and thus the enables to distinguish between uniaxial $\eta_{E,U}$ and planar $\eta_{E,P}$ extensional viscosity [107][108].

Table 6 Different invariant expressions for basic flows, where $II_{\underline{\underline{D}}}$ is second and $III_{\underline{\underline{D}}}$ third invariants of the strain rate tensor $\underline{\underline{D}}$, $II_{\underline{\underline{\bar{L}}}}$ is the second invariant of the objective velocity gradient $\underline{\underline{\bar{L}}}$ (velocity gradient tensor $\underline{\underline{L}}$) (adapted from [109])

*Type flow	Simple shear flow	Uniaxial extensional flow	Biaxial extensional flow	Planar extensional flow
$\underline{\underline{D}}$	$\begin{pmatrix} 0 & \dot{\gamma}/2 & 0 \\ \dot{\gamma}/2 & 0 & 0 \\ 0 & 0 & 0 \end{pmatrix}$	$\begin{pmatrix} \dot{\varepsilon} & 0 & 0 \\ 0 & -\dot{\varepsilon}/2 & 0 \\ 0 & 0 & -\dot{\varepsilon}/2 \end{pmatrix}$	$\begin{pmatrix} \dot{\varepsilon} & 0 & 0 \\ 0 & \dot{\varepsilon} & 0 \\ 0 & 0 & -2\dot{\varepsilon} \end{pmatrix}$	$\begin{pmatrix} \dot{\varepsilon} & 0 & 0 \\ 0 & 0 & 0 \\ 0 & 0 & -\dot{\varepsilon} \end{pmatrix}$
$\underline{\underline{L}} = \underline{\underline{\bar{L}}}$	$\begin{pmatrix} 0 & \dot{\gamma} & 0 \\ 0 & 0 & 0 \\ 0 & 0 & 0 \end{pmatrix}$	$\begin{pmatrix} \dot{\varepsilon} & 0 & 0 \\ 0 & -\dot{\varepsilon}/2 & 0 \\ 0 & 0 & -\dot{\varepsilon}/2 \end{pmatrix}$	$\begin{pmatrix} \dot{\varepsilon} & 0 & 0 \\ 0 & \dot{\varepsilon} & 0 \\ 0 & 0 & -2\dot{\varepsilon} \end{pmatrix}$	$\begin{pmatrix} \dot{\varepsilon} & 0 & 0 \\ 0 & 0 & 0 \\ 0 & 0 & -\dot{\varepsilon} \end{pmatrix}$
$II_{\underline{\underline{D}}}$	$\dot{\gamma}^2$	$3\dot{\varepsilon}^2$	$12\dot{\varepsilon}^2$	$4\dot{\varepsilon}^2$
$II_{\underline{\underline{\bar{L}}}}$	0	$3\dot{\varepsilon}^2$	$12\dot{\varepsilon}^2$	$4\dot{\varepsilon}^2$
$III_{\underline{\underline{D}}}$	0	$\frac{1}{4}\dot{\varepsilon}^2$	$-2\dot{\varepsilon}^2$	0

*More information on basic flows can be found in Chapter 2.

4.1.1 Yao model (Yao 2022)

The Yao model can applied to model the flow behavior of non-Newtonian fluids (both in shear and in extension) and also provides information on the elasticity of polymer melts. Yao [105] reformulated his original stress relation from the implicit dependence of the velocity gradient $\underline{\underline{L}}$ [108] into an explicit form. Thus, he created a simple form of the constitutive equation and obtained analytical relations to calculate the values of shear viscosity and extensional viscosity (uniaxial, biaxial and planar) [105]. Yao's model is based on a modified tensor form of Hook's law

$$\underline{\underline{\tau}} = G\underline{\underline{B}}^*, \tag{54}$$

where is the $\underline{\underline{\tau}}$ extra stress tensor and G is the linear elastic modulus, which can be obtained from the following equation:

$$G = G_0 \xi^{-\psi_Y}. \tag{55}$$

Here, the initial elastic modulus $G_0 = \eta_0 / \lambda_Y$, and $\xi^{-\psi_Y}$ is the shape function of elastic modulus, which is controlled by the strain hardening coefficient ψ_Y [59][105]

$$\xi = \frac{S_0}{S_0 + \lambda_Y \sqrt{\frac{2}{3} tr\left(\underline{\underline{D}} \cdot \underline{\underline{D}}\right)}}, \tag{56}$$

where S_0 is the ceiling stretch [110], λ_Y is the relaxation time at small strain, tr is a trace of a given tensor. The generalized Finger tensor $\underline{\underline{B}}^*$ has the following form:

$$\underline{\underline{B}}^* = \left[\exp(\xi^{\alpha_0} n_0 \lambda_Y \bar{L}) \cdot \exp(\xi^{\alpha_0} n_0 \lambda_Y \bar{L}^T)\right]^{\frac{1}{n}}, \tag{57}$$

where ξ^{α_0} is the shape of the function controlled parameter α_0 [59] [105], and n_0 is index of rotation recovery. The final explicit form of the discussed CE is as follows:

$$\underline{\underline{\tau}} = G_0 \xi^{-\psi_Y} \left[\exp\left(\xi^{\alpha_0} n_0 \lambda_Y \underline{\underline{\bar{L}}}\right) \cdot \exp\left(\xi^{\alpha_0} n_0 \lambda_Y \underline{\underline{\bar{L}}}^T\right)\right]^{\frac{1}{n_0}}. \tag{58}$$

According to the above equations, the expression for the steady shear viscosity η is

$$\eta = \eta_0 \frac{\xi_s^{-\psi_Y}}{\lambda_Y \dot{\gamma}} \frac{R_Y{}^{2/n_0} - \left(4/R_Y\right)^{2/n_0}}{2^{2/n_0}\sqrt{\gamma^2 + 4}}, \tag{59}$$

where $\dot{\gamma}$ is the shear rate, η_0 is zero shear rate viscosity, terms ξ_S, γ_Y and R_Y of Eq. 59 are given as follows:

$$\xi_s = \frac{S_0}{S_0 + \frac{\lambda_Y}{\sqrt{3}}\dot{\gamma}}, \quad \gamma_Y = \xi_s^{\alpha_0} n_0 \lambda_Y \dot{\gamma}, \quad R_Y = \sqrt{4 + \gamma_Y{}^2} + \gamma_Y. \tag{60}$$

Uniaxial viscosity extension $\eta_{E,U}$ can be found in the analytical relation

$$\eta_{E,U} = \frac{\eta_0}{\lambda_Y \dot{\varepsilon}} \xi_E^{-\psi_Y} \left[\exp\left(\xi_E^{\alpha_0} 2\lambda_Y \dot{\varepsilon}\right) - \exp\left(-\xi_E^{\alpha_0} \lambda_Y \dot{\varepsilon}\right)\right], \tag{61}$$

where ξ_E is formulated based on Eq. 56 as:

$$\xi_E = \frac{S_0}{S_0 + \lambda_Y \dot{\varepsilon}}.$$

Here $\dot{\varepsilon}$ is the extensional strain rate [59][108]. The given relations of the Yao model contain 6 adjustable parameters $n_0, \lambda_Y, \psi_Y, S_0, \alpha_0, \eta_0$ [105].

4.1.2 Modified Generalized Newtonian Fluid (mGNF) model (Zatloukal 2020)

The modified Generalized Newtonian fluid (mGNF) constitutive equation modified by Zatloukal [109] gives very satisfactory results of steady-state values of shear and extensional viscosity and is given by the following form:

$$\underline{\underline{\tau}} = 2\eta\left(II_{\underline{\underline{D}}}, III_{\underline{\underline{D}}}, II_{\underline{\underline{\bar{L}}}}\right)\underline{\underline{D}}. \tag{62}$$

As can be seen, in this model, the viscosity η does not depend only on the second invariant of the deformation rate tensor $II_{\underline{\underline{D}}} = tr\left(\underline{\underline{D}}^2\right)$ but also on the third invariant $II_{\underline{\underline{D}}} = \det\left(\underline{\underline{D}}\right)$ and the second invariant of the objective velocity gradient tensor $II_{\underline{\underline{\bar{L}}}} = 2tr\left(\underline{\underline{\bar{L}}}^2\right)$, (where tr is the trace and det is the determinant of the corresponding tensor. Table 6 shows the values of the invariant variables for different types of flows.) The expression for the viscosity is given as follows:

$$\eta\left(II_{\underline{\underline{D}}}, III_{\underline{\underline{D}}}, II_{\underline{\underline{\bar{L}}}}\right) = A_Z^{1-f}\eta\left(II_{\underline{\underline{D}}}\right)^f, \tag{63}$$

where A_Z is physically associated as

$$A_Z = \frac{3\eta_\infty^2}{\eta_{E,U\infty}}. \tag{64}$$

The function f is formulated as

$$f = \left\{\tanh\left[\lambda_1\left(1+\frac{1}{12\sqrt{3}}\right)^{-\psi}\left(\left|1+\frac{III_{\underline{\underline{D}}}}{II_{\underline{\underline{D}}}^{3/2}}\right|\right)^{\psi}\sqrt{II_{\underline{\underline{\bar{L}}}}}+\beta\right]\frac{1}{\tanh(\beta)}\right\}^{\zeta}. \tag{65}$$

The next term of Eq. 63 $\eta\left(II_{\underline{\underline{D}}}\right)$ is determined using the Carreau-Yasuda model [59] (without the temperature function α_T, - different models are provided in [46][50]) and is given by the following equation:

$$\eta\left(II_{\underline{\underline{D}}}\right) = \eta_\infty + \frac{\eta_0 + \eta_\infty}{\left[1+\left(\lambda_1\sqrt{II_{\underline{\underline{D}}}}\right)^a\right]^{\left(\frac{1-n}{a}\right)}}. \tag{66}$$

The described CE includes 10 adjustable parameters: 5 parameters $(\eta_0, \eta_\infty, \lambda_1, a, n)$ identifiable from the shear viscosity, 3 parameters $(\lambda_2, \beta, \zeta)$ identifiable from the uniaxial extensional viscosity, and 1 parameter (ψ_Z) identifiable from planar extensional viscosity. The exact meaning of these parameters is provided in [59][109].

The analytical expression for the calculation of steady shear viscosity η (neglecting η_∞ term) provided by the modified mGNF model is as follows:

$$\eta = \frac{\eta_0}{\left[1 + (\lambda_1 \dot{\gamma})^a\right]^{\left(\frac{1-n}{a}\right)}}, \tag{67}$$

and for uniaxial extensional viscosity $\eta_{E,U}$

$$\eta_{E,U} = 3A_Z^{\,1-\left[\frac{\tanh\left(\lambda_2\sqrt{3}\dot{\varepsilon}+\beta\right)}{\tanh(\beta)}\right]^{\zeta}} \left\{ \eta_\infty + \frac{\eta_0 - \eta_\infty}{\left[1+\left(\lambda_1\sqrt{3}\dot{\varepsilon}\right)^a\right]^{\frac{1-n}{a}}} \right\}^{\left[\frac{\tanh\left(\lambda_2\sqrt{3}\dot{\varepsilon}+\beta\right)}{\tanh(\beta)}\right]^{\zeta}} . \tag{68}$$

GNF models are widely used for the optimization of manufacturing processes such as film casting and film blowing and a deeper understanding of different flow instabilities (e.g. neck-in [64]) [109].

4.2 Viscoelastic constitutive equations

The CEs describing the behavior of viscoelastic materials (see Section 1.2) can be classified according to the form of notation into integral and differential [46][41][106]. In this thesis, only two differential equations will be used [103][104], which are introduced bellow.

4.2.1 Modified White-Metzner model (Barnes and Roberts 1992)

A simple and analytical modification of the Maxwell model by White and Metzner [111] assumes that the viscosity η and relaxation time λ are controlled by $II_{\underline{\underline{D}}}$. The White-Metzner (WM) model is given in tensor form as follows:

$$\underline{\underline{\tau}} + \lambda(II_{\underline{\underline{D}}})\overset{\nabla}{\underline{\underline{\tau}}} = 2\eta(II_{\underline{\underline{D}}})\underline{\underline{D}} . \tag{69}$$

Here, $\overset{\nabla}{\underline{\underline{\tau}}}$ is an upper convected time derivative of the stress tensor that can be defined as

$$\overset{\nabla}{\underline{\underline{\tau}}} = \frac{D\underline{\underline{\tau}}}{Dt} - \left(\underline{\underline{L}}\,\underline{\underline{\tau}} + \underline{\underline{\tau}}\,\underline{\underline{L}}^T\right) = \frac{\partial \underline{\underline{\tau}}}{\partial t} + (\nabla \cdot v)\underline{\underline{\tau}} - \left(\underline{\underline{L}}\,\underline{\underline{\tau}} + \underline{\underline{\tau}}\,\underline{\underline{L}}^T\right) \cdot \tag{70}$$

If the stress is homogeneous and the flow is steady, the time derivative of the stress $\frac{\partial \underline{\underline{\tau}}}{\partial t}$ and the convective transport term $(\nabla \cdot v)\underline{\underline{\tau}}$ are zero values [65]. The WM model can simply provide good information about the behavior of the polymer melt in shear flows, but it appears to be unusable in extensional flows as it provides unrealistic information about the extensional viscosity, which is trending to infinity. This problem was eliminated by Barnes and Roberts [112], who modified the WM model based on "the special and highly specific forms" [112] of deformation rate dependent viscosity $\eta\left(II_{\underline{\underline{D}}}\right)$ (based on the Carreau-Yasuda model [110], but originally the Cross model was used [112])

$$\eta\left(II_{\underline{\underline{D}}}\right) = \frac{\eta_0}{\left[1+\left(\lambda_1\sqrt{II_{\underline{\underline{D}}}}\right)^a\right]^{\left(\frac{1-n}{a}\right)}}, \tag{71}$$

and deformation rate dependent relaxation time $\lambda\left(II_{\underline{\underline{D}}}\right)$

$$\lambda\left(II_{\underline{\underline{D}}}\right) = \frac{\lambda_{EW}}{1+K_1\sqrt{II_{\underline{\underline{D}}}}}\,. \tag{72}$$

In the mWM η_0, λ_1, a, n are the 4 shear adjustable parameters, and K_1, λ_{EW} are the extensional constants, which must be carefully selected $\left(\lambda_{EW} / K_1 < \sqrt{3}/2\right)$ to keep the extensional viscosity η_E at the finite value [110][112]. Its calculation can be done according to the following relationship

$$\eta_E = \frac{2\eta(II_{\underline{\underline{D}}})}{1-\frac{2}{\sqrt{3}}\lambda\left(II_{\underline{\underline{D}}}\right)\sqrt{II_{\underline{\underline{D}}}}} + \frac{\eta(II_{\underline{\underline{D}}})}{1+\frac{1}{\sqrt{3}}\lambda\left(II_{\underline{\underline{D}}}\right)\sqrt{II_{\underline{\underline{D}}}}}\,. \tag{73}$$

The individual invariants are listed in Table 6 based on the extensional flow type. The same applies to the shear viscosity η, according to the Carreau-Yasuda model Eq. 67.

4.2.2 Modified Leonov model (Zatloukal 2003)

Leonov's original model [113] was in excellent agreement with measurements for many polymer melts and solutions in steady shear flows [103]. Leonov based his model on the theory of rubber elasticity, using “heuristic thermodynamic arguments” [64].

Leonov [113] thus, he constructed the mathematical relationship of stress tensor $\underline{\underline{\tau}}$ and elastic strain (defined by the recoverable Finger tensor $\underline{\underline{c}}^{(i)}$), in the following multi-mode equation (with "*i*" relaxation mode)

$$\underline{\underline{\tau}} = 2\sum_{i=1}^{\infty}\left(\underline{\underline{c}}^{(i)}\frac{\partial W_L^{(i)}}{\partial I^{(i)}_{1,\underline{\underline{c}}^{(i)}}} - \underline{\underline{c}}^{(i)^{-1}}\frac{\partial W_L^{(i)}}{\partial I^{(i)}_{2,\underline{\underline{c}}^{(i)}}}\right), \tag{74}$$

where $W_L^{(i)}$ is an elastic potential that depends on the values of the first $I^{(i)}_{1,\underline{\underline{c}}^{(i)}}$ and second $I^{(i)}_{2,\underline{\underline{c}}^{(i)}}$ invariants of the Finger recoverable tensor $\underline{\underline{c}}^{(i)}$ [44][114]

$$I^{(i)}_{1,\underline{\underline{c}}^{(i)}} = tr\left(\underline{\underline{c}}^{(i)}\right) = c_{xx}^{(i)} + c_{yy}^{(i)} + c_{zz}^{(i)}, \tag{75}$$

$$I^{(i)}_{2,\underline{\underline{c}}^{(i)}} = \frac{1}{2}\left\{\left[tr\left(\underline{\underline{c}}^{(i)}\right)\right]^2 - tr\left(\underline{\underline{c}}^{(i)^2}\right)\right\} = c_{xx}^{(i)^{-1}} + c_{yy}^{(i)^{-1}} + c_{zz}^{(i)^{-1}}. \tag{76}$$

A major disadvantage of the original Leonov model [113] was unrealistic behavior of the predicted extensional viscosity η_E, since its value remains virtually independent on the extensional strain rate $\dot{\varepsilon}$. This problem was partially solved in [115], by generalizing the elastic potential, $W_L^{(i)}$, into the following form:

$$W_L^{(i)} = \frac{3G_i}{2\left(n_L^{(i)}+1\right)}\left\{\left(1-\beta_L^{(i)}\right)\left[\left(\frac{I^{(i)}_{1,\underline{\underline{c}}^{(i)}}}{3}\right)^{n_L^{(i)}+1} - 1\right] + \beta_L^{(i)}\left[\left(\frac{I^{(i)}_{2,\underline{\underline{c}}^{(i)}}}{3}\right)^{n_L^{(i)}+1} - 1\right]\right\}. \tag{77}$$

After deriving the elastic potential, $W_L^{(i)}$, the equation (Eq. 74) can be transformed into the following form [114]

$$\underline{\underline{\tau}} = \sum_{i=1}^{\infty} G_i\left\{\underline{\underline{c}}^{(i)}\left[\left(\frac{I^{(i)}_{1,\underline{\underline{c}}^{(i)}}}{3}\right)^{n_L^{(i)}}\left(1-\beta_L^{(i)}\right)\right] - \underline{\underline{c}}^{(i)^{-1}}\left[\beta_L^{(i)}\left(\frac{I^{(i)}_{2,\underline{\underline{c}}^{(i)}}}{3}\right)^{n_L^{(i)}}\right]\right\}, \tag{78}$$

where G_i is the linear elastic modulus in (from Hooke's law [16]), $\beta_L^{(i)}$ and are $n_L^{(i)}$ non-linear numeric parameters [114].

Leonov's model is based on the premise that fading memory is characterized by an irreversible dissipation process that produces an irreversible rate of strain $\underline{\underline{e}}_p^{(i)}$

$$\underline{\underline{e}}_p^{(i)} = b_L^{(i)} \left[\underline{\underline{c}}^{(i)} - \frac{I_{1,\underline{\underline{c}}^{(i)}}^{(i)}}{3} \underline{\underline{\delta}} \right] - b_L^{(i)} \left[\underline{\underline{c}}^{(i)^{-1}} - \frac{I_{2,\underline{\underline{c}}^{(i)}}^{(i)}}{3} \underline{\underline{\delta}} \right], \tag{79}$$

where $\underline{\underline{\delta}}$ is the unit tensor, $b_L^{(i)}$ is the dissipation term that controls the dissipation process. Elastic strain $\underline{\underline{c}}^{(i)}$ is related to rate deformation $\underline{\underline{D}}$ according to the following equation:

$$\overset{\circ}{\underline{\underline{c}}}{}^{(i)} - \underline{\underline{c}}^{(i)} \underline{\underline{D}} - \underline{\underline{D}}\,\underline{\underline{c}}^{(i)} + 2 \underline{\underline{c}}^{(i)} \underline{\underline{e}}_p^{(i)} = 0, \tag{80}$$

where $\overset{\circ}{\underline{\underline{c}}}{}^{(i)}$ is the corotational (Jaumann) time derivative $\underline{\underline{c}}^{(i)}$ [106].

The parameter $b_L^{(i)}$ proposed in [116] already provided better results for the steady uniaxial extensional viscosity curve which however showed "unphysical sharp waviness" [103]. This problem was reduced by Zatloukal [103] by modifying the $b_L^{(i)}$ as

$$b_L^{(i)} = \frac{1}{4\lambda_i} \left\{ \exp\left[-\xi_L^{(i)} \sqrt{I_{1,\underline{\underline{c}}^{(i)}}^{(i)} - 3} \right] + \frac{\sinh\left[\upsilon^{(i)} \left(I_{1,\underline{\underline{c}}^{(i)}}^{(i)} - 3 \right) \right]}{\upsilon^{(i)} \left(I_{1,\underline{\underline{c}}^{(i)}}^{(i)} - 3 \right) + 1} \right\}, \tag{81}$$

where, $\xi_L^{(i)}$ and $\upsilon^{(i)}$ are dissipation parameters depending on the relaxation time λ_i and are usually determined based on experimental uniaxial extensional viscosity data [103][114].

The equations for the calculation of individual parameters (such as steady shear viscosity and steady uniaxial extensional viscosity) cannot be formulated due to the numerical character of the modified Leonov model (mLM). A major advantage of the mLM is its ability to describe a large amount of information about the flow behavior of polymer melts (such as transient shear viscosity, N_1 and N_2) using only the relaxation spectrum [46]. It is also widely used in different areas, e.g., in rubber compounding [117], modeling of polymer solution rheology [118], or in modeling of the extrusion film casting process [64][114].

II. ANALYSIS

5 SUMMARY OF THE STUDIED REASERCH FIELD

By deriving basic rheological concepts and quantities using continuum mechanics, the theoretical part gradually reaches the characteristic flows that occur not only in the processing of polymer melts, where the emphasis is placed on elongational flows and related topics. The following is a brief performance and comparison of some methods of determining extensional viscosity η_E. The method of their determination, based on measuring the entrance pressure drop Δp_{entr} using a capillary rheometer, is discussed thoroughly. After discussing the central theme, which will be summarized further, selected constitution equations for polymer melts were presented.

There are two ways of determining the entrance pressure loss (Bagley's plot or using an orifice die). Publications that compare them generally agree that the difference Δp_{entr} obtained from both methods is within the experimental error [30]. Another influence on the general level is found in using an approximation method for obtaining the elongational viscosity from the measured Δp_{entr} since different methods can provide different accurate results for various materials [71].

The intention of the thesis relates to the investigation of the influence of the design of the orifice die, i.e., the impact of the geometry of the flow channel on the size of the detected entrance pressure drop. Different effects, such as filling die exit region by polymer melt, the L/D ratio, the size of the entrance angle α, and the contraction ratio C_R, are observed and discussed in e.g. [28] [29][85][94][97]. Although Zatloukal and Musil [29] introduced a new “FreeFlow” orifice die design to eliminate unwanted filling die exit by the liquids, there is one area, which has not been systematically studied yet: the effect of the contraction ratio C_R or strain on the entrance pressure drop for highly viscoelastic fluids such as polymer melts.

Importance of the strain is pointed out by Rajagopalan [30], who discusses whether the melt is given enough time (or Hencky strain) to reach a steady state during contraction flow. Not only his numerical simulation shows that whether the melt reaches a steady state during the contraction flow is determined not only by the nature of the polymer material but also by the size of the Hencky strain, which is characterized by the contraction ratio C_R. The influence of C_R on the size of the Δp_{entr} was also experimentally observed by Kim and Dealy [28] for various materials, but to a limited extent and they do not discuss this issue in more depth.

Thus, this thesis primarily focuses on the systematic experimental investigation of the effect of the change in contraction ratio on the magnitude of entrance pressure drop (i.e. on the role of strain during contraction flow) together with other topics related to uniaxial extensional viscosity determination from entrance pressure drop measurements.

6 AIMS OF THE THESIS

The main aims of this thesis are defined as follows. Perform systematic high-pressure capillary rheometer measurements a using a new multi-part capillary die with zero capillary length, allowing to control the contraction ratio C_R while maintaining a constant capillary diameter. Based on these measurements, evaluate the effect of C_R on the measured entrance pressure drop for the branched low-density polyethylene melt. Evaluate different methods to determine uniaxial extensional viscosity for linear and branched polyolefin melts from entrance pressure drop measurements and compare obtained results with independent measurements made using the Sentmanat Extensional Rheometer (SER) and Extensional Viscosity Fixture (EVF). Select different constitutive equations and evaluate their ability to describe the measured shear viscosity and the non-monotonic character of the uniaxial extensional viscosity.

7 MATERIALS

The materials used in the experimental part of this thesis were chosen with respect to the experiments performed and to best demonstrate the described and investigated issues. In more detail, two materials, one branched LDPE and the other linear iPP, whose basic parameters are listed in Table 7.

Table 7 Basic characteristics of the polymer materials used.

Parameter	Polymer material	
	LDPE PG 7008	PP-A
Manufacturer	DOW	N/A
Density ρ $\left(\mathrm{g{\cdot}cm^{-3}}\right)$	0.918	0.900
Melt temperature T_m (°C)	105	165
Melt Mass-Flow Rate MFR $\left(\mathrm{g{\cdot}10min^{-1}}\right)$	7.7 ^{A}	0.3 ^{B}
Weight average molecular weight M_w $\left(\mathrm{g \cdot mol^{-1}}\right)$	278 400	669 000
Number average molecular weight M_n $\left(\mathrm{g \cdot mol^{-1}}\right)$	15 460	159 000
Z average molecular weight M_z $\left(\mathrm{g \cdot mol^{-1}}\right)$	766 340	1 654 000
Z+1 average molecular weights M_{z+1} $\left(\mathrm{g \cdot mol^{-1}}\right)$	1 268 490	N/A
Index polydispersity (IP = M_w/M_n) (1)	18.01	4.20
Average number of branches per 1000 total carbon LCBf (1)	1.89	0
Zero shear rate (Newtonian) viscosity η_0 (Pa·s) (at temperature)	188 000 (180 °C)	8 526 ^{C} (150 °C)

^{A} The MFR (at LDPE PG 7008) values were determined at a temperature of 190 °C of melt, which was acted upon by a weight weighing 2.16 kg. ^{B} The MFR (at PP-A) values were determined at a temperature of 230 °C of melt, which was acted upon by a weight weighing 2.16 kg. ^{C} Value determined from the discontinues relaxation spectrum (Table 14).

The above mentioned parameters and other information about the LDPE PG7008 are given in the material sheet (Appendix I). The MWD data are of the "absolute" type, measured by a combination of GPC, light scattering, and infrared detectors. The MWD curve for this material is provided in Fig. 43. Material data for the PP-A including complete molecular characteristics are taken from [119] .

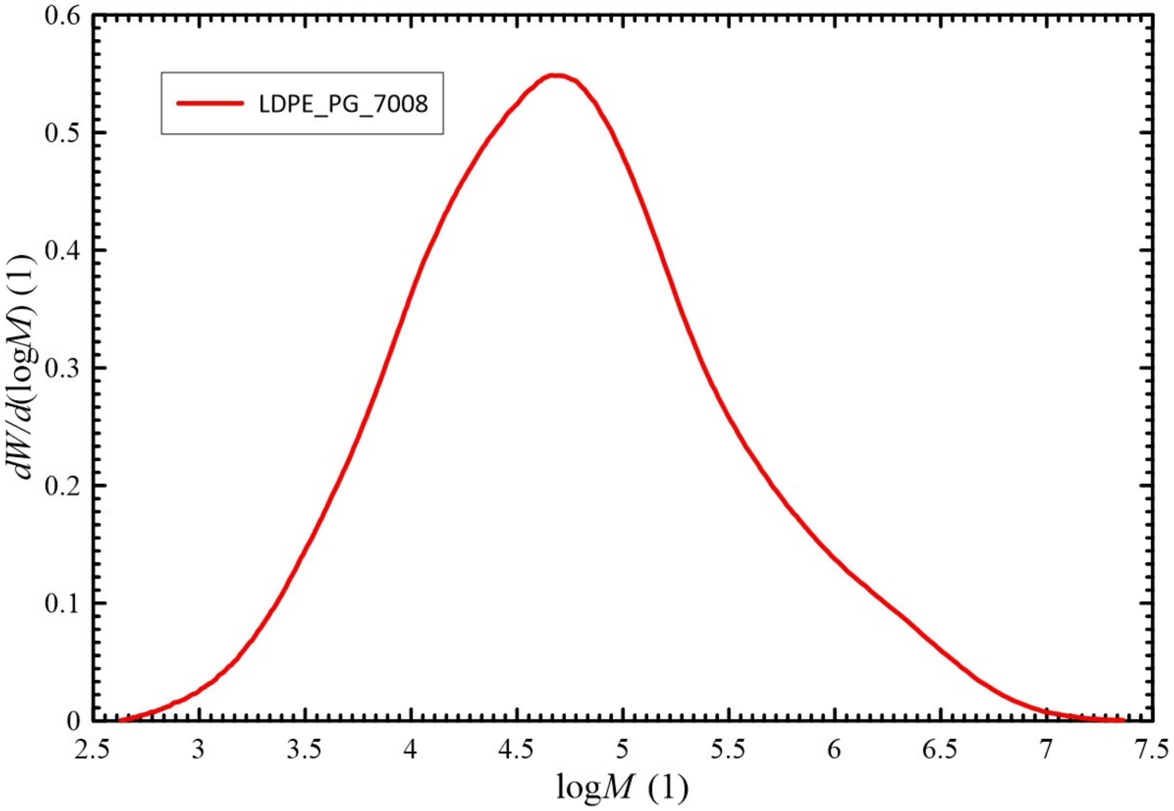

Figure 42 The molecular weight distribution curve of LDPE PG 7008 (data from DOW)

8 EQUIPMENT AND METHODS

This chapter provides a comprehensive summary of all used equipment and accessories used to fulfill this thesis's objectives. The equipment and accessories can be divided into two separate parts in which the experiments were carried out. These are the Rosand RH10 capillary rheometer and the ARES G2 rotary rheometer.

8.1 Capillary rheometer – Rosand RH10

The Rosand RH10 is a high-pressure capillary rheometer currently manufactured and distributed by the German company Netszch Gerätebau GmbH. This floor standing rheometer, characterized by its robust "H" frame construction, is widely used in academia and industry to investigate the rheological properties of polymers, coatings, foods, or ceramics at various strain rates and temperatures. It can also be used to measure *pvT* diagrams.

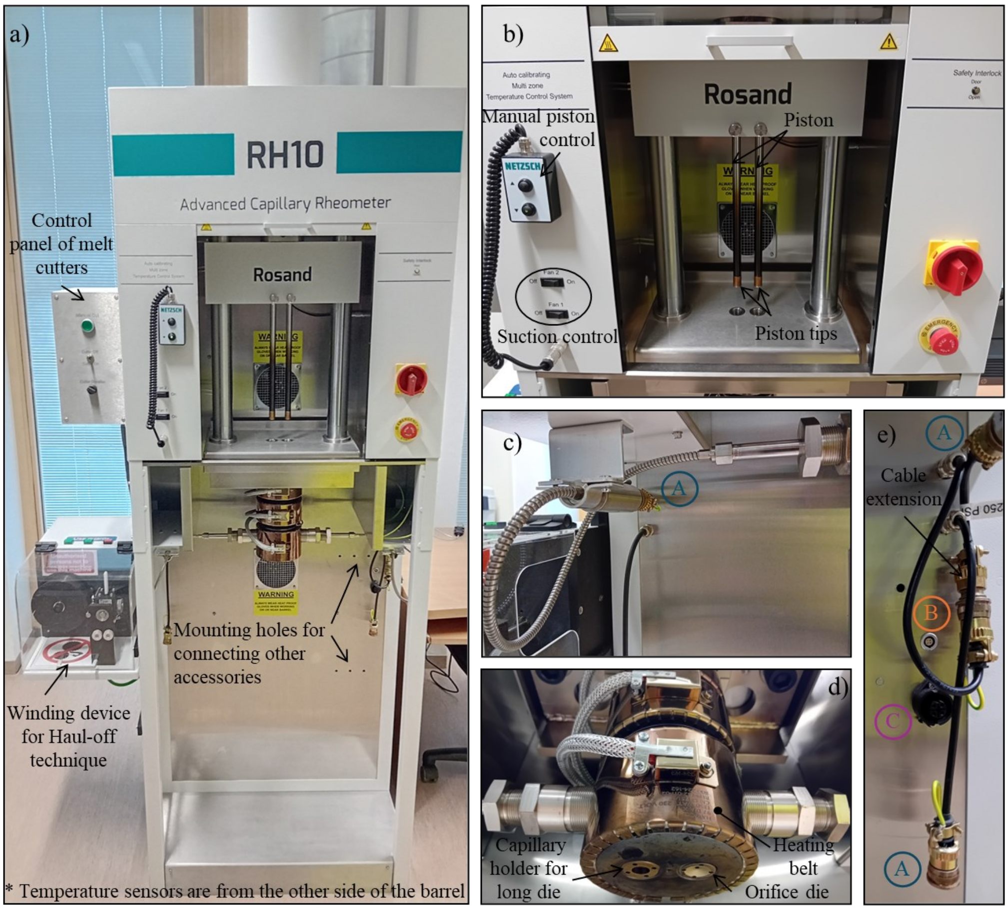

Figure 43 Rosand RH10 used in the experiment, a) general view including its accessories, b) view of the moving part, c) attachment of the pressure transducer and its connection via connector A (of which there are a total of 4 on the device), d) Bottom view of the heated barrel, e) Other connection options via connectors: B is for connecting the temperature sensor and C is for the heating belt

The Rosand RH10, on which experimental measurements were carried out (Fig. 43), consists of a working twin-bore heated barrel in which capillary dies are placed, which enables two measurements to be taken simultaneously. The motor and the control unit create the pistons' movement, which ensures their precisely regulated speed in a wide range with a maximum speed of 1200 mm·min^{-1}, and the maximum developed force can reach up to 100 kN. The working part of the device (barrel and pistons) is displayed and described in more detail in Fig. 44a. Three heating belts heat the three-part ceramic barrel. The exact temperature in each of them can be regulated separately because each part has its temperature sensor on the back side of the barrel (Fig. 43a). The standard temperature range is up to 400 °C, possibly up to 500 °C. When using a cooling barrel (oil cooling), the range is from (5 – 300) °C. To determine the pressure drop Δp of the polymer melt, pressure transducers are used, whose pressure sensors are mounted in the barrel, and the transducer itself is fixed in a holder and connected via connector A to the device according to Fig. 43c. Control of the entire device, including setting the measurement conditions, takes place in the SW Flowmaster version 8.91.

The equipment can also include several accessories, in addition to the mentioned capillary die (see Section 8.1.1) and pressure transducer (see Section 8.1.2), as well as systems for hauling off the extrudate for the Haul-off technique or cutting the melt (Fig. 43a). Furthermore, a so-called slit die can be used to measure the first normal stress difference N_1 via the exit pressure drop Δp_{exit} measurement, or the extrudate swell can be detected and quantified using a laser. For these additional systems, the rheometer is equipped with mounting holes and a connector for connecting temperature sensors (B) and pressure transducer (A) or heating belt (C), as can be seen in Fig. 43e,c. All available technical data are listed in the appendices (Appendix II). Further additional information is also provided on the manufacturer's website [120].

Since the measured pressure drop Δp in the barrel does not provide the actual shear stress on the capillary wall τ_{xy}, its value must be derived from the equation of motion of a general liquid in pressure driven flow (Fig. 8e) [16][18]. The so-called apparent shear stress at the capillary wall $\tau_{xy,APP}$ is introduced and defined as follows:

$$\tau_{xy,APP} = \frac{\Delta p}{2L}\frac{D}{2} = \frac{\Delta p}{2L}R\,. \tag{82}$$

where the symbols correspond to the illustration (Fig. 19), and R is the radius of the capillary. The apparent value of the shear strain rate at the capillary die is given as follows:

$$\dot{\gamma}_{APP} = \frac{4Q}{\pi R^3}, \tag{83}$$

The term “Apparent” is used here because the Eq. 84 represents the shear strain rate at the capillary wall only for Newtonian fluids in pressure-driven flow assuming the absence of wall slip [46]. Here Q is the volume flow rate defined based on illustration provided in Fig. 36 as follows:

$$Q = A_b v = \frac{\pi D_b^2}{4} v. \tag{84}$$

It is important to note that when the flow of polymer melt is fully developed (Fig. 36), the shear stress and shear strain rate are independent of the flow distance considering that the process is isothermal and the effect of pressure on viscosity can be neglected [46].

There are methodologies for obtaining real data from given apparent values (Eq. 82, 83) using corrections. The two concepts that have already been discussed (the Bagley plot in Section 3.1 or using an orifice die in Section 3.2) are used here to calculate the corrected shear stress. The corrected shear stress $\tau_{xy,corr}$ is obtained using Eq. 82, in which the total pressure drop is replaced by the capillary pressure drop (using Eq. 49 in Chapter 3), leading to the following expression:

$$\tau_{xy,corr} = \frac{\Delta p - \Delta p_{end}}{2L} R = \frac{\Delta p_{cap}}{2L} R. \tag{85}$$

Here the measured total pressure drop Δp is obtained from the long die (considering that the Δp_{end} is determined using the orifice die). To obtain the real value of the shear rate at the capillary wall from $\dot{\gamma}_{APP}$ (Eq. 83), the Rabinowitsch correction is most often used, which uses the non-Newtonian flow index n defined as

$$n = \frac{d\log(\tau_{xy,corr})}{d\log(\dot{\gamma}_{APP})}, \tag{86}$$

where n is the slope of in the corrected shear stress versus the apparent shear rate plot in a log-log scale [18]. The corrected shear rate is then given by

$$\dot{\gamma}_{corr} = \dot{\gamma}_{APP}\left(\frac{(3n+1)}{4n}\right). \tag{87}$$

As mentioned above, capillary rheometry uses many approximation methods to determine the elongational rheology of materials. In this work, the following three different methodologies were used to calculate the uniaxial extensional viscosity from the entrance pressure drop, Δp_{entr}, measurements: the standard Cogswell analysis, its modification, and Gibson analysis.

The standard Cogswell analysis [24] is based, in contrast to its predecessors, on the consideration of inhomogeneous extensional flow, and therefore, when deriving the entrance pressure drop Δp_{entr}, he considered the sum of shear and extensional losses [121]. The analysis is based on several assumptions discussed in [24] and the resulting equations are provided in Table 8.

Table 8 A summary table of the Cogswell equations, where the shear variables are given by Eqs. 83, 86, 87 (adapted from [24][121])

Extensional quantities	Equation for uniaxial extensional flow
Extensional strain rate:	$\dot{\varepsilon} = \frac{4}{3(n+1)} \frac{\tau_{xy,corr}\dot{\gamma}_{APP}}{\Delta P_{entr}}$
Extensional stress:	$\sigma_E = \frac{3(n+1)}{8} \Delta P_{entr}$
Extensional viscosity:	$\eta_E = \frac{\sigma_E}{\dot{\varepsilon}} = \frac{9(n+1)^2}{32} \frac{\Delta P_{entr}^2}{\tau_{xy,corr}\dot{\gamma}_{APP}}$

Padmanabhan modified Cogswell's analysis [121]. He proceeded in the same way as Cogswell in deriving the modified relations, but with the difference that he relaxed the original assumption of constant extensional viscosity during contraction flow and considered the power-law dependence of extensional viscosity on the extensional strain rate, according to the following equation

$$\eta_E = s\dot{\varepsilon}^{k-1}, \tag{88}$$

where s and k are the power-law material constants of extensional flow [26][30][121]. The parameter k can be determined using a direct equation as follows:

$$k = \frac{d\log(\Delta p_{entr})}{d\log(\dot{\gamma}_{APP})}, \tag{89}$$

where k can be determined from the slope of a log-log plot of entrance pressure drop Δp_{entr} versus the apparent shear strain rate $\dot{\gamma}_{APP}$. The resulting equations for calculating extensional quantities derived by Padmanabhan are presented in Table 9. It can be observed that when the parameter $k = 1$, the relations change to the original Cogswell equations (Table 9).

Table 9 A summary table of the Padmanabhan-modified Cogswell equations, where the shear variables are given by Eqs. 84, 86, 87 (adapted from [121])

Extensional quantities	Equation for uniaxial extensional flow
Extensional strain rate:	$\dot{\varepsilon}_{mC} = \dfrac{(1+k)^2}{3k^2(n+1)} \dfrac{\tau_{xy,corr}\dot{\gamma}_{APP}}{\Delta p_{entr}}$
Extensional stress:	$\sigma_{E,mC} = \dfrac{3k(n+1)}{2(1+k)^2}\Delta p_{entr}$
Extensional viscosity:	$\eta_{E,mC} = \dfrac{\sigma_{E,mC}}{\dot{\varepsilon}_{mC}} = \dfrac{9k^3(n+1)^2}{2(1+k)^4} \dfrac{\Delta p_{entr}^2}{\tau_{xy,corr}\dot{\gamma}_{APP}}$

Gibson's analysis is based on sink flow kinematics [71] and thus does not consider the presence of corner vortices as in the case of the Cogswell or Binding analysis. Gibson considers the flow by forced convergence, i.e., that the melt at all entry angles cannot freely choose how to form the convergent region [121].

Spherical coordinates with the origin on the axis line in the entry area were considered during the derivation. Hereafter, Gibson assumes the power-law dependence of extensional viscosity (according to the relation Eq. 88) and shear viscosity as follows:

$$\eta = m_p \dot{\gamma}^{n-1}, \tag{90}$$

where m_p and n are power-law shear flow material constants [26][30]. Gibson also assumed that extensional flow dominantly influences the entrance pressure drop Δp_{entr}. For this reason, it separates the shear part from the measured Δp_{entr} as follows

$$\Delta p_{entr,E} = \Delta p_{entr} - \frac{2(\sin\alpha)^{3n}\tau_{xy,corr}}{3n\pi^{3n+1}}\left[1-\left(\frac{R}{R_b}\right)^{3n}\right], \tag{91}$$

where $\Delta p_{\mathrm{entr,E}}$ is the entrance pressure drop due to elongational flow only. A summary of all the assumptions on which Gibson derived the equations listed in Table 10, including their derivation, can be found, e.g., in [43][121]. It is important to note that the power-law parameter k' is not defined according to (Eq. 89) but as follows

$$k' = \frac{d\log\left(\Delta p_{entr,E}\right)}{d\log\left(\dot{\gamma}_{APP}\right)}, \tag{92}$$

where k' can be determined from the slope of a log-log plot $\Delta p_{\mathrm{entr,E}}$ versus $\dot{\gamma}_{APP}$.

Table 10 A summary table of equations is derived from Gibson's analysis, where the shear variables are given by Eqs. 84, 86, 87 (adapted from [26][30])

Extensional quantities	Equation for uniaxial extensional flow
Extensional strain rate:	$\dot{\varepsilon}_G = \frac{\dot{\gamma}_{APP}}{4}\sin(\alpha)\left[1+\cos(\alpha)\right]$
Extensional stress:	$\sigma_{E,G} = \dfrac{\Delta p_{entr,E}}{\frac{2}{3k'}\left[1-\left(\frac{R}{R_b}\right)^{3k}\right]+\frac{I(k',\alpha)}{\left[\sin\alpha\left(1+\cos\alpha\right)\right]^n}}$ Where*: $I(k',\alpha)=\int_0^{\frac{\alpha}{2}}\left(1+\cos\beta_G\right)^{k'-1}\left(\sin\beta_G\right)^{k'+1}d\beta_G$
Extensional viscosity:	$\eta_{E,G} = \frac{\sigma_G}{\dot{\varepsilon}_G}$

*Where β_G is subtending angle and R_b is radius of barrel.

8.1.1 Capillary die

When determining the rheological behavior of the given polymer materials, standard capillary dies (long and orifice dies) were used, all listed together with their dimensions in Table 12. The technical drawings of all these used capillary dies can be found in the appendices (Appendix III). A long capillary die and an orifice die were always used during the measurements (Figs. 43, 44). It can be seen (Fig. 44) that the long die is inserted into the modified holder. Further, it is essential to note that the orifice dies used are those designed by Zatloukal and Musil [29][92] and have already been discussed in section 3.2.1.

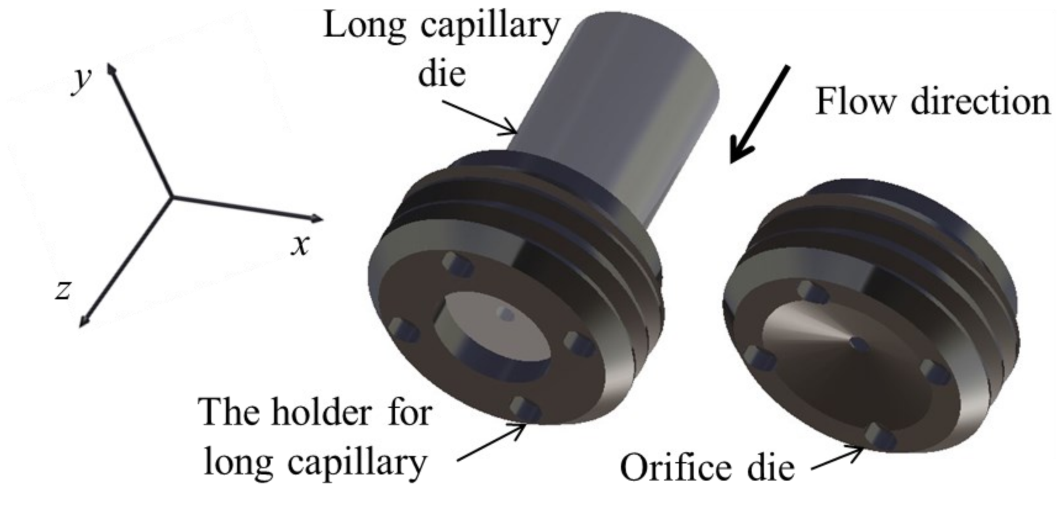

Figure 44 Standard capillary dies with a diameter of $D = 2$ mm

Table 11 Used standard capillary dies (long and orifice dies)

Type of capillary die	Diameter D (mm)	Length of capillary L (mm)	Entry contraction angle α (°)	*Hecky strain ε_H (1)
Orifice die	2	0,24	180	4,0
Long die		32		
Orifice die	3	0,36	180	3,2
Long die		42		

* The standard barrel diameter D_b = 15 mm is considered in the calculations.

Furthermore, special capillary dies were used to check and investigate the outlined problems. This is a relatively new and non-standard concept of multi-part capillary dies (internally referred to as "Strain dies"), which are protected and specified in more detail in the Patent [122]. The main parts of the Strain die (Fig. 45) creates a flow channel. It is about a transition part Fig. 45a (which is connected directly to the capillary rheometer), a wide barrel Fig. 45b (the so-called transformation chamber), and a narrow capillary Fig. 45c (orifice die), which enables considerable flexibility when measuring different materials and under various conditions. The assembly drawing can be found in the Appendix IV.

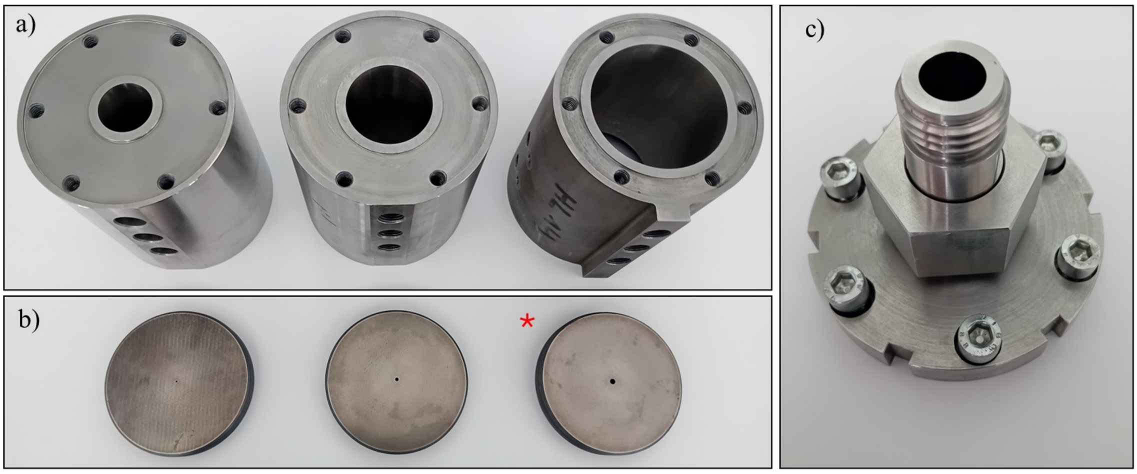

Figure 45 The main parts of the used Strain die with all build options. a) Strain die barrels with diameters of 25 mm, 40 mm, and 65 mm, b) Orifice die with diameters of 1 mm, 2 mm, and 3 mm, c) Unchanging transition part. (* Used orifice die in the experiment)

The Strain die barrel (diameters D_{bds}, Table 12) significantly increases the size of the flow channel, which increases maximum attainable Hencky strain ε_H, residence time and character of the extensional flow of the melt before entering the orifice die. In addition, it is possible to use up to nine Strain die assembly variants (nine different maximum attainable Hencky strains, see Table 12).

Table 12 Basic characteristics of the used Strain dies

*Diameter of the orifice die D (mm)	Diameter of the Strain die barrel D_{bsd} (mm)	Hecky strain ε_H (1)	Length of Strain die barrel L_{sd} (mm)
3	25	4.2	87
	40	5.2	
	65	6.2	

* All orifice dies have an entry angle of α = 180° and their lengths are identical to those provided in Table 11.

In Fig. 46, one can observe a specific model of the assembly of the discussed Strain die with a description of all parts. During the measurement, a heating belt is tightly connected around the outer shell of the transformation barrel. The temperature sensor can be placed in two holes with a diameter of 5 mm and three threaded holes (W1/2-20 UNF) located perpendicular to the flow direction and used to connect pressure sensors.

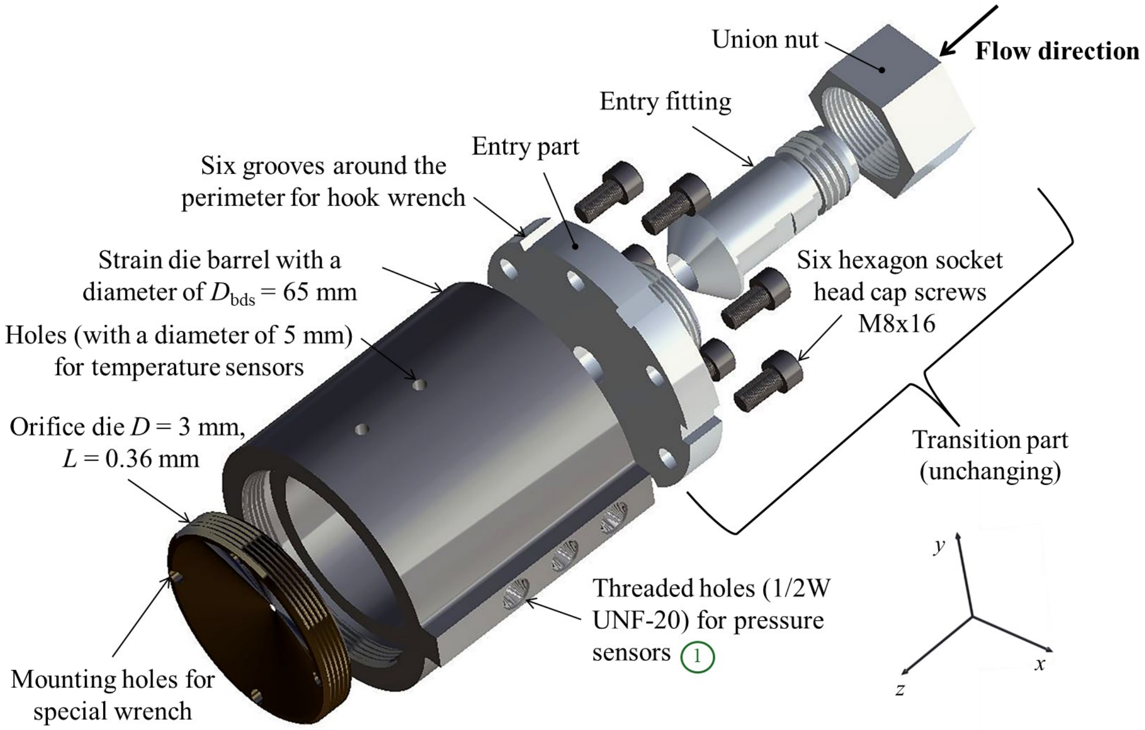

Figure 46 Exploded model view of the Strain die

8.1.2 Pressure transducers

Pressure transducers are almost the most essential element of a capillary rheometer. For accurate recording of the pressure drop during the processing of polymer melts and various experiments, systems with a separate sensor and transducer (Fig. 47) must be used, as the pressure transducer cannot usually be exposed to temperatures higher than 80 °C (sensor usually up to 400 °C). The sensing principle is based on the detection of pressure through a sensitive membrane located at the tip of the pressure sensor (Fig. 47b), which, due to the split system, transmits the detected mechanical stress through the transmission fluid (located in a closed capillary equipped with flexible armor). The transmission fluid stresses the second membrane in the transducer, which converts the detected pressure using the strain gauge into a small millivolt (mV) signal, from which the rheometer control system already operates.

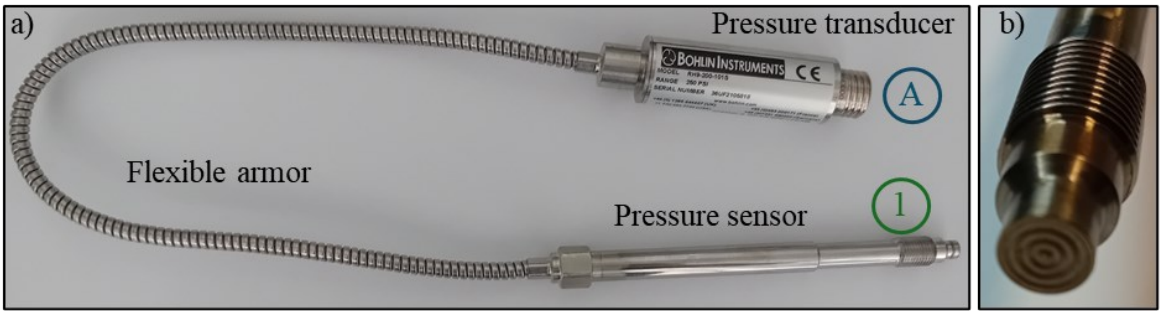

Figure 47 A pressure transducer system of one of those used in the measurement, a) Complete view, where 1 indicates the point of connection to the barrel (on the machine, transformation barrel or calibration device), and a shows the connection of the connector with the rheometer, b) A view of the sensor tip, equipped with a durable and sensitive metal membrane

The most frequently used transmission fluid was mercury, which has excellent properties, but according to legislation, it can only be used for academic purposes in EU countries. Therefore, manufacturers have developed many alternatives to replace mercury, including e.g., Oil, NaK (sodium-potassium), or Galistan (a liquid metal mixture of indium, gallium, and tin). Still, they all have their limitations and are thus an insufficient substitute [123].

All used pressure transducers are listed together with their identification parameters and range in Table 13. According to the SW capillary rheometer, the resolution of all transducers is 10^{-6} MPa, and their maximum error is associated with a specific model series (Appendix V).

Table 13 Used pressure transducers with their identification description

Internal designation	*Model	Serial number	Range (PSI)	Range (MPa)
250PSI MZ1	M21-8-M-P25D-1-4-D-A58 [C]	112812-160812	0-250	0-1.73
250PSI MZ2	M21-8-M-P25D-1-4-D-XMA58 2130X [C]	36UC1802745		
250PSI MZ3	M31-8-H-P03M-1-4-D-A58 [C]	36UF2105818		
250PSI MZ4	M21-8-M-P25D-1-4-D-A58 [C]	032513-163890		
250PSI_389[D]	V131-RE-CC/GK1/QJ [A]	127255		
500PSI MZ1	PT422A-5C-6/18 V [B]	09-20-99816692	0-500	0-3.45
500PSI MZ2	K31-8-M-P05C-1-4-D-S 2130X000X00 [C]	D18040832		
500PSI MZ3	M31-8-M-P05C-1-4-D-A58 [C]	092812-159210		
500PSI MZ4[D]	K31-8-M-P05C-1-D-S 2130X000X00 [C]	D17440727		
1500PSI 389[D]	K31-8-H-P15C-1-4-D-S 2130X000X00 [C]	22065977	0-1 500	0-10.34

*The manufacturers of the pressure transducer are [A] PG:50, [B] Dynisco and [C] Gefran. [D] Calibrated by the transducer supplier, which was Netszch Gerätebau GmbH. Calibration curves are Appendix VI (dependencies are shown in red).

8.1.3 Calibration pressure transducer

Since the extensional viscosity is very sensitive to small changes in the entrance pressure drop, as much effort as possible should be made to accurately identify it [30]. For the most accurate detection, especially at low strain rates, pressure transducers must be thoroughly calibrated.

During their production, emphasis is placed on the dependence between the determined compressive stress (polymer melt) and the millivolt voltage, which has a linear character. However, this only applies to higher values from the sensor's possible range, where so-called single-point calibration is sufficient, used for 500 PSI MZ1-4 sensors (Table 13 and calibration results are in the Appendix VI). During this calibration, the considered point (usually the higher value of the range) will linearly connect to zero pressure, and the slope of this linear line is called "gain". However, the problem of single-point calibration occurs in the lower part of the sensor range when the mentioned dependence becomes strongly non-linear and can significantly affect the entire measurement. Multi-point calibration was performed to increase the sensitivity of the pressure transducers 250 PSI MZ1-4 (Table 13). The CCS 20 type calibration device from the AM Messgeräte GMBH company was used for calibration, shown in the disconnected state in Fig. 48 (also for single-point calibration). It is a manual air device that calibrates a pressure transducer up to 2000 kPa (for a larger range, an oil device must be used). The calibrated pressure transducer is connected to the calibration device in area 1 (Fig. 48) and the capillary rheometer using connector A.

Figure 48 Used calibration device in an unconnected state. a) Indicator with a range of (0-2000) kPa, b) Indicator with a range of (0 – 20) kPa, c) View of the main part, i.e., the hand pump, which contains the entry for pressure sensor 1, d) Air hose connecting the indicator (input/output 2) and hand pump (input/output 3)

Calibration points were selected on a logarithmic scale almost throughout the sensor range. The percentage error indicates the degree of non-linearity or deviation from the linear correction (single point), which can be obtained from the following relationship:

$$Errors = \frac{100(p_{ref} - p_{trans})}{p_{trans}}, \tag{93}$$

where p_{ref} is the value displayed on the calibration device on one of the two indicators used (Fig. 48a,b), and p_{trans} is the value identified by the rheometer and shown in its SW, into which the calibration points are entered.

The individual calibration points were obtained according to the following procedure. First, it was necessary to ensure that p_{ref} and p_{trans} started from zero by regenerating the corresponding pressure value (if the pressure did not stabilize at zero, it was required to use the "Gain correction" command in SW Flowmaster). After that, it was possible to generate the desired pressure value (Fig. 48c) with the help of pressing levers, which can be more precisely set/fine-tuned by the "Pressure regulator" (Fig. 48c). When calibrating pressure values above 0.016 MPa, an indicator with a range of (0 – 2000) kPa was used. After stabilization, the p_{trans} value was recorded, and the pressure was released (Fig. 48c). On the contrary, for lower pressures in the range (0.001 – 0.016) MPa, the test mode was used as for standard measurement but empty (without material and at a constant speed of the pistons v_x = 10 mm·min^{-1}) due to fluctuations in the measured value. The resulting value was obtained as an average of 100 sampling numbers, and an indicator with a range was used to calibrate these values (0 – 20) kPa. If, after releasing the pressure in both cases, a zero value was not registered (in SW), the value was not written and subsequently repeated in the same way. In the case of a low range, the values were repeated at least three times to reduce the risk of measurement errors as much as possible. The created calibration curves, which were uploaded to SW, for individual sensors, can be found in the Appendix VI.

It is essential to mention that the calibration occurred at the laboratory temperature (23 °C) and not at operating temperature. This mistake is not as serious as it might seem at first glance. The reason is that the prime transmission fluid condition is its low thermal expansion which mercury completely fulfills, and its alternatives are also trying to achieve the same [123].

8.2 Rotational rheometer – Ares G2

Ares-G2 is the designation of a quality rotational rheometer developed and distributed by TA Instruments. It gained popularity mainly because of its accuracy and user-friendliness. It makes it possible to determine rheological parameters (modulus, viscosities, etc.) in a wide range of conditions for various materials (food, coatings, or polymers). Its most significant competitive advantage is the separate system of the motor (controlled quantities, frequency ω) and transducer (measured quantities, torque Tq). This technology, abbreviated as SMT, prevents results from being influenced by inertial contributions.

In addition, the Ares-G2 is versatile and capable of performing advanced rheological techniques, such as Long Amplitude Oscillation LAOS, analysis of rheological properties based on the Fourier transform, etc. Or even Dynamic Mechanical Analysis (DMA).

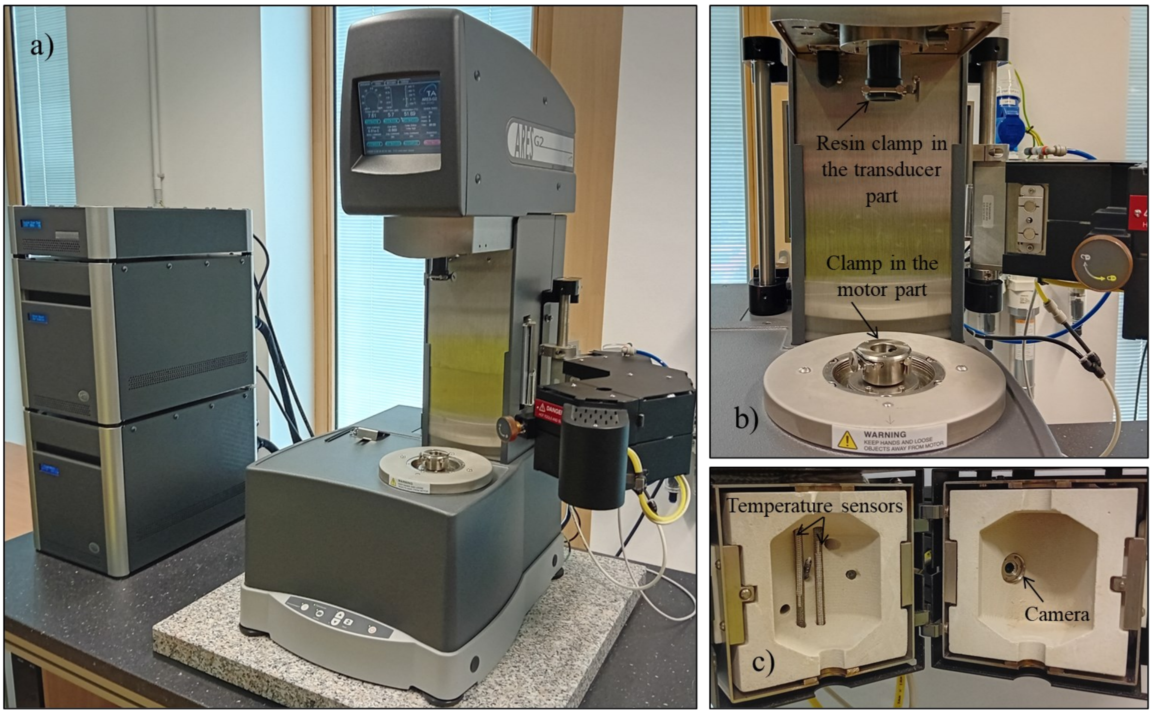

Figure 49 Ares G2 rotational rheometer, a) General view of the device with the computing station in the left part (black boxes), b) View of the clamps of the motor and transducer parts, c) Inside the Forced Convection Oven (FCO) with ceramic insulation and other components

The Ares – G2 rotational rheometer used is shown in Fig. 49. It consists of a rigid frame, in the lower part of which there is a motor part with air bearings and a powerful motor. The transducer in the upper area part records the torque and normal stress using sensors with different ranges and accuracy. Any calibration of these sensors is carried out using calibration tools (calibration fixture, pully, calibration line, and weight) and instructions, which are part of the control software of the TRIOS. The device also includes a Forced Convection Oven (FCO), which can work from -160 °C to 600 °C, and up to five thermocouples can control the set temperature. The FCO also includes a camera and a LED lamp, which together enable the creation of a high-quality recording of measurements in real-time. An inert environment can also be created in FCO. It is important to emphasize that compressed air of the required purity and pressure range of (0.5 – 0.6) MPa must be continuously supplied to the device throughout its operation. Otherwise, severe damage could occur to the motor and the transducer. Other parameters related to the equipment used can be found in the technical sheet (Appendix VII) or on the manufacturer's website [123].

In addition to the already mentioned FCO, some other accessories can be connected to the device. The geometries and measurement methods used will be presented further.

8.2.1 Parallel Plate Geometry

Measurement using parallel plate geometries can describe polymer melts' Linear Viscoelastic (LVE) behavior (Pipkin diagram Fig. 4). Small Amplitude Oscillation Shear tests (SAOS) are the most common way to determine these characteristics. In these experiments, a polymer sample of the required dimensions is inserted into the gap between the plates (Fig. 50). During measurement, the bottom plate oscillates with a certain frequency and amplitude (maximum applied deformation or stress) [18][38][123].

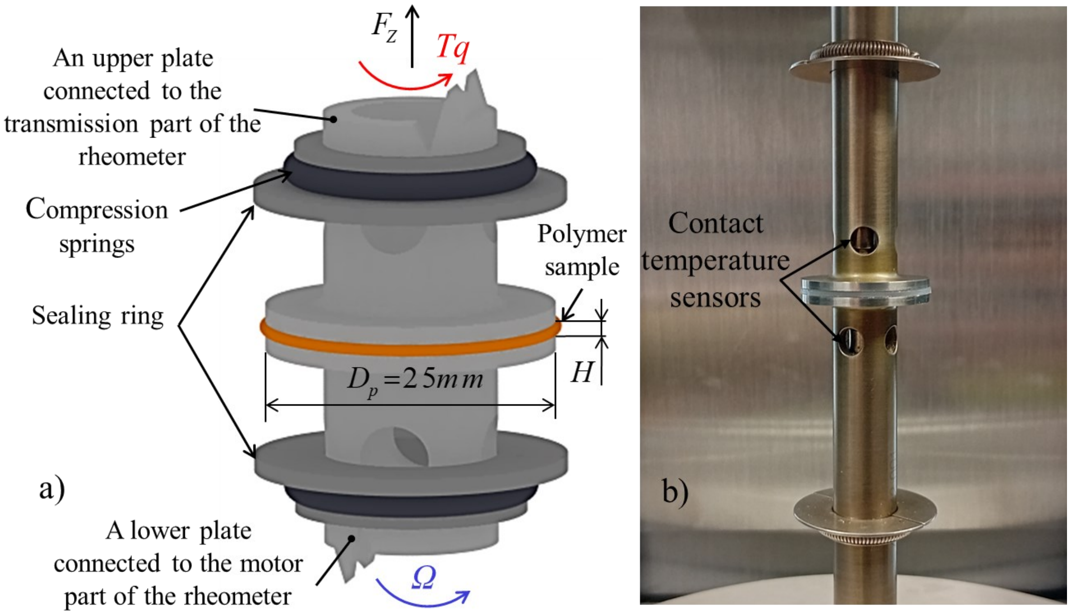

Figure 50 Parallel plate geometries, a) Schematic illustration with a description of individual parts, where Tq and F_z are the detected torque and normal force, respectively, and Ω is rotational speed (frequency ω and amplitude γ_0 are considered in oscillation modes), b) View of the geometry before the start of the test

The polymer samples were prepared by pressing from the granulate (the size of the weight was 15.6 g) into plates with dimensions (100 x 100 x 1) mm. The granulate was poured into a prepared preparation with two PET foils and then put into a heated (150 °C) manual spindle press for 5 minutes. After that, the entire preparation was moved to a cold hydraulic press and was freely cooled for 5 minutes to a temperature of around 30 °C. Circular samples with a diameter of 25 mm were cut out of the produced plates using a table hydraulic press.

8.2.2 Sentmanat Extensional Rheometer (SER)

The Sentmanat Extensional Rheometer (SER) is a universal test platform fundamentally based on Counter-Rotating Drums (CRD) methods, as discussed in Section 2.5.1. It is a precise and very often used method that provides information on the course of the transient extensional viscosity of polymer melts as well as elastomers. Its compatibility (according to type) with commercially available rotary rheometers is a significant advantage. A more thorough description of this device and other information can be found on the website of the manufacturer Xpansion Instruments [124] or, for example, in the articles [53][60][80].

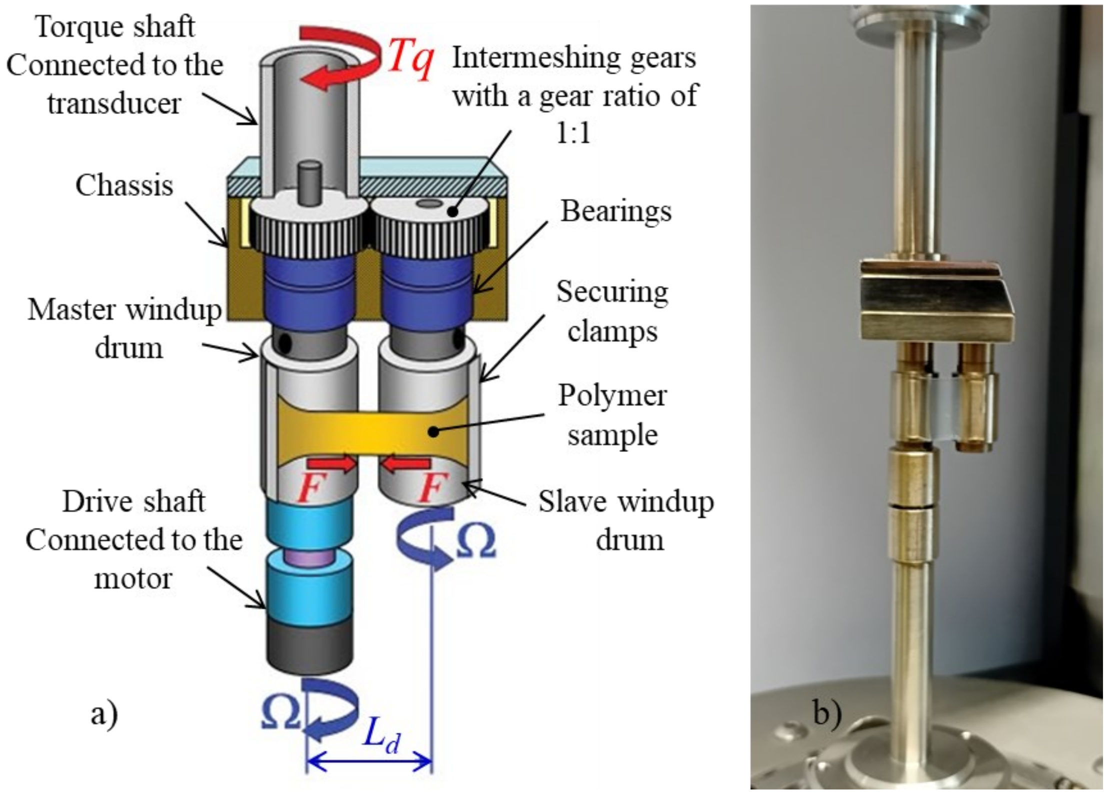

Figure 51 Universal testing platform SER, a) Schematic illustration with a description of individual parts, where Tq is the detected torque, Ω is the constant speed of rotation of the drums, and L_d is the distance between them [124], b) A view of the device before the start of the experiment test

In this work, the third generation of this device, SER3-A (Fig. 51), was used, which, among other things, tries to minimize the unwanted effect of gear transmission and bearings. This type (SER3-A) is intended for the ARES-G2 rheometer described above. The device consists of two parallel rotating drums (master and slave) stored in bearings whose axes have a constant distance L_d from each other. The revolutions from the master drum (connected via the drive shaft to the motor) are transmitted to the slave drum using a transmission gear. At the beginning of the experiment, a polymer sample with defined dimensions is placed on heated drums and can be secured by clamps (which were not used during the measurement). During the measurement, the rotational movement of the drums is converted to a linear one, which stretches the sample.

The disadvantages of SER are mainly in the small range of extensional rate (Table 1), limited Hencky strain, and the sagging of the sample before it is stretched [60][77], which can be done with some types of fixtures (SER3-P) by immersing it in silicone oil. On the other hand, the most significant advantages are quick and easy testing and the small weight of the test sample (Table 1).

The test specimens were cut from plates with dimensions of (100 x 100 x 0.5) mm, forming similarly and under the same conditions as the plates for SAOS (Section 8.2.1). The cutting tool firmly defines the samples' width, and the length is chosen according to the experiment's needs (However, it must not be less than the distance between the drums L_d). The thickness of the sample was measured using a micrometer and entered into the SW rheometer to determine the extensional viscosity correctly.

8.2.3 Extensional Viscosity Fixture (EVF)

The Extensional Viscosity Fixture (EVF), shown in Fig. 52 forms an alternative to the previous SER concept. The device works on a similar principle, with the difference that during measurement, the master drum does rotate around its axis but also rotates around the axis of the stationary slave drum (which is connected to the transducer part of the rheometer). This essentially eliminated the problem of gearing and bearings affecting the measurement, so no calibrations are necessary [123].

However, it also has its disadvantages, for example in the impossibility of observing the stretching of the sample and thus creating a telling record of measurements that can be performed up to $\varepsilon_H = 4$ (the limit extensional rate is $\dot{\varepsilon} = 10\ \mathrm{s}^{-1}$ [57]). It is also possible to discuss whether there is significant bending deformation of the torque shaft (to which the slave drum is attached). This could introduce another slight distortion of the obtained results. Further and more detailed information can be found both at the stands of the manufacturer TA Instruments [123] or with the calculation equations in the article [57]. It is also important to note that during the measurement, as with SER, the temperature inside the FCO is only monitored, not the actual temperature of the sample.

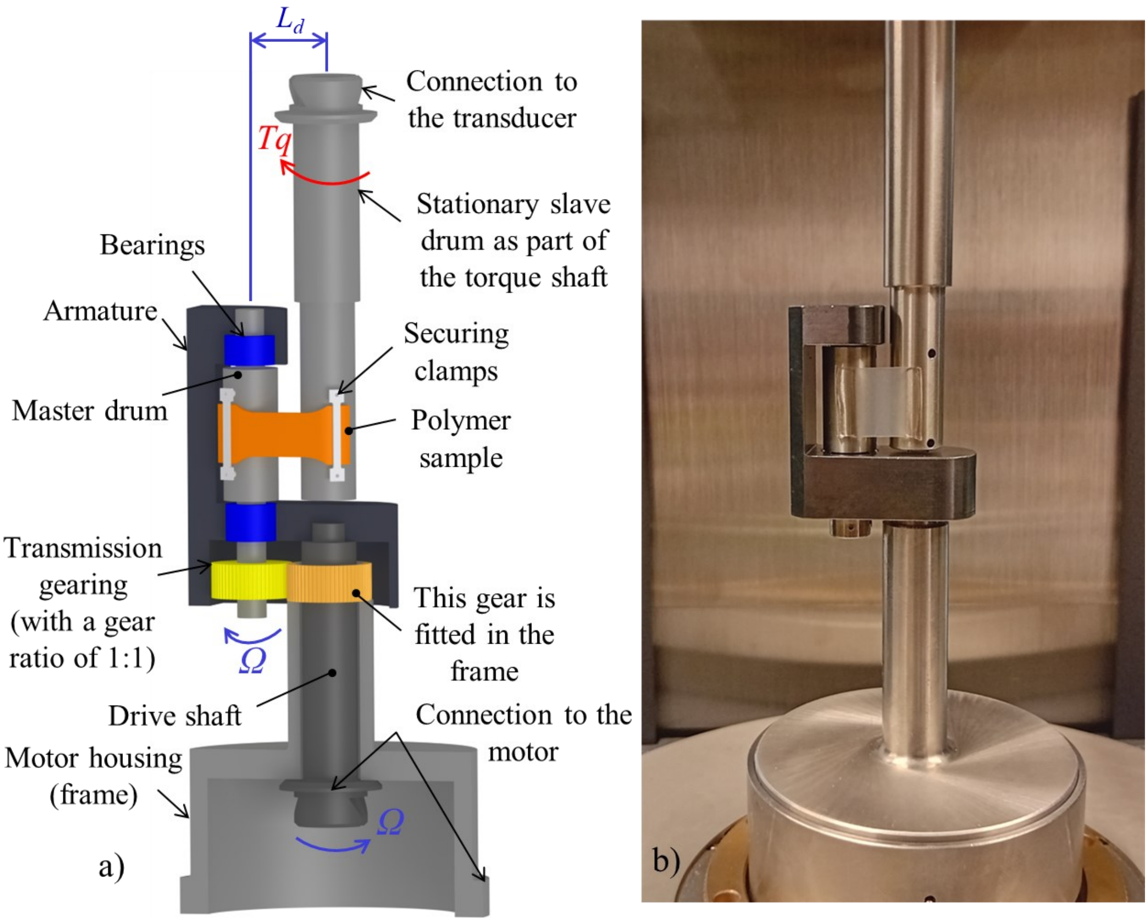

Figure 52 Extensional viscosity fixture (EVF), a) Schematic representation with description of individual parts, where Tq is the detected torque, Ω is constant speed of rotation, and L_d is the distance between the drums, b) View of the geometry before the start of the test

Polymer samples were taken from the same plates and in the same way as for the measurements on SER3-A.

9 RESULTS AND DISCUSSION

Rotational rheometry

This section discusses the results obtained from measurements on the Ares-G2 rotational rheometer, specifically when using the parallel plate geometry (Section 8.2.3).

All oscillatory measurements were carried out on LDPE PG 7008. First, a strain sweep test was performed, which was used to search for the viscoelastic region (LVE - a region where the moduli and complex viscosity are independent of the strain). The strain sweep measurement was performed at a constant frequency of ω = 10 rad·s^{-1} (the approximate mean value of the device range) and a temperature of 150 °C. The results (Fig. 56) show that the LVE region occurs roughly at strains (γ_0 = 50 %). Therefore, the standard deformation value used for polyolefins (γ_0 = 1 %, Fig. 56) could be chosen for the frequency sweep tests. These tests were carried out in the entire possible range of frequencies and at four different temperatures (130 °C, 150 °C, 170 °C, 190 °C); their results are shown in Figs. 57-60. From the shown dependencies, a Master curve (Fig. 61) was constructed using TTS (Time-Temperature Superposition principle) at a reference temperature of T = 150 °C, from which the discontinues relaxation spectrum was obtained (see Table 14).

Table 14 Parameters of the discontinues relaxation spectrum obtained from rotational rheometry. Here λ_i is relaxation time and G_i is relaxation modulus

i	λ_i (s)	G_i (Pa)
1	0.000077	453945.0000
2	0.001263	71391.8000
3	0.005465	36893.6000
4	0.019583	15801.5000
5	0.056531	8746.5900
6	0.157078	4965.1600
7	0.432648	2538.5300
8	1.162300	1297.4100
9	3.664230	597.7880
10	13.463600	134.3550
11	62.156400	0.1428
12	340.471000	0.0052

*Where i is the number of spectrum modes. Zero shear rate viscosity η_0 is obtained as the sum of multiples of λ_i and G_i.

The master curve was fitted by the Maxwell model (based on relations provided in [38]). Maxwell model predictions for oscillatory measurements at different temperatures were made using the temperature shift factor (Table 15) and discontinuous relaxation spectrum. Based on the temperature shift factor, an Arrhenius plot (Fig. 62) was compiled and the value of the activation energy E_a for the material used was determined.

Table 15 Temperature shift factor a_T obtained from Time-Temperature superposition principle (TTS)

T (°C)	a_T (1)
130	2.075
150	1.000
170	0.530
190	0.294

From the above results, it can be concluded that the Maxwell model utilizing the discontinues relaxation spectrum has high ability to describe all experimental data performed under shear oscillation flow at different temperatures.

Determination of uniaxial extensional viscosity using SER and EVF

Transient uniaxial extensional viscosities (i.e. time dependent viscosities) for LDPE material PG 7008 at 150 °C for eight different extensional strain rates $\dot{\varepsilon}$ were determined using devices presented in Section 8.2.2 (SER) and 8.2.3 (EVF). The measured experimental data are provided in Figs. 63, 64. The steady-state uniaxial extensional viscosity data was subsequently determined from these data at Hencky strains ε_{H} of 3.2 (for comparison with capillary rheometry) and 4 (which is essentially a limit value).

The obtained experimental data allow for comparing both devices working on a similar principle for specific materials and conditions. It is noticeable that EVF, compared to SER, provides lower quality results at low $\dot{\varepsilon}$ (Fig. 64). In contrast, the EVF shows a smoother measurement record since the SER is loaded by the friction of its mechanism. On most of the transient curves summarized in Figs. 63, 64, it is possible to observe (better with EVF) a peak, which indicates the wrapping of the material on itself when Hencky strain is higher than about 4.

Description of standard setting of capillary rheometer

Rheological measurements were performed on a capillary rheometer with a standard setting, and a standard capillary dies at different temperatures for two polymer materials (PP-A, LDPE PG 7008).

Both barrels of the rheometer were filled with polymer samples in the form of granules, in such a way as to ensure the greatest possible homogeneity of the melt and to avoid the presence of air bubbles. For these reasons, the so-called pre-test was also included, consisting of two compression phases combined with two preheating phases (first compression - first preheating - second compression - second preheating). The specific values of the pre-test are given in Table 16, 17. It is also necessary to mention the pressure equilibrium conditions set in the SW, which were tested and for all stated measurement results at the standard setting, were as follows: Error = 0.5 %, Window = 16, Average = 16, Maximum Samples numbers = 400.

Comparison of uniaxial extensional viscosity data determined from entrance pressure drop measurement (using standard setting) and from Münstedt Tensile Rheometer for the linear polymer PP-A

In this section, the extensional viscosity data for linear PP determined from entrance pressure drop measurements and from Münstedt Tensile Rheometer (the device in Fig. 18b) are compared.

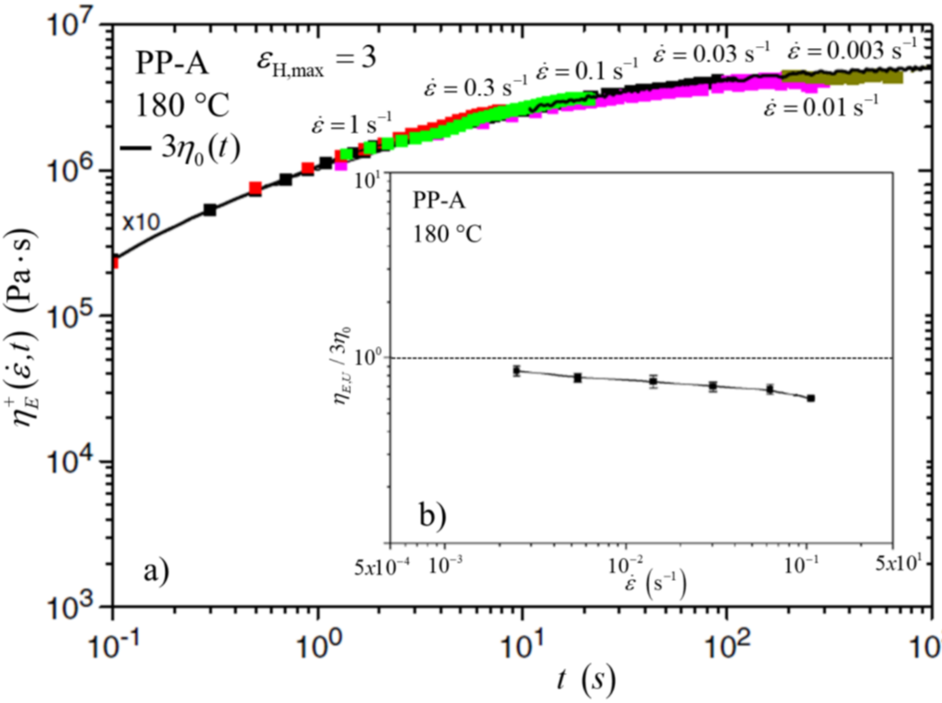

Figure 53 Extensional viscosity data for PP-A at 180 °C obtained from the Münstedt tensile Rheometer used in several publications (Taken and adapted from [75][125]). a) Transient uniaxial extensional viscosity $\eta_E^+(\dot{\varepsilon},t)$ determined in the range of extensional rate $\dot{\varepsilon}$ (0.003 – 1) s^{-1} from which values of steady-state uniaxial extensional viscosities $\eta_{E,U}$ were determined, b) Steady-state uniaxial extension viscosity $\eta_{E,U}$ at different extensional rates $\dot{\varepsilon}$

The experimental data shown in Fig. 53 were digitized using Didger 3 software. A comparative measurement was then performed at the same temperature (T = 180 °C) on a capillary rheometer with standard settings. Standard capillary dies D = 2 mm (Fig. 44 and Table 11) with Hencky strain $\varepsilon_{\mathrm{H}} = 4$ were used during the measurements. A larger ε_{H} than is stated in the comparative papers ($\varepsilon_{\mathrm{H,max}} = 3$) was chosen in order to guarantee the achievement of a high strain even at low $\dot{\gamma}_{\mathrm{APP}}$. The applied shear rate range with the used pressure transducers can be found in Table 16.

Table 16 Shear rate ranges and pressure transducers for extensional viscosity measurement from entrance pressure drop data using the standard setting of capillary rheometer (utilizing standard orifice die with D = 2 mm) for PP-A. Here $\dot{\gamma}_{APP}$ is the apparent shear rate and v_{x} is the speed piston

Used pressure transducer		$\dot{\gamma}_{APP}\ (\mathrm{s}^{-1})$	$v_x\ (\mathrm{mm\cdot min^{-1}})$
p_{left} (on long capillary die)	p_{right} (on orifice die)		
1 500PSI 389	250PSI 389	21.930	5.848
		12.000	3.200
		6.928	1.848
		4.000	1.067
		2.191	0.584
		1.200	0.320
		0.693	0.185

* Pre-test conditions: first and second compression (v_{x} = 5.84 mm·min^{-1}, p_{left} = 2 MPa, p_{right} = 0.2 MPa), first heating (3 min at 180 °C), and second heating (5 min at 180 °C).

Three different methodologies to determine uniaxial extensional viscosity from the measured entrance pressure drop were used and the obtained data were compared with extensional viscosities determined by Münstedt Tensile Rheometer (see Figs. 65-67). It can be seen that the Gibson (Fig. 67) and the modified Cogswell (Fig. 66) approaches yield extensional viscosities that are practically the same as those obtained from the Münstedt Tensile Rheometer. On the other hand, the original Cogswell's approach overestimates the experimental data from the Münstedt Tensile Rheometer as can be seen in Fig. 65. These conclusions correspond very well with previous published data on linear polymer melts discussed in Section 3.3. The observation that the modified Cogswell can describe extensional rheology for linear polymer melts is reported here for the first time.

Determination of uniaxial extensional viscosity from entrance pressure drop measurement for branched LDPE polymer using standard setting of capillary rheometer

Uniaxial extensional viscosity data for the branched LDPE PG 7008 were determined from entrance pressure drop measurements at 150 °C with standard settings and standard capillary dies $D = 3$ mm providing maximum attainable Hencky strain $\varepsilon_{\mathrm{H}} = 3.2$ according to Eq. 53 (see Table 11). The applied shear rate range and the pressure transducers used are summarized in Table 17. As can be seen, the entire measurement range was divided into three sections: low, middle, and high.

Table 17 Shear rate ranges and pressure transducers for extensional viscosity measurement from entrance pressure drop data using the standard setting of capillary rheometer (utilizing standard orifice die $D = 3$ mm) for LDPE PG 7008

Measuring ranges	Used pressure transducer		$\dot{\gamma}_{APP}\ (\mathrm{s^{-1}})$	$v_x\ (\mathrm{mm \cdot min^{-1}})$
	p_{left} (on long capillary die)	p_{right} (on orifice die)		
High [A, B]	1 500PSI 389	500PSI MZ4	495.113	445.601
			338.052	304.247
			230.031	207.028
Middle	1 500PSI 389	500PSI MZ4	147.024	132.322
			100.015	90.013
			68.107	61.297
			46.404	41.764
Low	500PSI MZ4	250PSI MZ4	31.625	28.463
			21.555	19.400
			14.678	13.210
			9.993	8.993
			6.818	6.136
			4.643	4.178
			3.162	2.846
			2.154	1.939
			1.468	1.321
			1.000	0.900

[A] Individual values of $\dot{\gamma}_{APP}$ (apparent shear rate) or v_{x} (speed piston) in the High measuring range were measured separately. Pre-test conditions: first and second compression ($v_{\mathrm{x}} = 15$ mm·min^{-1}, $p_{\mathrm{left}} = 1.4$ MPa, $p_{\mathrm{right}} = 0.15$ MPa), first heating (3 min at 150 °C), and second heating (5 min at 150 °C). [B] Some pressure equilibrium conditions were changed (namely window and average = 8) due to possible oscillations caused by flow instabilities typically occurring at high strain rates.

The uniaxial extension viscosity $\eta_{\mathrm{E,U}}$ was determined using Cogswell, modified Cogswell, and Gibson analyses and compared to $\eta_{\mathrm{E,U}}$ obtained from SER measurements at the same

Hencky strain value ε_{H} = 3.2 (see Figs. 68-70). EVF was not considered, as the values of extensional viscosity from EVF and SER for given Hencky strain was practically the same. It can be seen that the original Cogswell analysis provides the best agreement with the extensional viscosity data obtained from SER. The modified Cogswell analysis provides extensional viscosity with the same slope (at the high strain rates) as the extensional viscosity data obtained from SER but it underestimates the strain-hardening compared to the original Cogswell analysis. Gibson's analysis was found to significantly underestimates the extensional data compared to SER data, which is also in good agreement with the open literature. Figure 71 shows again the strain rate dependence of uniaxial extensional viscosity obtained from Cogswell analysis (Fig. 68), from which it is visible that up to a certain extension rate $\dot{\varepsilon}$, $\eta_{\mathrm{E,U}}$ from Cogswell analysis yields smaller extensional viscosity values than those obtained from SER at ε_{H} = 3.2 (Fig. 68). To investigate this differences, the values of ε_{H} were determined from transient SER data, which corresponds to the same $\dot{\varepsilon}$ and $\eta_{\mathrm{E,U}}$ values determined from the Cogswell analysis. These values were found to be as follows ε_{H} = 1.5, ε_{H} = 2, ε_{H} = 2.5, i.e. lower than maximum attainable strain 3.2. Considering the validity of the Cogswell methodology, it can be concluded that the true value of ε_{H} achieved during abrupt contraction flow of branched LDPE melt at low $\dot{\varepsilon}$ is smaller than maximum attainable strain predicted by Eq. 53.

In addition, the validity of the Cox-Merz rule can be observed for the tested LDPE, as the strain-rate-dependent shear viscosity agrees very well with the frequency-dependent complex viscosity, as shown in (Fig. 68-71).

Investigation of contraction ratio on the entrance pressure drop measurement for branched LDPE polymer using modified setting of capillary rheometer (Strain die)

This section presents and discusses measurements using the Strain dies (listed in Section 8.1.1). In addition to the explanation of the measurement methodology, the discussions will focus on the influence of the contraction ratio (keeping the orifice die diameter constant), which is schematically shown in Fig. 54a.

In addition to the flow channel whose parameters correspond to the values listed in Table 11, it can be seen that three pressure transducers are attached to the head itself, detecting the pressure drop (p_2, p_3, p_4) along almost the entire length of the flow channel. In addition, the pressure drop (p_1) in the barrel of the rheometer, to which the die is connected, is also measured.

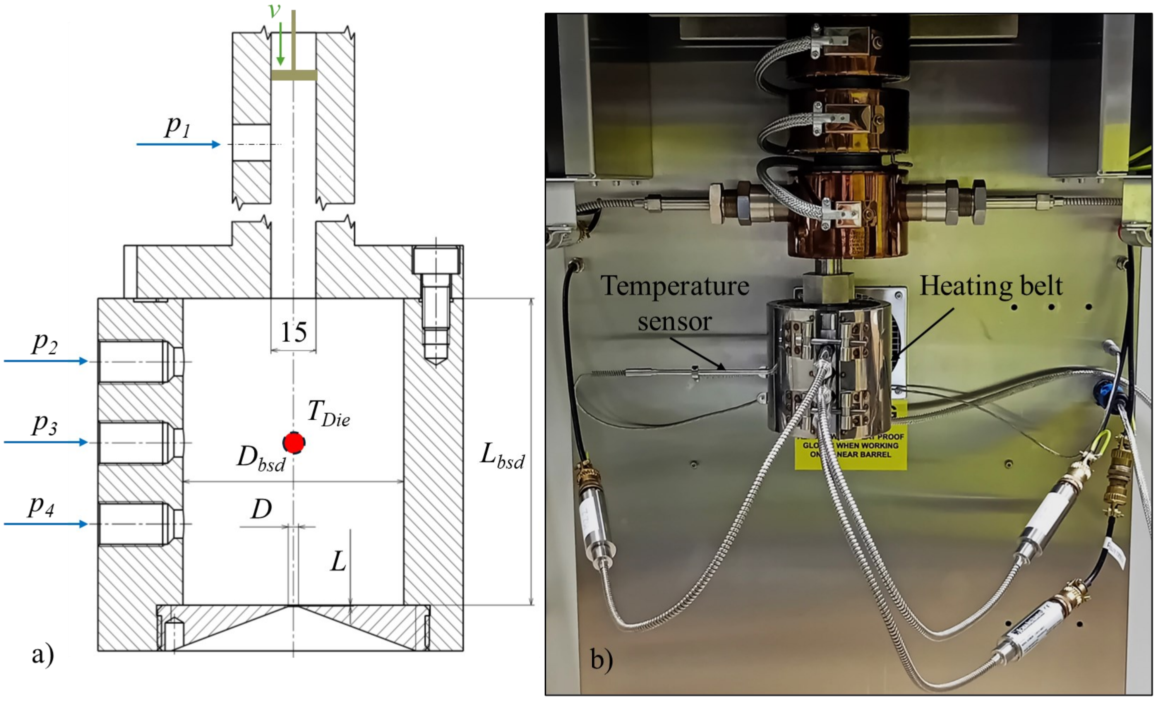

Figure 54 a) Schematic representation of the Strain die head, where the individual dimensions correspond to Table 11, 12. The illustration also shows the positions of the individual pressure (p_1, p_2, p_3, p_4) and temperature (T_{Die}) sensors. b) Realistic view of the used Strain die assembly

The heating belt ensures heating of the Strain die to the desired temperature and is regulated using a temperature sensor. The Figs. 54, 55 provide the diagram as well as real photos of the connected strain die (Fig. 54b, 55).

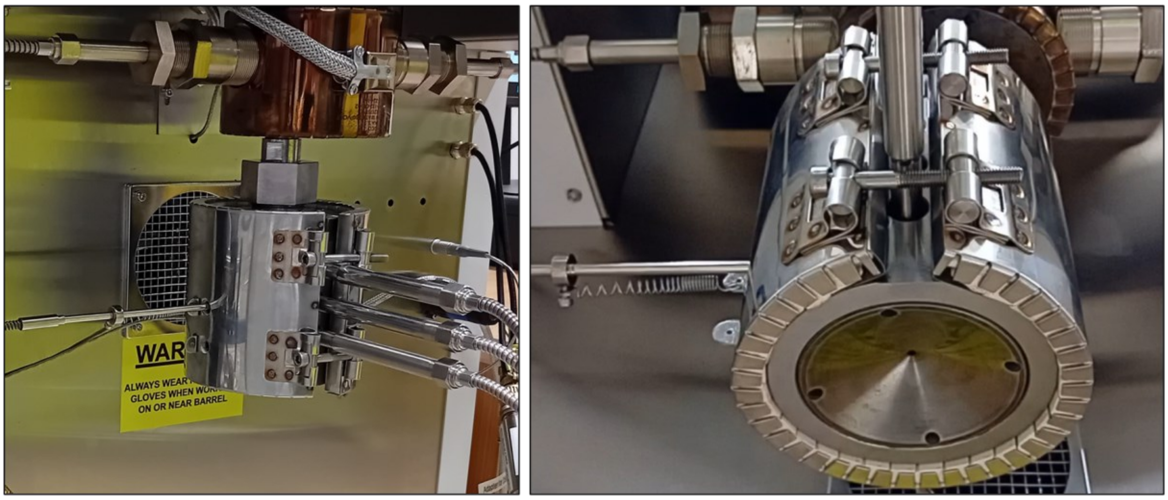

Figure 55 Additional views of the attached strain die including a bottom view of the orifice (freeflow) die

The very concept of the Strain die head allows the use of different diameters of the strain die barrel D_{bsd}, and the diameter of the orifice die D. In this work, the strain die diameter was varied, while the orifice die diameter remained unchanged, equal to 3mm (see Table 12 for further details). The measurements on the strain were performed for branched LDPE PG 7008 at a temperature of 150 °C to maintain clear focus.

Table 18 Shear rate ranges and pressure transducers for entrance pressure drop measurements using the modified setting of capillary rheometer (utilizing the Strain die with varied barrel diameters according to Table 12 while keeping the orifice die diameter unchanged D = 3 mm) for LDPE PG 7008

Measuring ranges	Used pressure transducer	$\dot{\gamma}_{APP}\ \left(\mathrm{s}^{-1}\right)$	$v_x\ \left(\mathrm{mm}\cdot\mathrm{min}^{-1}\right)$
High [A, B]	p_1 = 500PSI MZ4 p_2 = 500PSI MZ1 p_3 = 500PSI MZ2 p_4 = 250PSI MZ3	445.567	495.074
		304.245	338.050
		207.031	230.034
Middle	p_1 = 250PSI MZ4 p_2 = 250PSI MZ1 p_3 = 250PSI MZ2 p_4 = 250PSI MZ3	132.316	147.018
		90.014	100.016
		61.300	68.111
		41.770	46.411
Low	p_1 = 250PSI MZ4 p_2 = 250PSI MZ1 p_3 = 250PSI MZ2 p_4 = 250PSI MZ3	28.446	31.606
		19.348	21.498
		13.206	14.673
		9.003	10.003
		6.131	6.813
		4.182	4.647
		2.850	3.167
		1.940	2.156
		1.320	1.467
		0.900	1.000

[A]Individual values of $\dot{\gamma}_{APP}$ (apparent shear rate) or v_x (speed piston) in the High section were measured separately. [B] Only for measurements with D_{bds} = 65 mm, the high range was extended by the value $\dot{\gamma}_{APP}$ = 725 s^{-1} (v_x = 652.593 $mm \cdot min^{-1}$).

Measurements were made over a wide range of apparent shear rates using the most sensitive pressure transducers (see Table 18). Before the actual measurement, after thorough filling the barrel with polymer pellets, a pre-test with the following parameters was applied: first and second compression (v_x = 25 $mm \cdot min^{-1}$, $p_{1\text{-}4}$ = 0.15 MPa), first heating (3 min at 150 °C), and second heating (5 min at 150 °C). These conditions and the entire test were manually defined using a script in the rheometer software (see Appendix VIII). The pressure equilibrium conditions were set as in the standard setting: Error = 0.5 %, Window = 16, Average = 16, Maximum Samples numbers = 400. In order to accommodate the possible pressure oscillation caused by decreased flow stability typically occurring at high flow rates (i.e. in the High and Middle range), the pressure equilibrium conditions were changed using the following parameters: Window and Average = 8. The other parameters defining the pressure equilibrium remained the same.

Fig. 72 shows a typical example of the time-dependent pressures measured by all four pressure transducers in the start-up flow regime using $\dot{\gamma}_{APP}$ = 230 s^{-1} and the strain die barrel D_{bsd} = 65 mm. Similarly, Fig. 73 provides a typical example of the time-dependent pressures measured for the series of gradually decreased apparent shear rates (full Middle range, see Table 18). In both cases, it is clearly seen that p_1 is higher than $p_{2\text{-}4}$. The magnitude of this difference is associated with the energy consumed for polymer melt transport from a narrow to a wide flow channel (in this particular case, from a 15mm diameter circular channel to a 65mm diameter circular channel). In addition, the results indicate that the flow in the strain die is fully developed and there is minimal pressure drop inside the Strain die barrel as can be deduced from the values of $p_{2\text{-}4}$ which very close to each other.

Steady-state pressure values for each pressure transducer and given apparent shear rate were obtained from the pressure-time dependencies using predefined equilibrium conditions. These values for different barrel diameters (15mm, 25mm, 40mm, 65mm) and different pressure transducers are shown in Figs. 74-77. Interestingly, there is clear evidence that for the LDPE sample tested and for a given temperature, the pressure drop decreases with increasing barrel diameter. This indicates that first, the actual value of the Hencky strain ε_{H} does not reaches the maximum attainable strain defined by Eq. 53. Second, the actual Hencky strain can decrease with increased contraction ratio C_R (defined as the ratio of barrel diameter to orifice die diameter) even if the maximum attainable strain increases with C_R according to Eq. 53. This could be explained by the presence of a vortex, typically found in sudden contraction flows for branched polymers such as LDPE, which could change its shape and size with an apparent shear rate that has strong impact on the actual shape and entrance angle of the convergence channel significantly narrowing the flow channel in comparison with the flow geometry given by the Strain die walls. Increased residence time due to increased C_R allowing extensional stress relaxation during the sudden contraction flow could be another important factor causing that overall strain is reduced. Thus, the Weissenberg number (defined by Eq. 13) determined in the barrel and at the entrance region could be a useful parameter to quantify these effects.

In order to capture the effect of C_R on the measured pressure drop, it was possible to apply a simple horizontal shift a_k for all pressure curves (by choosing D_b = 15 mm as the reference value) and generate master curves that are shown in Figs. 78-81.

Table 19 a_k values from shift analysis together with contraction ratio C_R values for individual barrel diameters (D_{bsd} is barrel strain die, and D_b is standard barrel)

Pressure transducer	D_b or D_{bsd} (mm)	C_R (1)	a_k (1)
p_2	15	5	1.0000
	25	8.3	0.8458
	40	13.3	0.7620
	65	21.7	0.4637
p_3	15	5	1.0000
	25	8.3	0.8375
	40	13.3	0.7574
	65	21.7	0.4544
p_4	15	5	1.0000
	25	8.3	0.8061
	40	13.3	0.7216
	65	21.7	0.4323

The obtained horizontal shifts a_k were plotted for each pressure $p_{2\text{-}4}$ as a function of the contraction ratio C_R. It was found that a_k linearly scales with C_R as can be visible in Figs. 82-84. Table 19 summarizes all input data to construct these dependencies.

Knowledge of the presented master curves and the a_k versus C_R dependencies for given material and flow conditions opens up new possibilities for correcting the measured entrance pressure drop data in order to more accurately determine extensional viscosities.

Modeling of measured rheological data for LDPE PG7008 using different constitutive equations

In this section, the measured rheological data for LDPE PG7008 were used to investigate the ability of the various constitutive equations presented in Chapter 4 to simultaneously describe shear viscosity and uniaxial extensional viscosity data exhibiting a very strong non-monotonic character. For this purpose, the following constitutive equations were chosen: modified Leonov model, Yao model, modified White-Metzner (mWM) model, and modified Generalized Newtonian (mGNF) model. Note that the analysis here is not performed for the linear polymer PP-A, as it shows a simple monotonic decrease in uniaxial extensional viscosity with increased strain rate, which is not a challenging task for the selected constitutive equations as reported in the open literature.

Measured shear data from a rotary (based on Cox-Merz Rule) and capillary (standard setting) rheometer and extensional viscosity data from SER taken at the Hecky strain ε_H = 4 were used to test selected constitutive equations. The fitting error was expressed for each model using the Root Mean Squared Error (RMSE), which is defined by the following relation:

$$RMSE = \sqrt{\frac{1}{n}\sum_{i=1}^{n}\left[\log\left(n_{m,i}\right) - \log\left(n_{p,i}\right)\right]^2}, \tag{94}$$

where n is the total number of values in the set, $n_{m,i}$ is the measured value, and $n_{p,i}$ is the predicted value [21].

A comparison between the experimental data and model fits/predictions are provided in Figs. 85-88 and corresponding model parameters (along with RMSE) are given in Tables 20-23. Steady shear and uniaxial extensional viscosities were used to identify the parameters of mWM, mGNF, and Yao models, while in the case of the modified Leonov model, discontinues relaxation spectrum obtained from SAOS (see Table 14) was used as the fixed values, and all remaining nonlinear parameters were identified only on steady uniaxial extensional viscosity data.

Table 20 Parameters of the modified Leonov model for LDPE PG 7008 at 150 °C ($n_{L,i} = \beta_{L,i} = 0$)

i	λ_i (s)	G_i (Pa)	$\xi_{L,i}$ (1)	υ_i (1)	RMSE (1)
1	0.000077	453945.0000	0	0.1000	0.04130
2	0.001263	71391.8000	0	0.1000	
3	0.005465	36893.6000	0	0.1000	
4	0.019583	15801.5000	0	0.1000	
5	0.056531	8746.5900	0	0.1000	
6	0.157078	4965.1600	0	0.1	
7	0.432648	2538.5300	0	0.1	
8	1.162300	1297.4100	0.320	0.0015	
9	3.664230	597.7880	0.350	0.0010	
10	13.463600	134.3550	0.302	0.0003	
11	62.156400	0.1428	0.250	0.00000015	
12	340.471000	0.0052	0	0	

Table 21 Parameters of the Yao model for LDPE PG 7008 at 150 °C.

η_0 (Pa·s)	λ_Y (s)	ψ_Y (1)	S_0 (1)	α_0 (1)	n_0 (1)	RMSE (1)
8 526.63	63.4341	0.5410	2.9221	0.9941	0.8020	0.06696

Table 22 Parameters of the modified White-Metzner (mWM) model for LDPE PG 7008 at 150 °C $\left(\lambda_{EW} / K_1 < \sqrt{3}/2\right)$.

η_0 (Pa·s)	λ_1 (s)	a (1)	n (1)	λ_{EW} (s)	K_1 (1)	RMSE (1)
8 526.63	0.7068	0.5757	0.3860	55.5658	65.9813	0.07069

Table 23 Parameters of the modified Generalized Newtonian fluid (mGNF) model for LDPE PG 7008 at 150 °C where $\beta = \zeta$, $A_Z = 10^{-8}$ Pa·s (taken from [109]), $\psi_Z = 0$.

η_0 (Pa·s)	λ_1 (s)	a (1)	n (1)	λ_2 (s)	β (1)	RMSE (1)
8 526.63	0.5672	0.3663	0.5418	1.2959	0.033	0.08376

As can be seen, all constitutive equations used have high ability to describe the measured data. Although the differences between the models are small, their ability to describe the measured rheological data according to RSME decreases in the following order: modified Leonov model (RMSE = 0.04130), Yao model (RMSE = 0.06696), mWM model (RMSE = 0.07069) and mGNF model (RMSE = 0.08376).

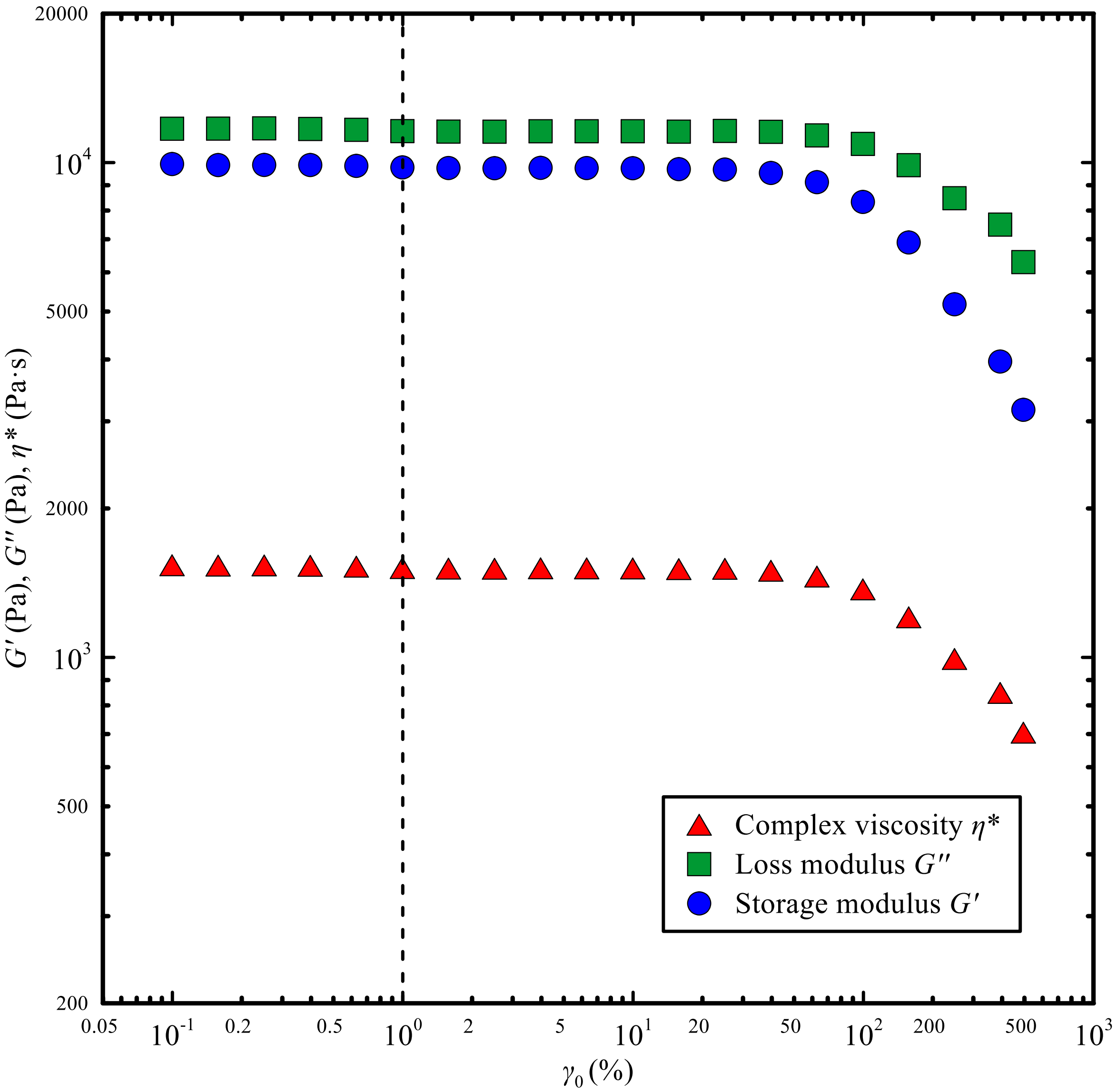

Figure 56 Complex viscosity η^*, Storage G' and Loss G'' moduli obtained from the Strain sweep test at a constant value of the frequency $\omega = 10$ rad·s^{-1} (rheometer range mean) and a temperature of 150 °C for the LDPE PG 7008. The dashed line represents the value ($\gamma_0 = 1$ %) used in the frequency sweep test.

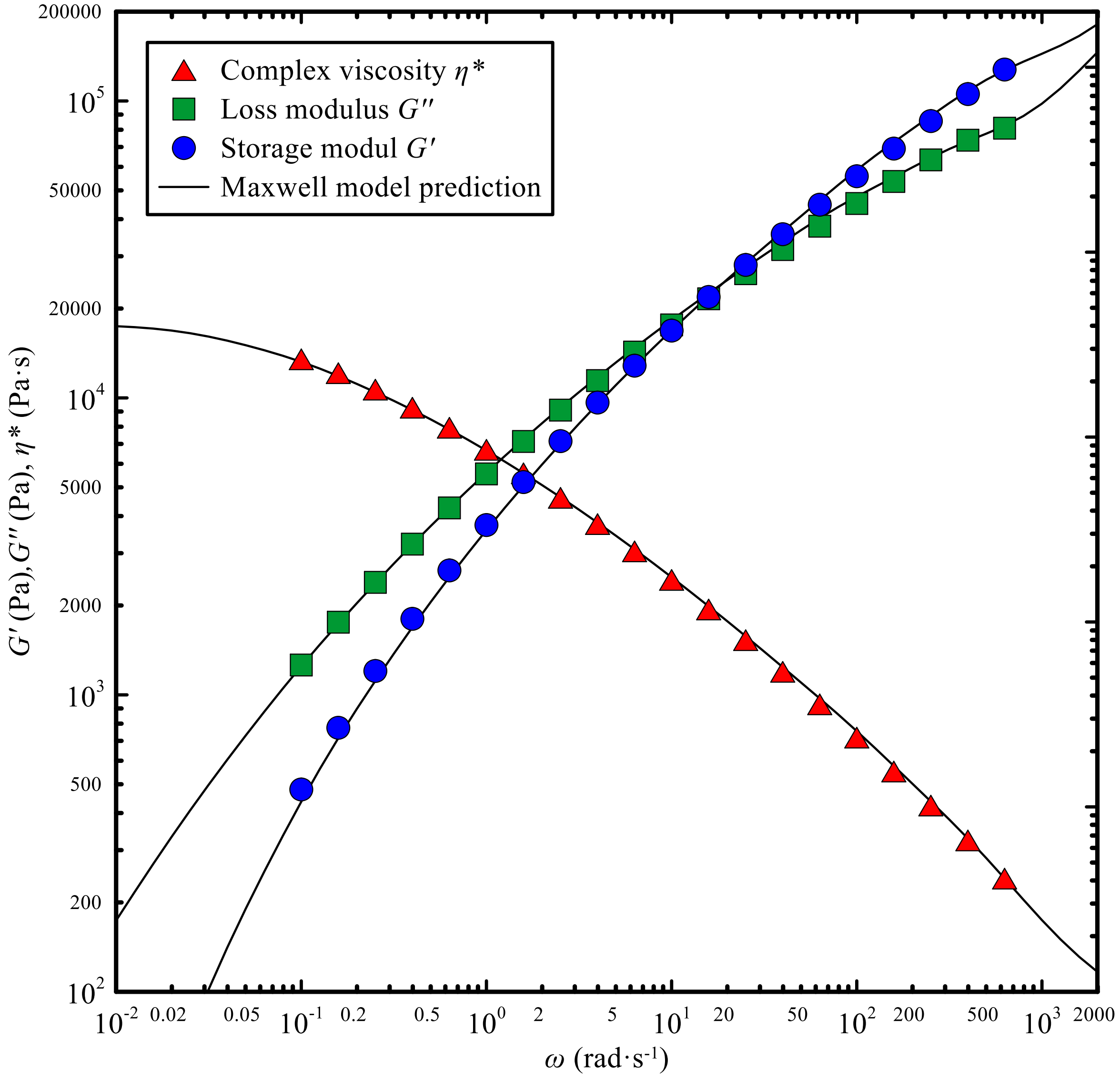

Figure 57 Comparison between the frequency dependent Complex viscosity η^*, Storage *G'* and Loss *G''* moduli and the Maxwell model predictions (using discontinues relaxation spectrum) for LDPE PG 7008 at 130 °C

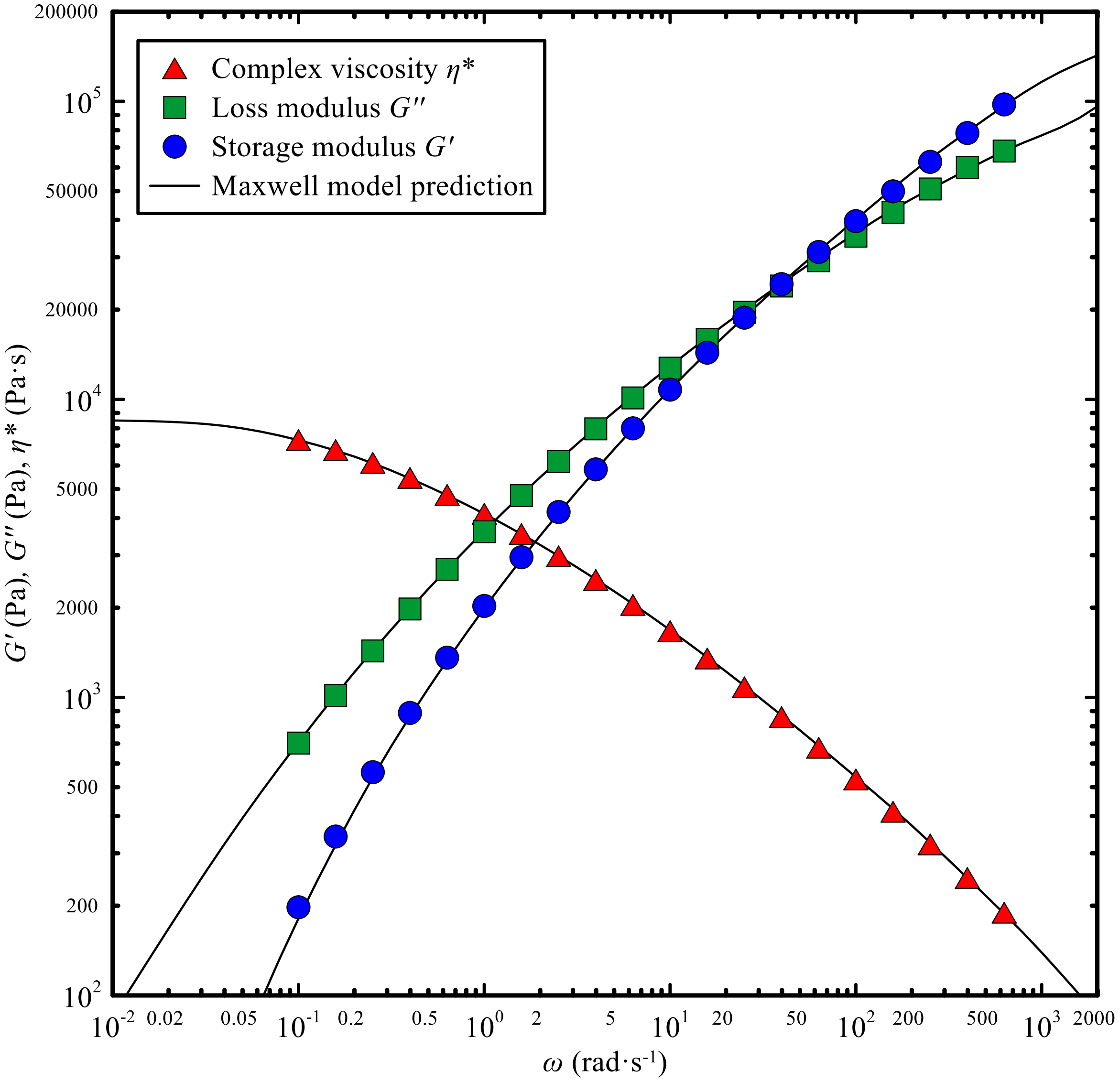

Figure 58 Comparison between the frequency dependent Complex viscosity η^*, Storage *G'* and Loss *G''* moduli and the Maxwell model predictions (using discontinues relaxation spectrum) for LDPE PG 7008 at 150 °C

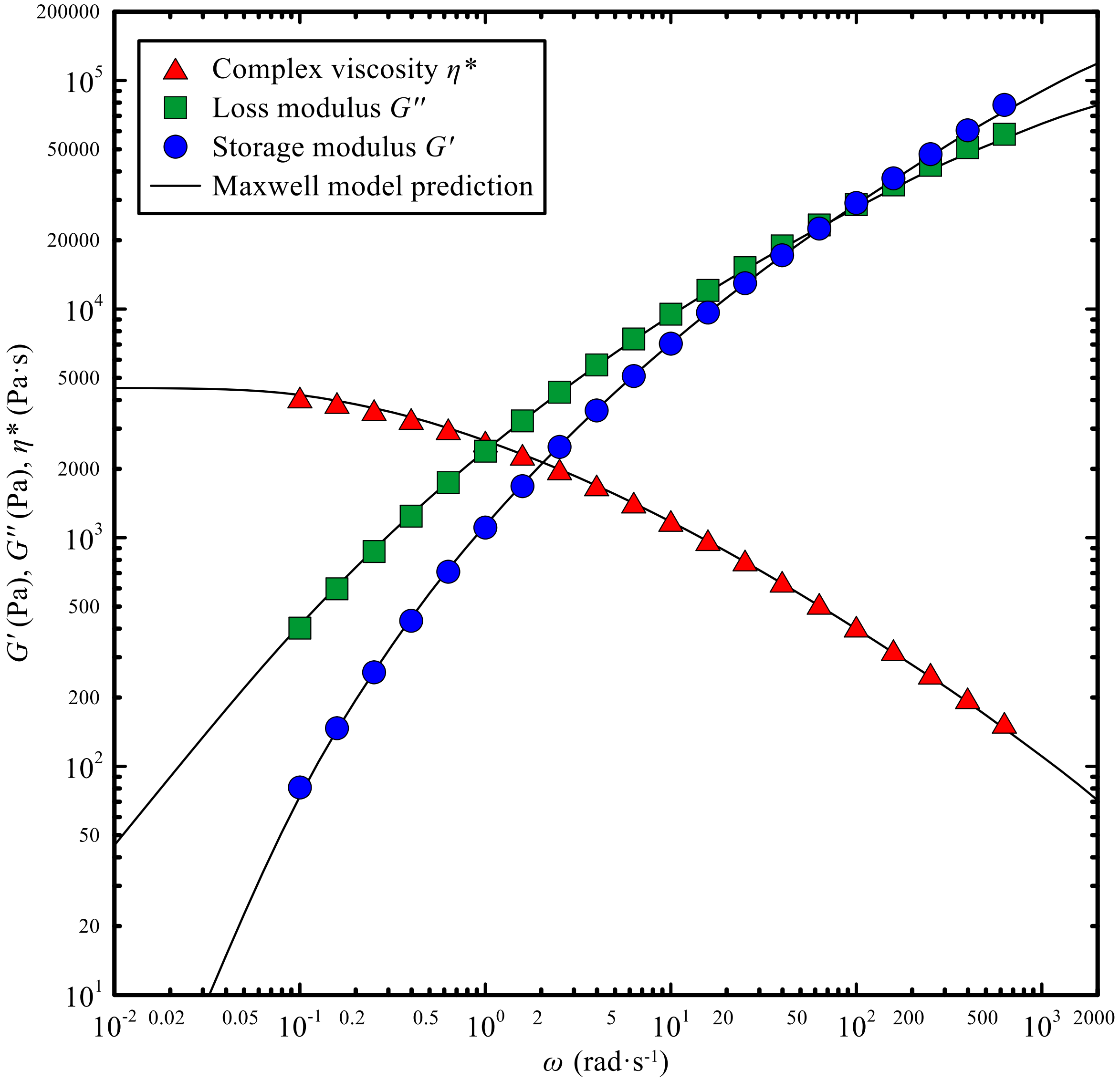

Figure 59 Comparison between the frequency dependent Complex viscosity η^*, Storage *G'* and Loss *G''* moduli and the Maxwell model predictions (using discontinues relaxation spectrum) for LDPE PG 7008 at 170 °C

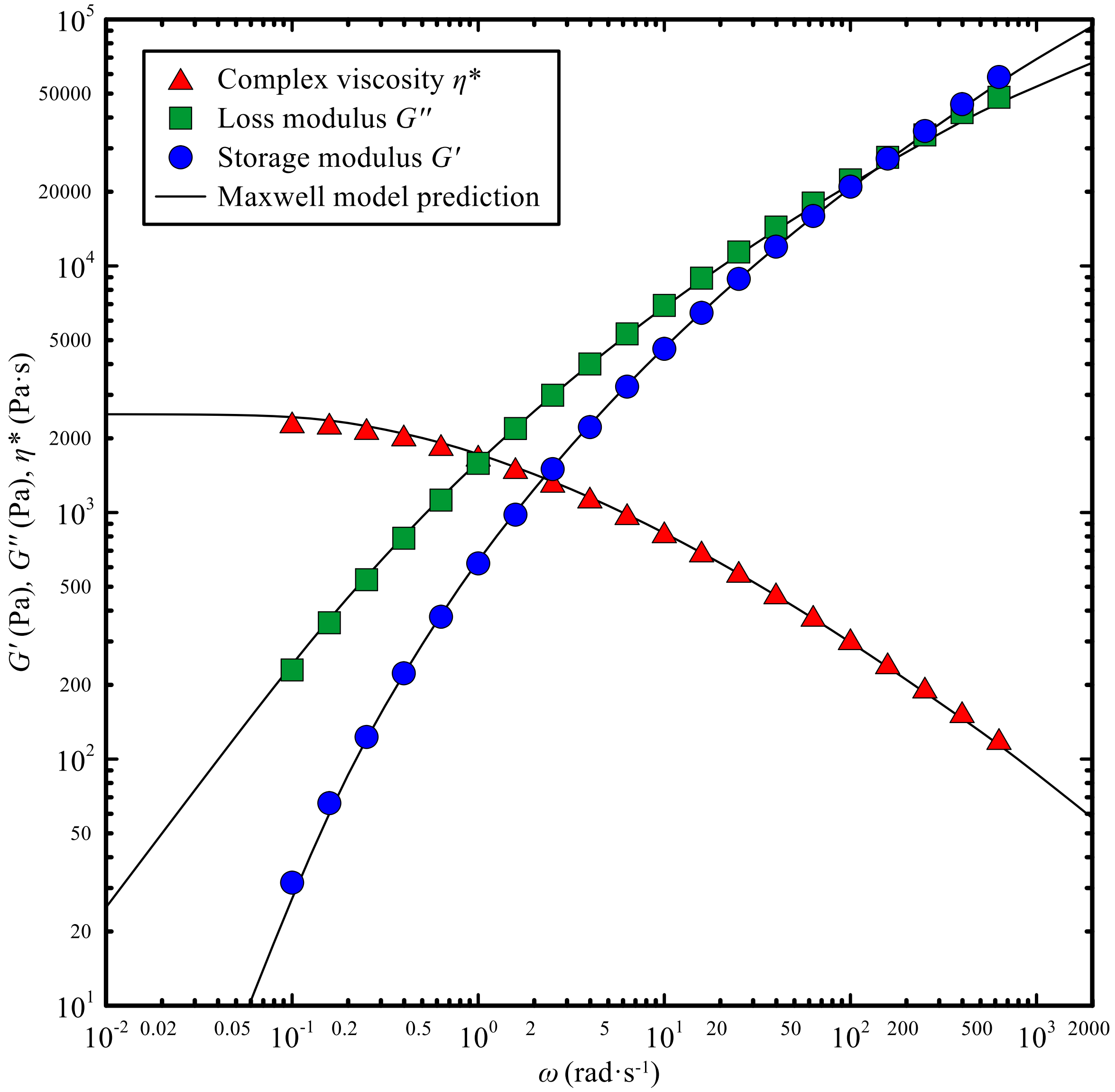

Figure 60 Comparison between the frequency dependent Complex viscosity η^*, Storage *G'* and Loss *G''* moduli and the Maxwell model predictions (using discontinues relaxation spectrum) for LDPE PG 7008 at 190 °C

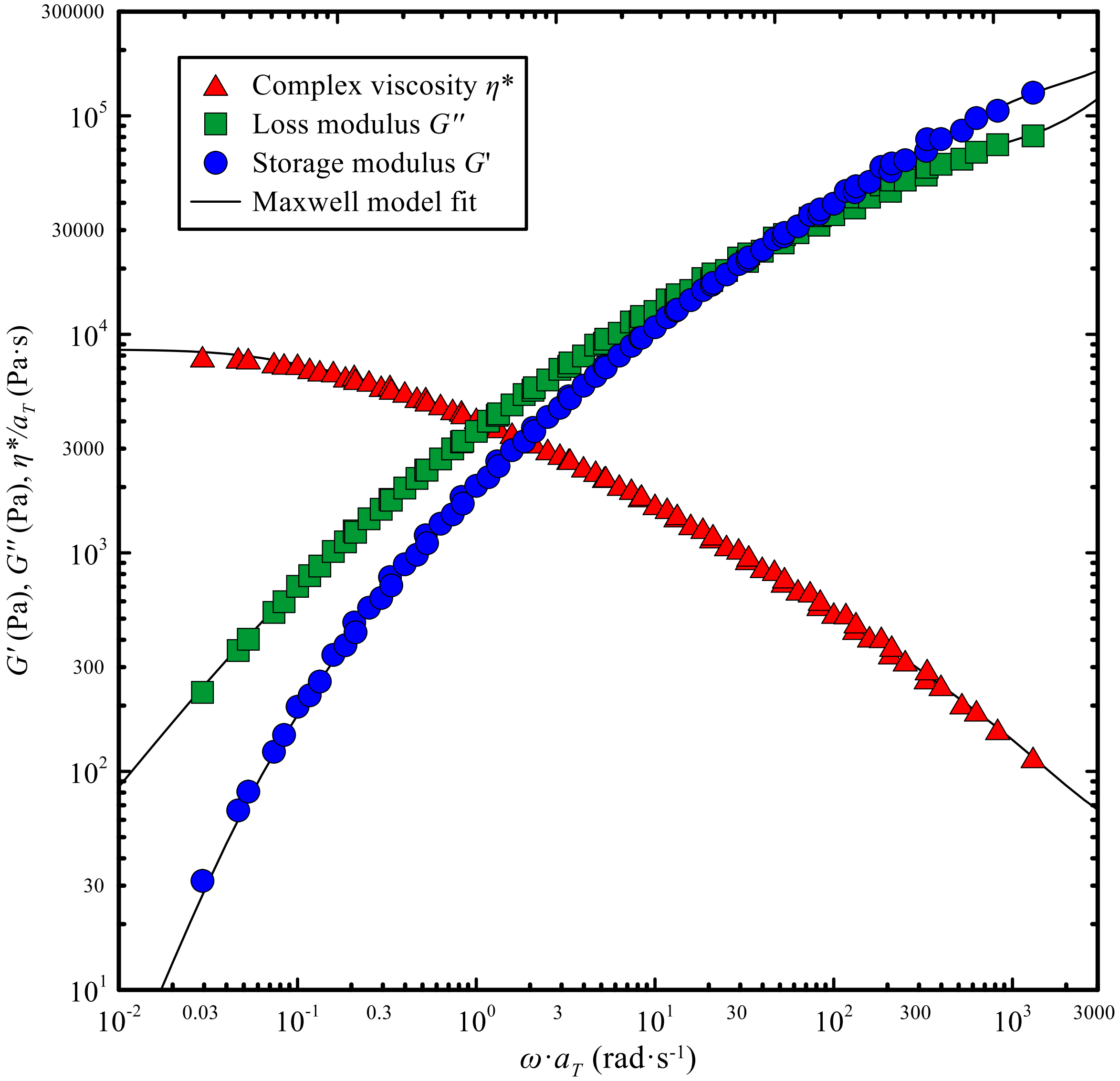

Figure 61 Master curve obtained by time-temperature superposition principle (TTS) using the measured frequency dependent Complex viscosity η^*, Storage G' and Loss G'' provided in Figs. 57-60 for LDPE PG 7008 at 190 °C. Solid line represents the Maxwell model fits using discontinues relaxation spectrum

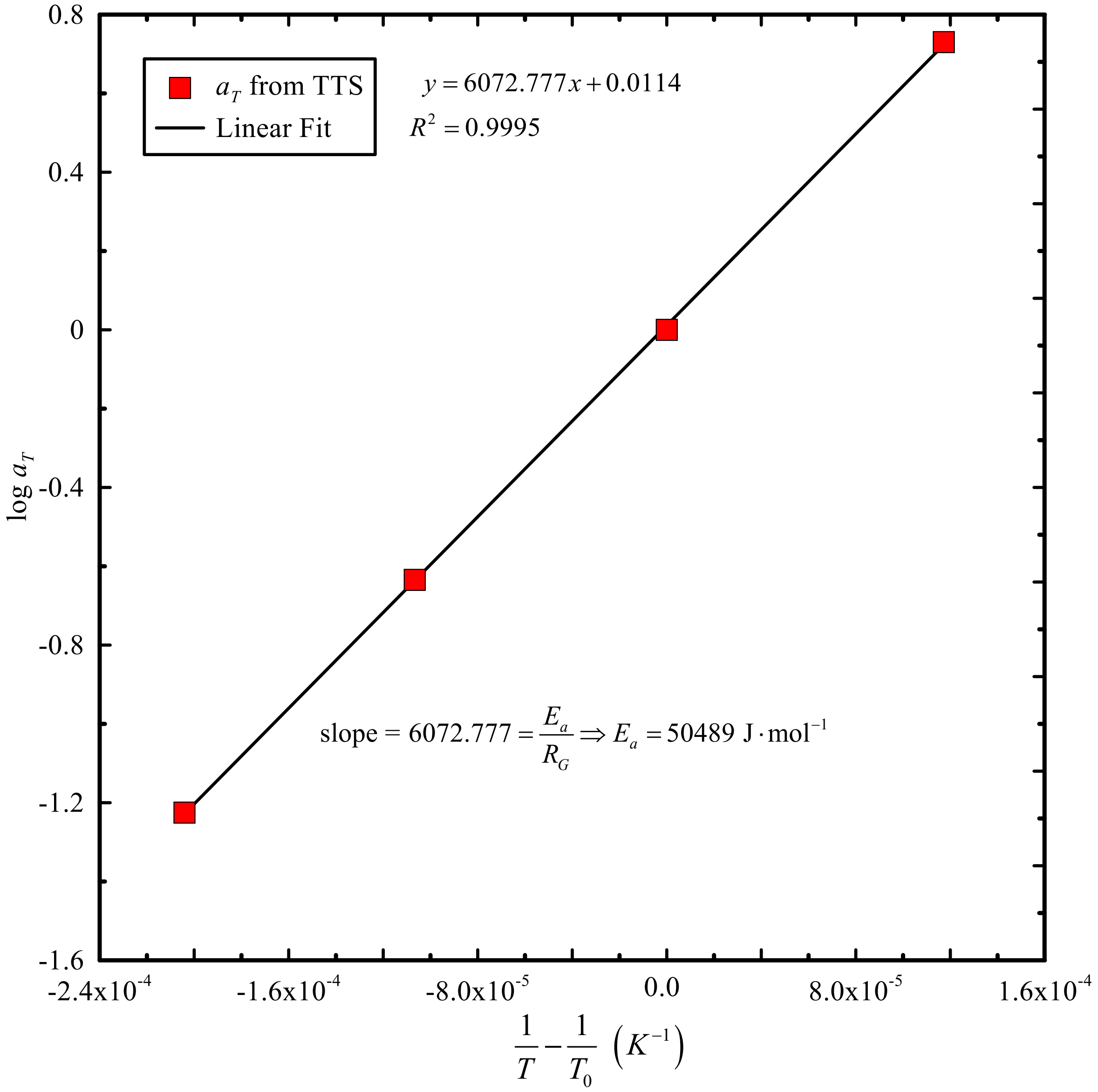

Figure 62 Arrhenius plot showing shift factor a_T as a function of temperature for LDPE PG 7008 together with the calculated flow activation energy E_a (where R is the universal gas constant)

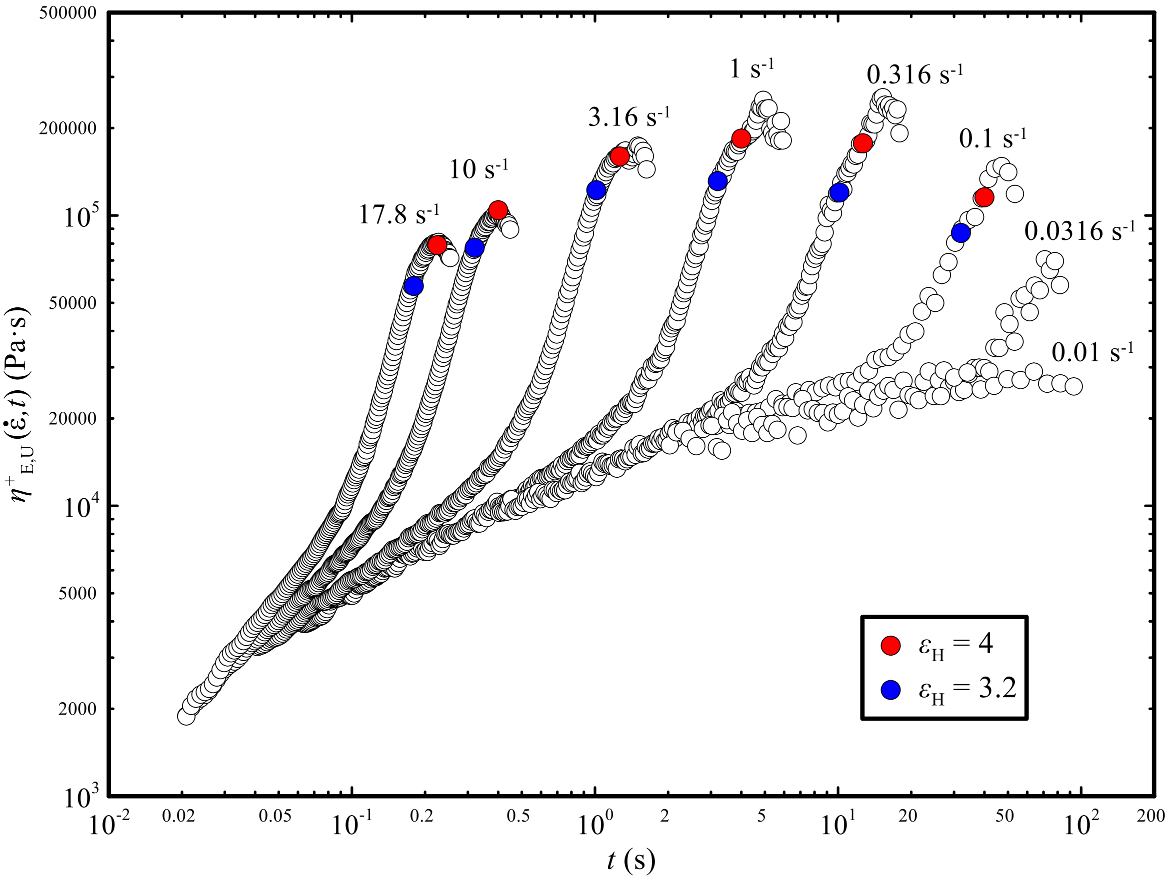

Figure 63 Transient uniaxial extensional viscosity $\eta_E^+(\dot{\varepsilon},t)$ versus time t in the range of extensional strain rate $\dot{\varepsilon}$ (0.01 – 17.8) s^{-1} for LDPE PG 7008 at 150 °C with marked values at two Hencky strains ε_H . The data was obtained using a Sentmanat Extensional Rheometer (SER)

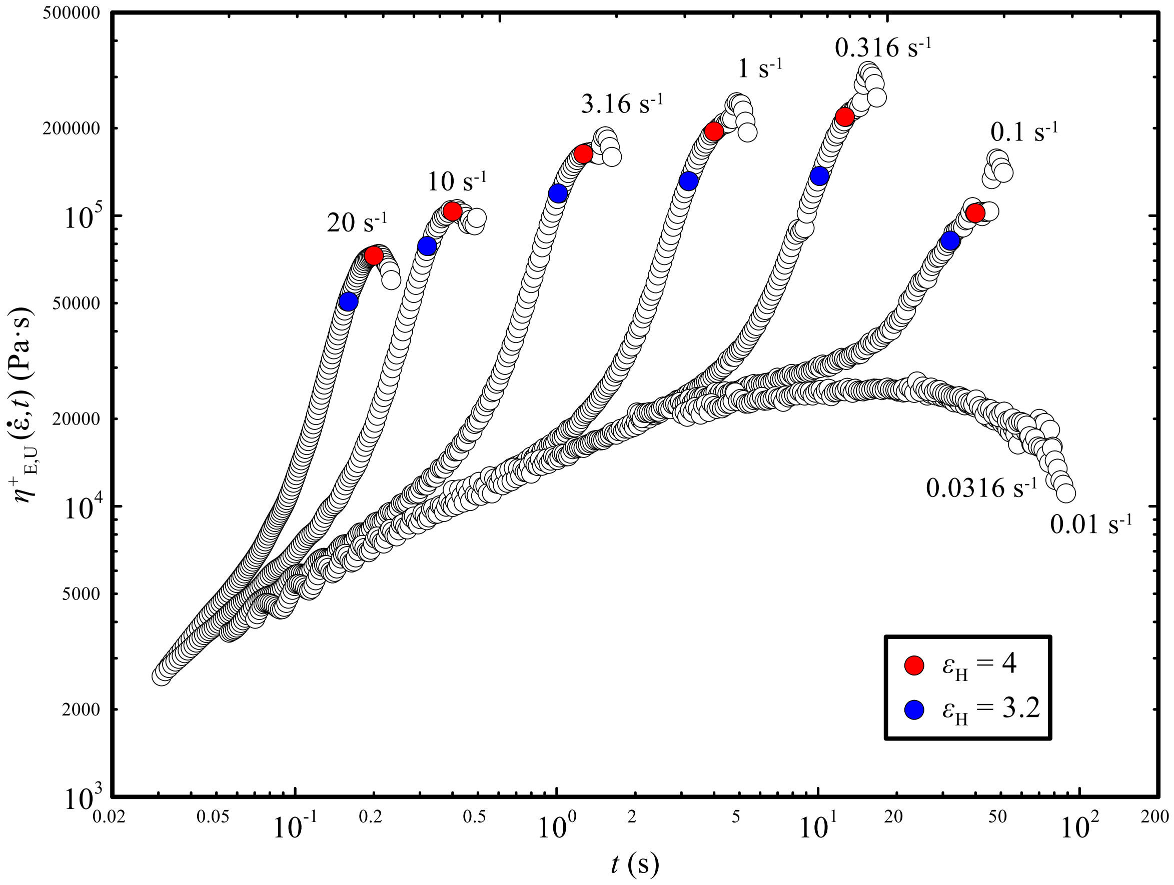

Figure 64 Transient uniaxial extensional viscosity $\eta_E^+(\dot{\varepsilon},t)$ versus time t in the range of extensional strain rate $\dot{\varepsilon}$ (0.01 – 20) s^{-1} for LDPE PG 7008 at 150 °C with marked values at two Hencky strains ε_H. The data was obtained using an Extensional Viscosity Fixture (EVF)

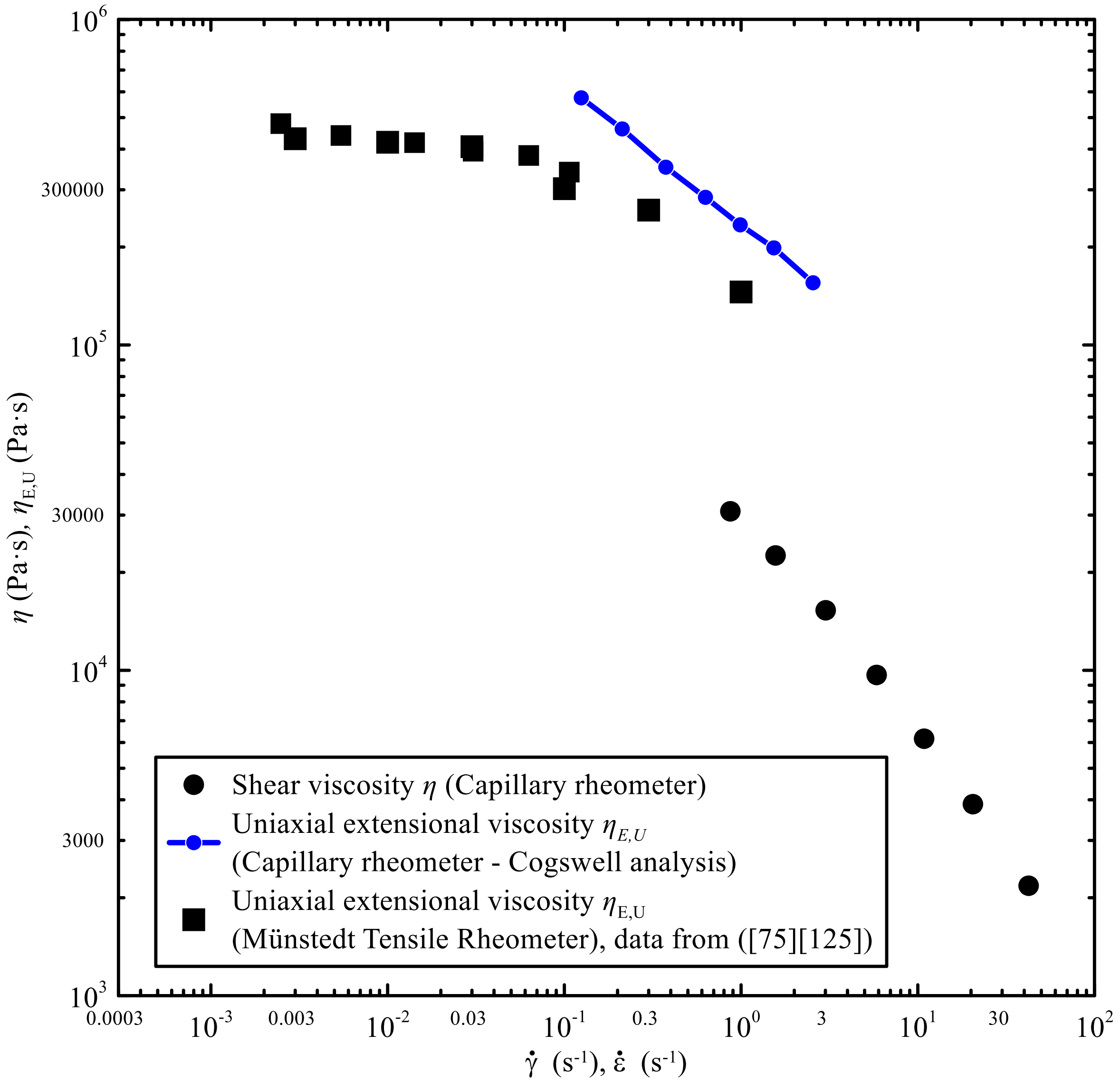

Figure 65 Shear η and uniaxial extensional viscosity $\eta_{E,U}$ versus shear $\dot{\gamma}$ and extensional strain rate $\dot{\varepsilon}$ obtained from pressure drop measurements on capillary rheometer using Cogswell analysis for PP-A at 180 °C. Full squares represents corresponding uniaxial extensional viscosity data from the Münstedt tensile rheometer

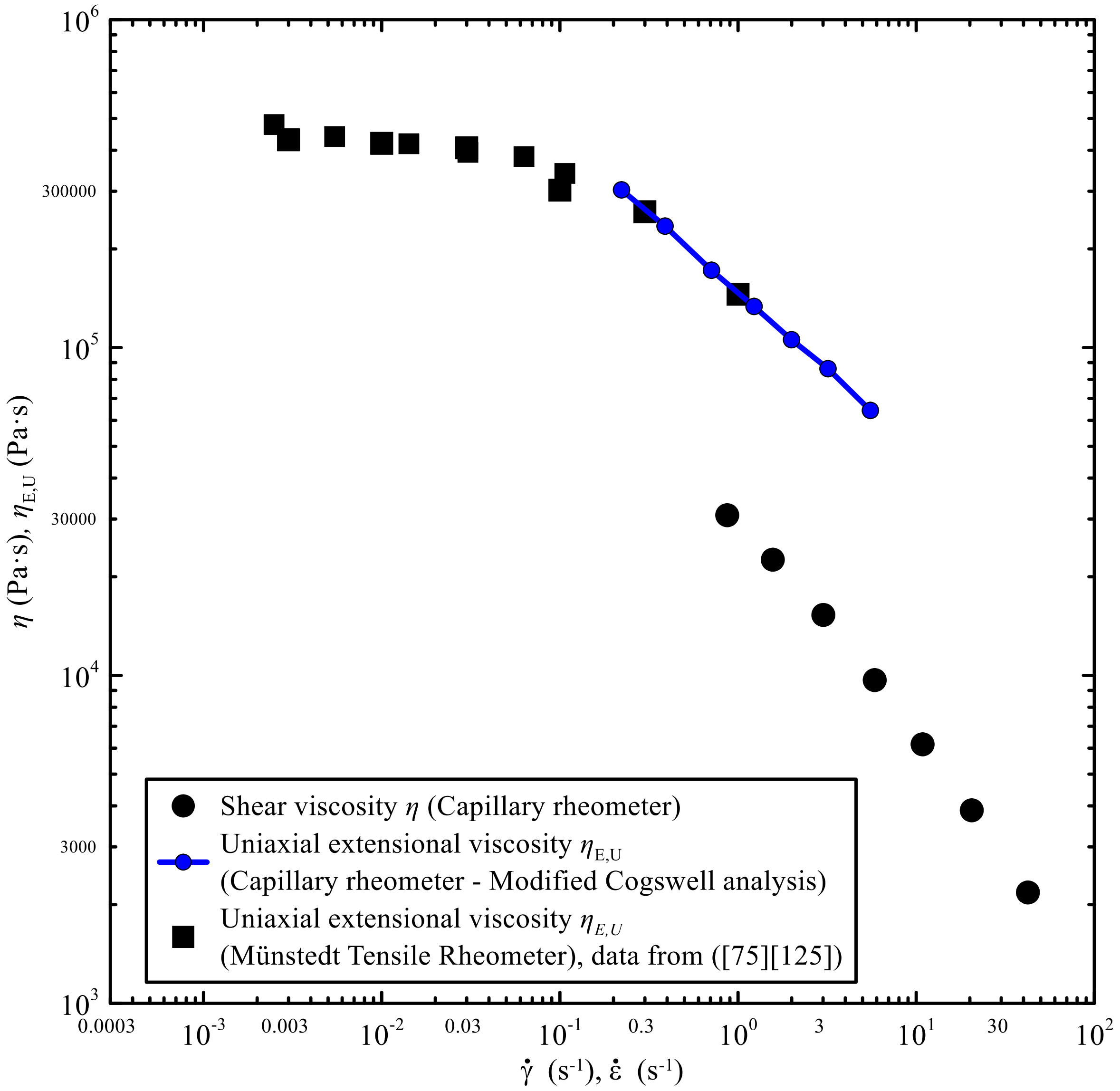

Figure 66 Shear η and uniaxial extensional viscosity $\eta_{E,U}$ versus shear $\dot{\gamma}$ and extensional strain rate $\dot{\varepsilon}$ obtained from pressure drop measurements on capillary rheometer using modified Cogswell analysis for PP-A at 180 °C. Full squares represents corresponding uniaxial extensional viscosity data from the Münstedt tensile rheometer

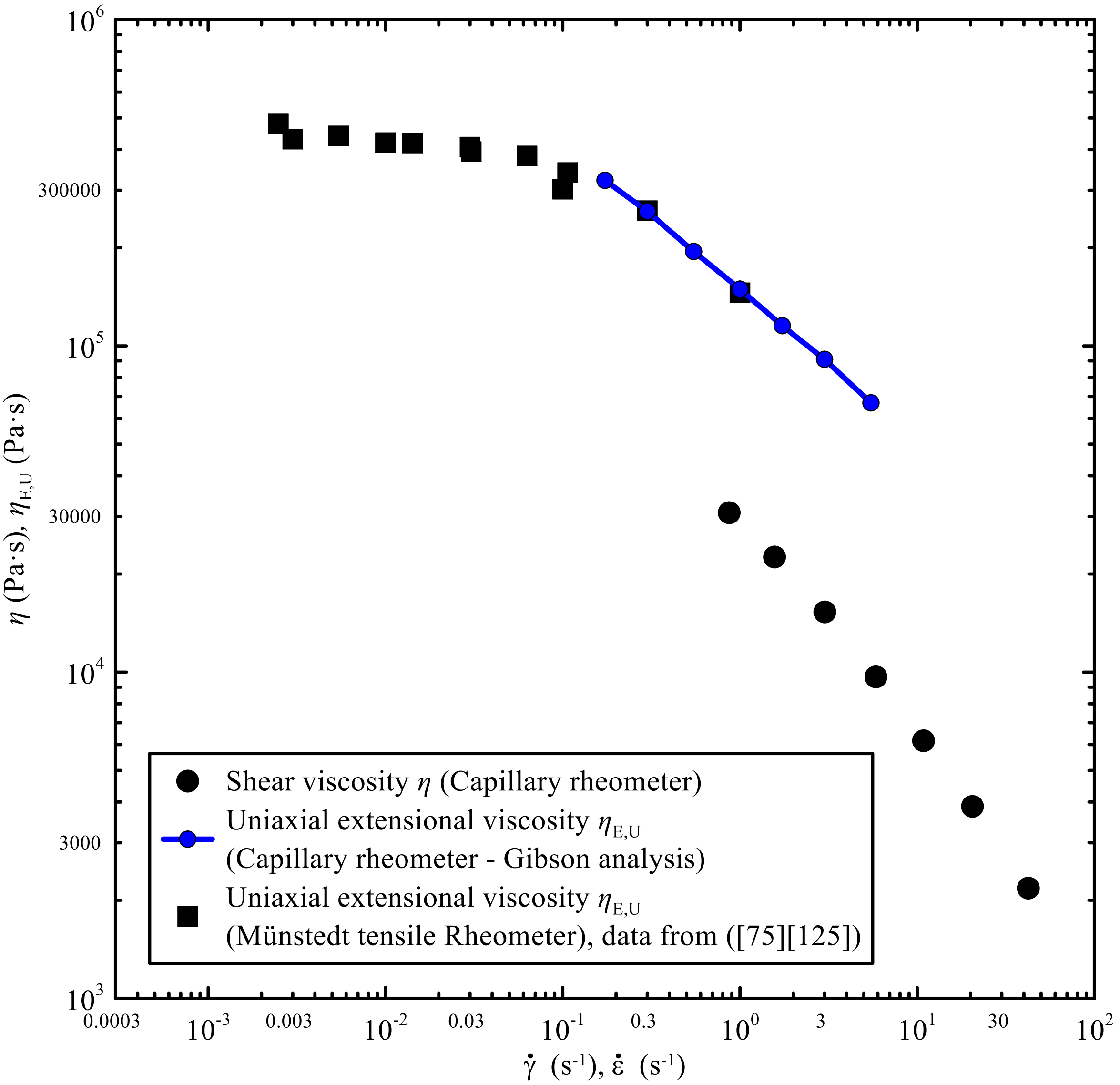

Figure 67 Shear η and uniaxial extensional viscosity $\eta_{E,U}$ versus shear $\dot{\gamma}$ and extensional strain rate $\dot{\varepsilon}$ obtained from pressure drop measurements on capillary rheometer using Gibson analysis for PP-A at 180 °C. Full squares represents corresponding uniaxial extensional viscosity data from the Münstedt tensile rheometer

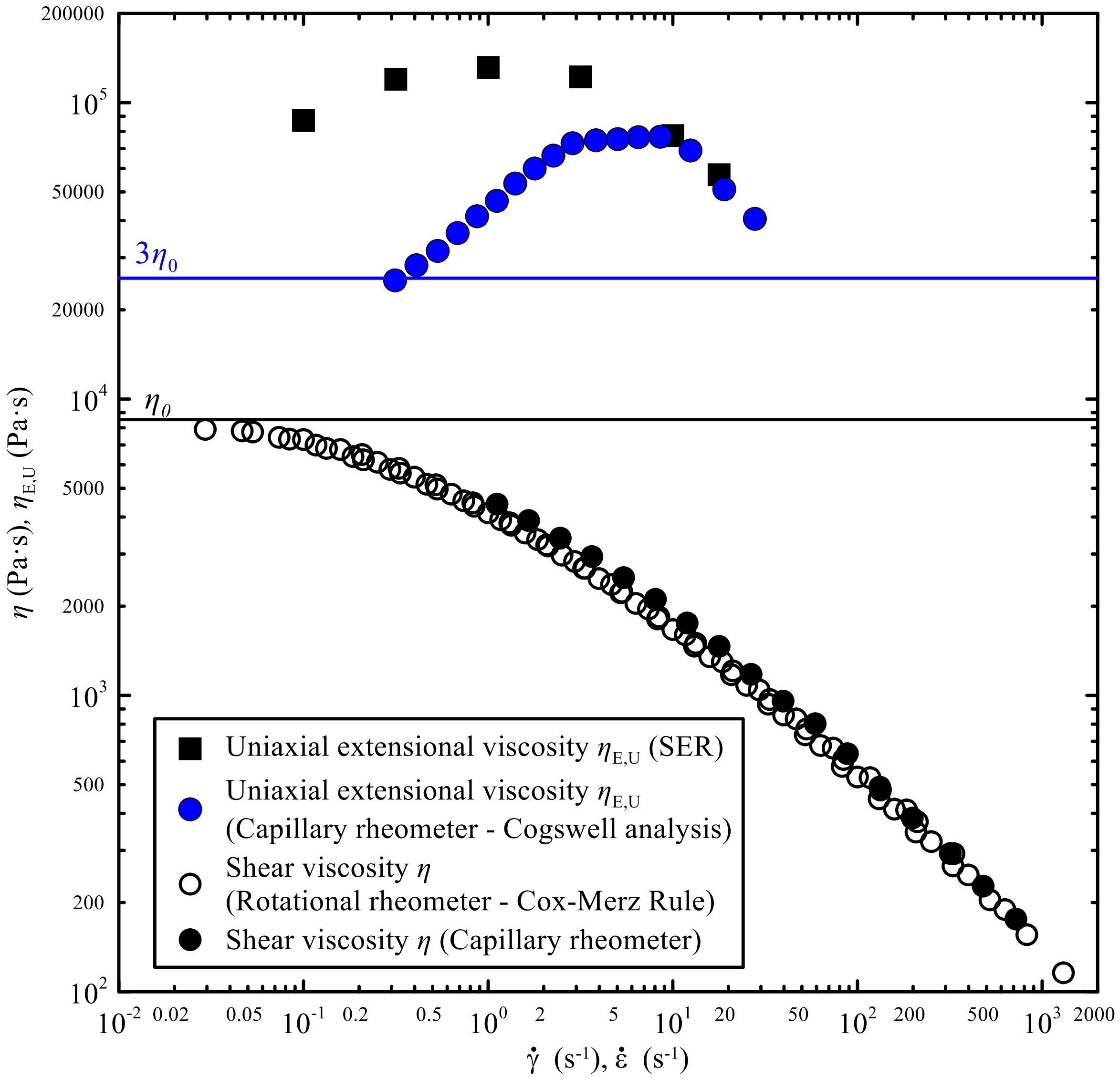

Figure 68 Shear η and extensional uniaxial viscosity $\eta_{E,U}$ versus shear $\dot{\gamma}$ and extensional strain rate $\dot{\varepsilon}$ measured on a capillary rheometer using Cogswell analysis (using standard setting), which are compared to values obtained from the Sentmanat extensional rheometer (at Hencky strain $\varepsilon_H = 3.2$) and SAOS data using the Cox-Merz rule for LDPE PG 7008 at 150 °C

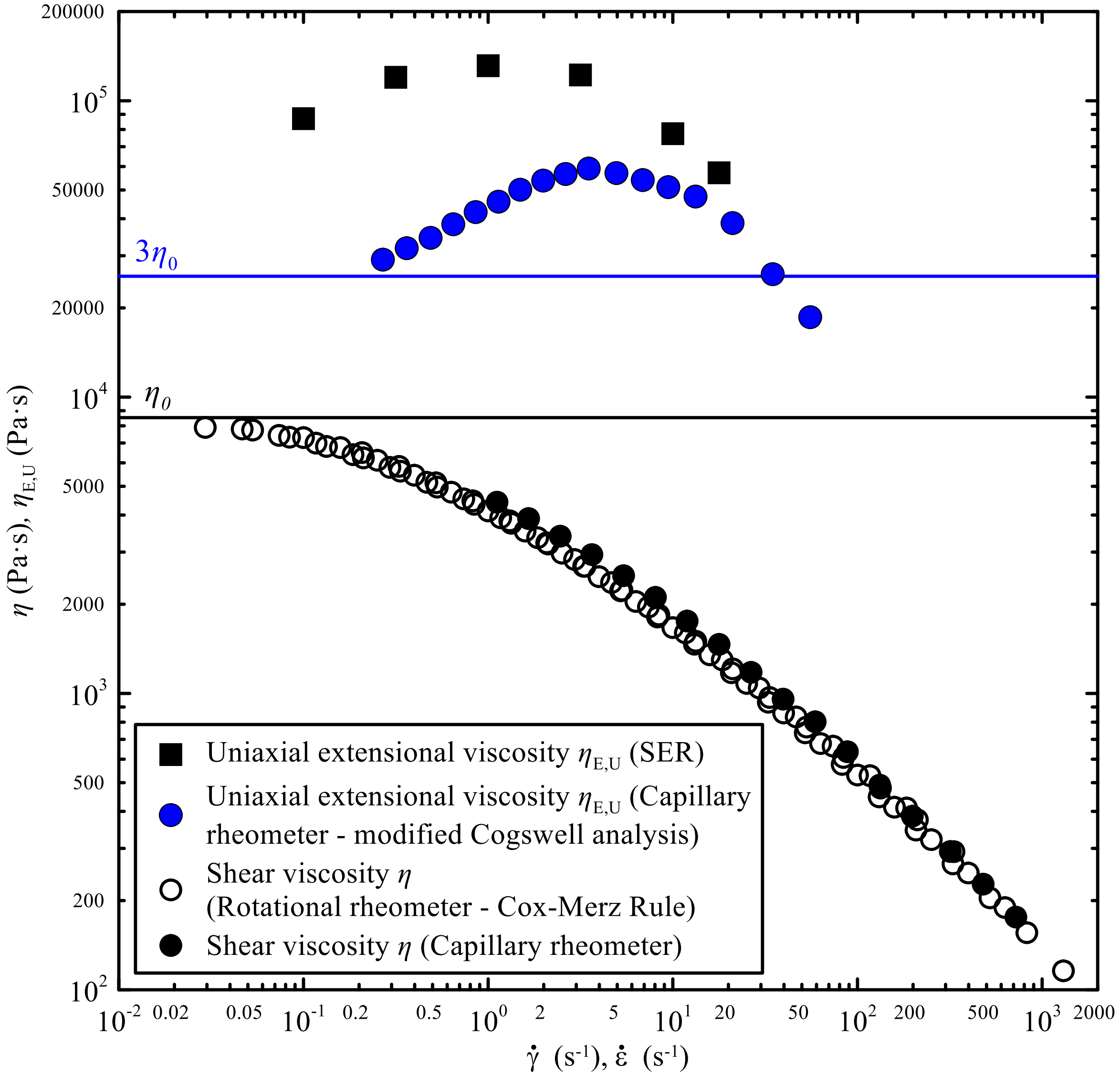

Figure 69 Shear η and extensional uniaxial viscosity $\eta_{E,U}$ versus shear $\dot{\gamma}$ and extensional strain rate $\dot{\varepsilon}$ measured on a capillary rheometer using modified Cogswell analysis (using standard setting), which are compared to values obtained from the Sentmanat extensional rheometer (at Hencky strain $\varepsilon_H = 3.2$) and SAOS data using the Cox-Merz rule for LDPE PG 7008 at 150 °C

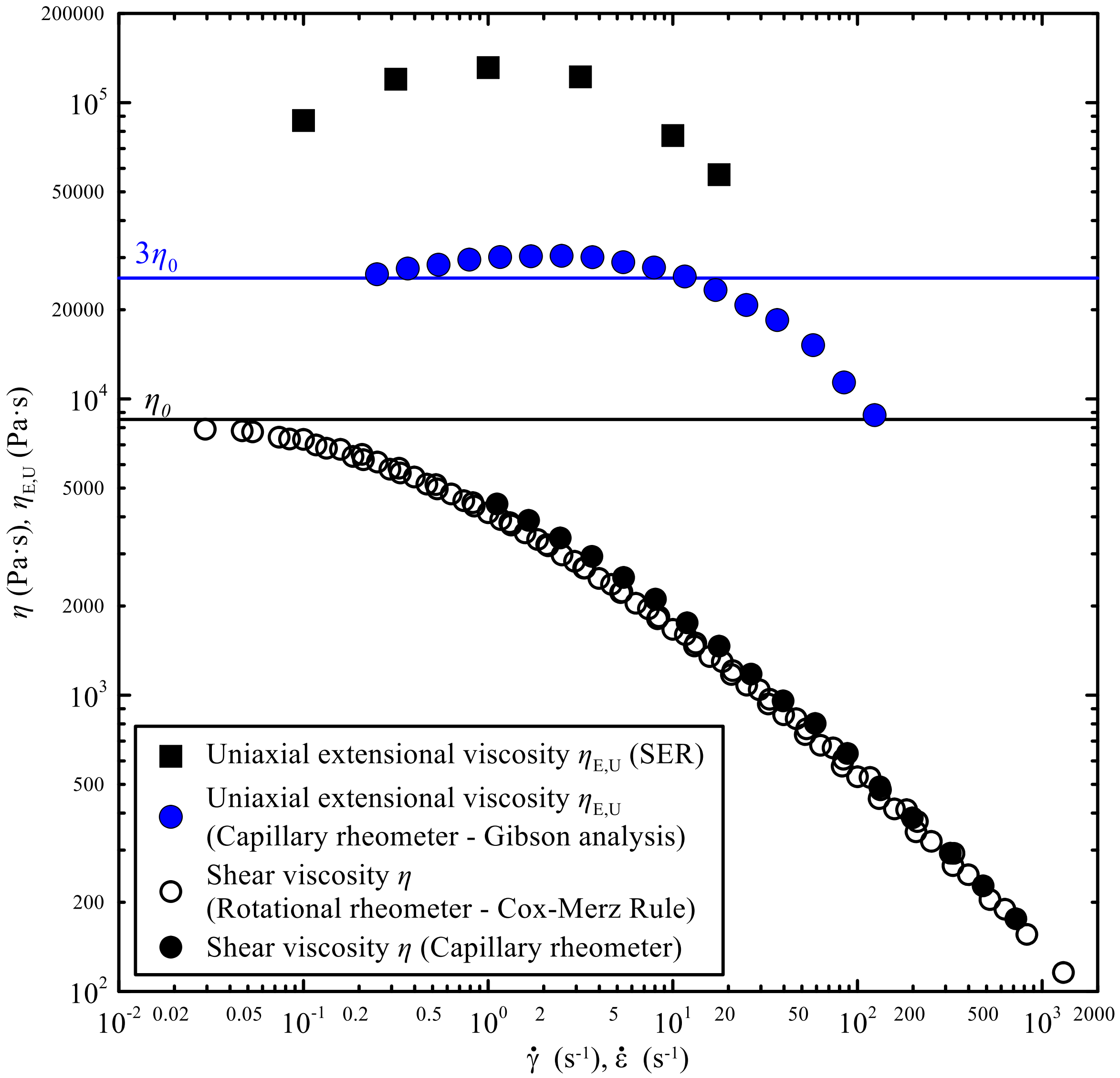

Figure 70 Shear η and extensional uniaxial viscosity $\eta_{E,U}$ versus shear $\dot{\gamma}$ and extensional strain rate $\dot{\varepsilon}$ measured on a capillary rheometer using modified Gibson analysis (using standard setting), which are compared to values obtained from the Sentmanat extensional rheometer (at Hencky strain $\varepsilon_H = 3.2$) and SAOS data using the Cox-Merz rule for LDPE PG 7008 at 150 °C

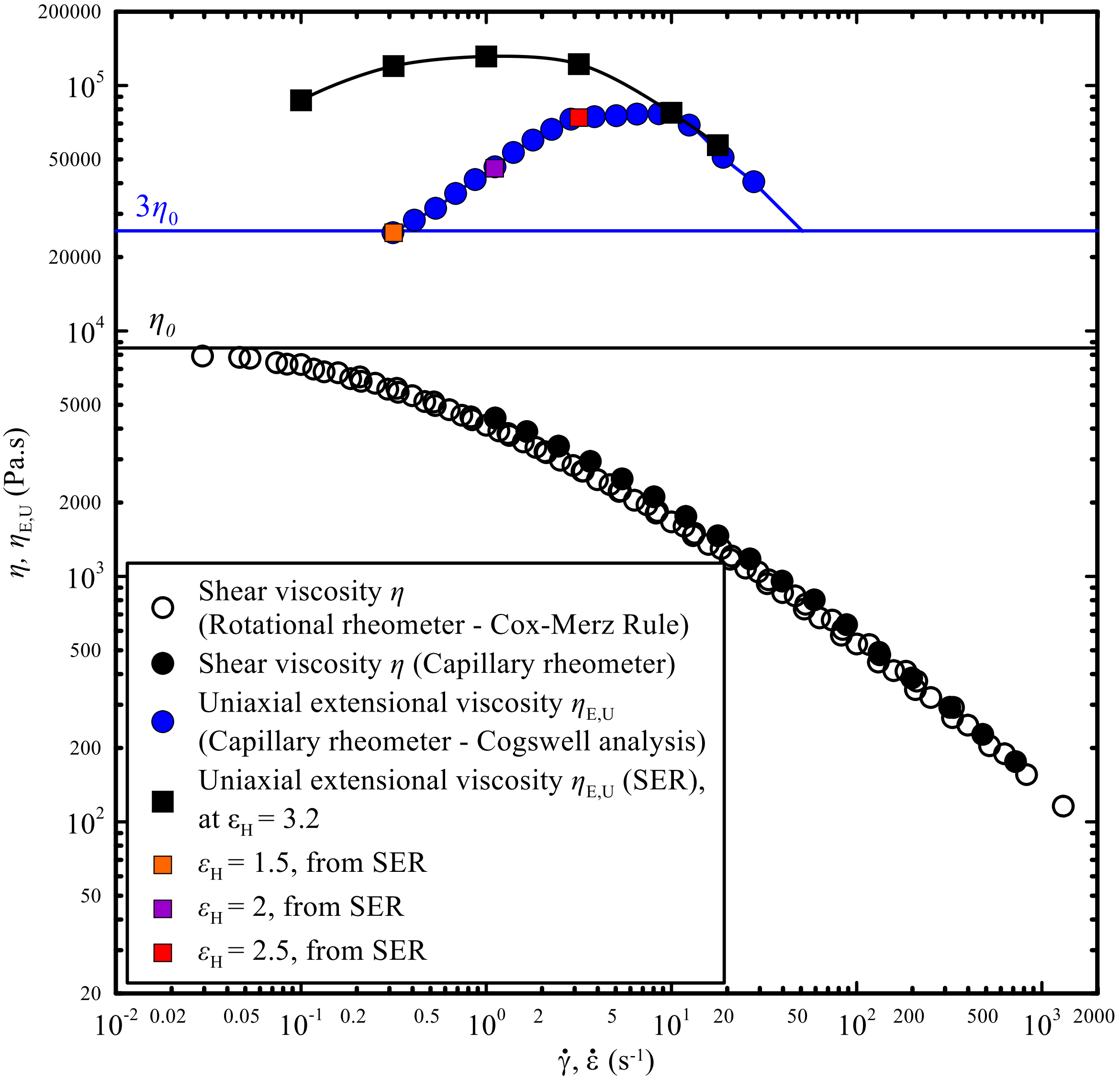

Figure 71 Shear η and extensional uniaxial viscosity $\eta_{E,U}$ versus shear $\dot{\gamma}$ and extensional strain rate $\dot{\varepsilon}$ measured on a capillary rheometer using Cogswell analysis (using standard setting), which are compared to values obtained from the Sentmanat extensional rheometer (at Hencky strain $\varepsilon_H = 3.2$) and SAOS data using the Cox-Merz rule for LDPE PG 7008 at 150 °C The marked points represents the Hencky strain values ε_H, determined from SER measurements provided in Fig. 63

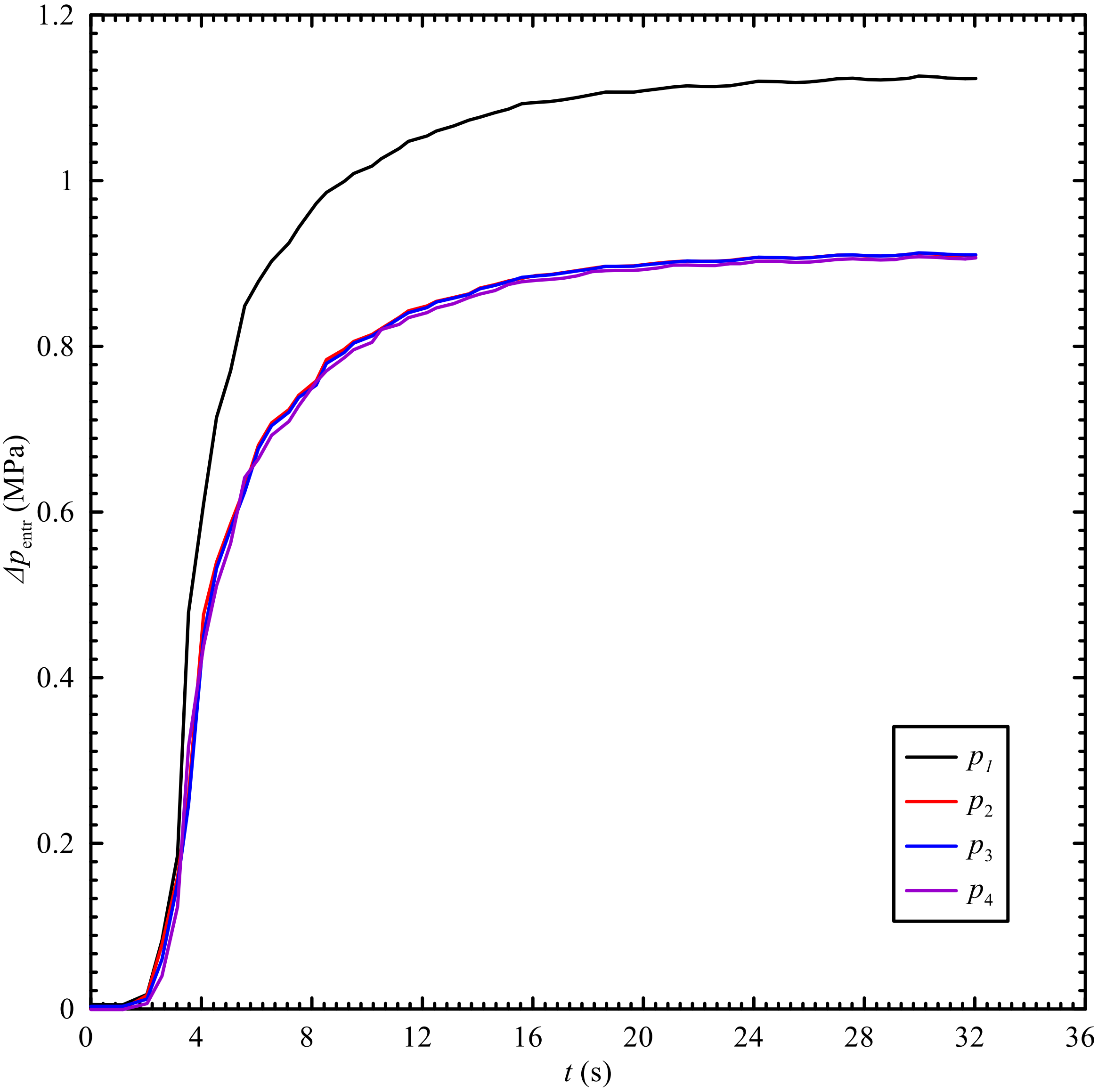

Figure 72 The time-dependent pressures measured by all four pressure transducers in the start-up flow regime using $\dot{\gamma}_{APP}$ = 230 s^{-1} using the strain die with barrel diameter 65 mm and orifice die diameter 3 mm for LDPE PG 7008 at 150 °C.

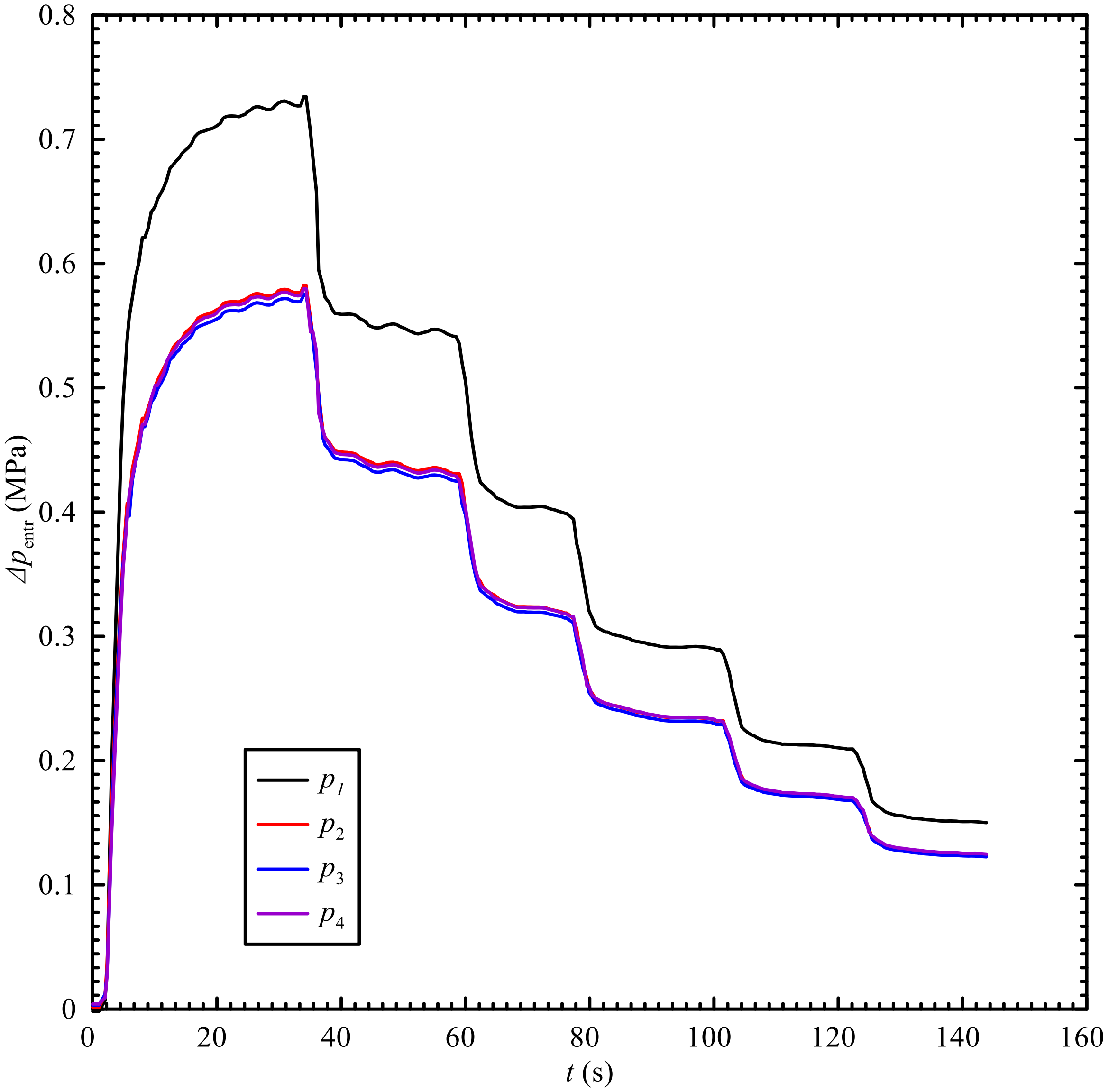

Figure 73 The time-dependent pressures measured for the series of gradually decreased apparent shear rates (full Middle range, see Table 18) using the Strain die with barrel diameter 65 mm and orifice die diameter 3 mm for LDPE PG 7008 at 150 °C.

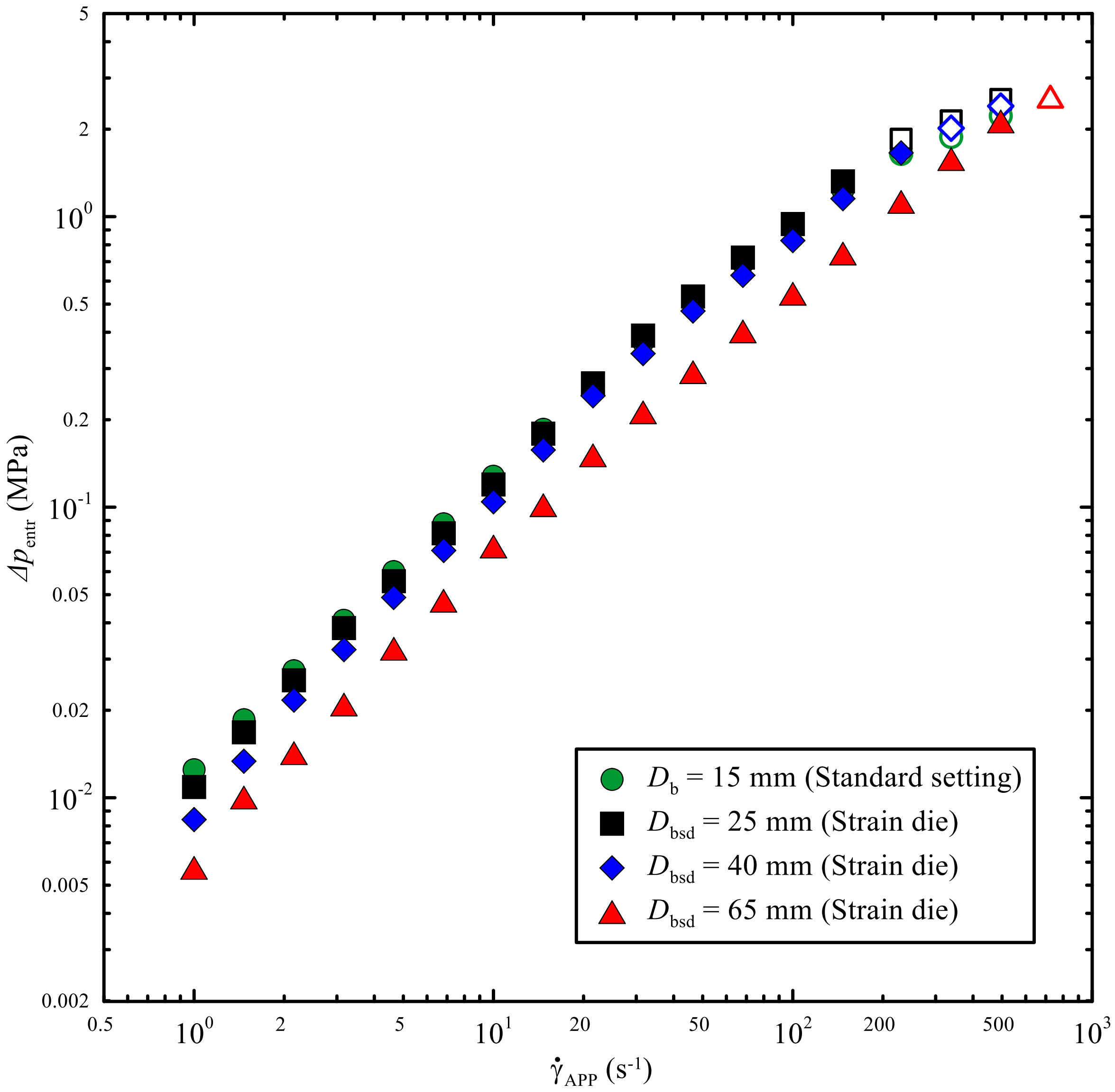

Figure 74 Entrance pressure drop Δp_{entr} (data from the pressure transducer p_1) versus apparent shear rate $\dot{\gamma}_{APP}$ for different barrel diameters for the apparent shear rate range defined in Table 18 for LDPE PG 7008 at 150 °C. Unfilled symbols represent the presence of melt rupture flow instability. Here D_{bsd} is barrel diameter of the Strain die, and D_b is standard barrel diameter.

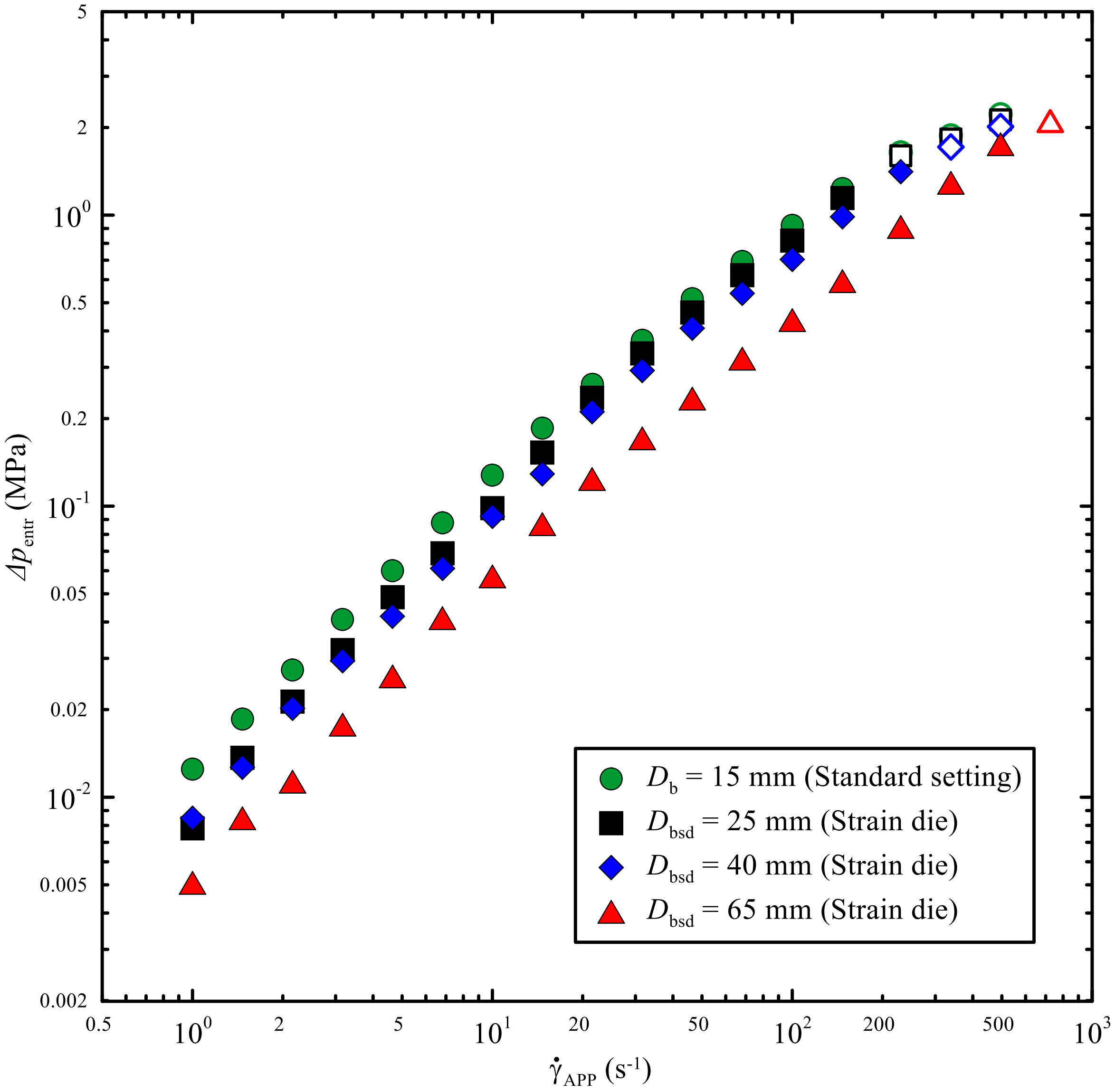

Figure 75 Entrance pressure drop Δp_{entr} (data from the pressure transducer p_2) versus apparent shear rate $\dot{\gamma}_{APP}$ for different barrel diameters for the apparent shear rate range defined in Table 18 for LDPE PG 7008 at 150 °C. Unfilled symbols represent the presence of melt rupture flow instability. Here D_{bsd} is barrel diameter of the Strain die, and D_b is standard barrel diameter.

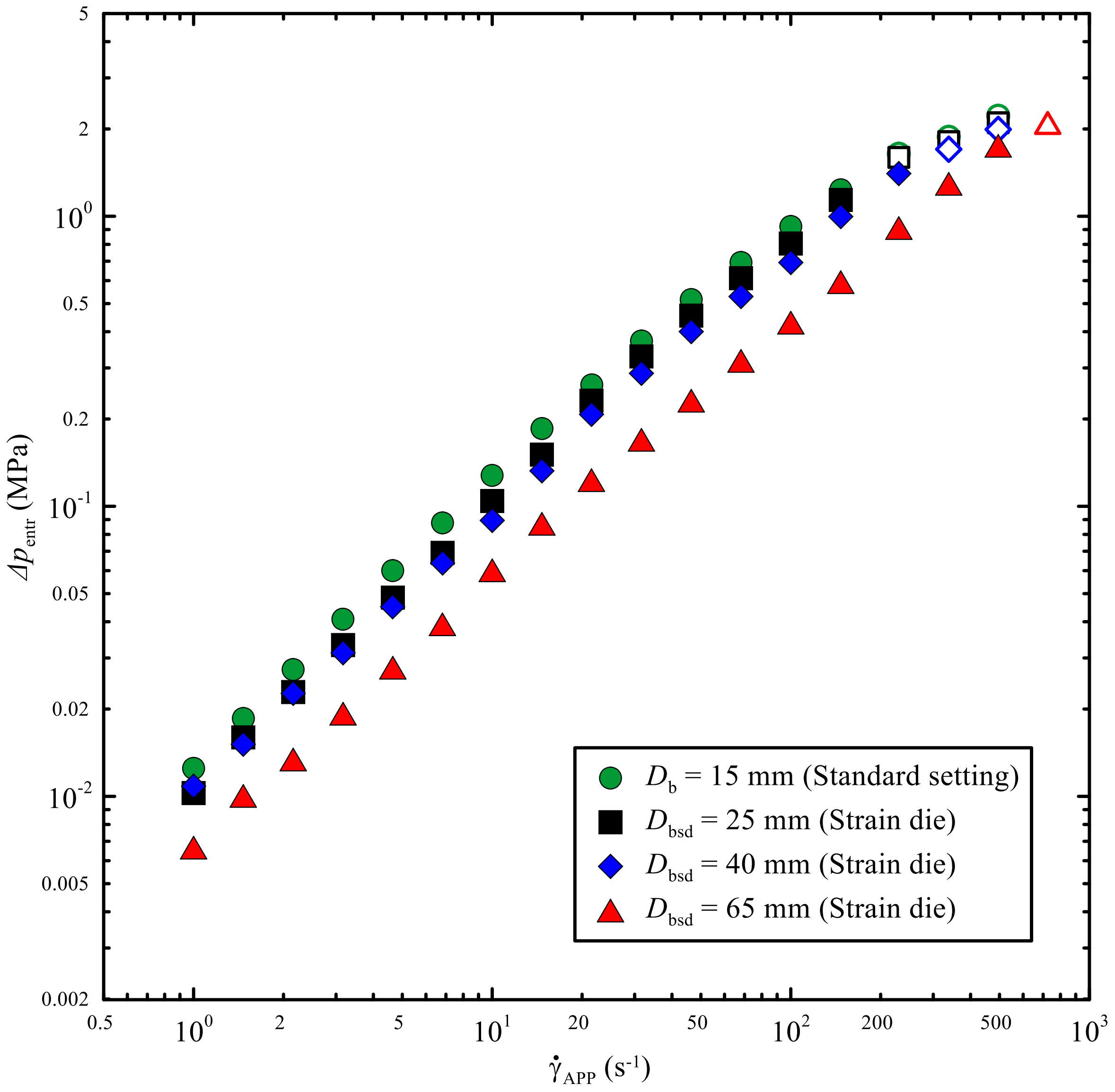

Figure 76 Entrance pressure drop Δp_{entr} (data from the pressure transducer p_3) versus apparent shear rate $\dot{\gamma}_{APP}$ for different barrel diameters for the apparent shear rate range defined in Table 18 for LDPE PG 7008 at 150 °C. Unfilled symbols represent the presence of melt rupture flow instability. Here D_{bsd} is barrel diameter of the Strain die, and D_b is standard barrel diameter.

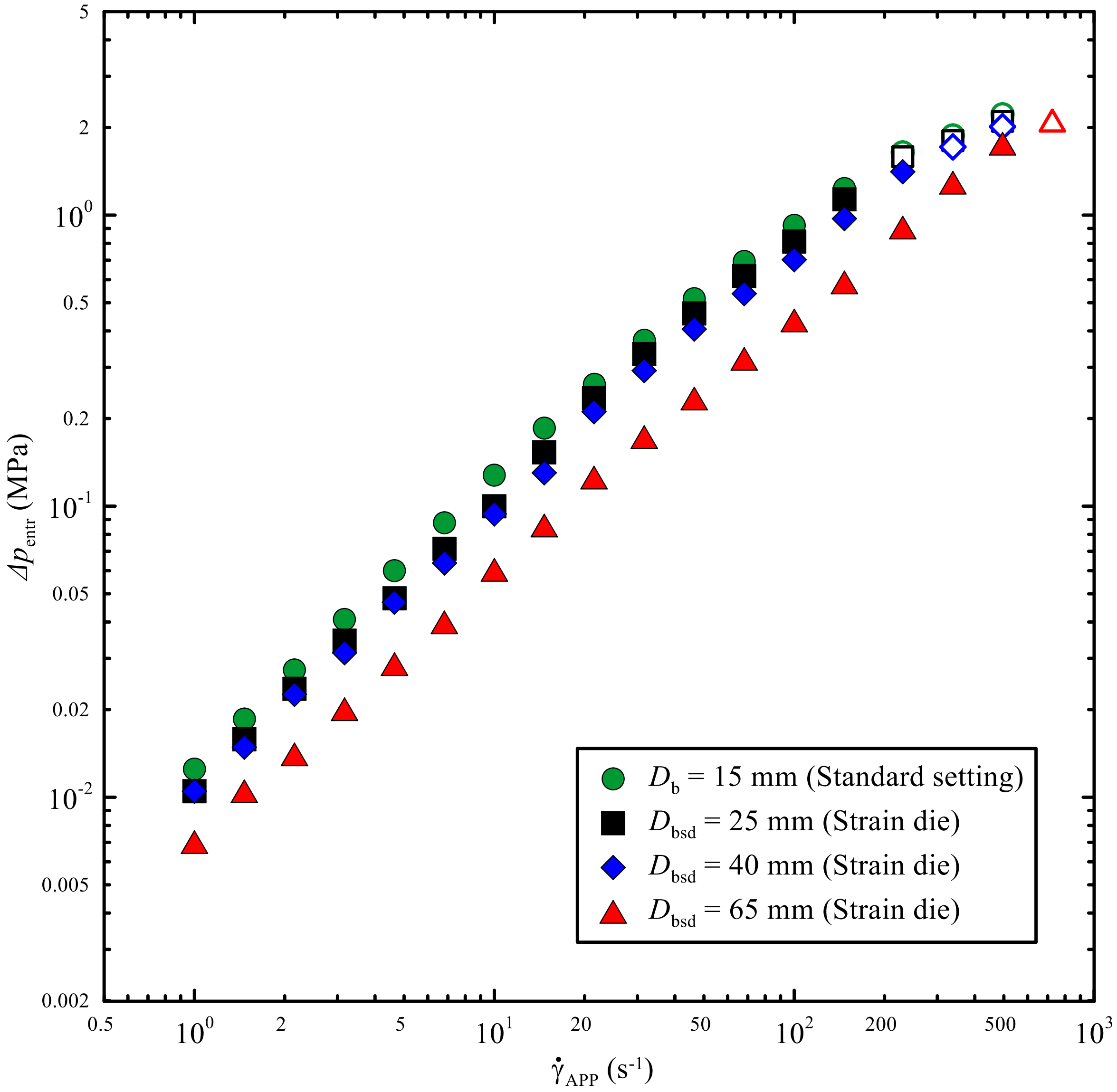

Figure 77 Entrance pressure drop Δp_{entr} (data from the pressure transducer p_4) versus apparent shear rate $\dot{\gamma}_{APP}$ for different barrel diameters for the apparent shear rate range defined in Table 18 for LDPE PG 7008 at 150 °C. Unfilled symbols represent the presence of melt rupture flow instability. Here D_{bsd} is barrel diameter of the Strain die, and D_b is standard barrel diameter.

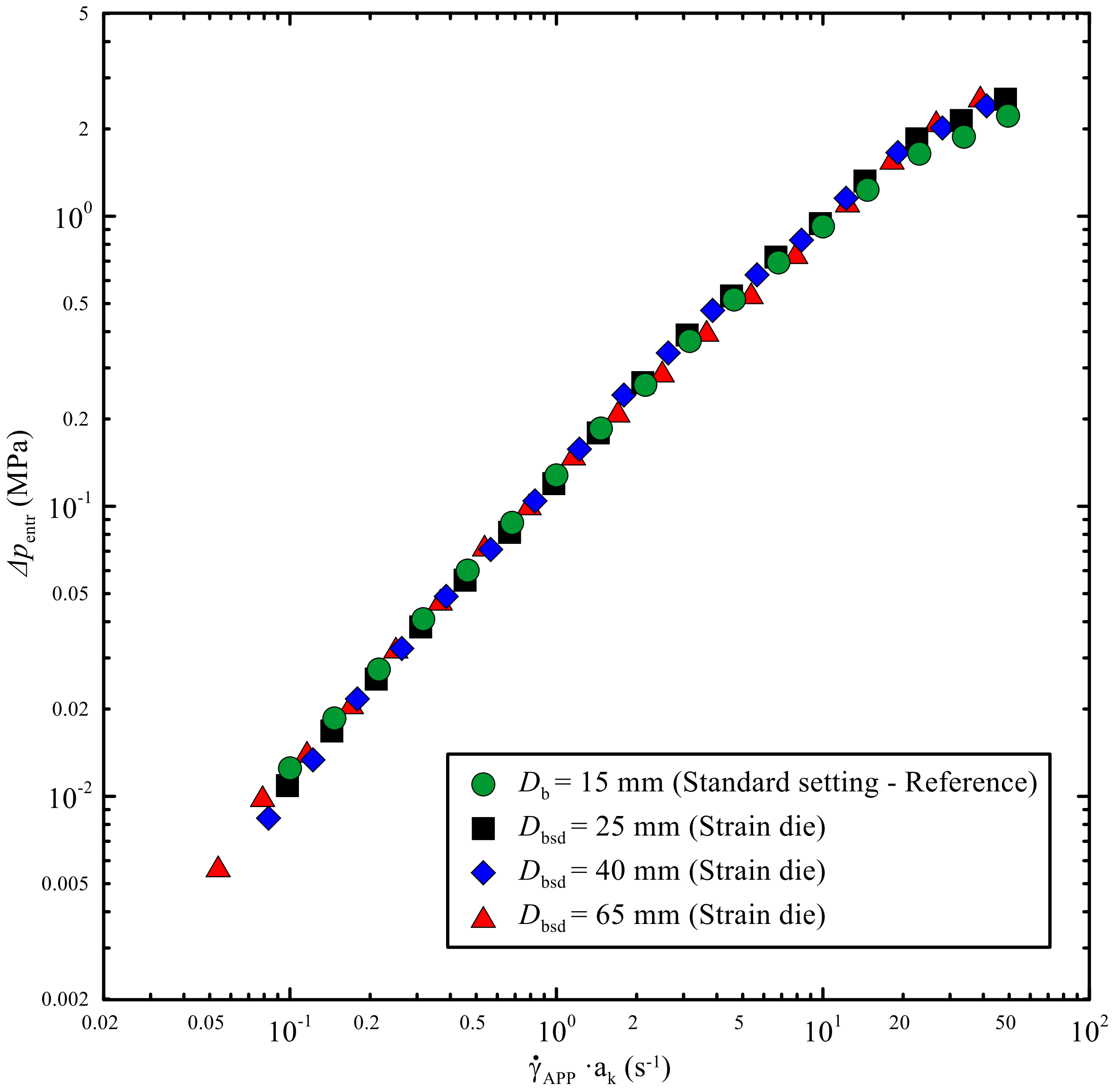

Figure 78 Master curve for p_1 (from LDPE PG 7008 data at 150 °C provided in Fig. 74) obtained using the horizontal shift factor a_k. The standard barrel diameter D_b= 15mm was chosen as a reference value. Here D_{bsd} is barrel diameter of the Strain die.

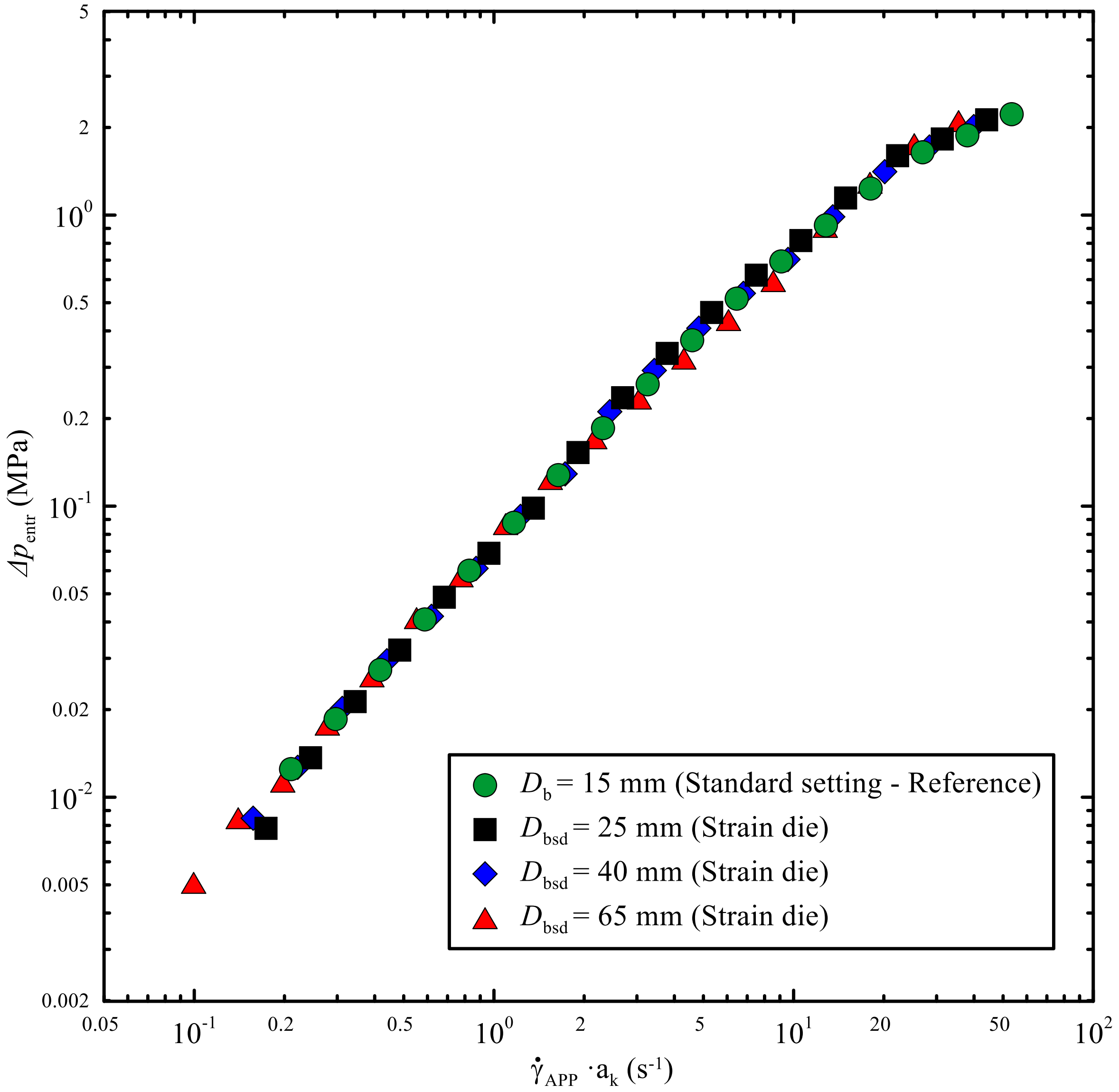

Figure 79 Master curve for p_2 (from LDPE PG 7008 data at 150 °C provided in Fig. 75) obtained using the horizontal shift factor a_k. The standard barrel diameter D_b= 15mm was chosen as a reference value. Here D_{bsd} is barrel diameter of the Strain die.

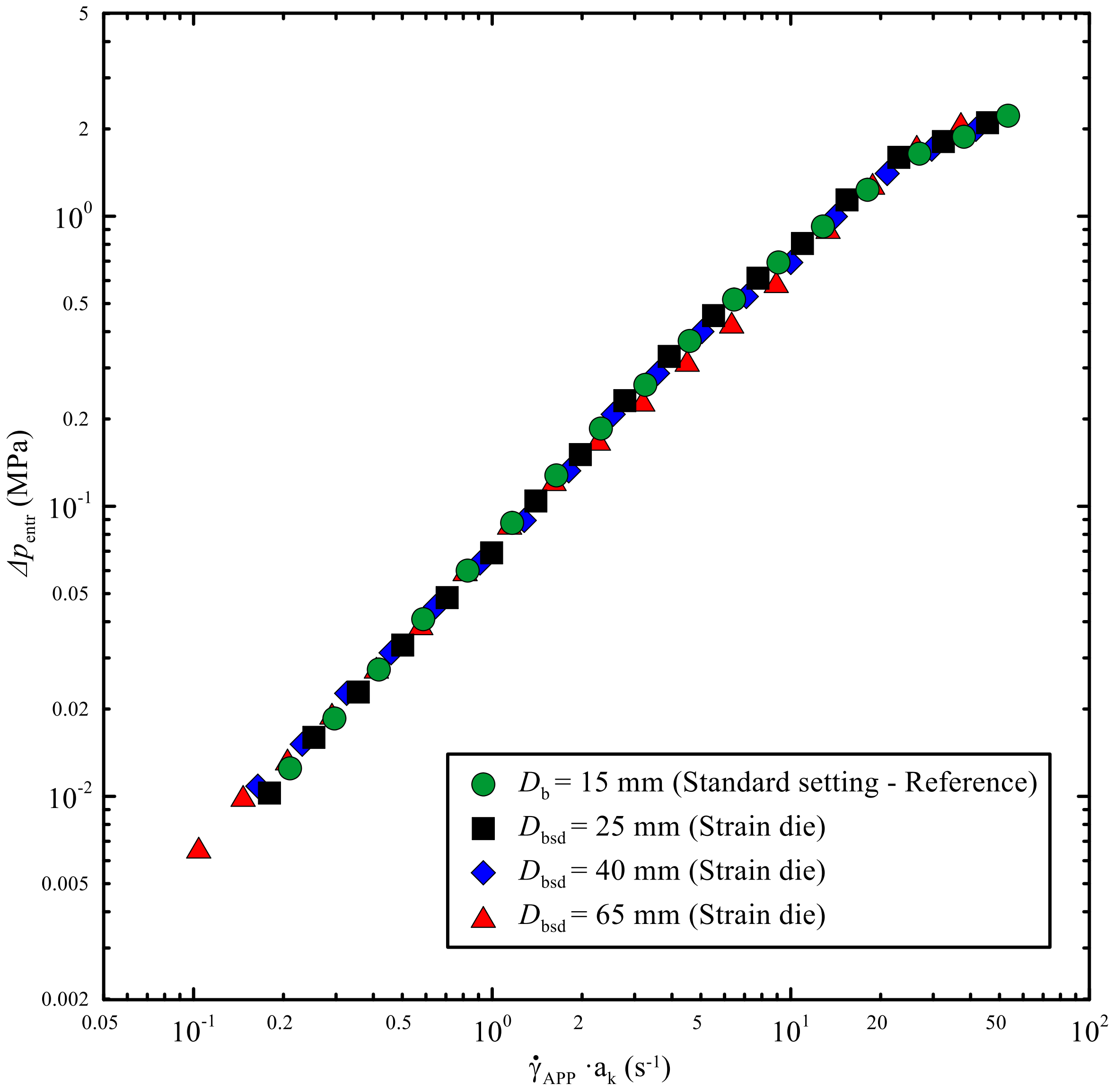

Figure 80 Master curve for p_3 (from LDPE PG 7008 data at 150 °C provided in Fig. 76) obtained using the horizontal shift factor a_k. The standard barrel diameter D_b= 15mm was chosen as a reference value. Here D_{bsd} is barrel diameter of the Strain die.

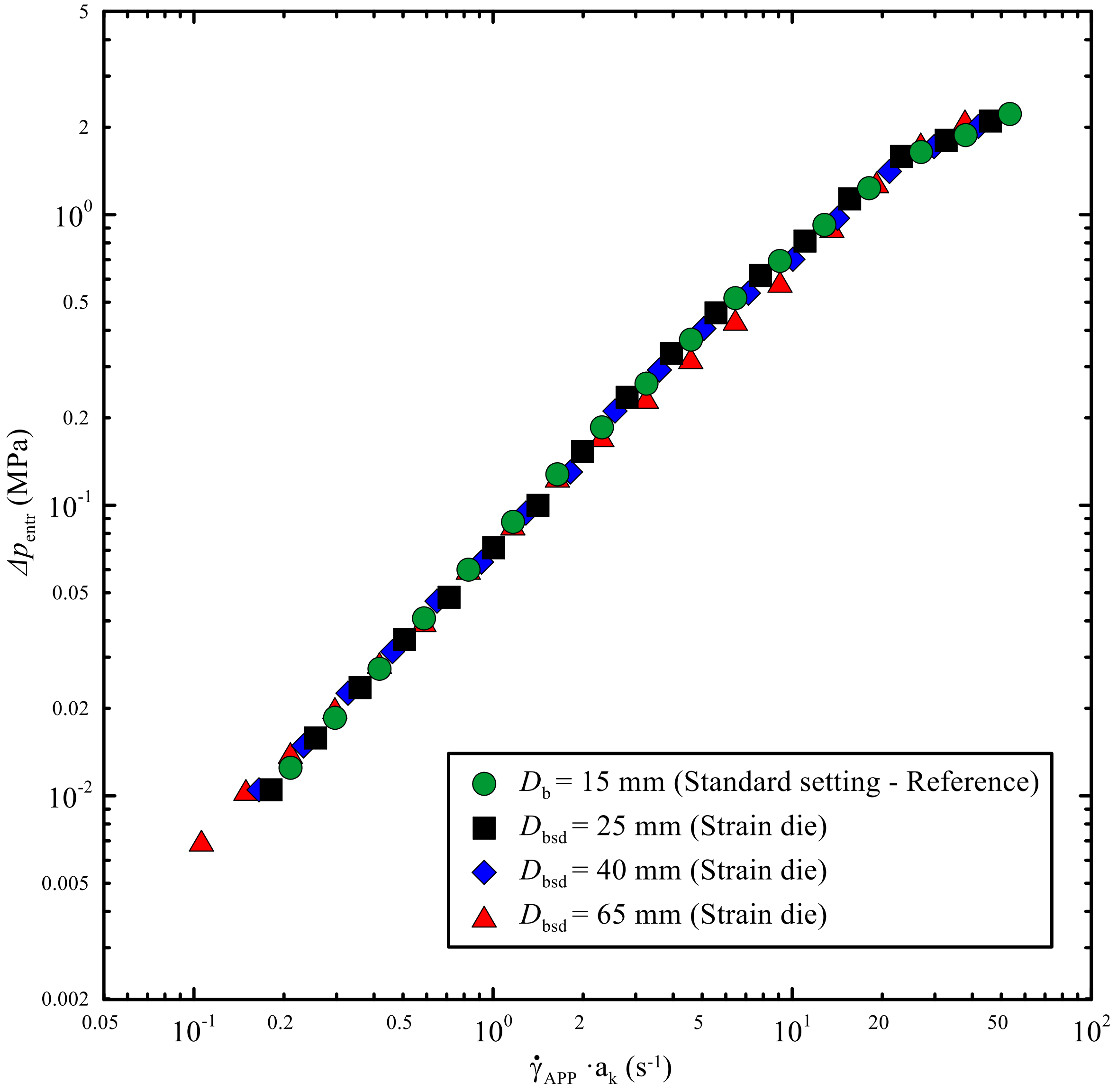

Figure 81 Master curve for p_4 (from LDPE PG 7008 data at 150 °C provided in Fig. 77) obtained using the horizontal shift factor a_k. The standard barrel diameter D_b= 15mm was chosen as a reference value. Here D_{bsd} is barrel diameter of the Strain die.

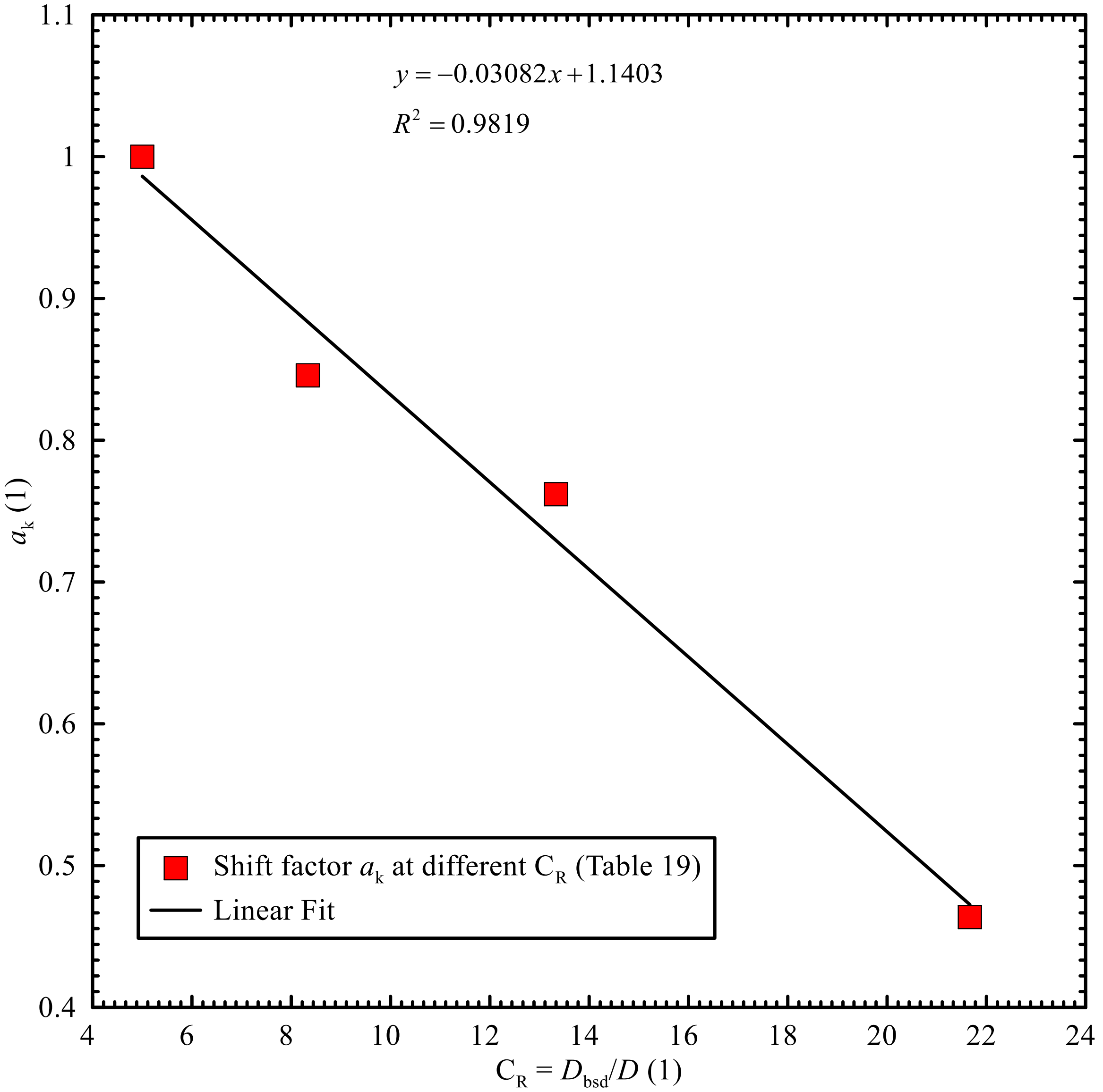

Figure 82 Shift factor a_k versus contraction ratio C_R for p_2 along with a linear fit for LDPE PG 7008 at 150 °C

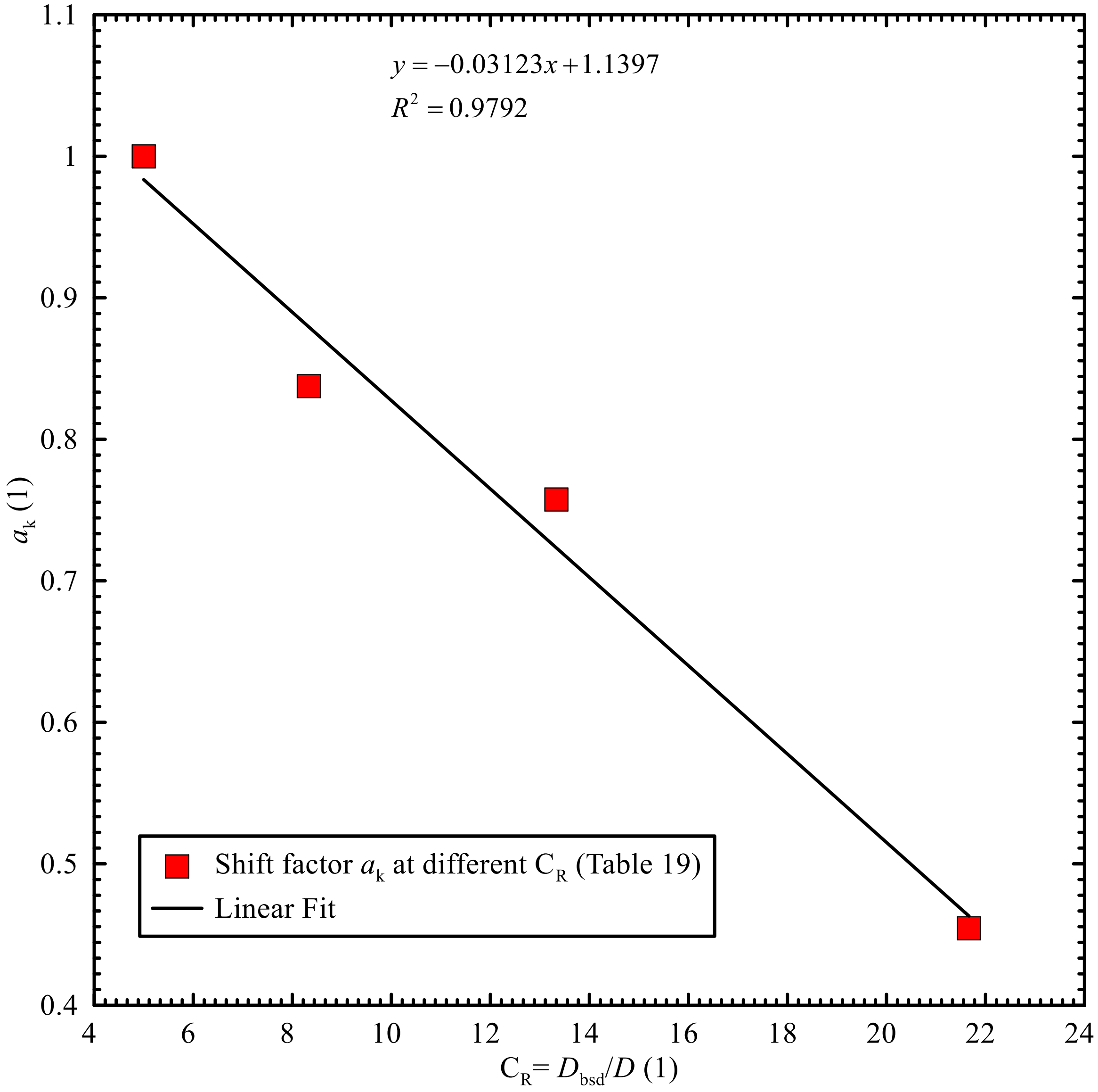

Figure 83 Shift factor a_k versus contraction ratio C_R for p_3 along with a linear fit for LDPE PG 7008 at 150 °C

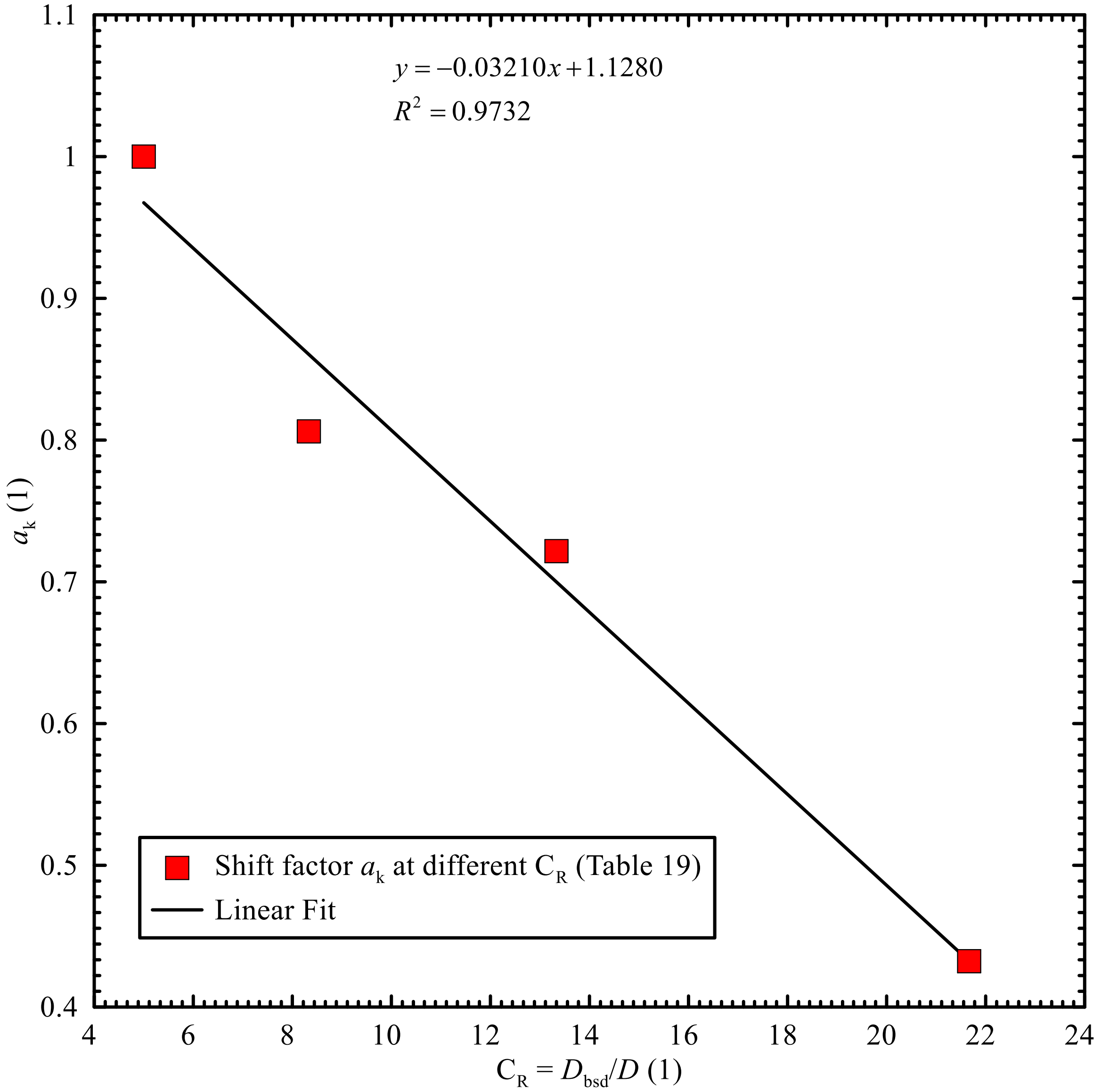

Figure 84 Shift factor a_k versus contraction ratio C_R for p_4 along with a linear fit for LDPE PG 7008 at 150 °C

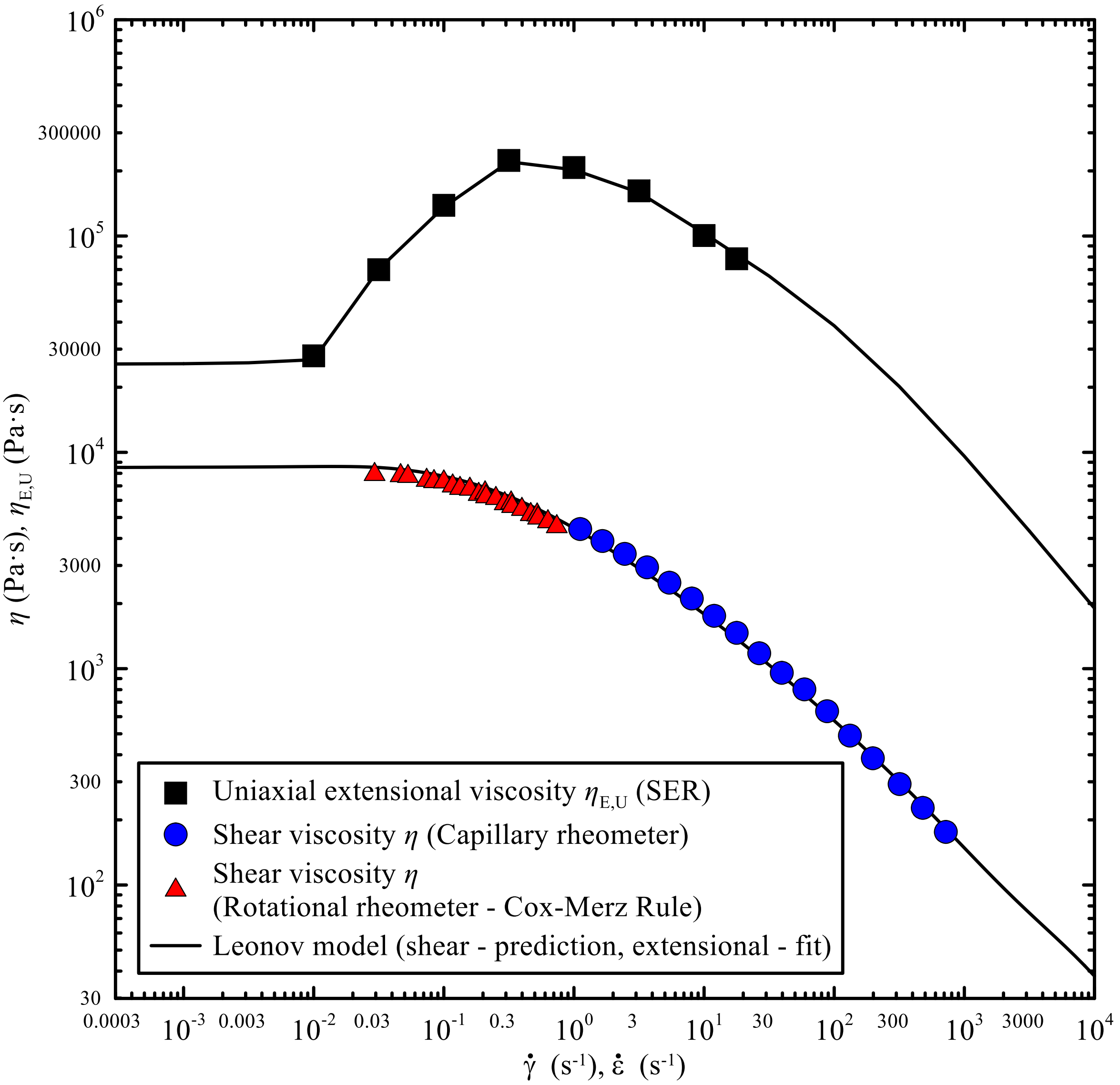

Figure 85 Shear η and uniaxial extensional viscosity $\eta_{E,U}$ versus shear $\dot{\gamma}$ and extensional strain rate $\dot{\varepsilon}$ measured on capillary and rotational rheometer for LDPE PG 7008 at 150 °C, with modified Leonov model fit and prediction. $\eta_{E,U}$ was taken from SER at Hencky strain $\varepsilon_H \approx 4$

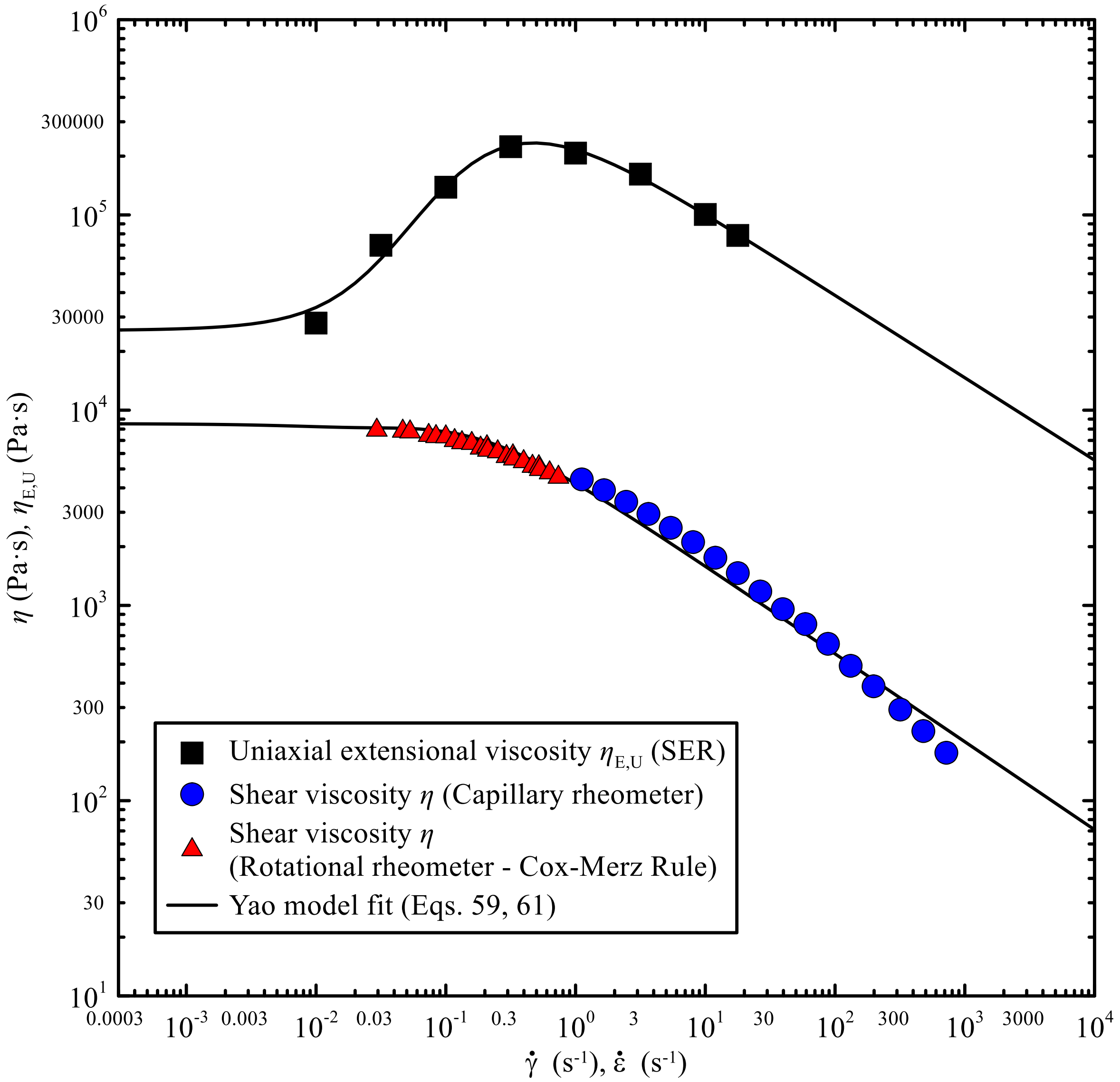

Figure 86 Shear η uniaxial extensional viscosity $\eta_{E,U}$ versus shear $\dot{\gamma}$ and extensional strain rate $\dot{\varepsilon}$ measured on capillary and rotational rheometer for LDPE PG 7008 at 150 °C, with Yao model fit $\eta_{E,U}$ was taken from SER at Hencky strain $\varepsilon_H \approx 4$

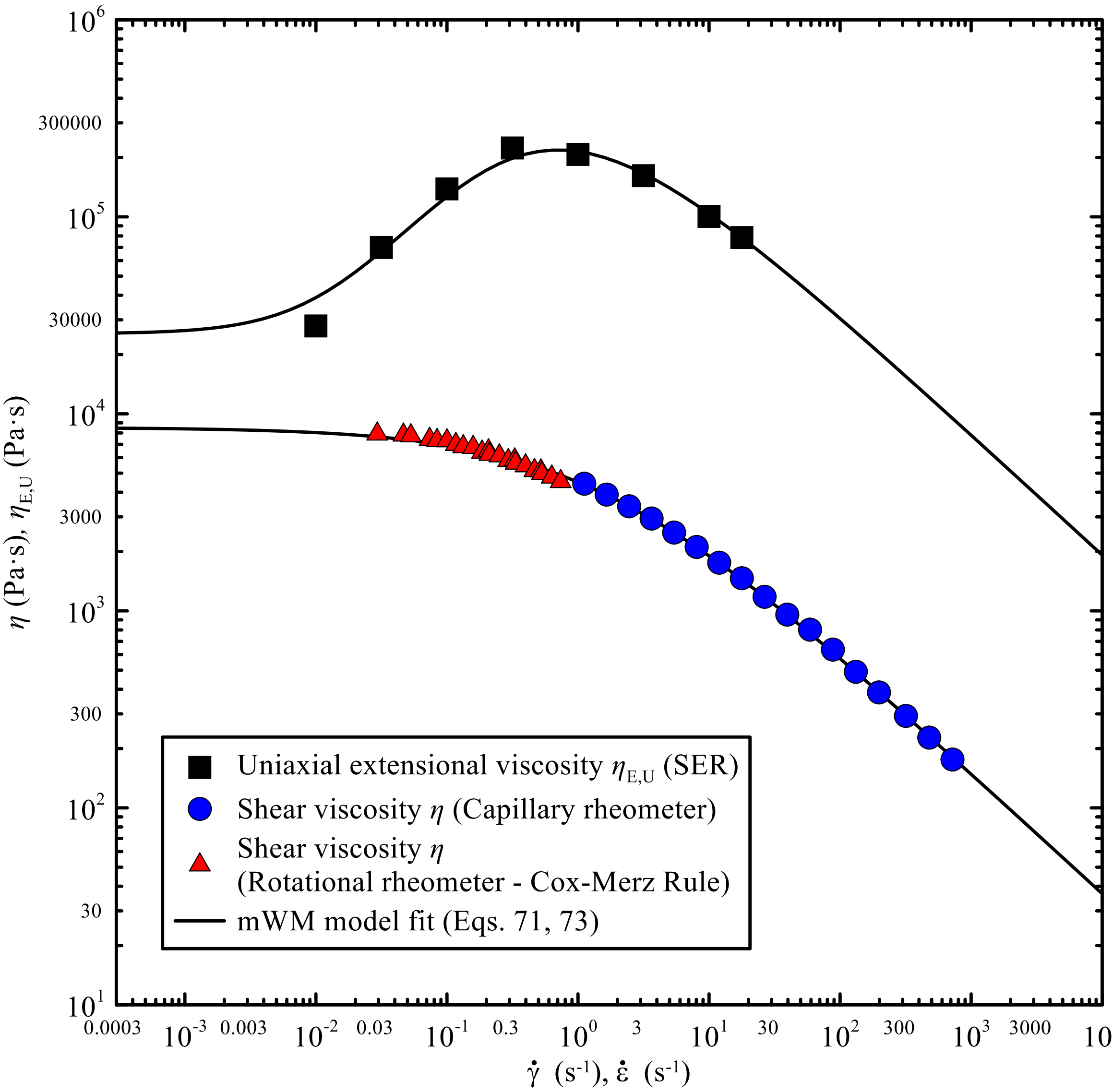

Figure 87 Shear η and uniaxial extensional viscosity $\eta_{E,U}$ versus shear $\dot{\gamma}$ and extensional strain rate $\dot{\varepsilon}$ measured on capillary and rotational rheometer for LDPE PG 7008 at 150 °C, with modified White-Metzner (mWM) model fit . $\eta_{E,U}$ was taken from SER at Hencky strain $\varepsilon_H \approx 4$

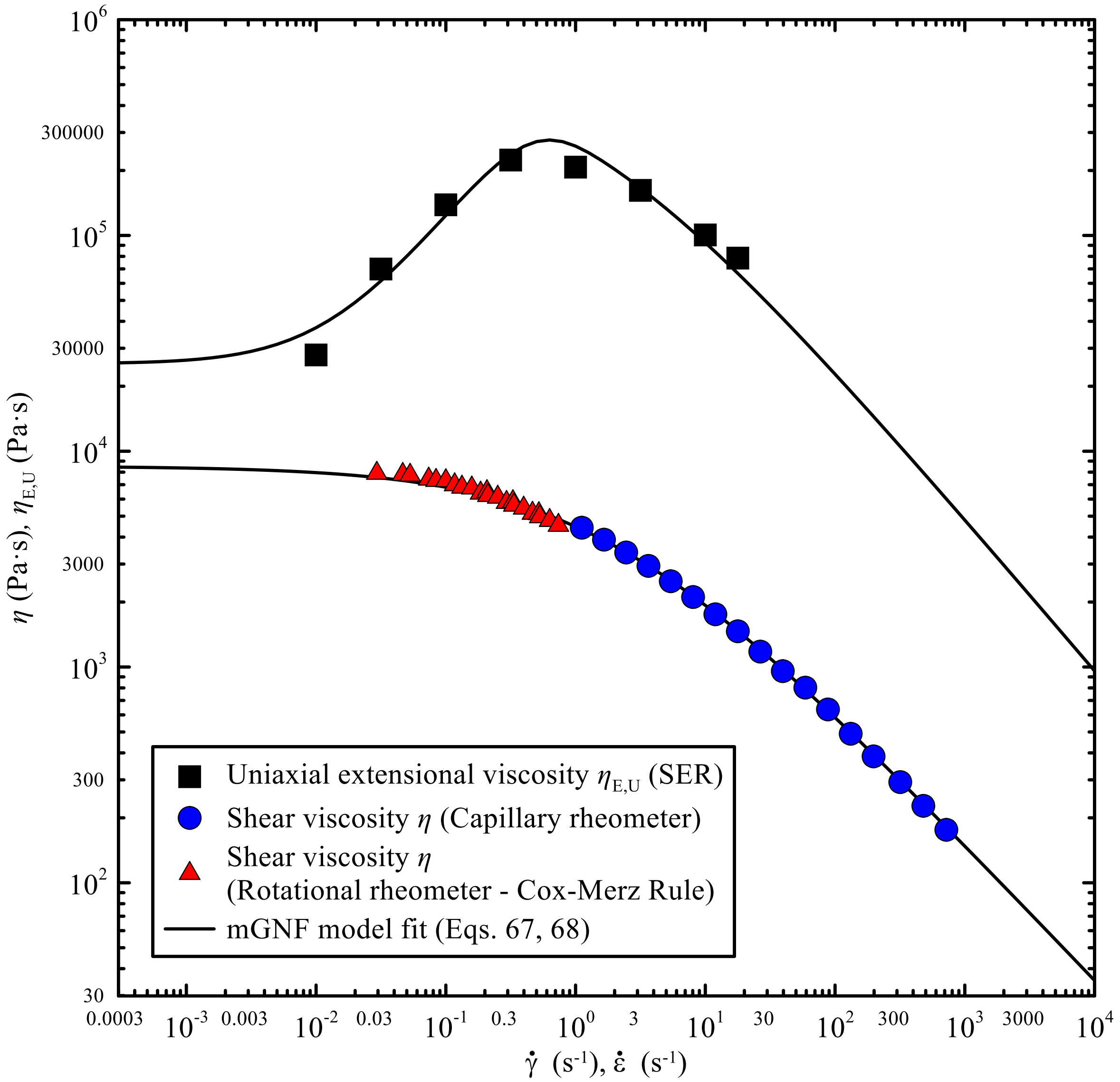

Figure 88 Shear η and uniaxial extensional viscosity $\eta_{E,U}$ versus shear $\dot{\gamma}$ and extensional strain rate $\dot{\varepsilon}$ measured on capillary and rotational rheometer for LDPE PG 7008 at 150 °C, with modified Generalized Newtonian Fluid (mGNF) model fit. $\eta_{E,U}$ was taken from SER at Hencky strain $\varepsilon_H \approx 4$

CONCLUSION

Systematic high-pressure capillary rheometer measurements were performed for branched LDPE melt at wide range of strain rates using a new multi-part capillary die with zero capillary length ("Strain die"), allowing to control the contraction ratio C_R while maintaining a constant capillary diameter. It was discovered that for the investigated polymer and flow condition used, the measured entrance pressure drop surprisingly decreases with the increasing C_R. This indicates that the magnitude of the current Hencky strain ε_{H} during abrupt contraction flow is less than its maximum attainable value. The reduction in strain magnitude during flow can be attributed to excessive corner vortices size, which actually reduces the flow geometry cross-section, or excessive residence time, which increases the level of wasted Hencky strain ε_{H}. From the measured data collected from all connected pressure transducers at different C_R values, a single Master curve could be created using a simple horizontal shift factor a_k. This indicates that the measured entrance pressure data could be corrected using the a_k, which would make the determination of extensional viscosity more accurate.

Various methods were evaluated for the determination of uniaxial extensional viscosity for linear and branched polyolefin melts from entrance pressure drop measurements. For a linear PP melt, the uniaxial extensional viscosity obtained using the Gibson analysis was found to show good agreement with experimental data from the Münstedt Extensional Rheometer, while the original Cogswell analysis gave overestimated results. Interestingly, the modified version of Cogswell's analysis proposed by Padmanabhan gave good results, comparable to Gibson's analysis. For branched LDPE, Cogswell's analyses showed much better agreement with the experimental data obtained from Sentmanat Elongation Rheometer (SER) than Gibson's analysis that underestimated dependencies the SER data. It was found that the maximum attainable Hencky strain $\varepsilon_{\mathrm{H,max}}$ can only be reached at high extensional strain rates, but at low strain rates (i.e. in the strain hardening region), it seems that the actual values of the Hencky strain ε_{H} are lower than $\varepsilon_{\mathrm{H,max}}$. This conclusion is based on a direct comparison of the extensional viscosities obtained from the Cogswell analysis and the Sentmanat Elongation Rheometer (SER) at the same extensional strain rate and the assumption that the Cogswell analysis is valid.

From the Sentmanat Extensional Rheometer (SER) and Extensional Viscosity Fixture (EVF) measurements, it was found that the SER provides a less smoother stress-over-time record than the EVF due to the presence of friction in its motion mechanism. On the other hand, it seems to provide more reliable data at very low strain rates.

Four different advanced constitutive equations (namely modified Leonov model, Yao model, modified White-Metzner model, and modified Generalized Newtonian model) were selected and tested to understand their ability to describe the shear viscosity and the non-monotonic character of the uniaxial extensional viscosity. It was shown that all four models have very high ability to describe the relevant experimental with sufficient accuracy, which supports the validity of the measured data and the physical background of the models used.

BIBLIOGRAPHY

[1] HATZIKIRIAKOS, Savvas Georgios and MIGLER, Kalman. *Polymer processing instabilities: control and understanding*. Second ed. Boca Ranton: CRC Press, 2020. ISBN 978-0-367-57818-3.

[2] AGASSANT, Jean-François; AVENAS, Pierre; CARREAU, Pierre; VERGNES, Bruno and VINCENT, Michel. *Polymer processing: principles and Modeling*. Second ed. Munich: Carl Hanser Verlag, 2017. ISBN 978-1569906057.

[3] WILCZYŃSKI, Krzysztof. *Rheology in polymer processing: modeling and Simulation*. Munich: Hanser Publishers, 2021. ISBN 978-1-56990-660-6.

[4] DUŠEK, Karel and JOANNY, Jean-François. *Polymer characterization: Rheology, Laser Interferometry, Electrooptics*. Berlin: Springer Berlin, 2010. ISBN 978-3-642-13531-6.

[5] ZATLOUKAL, Martin; KOPYTKO, Walter; LENGÁLOVÁ, Anežka and VLČEK, Jiří. *Theoretical and experimental analysis of interfacial instabilities in coextrusion flows*. Online. Journal of Applied Polymer Science. Vol. 98 (2005), no. 1, p. 153-162. ISSN 0021-8995. Available from: https://doi.org/10.1002/app.22030. [Accessed 15 September 2023].

[6] MEWIS, Jan and WAGNER, Norman J. *Colloidal suspension rheology*. Online. Cambridge: Cambridge University Press, 2012. ISBN 978-0-521-51599-3.

[7] STANCIU, Ioana. *Rheology of polymer solutions*. LAP LAMBERT Academic Publishing, 2017. ISBN 9783330035270.

[8] DERKACH, Svetlana. *Rheology of emulsions*. Online. Advances in Colloid and Interface Science. Vol. 151 (2009), no. 1-2, p. 1-23. ISSN 0001-8686. Available from: https://doi.org/10.1016/j.cis.2009.07.001. [Accessed 12 August 2023].

[9] AHMED, Jasim; PTASZEK, Pawel and BASU, Santanu. *Advances in food rheology and its applications*. Second ed. Kidlington: Elsevier, 2016. ISBN 978-0-12-823983-4.

[10] OSTERHOLD, Michael. *Physical Characterization of Coatings: Introduction to Rheology and Surface Analysis*. Berlin: Logos Verlag, 2020. ISBN 978-3832550493.

[11] LABA, Dennis. *Rheological Properties of Cosmetics and Toiletries*. New York: Routledge, 1993. ISBN 0824790901.

[12] IRGENS, Fridtjov. *Rheology and non-Newtonian fluids*. Cham: Springer Switzerland, 2014. ISBN 978-3-319-01052-6.

[13] MITSOULIS, Evan and HATZIKIRIAKOS, Savvas G. Rheological Properties Related to Extrusion of Polyolefins. Online. Polymers. Vol. 13 (2021), no. 4, p. 489 ISSN 2073-4360. Available from: https://doi.org/10.3390/polym13040489. [Accessed 10 January 2024].

[14] WEN, Yu-Ho; WANG, Chen-Chieh; CYUE, Guo-Sian; KUO, Rong-Hao; HSU, Chia-Hsiang et al. *Extensional rheology of linear and branched polymer melts in fast converging flows*. Online. Rheologica Acta. Vol. 62 (2023), no. 4, p. 183-204. ISSN 0035-4511. Available from: https://doi.org/10.1007/s00397-023-01387-y. [Accessed 22 October 2023].

[15] TSENG, Huan-Chang. *Numerical visualization of extensional flows in injection molding of polymer melts*. Online. International Polymer Processing. Vol. 38 (2023), no. 2, p. 175-182. ISSN 0930-777X. Available from: https://doi.org/10.1515/ipp-2022-4316. [Accessed 14 September 2023].

[16] MACOSKO, Christopher W. *Rheology: Principles, Measurements and Applications*. New York: John Wiley, 1993. ISBN 978-0-471-18575-8.

[17] MÜNSTEDT, Helmut and SCHWARZL, Friedrich R. *Deformation and Flow of Polymeric Materials*. Berlin: Springer Berlin Heidelberg, 2014. ISBN 978-3-642-55408-7.

[18] MORRISON, Fiath A. *Understanding rheology*. New York: Oxford University Press, 2001. ISBN 978-0-19-514166-5.

[19] MALKIN, Aleksandr J. and ISAYEV, Avraam I. *Rheology: Concept, Methods, and Applications*. fourth ed. Toronto: ChemTec Publishing, 2022. ISBN 978-1-927885-93-2.

[20] HRISTOV, Velichko and VLACHOPOULOS, John. *A Study of Entrance Pressure Loss in Filled Polymer Melts*. Online. Applied Rheology. Vol. 17 (2007), 57191. ISSN 1617-8106. Available from: https://doi.org/10.1515/arh-2007-0019. [Accessed 10 December 2023].

[21] DRABEK, Jiri; ZATLOUKAL, Martin and MARTYN, Mike. *Effect of molecular weight on secondary Newtonian plateau at high shear rates for linear isotactic melt blown polypropylenes*. Online. Journal of Non-Newtonian Fluid Mechanics. Vol. 251 (2018), no. 1, p. 107-118. ISSN 0377-0257. Available from: https://doi.org/10.1016/j.jnnfm.2017.11.009. [Accessed 3 November 2023].

[22] TORDELLA, John P. *Capillary Flow of Molten Polyethylene: A Photographic Study of Melt Fracture*. Online. Transactions of the Society of Rheology. Vol. 1 (1957), no. 1, p. 203-212. ISSN 0038-0032. Available from: https://doi.org/10.1122/1.548816. [Accessed 14 September 2023].

[23] MUSIL, Jan and ZATLOUKAL, Martin. *Historical Review of Secondary Entry Flows in Polymer Melt Extrusion*. Online. Polymer Reviews. Vol. 59 (2019), no. 2, p. 338-390. ISSN 1558-3724. Available from: https://doi.org/10.1080/15583724.2018.1481428. [Accessed 15 September 2023].

[24] COGSWELL, Frederic N. *Converging flow of polymer melts in extrusion dies*. Online. Polymer Engineering and Science. Vol. 12 (1972), no. 1, p. 64-73. ISSN 0032-3888. Available from: https://doi.org/10.1002/pen.760120111. [Accessed 12 January 2024].

[25] BINDING, David M. *An approximate analysis for contraction and converging flows*. Online. Journal of Non-Newtonian Fluid Mechanics. Vol. 27 (1988), no. 2, p. 173-189. ISSN 0377-0257. Available from: https://doi.org/10.1016/0377-0257(88)85012-2. [Accessed 12 January 2024].

[26] GIBSON, Arthur G. *Die entry flow of reinforced polymers*. Online. Composites. Vol. 20 (1989), no. 1, p. 57-64. ISSN 0010-4361. Available from: https://doi.org/10.1016/0010-4361(89)90683-6. [Accessed 12 January 2024].

[27] KIM, Seungoh and DEALY, John M. *Design of an orifice die to measure entrance pressure drop*. Online. Journal of Rheology. Vol. 45 (2001), no. 6, p. 1413-1419. ISSN 0148-6055. Available from: https://doi.org/10.1122/1.1410374. [Accessed 10 January 2024].

[28] KIM, Seungoh and DEALY, John M. *Gross melt fracture of polyethylene. I: A criterion based on tensile stress*. Online. Polymer Engineering & Science. Vol. 42 (2002), no. 3, p. 482-494. ISSN 0032-3888. Available from: https://doi.org/10.1002/pen.10965. [Accessed 10 January 2024].

[29] ZATLOUKAL, Martin and MUSIL, Jan. *Analysis of entrance pressure drop techniques for extensional viscosity determination*. Online. Polymer Testing. Vol. 28 (2009), no. 8, p. 843-853. ISSN 0142-9418. Available from: https://doi.org/10.1016/j.polymertesting.2009.07.007. [Accessed 15 January 2024].

[30] RAJAGOPALAN, Dilip. *Computational analysis of techniques to determine extensional viscosity from entrance flows*. Online. Rheologica Acta. Vol. 39 (2000), no. 2, p. 138-151. ISSN 0035-4511. Available from: https://doi.org/10.1007/s003970050014. [Accessed 14 January 2024].

[31] BINGHAM, Eugene C. *The History of the Society of Rheology*. Online. The Society of Rheology. 1944. Available from: https://www.rheology.org/sor/History/Bingham-History_of_SoR_1924-1944.pdf. [Accessed 15 September 2023].

[32] VLACHOPOULOS, John. *Fundamentals of Fluid Mechanics*. Online. Revised internet ed. Dundas: POLYDYNAMICS, 2016. ISBN 978-0-9952407-0-4. Available from: https://www.researchgate.net/publication/315695099_Fundamentals_of_Fluid_Mechanics. [Accessed 14 October 2023].

[33] BINGHAM, Eugene C. *Rheology. I: The nature of fluid flow*. Online. Journal of Chemical Education. Vol. 6 (1929), no. 6, p. 1113-1119. ISSN 0021-9584. Available from: https://doi.org/10.1021/ed006p1113. [Accessed 15 September 2023].

[34] REINER, Marcus. *The Deborah Number*. Online. Physics Today. Vol. 17 (1964), no. 1, p. 62. ISSN 0031-9228. Available from: https://doi.org/10.1063/1.3051374. [Accessed 21 September 2023].

[35] TANNER, Roger I. *Engineering Rheology*. Second ed. New York: Oxford University Press, 2002. ISBN 0-19-856473-2.

[36] BINGHAM, Eugene C. *The New Science of Rheology*. Online. Review of Scientific Instruments. Vol. 4 (1933), no. 9, p. 473-476. ISSN 0034-6748. Available from: https://doi.org/10.1063/1.1749180. [Accessed 15 September 2023].

[37] WANG, Shi-Qing. *Nonlinear Polymer Rheology*. Online. Wiley, 2017. ISBN 9780470946985.

[38] DEALY, John M. and WANG, Jian. *Melt Rheology and its Applications in the Plastics Industry*. Second ed. Engineering Materials and Processes. Dordrecht: Springer Netherlands, 2013. ISBN 978-94-007-6394-4.

[39] LAI, Michael W.; RUBIN, David and KREMPL, Erhard. *Introduction to continuum mechanics*. Fourth ed. Boston: Butterworth-Heinemann (Elsevier), 2010. ISBN 978-0-7506-8560-3.

[40] TADMOR, Zehev and GOGOS, Costas G. *Principles of polymer processing*. Second ed. Hoboken: Wiley, 2006. ISBN 978-0-471-38770-1.

[41] BIRD, Byron R.; AMRSTRONG, Robert C. and HASSAGER, Ole. *Dynamics of Polymeric Liquids, Volume 1: Fluid Mechanics*. Second ed. Wiley, 1987. ISBN 978-0-471-80245-7.

[42] GUPTA, B. R. *Rheology Applied in Polymer Processing*. London: CRC Press, 2022. ISBN 9781003344971.

[43] Musil, Jan. *Development of Improved Entrance Pressure Drop Technique for Extensional Viscosity Determination* Online, Master Thesis, Supervisor prof. Ing. Martin Zatloukal, Ph.D. Zlín: Tomas Bata University in Zlín, Department of Technology, 2008. Available from: http://hdl.handle.net/10563/7466. [Accessed 10 November 2023].

[44] ZATLOUKAL, Martin. *Viscoelastic Constitutive Equations in Modeling of Polymer Processing*. Doctoral Thesis, Supervisor: prof. Ing. Petr Sáha, CSc. Zlín: Brno University of Technology, Faculty of Technology, 2000.

[45] BAIRD, Donald G. and COLLIAS, Dimitris I. *Polymer processing*. Second ed. Hoboken, New Jersey: Wiley, 2014. ISBN 978-0-470-93058-8.

[46] DEALY, John M.; READ, Daniel J. and LARSON, Ronald G. *Structure and Rheology of Molten Polymers*. Second ed. Munich: Carl Hanser Verlag, 2018. ISBN 978-1-56990-611-8.

[47] OSSWALD Tim and RUDOLPH, Natalie. *Polymer Rheology: Fundamentals and Applications*. Munich: Carl Hanser Verlag, 2015. ISBN 978-1-5231-0129-0.

[48] POOLE, Robert J. *The Deborah and Weissenberg numbers*. Online. Rheology Bulletin. Vol. 53 (2012), no. 2, p. 32-39. Available from: https://pcwww.liv.ac.uk/~robpoole/PAPERS/POOLE_45.pdf. [Accessed 21 November 2023].

[49] DENN, Morton M. *Just what did Deborah say?* Online. Rheology Bulletin. Vol. 80 (2011), no. 1, p. 12,15 ISSN 0035-4538. Available from: https://www.rheology.org/sor/publications/RheoBulletin/RB2011Jan.pdf. [Accessed 20 September 2023].

[50] VLACHOPOULOS, John and POLYCHRONOPOULOS, Nickolas D. *Understanding Rheology and Technology of Polymer Extrusion*. Online. Dundas: POLYDYNAMICS, 2019. ISBN 978-0-9952407-3-5. Available from: https://www.researchgate.net/publication/336141022_Understanding_Rheology_and_Technology_of_Polymer_Extrusion_First_Edition. [Accessed 14 October 2023].

[51] DEALY, John M. *Weissenberg and Deborah Numbers: Their Definition and Use*. Online. Rheology Bulletin. Vol. 79 (2010), no. 2, p 14-18. ISSN 0035-4538. Available from: https://www.rheology.org/sor/Publications/RheoBulletin/RB2010Jul.pdf. [Accessed 10 October 2023].

[52] FERRÁS, Luís L.; FORD, Neville J.; MORGADO, Maria L.; REBELO, Magda; MCKINLEY, Gareth H. et al. *Theoretical and numerical analysis of unsteady fractional viscoelastic flows in simple geometries.* Online. Computers & Fluids. Vol. 174 (2018), no 1, p. 14-33. ISSN 0045-7930. Available from: https://doi.org/10.1016/j.compfluid.2018.07.004. [Accessed 23 November 2023].

[53] AHO, Johanna. *Rheological characterization of polymer melts in shear and extension: measurement reliability and data for practical processing*. Online, Doctoral Thesis, Supervisor: Prof. Dr. Ing. Manfred H. Wagner. Tampere: Tampere University of Technology, Department of Material Science, 2011. Available from: https://urn.fi/URN:NBN:fi:tty-2011050914663. [Accessed 10 November 2023].

[54] COSTANZO, Salvatore; IANNIRUBERTO, Giovanni; MARRUCCI, Giuseppe and VLASSOPOULOS, Dimitris. *Measuring and assessing first and second normal stress differences of polymeric fluids with a modular cone-partitioned plate geometry*. Online. Rheologica Acta. Vol. 57 (2018), no. 5, p 363-376. ISSN 0035-4511. Available from: https://doi.org/10.1007/s00397-018-1080-1. [Accessed 12 November 2023].

[55] NARIMISSA, Esmaeil; SCHWEIZER, Thomas and WAGNER, Manfred H. *A constitutive analysis of nonlinear shear flow*. Online. Rheologica Acta. Vol. 59 (2020), no. 7, p. 487-506. ISSN 0035-4511. Available from: https://doi.org/10.1007/s00397-020-01215-7. [Accessed 1 November 2023].

[56] DRABEK, Jiri and ZATLOUKAL, Martin. *Melt blown technology for production of polymeric microfibers/nanofibers: A review.* Online. Physics of Fluids. Vol. 31 (2019), no. 9, p. 091301. ISSN 1070-6631. Available from: https://doi.org/10.1063/1.5116336. [Accessed 2 November 2023].

[57] HODDER, Peter and FRANCK, Aly. *A New Tool for Measuring Extensional Viscosity*. Online. Annual Transactions of the Nordic Rheology Society. Vol. 13 (2005). Available from: https://nrs.blob.core.windows.net/pdfs/nrspdf-7580dd55-a975-4ee3-b9e4-a03089373a39.pdf. [Accessed 29 November 2023].

[58] MEISSNER, Joachim.; RAIBLE, Tilmann and STEPHENSON, Stuart E. *Rotary Clamp in Uniaxial and Biaxial Extensional Rheometry of Polymer Melts*. Online. Journal of Rheology. Vol. 25 (1981), no. 1, p. 1-28. ISSN 0148-6055. Available from: https://doi.org/10.1122/1.549612. [Accessed 6 January 2024].

[59] DRABEK, Jiri and ZATLOUKAL, Martin. *Measurement and modeling of uniaxial and planar extensional viscosities for linear isotactic polypropylenes*. Online. Physics of Fluids. Vol. 35 (2023), no. 1, p. 013105. ISSN 1070-6631. Available from: https://doi.org/10.1063/5.0138220. [Accessed 2024-02-08].

[60] AHO, Johanna; BOETKER, Johan P.; BALDURSDOTTIR, Stefania and RANTANEN, Jukka. *Rheology as a tool for evaluation of melt processability of innovative dosage forms*. Online. International Journal of Pharmaceutics. Vol. 494 (2015), no. 2, p. 623-642. ISSN 0378-5173. Available from: https://doi.org/10.1016/j.ijpharm.2015.02.009. [Accessed 12 November 2023].

[61] CARREAU, Pierre J.; DE KEE, Daniel C. R and CHHABRA, Raj P. *Rheology of Polymeric Systems: Principles and Applications*. Second ed. Munich: Carl Hanser Verlag, 2021. ISBN 978-1-56990-722-1.

[62] PETRIE, Christopher J.S. *Extensional viscosity: A critical discussion.* Online. Journal of Non-Newtonian Fluid Mechanics. Vol. 137 (2006), no. 1-3, p. 15-23. ISSN 03770257. Available from: https://doi.org/10.1016/j.jnnfm.2006.01.011. [Accessed 21 November 2023].

[63] MÜNSTEDT, Helmut. *Extensional Rheology and Processing of Polymeric Materials*. Online. International Polymer Processing. Vol. 33 (2018), no. 5, p. 594-618. ISSN 2195-8602. Available from: https://doi.org/10.3139/217.3532. [Accessed 6 January 2024].

[64] BARBORIK, Tomas and ZATLOUKAL, Martin. *Steady-state modeling of extrusion cast film process, neck-in phenomenon, and related experimental research: A review*. Online. Physics of Fluids. Vol. 32 (2020), no. 6, p. 061302. ISSN 1070-6631. Available from: https://doi.org/10.1063/5.0004589. [Accessed 10 January 2024].

[65] ZATLOUKAL, Martin. *Behavior of Constitutive Equations for Polymer Melts in Different Flow Situations*. Master Thesis, Supervisor: doc. Ing. Jiří Vlček, CSc. Zlín: Brno University of Technology, Faculty of Technology, 1997.

[66] MÜNSTEDT, Helmut. *Various features of melt strain hardening of polymeric materials in uniaxial extension and their relation to molecular structure: review of experimental results and their interpretation*. Online. Rheologica Acta. Vol. 62 (2023), no. 7-8, p. 333-363. ISSN 0035-4511. Available from: https://doi.org/10.1007/s00397-023-01400-4. [Accessed 5 November 2023].

[67] MÜNSTEDT, Helmut and STARÝ, Zdeněk. *Steady states in extensional flow of strain hardening polymer melts and the uncertainties of their determination*. Online. Journal of Rheology. Vol. 57 (2013), no. 4, p. 1065-1077. ISSN 0148-6055. Available from: https://doi.org/10.1122/1.4803932. [Accessed 5 November 2023].

[68] IANNIRUBERTO, Giovanni; MARRUCCI, Giuseppe and MASUBUCHI, Yuichi. *Melts of Linear Polymers in Fast Flows*. Online. Macromolecules. Vol. 53 (2020), no. 13, p. 5023-5033. ISSN 0024-9297. Available from: https://doi.org/10.1021/acs.macromol.0c00693. [Accessed 18 December 2023].

[69] ZATLOUKAL, Martin and DRABEK, Jiri. *Reduction of monomeric friction coefficient for linear isotactic polypropylene melts in very fast uniaxial extensional flow*. Online. Physics of Fluids. Vol. 33 (2021), no. 5, p. 051703 ISSN 1070-6631. Available from: https://doi.org/10.1063/5.0050859. [Accessed 15 January 2024].

[70] MATSUMIYA, Yumi and WATANABE, Hiroshi. *Non-Universal Features in Uniaxially Extensional Rheology of Linear Polymer Melts and Concentrated Solutions: A Review.* Online. Progress in Polymer Science. Vol. 112 (2021), 101325. ISSN 0079-6700. Available from: https://doi.org/10.1016/j.progpolymsci.2020.101325. [Accessed 12 November 2023].

[71] MACOSKO, Christopher W. *Extensional rheometry via flow through an abrupt contraction: A short review.* Conference Proceedings. In: Novel Trends in Rheology IX. Zlín: AIP Conference Proceedings. Vol. 2997 (2023), 020001. ISBN 978-07354-4547-5.

[72] ROSELLO, Maxime; SUR, Samrat; BARBET, Bruno and ROTHSTEIN, Jonathan P. *Dripping-onto-substrate capillary breakup extensional rheometry of low-viscosity printing inks*. Online. Journal of Non-Newtonian Fluid Mechanics. Vol. 266 (2019), no. 1, p. 160-170. ISSN 0377-0257. Available from: https://doi.org/10.1016/j.jnnfm.2019.03.006. [Accessed 4 January 2024].

[73] DINIC, Jelena; ZHANG, Yiran; JIMENEZ, Leidy N. and SHARMA, Vivek. *Extensional Relaxation Times of Dilute, Aqueous Polymer Solutions*. Online. ACS Macro Letters. Vol. 4 (2015), no. 7, p. 804-808. ISSN 2161-1653. Available from: https://doi.org/10.1021/acsmacrolett.5b00393. [Accessed 12 November 2023].

[74] DRÁBEK, Jiří. *Applied rheology for production of polypropylene nanofibers*. Online, Master Thesis, Supervisor prof. Ing. Martin Zatloukal, Ph.D. Zlín: Tomas Bata University in Zlín, Department of Technology, 2013. Available from: http://hdl.handle.net/10563/24540. [Accessed 3 November 2023].

[75] AUHL, Dietmar; Stadler, Florian. J and MÜNSTEDT, Helmut. *Rheological properties of electron beam-irradiated polypropylenes with different molar masses*. Online. . Rheologica Acta. Vol. 51 (2012), p. 979-989. ISSN 0035-4511. Available from: https://doi.org/10.1007/s00397-012-0646-6. [Accessed 25 April 2024].

[76] MEISSNER, Joachim and HOSTETTLER, Jürg. *A new elongational rheometer for polymer melts and other highly viscoelastic liquids*. Online. Rheologica Acta. Vol. 33 (1994), no. 1, p. 1-21. ISSN 0035-4511. Available from: https://doi.org/10.1007/BF00453459. [Accessed 6 January 2024].

[77] ANDRADE, Raúl J.; HARRIS, Paul and MAIA, Joao M. *High strain extensional rheometry of polymer melts: Revisiting and improving the Meissner design.* Online. Journal of Rheology. Vol. 58 (2014), no. 4, p. 869-890. ISSN 0148-6055. Available from: https://doi.org/10.1122/1.4875349. [Accessed 18 November 2023].

[78] PADMANABHAN, Mahesh; KASEHAGEN, Leo J. and MACOSKO, Christopher W. *Transient extensional viscosity from a rotational shear rheometer using fiber-windup technique*. Online. Journal of Rheology. Vol. 40 (1996), no. 4, p. 473-481. ISSN 0148-6055. Available from: https://doi.org/10.1122/1.550792. [Accessed 3 January 2024].

[79] AUHL, Dietmar; HOYLE, David M.; HASSELL, David; LORD, Timothy D.; HARLEN, Oliver G. et al. *Cross-slot extensional rheometry and the steady-state extensional response of long chain branched polymer melts*. Online. Journal of Rheology. Vol. 55 (2011), no. 4, p. 875-900. ISSN 0148-6055. Available from: https://doi.org/10.1122/1.3589972. [Accessed 8 January 2024].

[80] SENTMANAT, Martin L. *Miniature universal testing platform: from extensional melt rheology to solid-state deformation behavior*. Online. Rheologica Acta. Vol. 43 (2004), no. 6, p. 657-669. ISSN 0035-4511. Available from: https://doi.org/10.1007/s00397-004-0405-4. [Accessed 10 December 2023].

[81] TANG, Dahang; MARCHESINI, Flávio H.; CARDON, Ludwig and D'HOOGE, Dagmar R. *Evaluating the exit pressure method for measurements of normal stress difference at high shear rates*. Online. Journal of Rheology. Vol. 64 (2020), no. 3, p. 739-750. ISSN 0148-6055. Available from: https://doi.org/10.1122/1.5145255. [Accessed 14 January 2024].

[82] DRABEK, Jiri and ZATLOUKAL, Martin. *Rheological evaluation of melt blown polymer melt*. Conference Proceedings. In: Novel Trends in Rheology V. Zlín: AIP Conference Proceedings. Vol. 1526 (2013), no. 1, p. 237-247. ISBN 978-0-7354-1151-7.

[83] PÉREZ-SALAS, Karen Y.; SÁNCHEZ, Salvador; VELASCO-SEGURA, Roberto; ASCANIO, Gabriel; RUIZ-HUERTA, Leopoldo et al. *Rheological transient effects on steady-state contraction flows*. Online. Rheologica Acta. Vol. 62 (2023), no. 4, p. 171-181. ISSN 1435-1528. Available from: https://doi.org/10.1007/s00397-023-01385-0. [Accessed 3 January 2024].

[84] PADMANABHAN, Mahesh and MACOSKO, Christopher W. *Extensional viscosity from entrance pressure drop measurements*. Online. Rheologica Acta. Vol. 36 (1997), no. 2, p. 144-151. ISSN 0035-4511. Available from: https://doi.org/10.1007/BF00366820. [Accessed 3 January 2024].

[85] AHO, Johanna and SYRJÄLÄ, Seppo. *Determination of the entrance pressure drop in capillary rheometry using Bagley correction and zero-length capillary*. Online. Annual Transactions of the Nordic Rheology Society, Vol. 14 (2006), Available from: https://nrs.blob.core.windows.net/pdfs/nrspdf-c6cb3c12-2c2f-4ff2-b6a5-08f0a5c32974.pdf. [Accessed 11 November 2023].

[86] SUNDER, Joachim and GOETTFERT, Axel. *Extensional flow properties from entrance pressure Measurements Using Zero Length Die Versus Bagley Correction*. Conference Proceedings. In: Annual Technical Conference – ANTEC 2001. Dallas: Society of Plastics Engineers, Vol. 1 Processing, 2001, p. 196-204. ISBN 978-1-58716-098-1.

[87] MARSH, Bob. *Capillary Rheology of Thermoplastics: An Overview*. Online. 2022. Available from: https://analyzing-testing.netzsch.com/en/blog/2022/capillary-rheology-of-thermoplastics-an-overview. [Accessed 2 January 2024].

[88] AHO, Johanna and SYRJÄLÄ, Seppo. *Evaluation of Different Methods for Determining the Entrance Pressure Drop in Capillary Rheometry*. Online. Applied Rheology. Vol. 18 (2008), no. 6, p. 63258. ISSN 1617-8106. Available from: https://doi.org/10.1515/arh-2008-0022. [Accessed 6 January 2024].

[89] AHO, Johanna and SYRJÄLÄ, Seppo. Measurement of the pressure dependence of viscosity of polymer melts using a back pressure-regulated capillary rheometer. Online. Journal of Applied Polymer Science. Vol. 117 (2010), no. 2, p. 1076-1084. ISSN 0021-8995. Available from: https://doi.org/10.1002/app.31754 [Accessed 12 November 2023].

[90] HATZIKIRIAKOS, Savvas G. and MITSOULIS, Evan. *Excess pressure losses in the capillary flow of molten polymers*. Online. Rheologica Acta. Vol. 35 (1996), no. 6, p. 545-555. ISSN 0035-4511. Available from: https://doi.org/10.1007/BF00396506. [Accessed 2 January 2024].

[91] MITSOULIS, Evan; HATZIKIRIAKOS, Savvas. G.; CHRISTODOULOU, Kostas. and VLASSOPOULOS, Dimitris. *Sensitivity analysis of the Bagley correction to shear and extensional rheology*. Online. Rheologica Acta. Vol. 37 (1998), no. 5, p. 438-448. ISSN 0035-4511. Available from: https://doi.org/10.1007/s003970050131. [Accessed 10 January 2024].

[92] Univerzita Tomáše Bati ve Zlíně (Czech Republic). *Vytlačovací hlava s inertní kapilárou s nulovou délkou*. Martin Zatloukal, Jan Musil. Logged: 07.11.2008. CZ 19221 U1 Utility model. Available from: https://isdv.upv.gov.cz/webapp/!resdb.pta.frm. [Accessed 15 September 2023].

[93] ZATLOUKAL, Martin. *Evaluation of temperature-strain rate dependent uniaxial and planar elongational viscosities for branched LDPE polymer melt*. Conference Proceedings. In: Novel Trends in Rheology V. Zlín: AIP Conference Proceedings. Vol. 1526 (2013), no. 1, p. 184-193. ISBN 978-0-7354-1151-7.

[94] KELLY, Adrian L. *On-line shear and extensional rheometry of polymer melts in the extrusion process*. Online, Doctoral Thesis, Supervisor: prof. Philip D. Coates. Bradford: University of Bradford, Department of Mechanical and Manufacturing Engineering, 1997. Available from: https://bradscholars.brad.ac.uk/handle/10454/2796. [Accessed 10 January 2024].

[95] ZATLOUKAL, Martin; VLCEK, Jiri; TZOGANAKIS, Costas and SAHA, Petr. *Improvement in techniques for the determination of extensional rheological data from entrance flows: computational and experimental analysis*. Online. Journal of Non-Newtonian Fluid Mechanics. Vol. 107 (2002), no. 1-3, p. 13-37. ISSN 0377-0257. Available from: https://doi.org/10.1016/S0377-0257(02)00111-8. [Accessed 25 September 2023].

[96] RIDES, Martin; KELLY, Adrian L. and ALLEN, Crispin R.G. *An investigation of high rate capillary extrusion rheometry of thermoplastics*. Online. Polymer Testing. Vol. 30 (2011), no. 8, p. 916-924. ISSN 0142-9418. Available from: https://doi.org/10.1016/j.polymertesting.2011.08.011. [Accessed 8 January 2024].

[97] MITSOULIS, Evan and HATZIKIRIAKOS, Savvas G. *Bagley correction: the effect of contraction angle and its prediction.* Online. Rheologica Acta. Vol. 42 (2003), no. 4, p. 309-320. ISSN 0035-4511. Available from: https://doi.org/10.1007/s00397-003-0294-y. [Accessed 11 January 2024].

[98] BOGER, David. V. and BINNINGTON, Rod. J. *Circular entry flows of fluid M1*. Online. Journal of Non-Newtonian Fluid Mechanics. Vol. 35 (1990), no. 2-3, p. 107-118. ISSN 0377-0257. Available from: https://doi.org/10.1016/0377-0257(90)85058-7. [Accessed 15 September 2023].

[99] RIDES, Martin and CHAKRAVORTY, Sekhar. *Review of converging flow methods for determining the extensional flow behaviour of polymer melts*. Centre for Materials Measurement and Technology, 1997. ISSN 1361-4061.

[100] BINDING, David M. *Further considerations of axisymmetric contraction flows*. Online. Journal of Non-Newtonian Fluid Mechanics. Vol. 41 (1991), no. 1-2, p. 27-42. ISSN 0377-0257. Available from: https://doi.org/10.1016/0377-0257(91)87034-U. [Accessed 12 January 2024].

[101] LAUN, Martin H. and SCHUCH, Horst. *Transient Elongational Viscosities and Drawability of Polymer Melts*. Online. Journal of Rheology. Vol. 33 (1989), no. 1, p. 119-175. ISSN 0148-6055. Available from: https://doi.org/10.1122/1.550058. [Accessed 13 January 2024].

[102] MACKAY, Michael E. and ASTARITA, Gianni. *Analysis of entry flow to determine elongation flow properties revisited*. Online. Journal of Non-Newtonian Fluid Mechanics. Vol. 70 (1997), no. 3, p. 219-235. ISSN 0377-0257. Available from: https://doi.org/10.1016/S0377-0257(96)01540-6. [Accessed 4 January 2024].

[103] ZATLOUKAL, Martin. *Differential viscoelastic constitutive equations for polymer melts in steady shear and elongational flows*. Online. Journal of Non-Newtonian Fluid Mechanics. Vol. 113 (2003), no. 2-3, p. 209-227. ISSN 0377-0257. Available from: https://doi.org/10.1016/S0377-0257(03)00112-5. [Accessed 10 January 2024].

[104] ZATLOUKAL, Martin; PIVOKONSKÝ, Radek; MARTYN, Mike T. and FILIP, Petr. *Applicability of advanced constitutive equations for coextrusion flows of polyolefin melts*. Conference Proceedings In: Annual Technical Conference – ANTEC 2007. Cincinnati: Society of Plastics Engineers, 2007, p. 1933-1937. ISBN 978-0-9753707-5-9.

[105] YAO, Donggang. *An explicit non-Newtonian fluid model for polymeric flow with finite stretch*. Conference Proceedings. In: Annual Technical Conference – ANTEC 2022. Charlotte: Society of Plastics Engineers, 2022, p. 86-91. ISBN 978-1-71386-515-5.

[106] LARSON, Ronald G. *Constitutive equations for polymer melts and solutions*. Boston: Butterworth-Heinemann (Elsevier), 1988. ISBN 0-409-90119-9.

[107] POOLE, Robert J. *Inelastic and flow-type parameter models for non-Newtonian fluids*. Online. Journal of Non-Newtonian Fluid Mechanics. Vol. 320 (2023), 105106. ISSN 0377-0257. Available from: https://doi.org/10.1016/j.jnnfm.2023.105106. [Accessed 10 January 2024].

[108] YAO, Donggang. *A non-Newtonian fluid model with an objective vorticity*. Online. Journal of Non-Newtonian Fluid Mechanics. Vol. 218 (2015), no. 1, p. 99-105. ISSN 0377-0257. Available from: https://doi.org/10.1016/j.jnnfm.2015.02.002. [Accessed 12 January 2024].

[109] ZATLOUKAL, Martin. *Frame-invariant formulation of novel generalized Newtonian fluid constitutive equation for polymer melts*. Online. Physics of Fluids. Vol. 32 (2020), no. 9, p. 091705. ISSN 1070-6631. Available from: https://doi.org/10.1063/5.0024351. [Accessed 11 January 2024].

[110] DRABEK, Jiri and ZATLOUKAL, Martin. *Evaluation of Thermally Induced Degradation of Branched Polypropylene by Using Rheology and Different Constitutive Equations*. Online. Polymers. Vol. 8 (2016), no. 9, p. 317. ISSN 2073-4360. Available from: https://doi.org/10.3390/polym8090317. [Accessed 11 January 2024].

[111] WHITE, James L. and METZNER, Arthur B. *Development of constitutive equations for polymeric melts and solutions*. Online. Journal of Applied Polymer Science. Vol. 7 (1963), no. 5, p. 1867-1889. ISSN 0021-8995. Available from: https://doi.org/10.1002/app.1963.070070524. [Accessed 14 January 2024].

[112] BARNES, H.A. and ROBERTS, G.P. *A simple empirical model describing the steady-state shear and extensional viscosities of polymer melts*. Online. Journal of Non-Newtonian Fluid Mechanics. Vol. 44 (1992), no. 1, s. 113-126. ISSN 0377-0257. Available from: https://doi.org/10.1016/0377-0257(92)80047-2. [Accessed 9 January 2024].

[113] LEONOV, Arkadii I. *Nonequilibrium thermodynamics and rheology of viscoelastic polymer media*. Online. Rheologica Acta. Vol. 15 (1976), no. 2, p. 85-98. ISSN 0035-4511. Available from: https://doi.org/10.1007/BF01517499. [Accessed 14 January 2024].

[114] BARBORIK, Tomas and ZATLOUKAL, Martin. *Viscoelastic non-isothermal modeling of film extrusion for membrane production including flow induced crystallization*. Online. Physics of Fluids. Vol. 34 (2022), no.6, p. 063103. ISSN 1070-6631. Available from: https://doi.org/10.1063/5.0093288. [Accessed 18 November 2023].

[115] SIMHAMBHATLA, Murthy and LEONOV, Arkadii I. *On the rheological modeling of viscoelastic polymer liquids with stable constitutive equations*. Online. Rheologica Acta. Vol. 34 (1995), no. 3, p. 259-273. ISSN 0035-4511. Available from: https://doi.org/10.1007/BF00396016. [Accessed 14 January 2024].

[116] LEONOV, Arkadii I. *Constitutive Equations for Viscoelastic Liquids*: *Formulation, Analysis and Comparison with date*. In: SIGINER, Dennis A.; DE KEE, Daniel and CHHABRA, Raj P. *Advances in the Flow and Rheology of Non-Newtonian Fluids Part A*. Elsevier Science, 1999, 519-576. ISBN 9780080540559.

[117] POLE, Sandeep S. and ISAYEV, Avraam I. *The nonlinear stress relaxation behavior after a step shear of star-shaped styrene-butadiene rubber filled with precipitated silica: Experiment and simulation*. Online. Journal of Applied Polymer Science. Vol. 138 (2021), 50080. ISSN 0021-8995. Available from: https://doi.org/10.1002/app.50080. [Accessed 14 January 2024].

[118] SONG, Hyeong Yong; KONG, Hyo Jae; KIM, Si Yoon and HYUN, Kyu. *Evaluating predictability of various constitutive equations for MAOS behavior of entangled polymer solutions. Online*. Journal of Rheology. Vol. 64 (2020), no. 3, p. 673-707. ISSN 0148-6055. Available from: https://doi.org/10.1122/1.5139685. [Accessed 14 January 2024].

[119] AUHL, Dietmar. *Molekulare Struktur und rheologische Eigenschaften strahlenmodifizierter Polypropylene*. Online, Doctoral Thesis, Supervisor: Prof. Dr. Ing. Manfred H. Wagner. Erlangen: Der Technischen Fakultät der Universität Erlangen-Nürnberg, 2006.

[120] Netzsch website: Capillary rheometer Rosand RH10. Online. Available from: Rosand RH7/10 - NETZSCH Analyzing & Testing. [Accessed 20 April 2024].

[121] PADMANABHAN, Mahesh. *Evaluation of the entrance pressure drop method to estimate extensional viscosity*. Master Thesis, Supervisor: Prof. Chris Macosko. Minesota: University of Minnesota, Department of Chemical Engineering and Materials Science, 1993.

[122] Univerzita Tomáše Bati ve Zlíně (Czech Republic). *Vytlačovací hlava pro transformaci normálových napětí polymerní taveniny*. Martin Zatloukal. Logged: 06.11.2017. CZ 31960 U1 Utility model. Available from: https://isdv.upv.gov.cz/webapp/!resdb.pta.frm. [Accessed 5 April 2023].

[123] *What are Mercury Fill Sensors?* Online. Dynisco 2019. Available from: https://www.azom.com/article.aspx?ArticleID=17470

[124] Xpansion Instruments website. Online. Available from: Xpansion Instruments - Extensional Rheology and Material Testing and Processing Products. [Accessed 22 April 2024].

[125] MÜNSTEDT, Helmut and AUHL, Dietmar. *Rheological measuring techniques and their relevance for the molecular characterization of polymers*. Online. . Journal of Non-Newtonian Fluid Mechanics. Vol. 128 (2005), no. 1, p. 62-39. ISSN 0377-0257. Available from: doi:10.1016/j.jnnfm.2005.03.011. [Accessed 25 April 2024].

LIST OF ABBREVIATIONS

List of symbols:

x, y, z	axes of the Cartesian coordinate system	(1)
$\underline{\underline{\sigma}}$	total stress tensor	(Pa)
p	pressure	(Pa)
$\underline{\underline{\tau}}$	extra stress tensor, without p	(Pa)
$\tau_{xx}, \tau_{yy}, \tau_{yy}$	normal stress	(Pa)
$\tau_{xy}, \tau_{yz}, \tau_{zx}$	combined shear stress	(Pa)
λ_{ER}	extension ratio	(1)
ds'	infinitesimal distance	(m)
ε	scalar deformation	(1)
$\underline{\underline{\varepsilon}}$	strain tensor	(1)
$\underline{u}$	displacement vector	(m)
d	infinitesimal strain tensor	(1)
$\underline{\nabla}$	nabla operator (vector quantity)	(m^{-1})
$\underline{\underline{g}}$	relative displacement gradient tensor	(1)
$\underline{\underline{\theta}}$	rotation tensor	(1)
$\underline{v}$	velocity vector	(m$\cdot$s^{-1})
$\underline{\underline{L}}$	velocity gradient tensor	(s^{-1})
$\underline{\underline{W}}$	vorticity tensor	(s^{-1})
$\underline{\underline{L^T}}$	transposed velocity gradient tensor	(s^{-1})
$\underline{\underline{D}}$	strain rate tensor	(s^{-1})
λ	relaxation time	(s)

Θ	characteristic flow time	(s)
$\dot{\gamma}$	shear rate	(s^{-1})
De	Deborah Number	(1)
Wi	Weissenberg number	(1)
γ_0	shear strain amplitude	(1)
ω	oscillation frequency	($rad \cdot s^{-1}$)
γ	shear strain	(1)
t	time	(s)
N_1, N_2	first and second normal stress differences	(Pa)
η_0	zero shear rate (Newtonian) viscosity	(Pa·s)
η	viscosity dependent shear rate	(Pa·s)
$\psi_1 = \psi_2$	first and second normal stress difference coefficients	(Pa)
$\eta^+(\dot{\gamma}, t)$	transient shear viscosity growth on time	(Pa·s)
x, φ, z	cylindrical coordinates	(1)
α_{co}	cone angle	(°)
l_0	original length	(m)
l	length after deformation	(m)
$\dot{\varepsilon}$	extensional rate	(s^{-1})
m	Meissner's parameter	(1)
F	force	(N)
$\sigma_{E,U}$	uniaxial extensional stress	(Pa)
$\eta_{E,U}$	uniaxial extensional viscosity	(Pa·s)
Tr	Trouton ratio	(1)
$\sigma_{E,B}$	biaxial extensional stress	(Pa)

$\eta_{E,B}$	biaxial extensional viscosity	(Pa·s)
$\sigma_{E,P}$	planar extensional stress	(Pa)
$\eta_{E,P}$	planar extensional viscosity	(Pa·s)
$\eta_E^+(\dot{\varepsilon},t)$	transient uniaxial extensional viscosity	(Pa·s)
$\eta_{E,0}(\dot{\varepsilon},t)$	linear viscoelastic envelope for transient extensional viscosity	(Pa·s)
$\eta_0(\dot{\gamma},t)$	linear viscoelastic envelope for transient shear viscosity	(Pa·s)
λ_i	relaxation time in the "*i*" relaxation mode	(s)
G_i	relaxation modulus in the "*i*" relaxation mode	(s)
λ_R	Rouse time	(s)
λ_0	Macroscopic relaxation time	(s)
W_{iR}	Rouse-Weissenberg number	(1)
$\lambda_{\mathrm{R}S}$	Rouse stress relaxation time	(s)
$\eta_{E,U\infty}$	uniaxial extensional viscosity in the second Newtonian plateau	(Pa·s)
M	molecular weight	(g·mol^{-1})
Mc	critical molecular weight	(g·mol^{-1})
R_{G}	gas constant $\left(R_{\mathrm{G}} = 8.314\ \mathrm{J\cdot K^{-1}\cdot mol^{-1}}\right)$	$(\mathrm{J\cdot K^{-1}\cdot mol^{-1}})$
T	thermodynamic temperature	(K)
ρ	density	(kg·m^3)
a_M	exponent dependent on Mc	(1)
Δp_{entr}	entrance pressure drop	(Pa)
D_b	barrel diameter	(m)
D	capillary die diameter	(m)
L	capillary die length	(m)

α	entry contraction angle	(°)
v_x	piston displacement speed	$(\mathrm{m \cdot s^{-1}})$
$\mathit{\Delta} p_{\mathrm{cap}}$	capillary pressure drop	(Pa)
Δp_{end}	end pressure drop	(Pa)
$\mathit{\Delta} p_{\mathrm{exit}}$	exit pressure drop	(Pa)
$\mathit{\Delta} p$	total pressure drop	(Pa)
L/D	the ratio of the length to the diameter of the capillary die	(1)
$\dot{\gamma}_{\mathrm{APP}}$	apparent shear rate	$(\mathrm{s^{-1}})$
η_{entr}	apparent entrance viscosity	$(\mathrm{Pa \cdot s})$
Q	volumetric flow rate	$(\mathrm{m^3 \cdot s^{-1}})$
A_b	cross-sectional area of the barrel (Fig. 35)	$(\mathrm{m^2})$
A_c	cross-sectional area of the capillary die (Fig. 35)	$(\mathrm{m^2})$
$v_{z,b}$	mean velocity in the barrel (Fig. 35)	$(\mathrm{m \cdot s^{-1}})$
$v_{z,c}$	mean velocity in the capillary (Fig. 35)	$(\mathrm{m \cdot s^{-1}})$
$\mathrm{C_R}$	contraction ratio	(1)
ε_{PTT}	parameters PPT model	(1)
$\eta_{ENT,0}$	zero apparent entrance viscosity	$(\mathrm{Pa \cdot s})$
$(L/D)_{Tr}$	effective entry length correction	(1)
$\eta_{E,U\,\max}$	maximum uniaxial extensional viscosity	$(\mathrm{Pa \cdot s})$
$II_{\underline{\underline{D}}}$	second invariant of the strain rate tensor $\underline{\underline{D}}$	$(\mathrm{s^{-2}})$
$III_{\underline{\underline{D}}}$	third invariant of the strain rate tensor $\underline{\underline{D}}$	$(\mathrm{s^{-2}})$
$\underline{\underline{\bar{L}}}$	objective velocity gradient tensor	$(\mathrm{s^{-1}})$
$\underline{\underline{\bar{W}}}$	objective vorticity tensor	$(\mathrm{s^{-1}})$

$II_{\underline{\underline{\bar{L}}}}$	second invariants of the objective velocity gradient $\underline{\underline{\bar{L}}}$	(s^{-2})
G	linear elastic modulus	(Pa)
$\underline{\underline{B}}^{*}$	generalized Finger tensor	(Pa)
G_0	initial elastic modulus	(Pa)
$n_0, \psi_Y, S_0, \alpha_0$	dimensionless parameters of the Yao model	(1)
λ_Y	relaxation time specific for Yao model	(s)
tr, det	trace and the determinant of the corresponding tensor	(1)
α_T	temperature function	(1)
A_Z	the mGNF model fixed parameter	(Pa·s)
η_∞	infinite viscosity in the mGNF model	(Pa·s)
a	dimensionless parameters of the Carreau-Yasuda model	(1)
n	index of non-Newtonian flow behavior	(1)
λ_1	shear relaxation time in the Carreau-Yasuda model	(s)
β, ζ	dimensionless parameters of the mGNF model	(1)
λ_2	relaxation time specific for mGNF model	(s)
ψ_Z	planar extensional viscosity parameter (mGNF model)	(1)
$\overset{\nabla}{\underline{\underline{\tau}}}$	upper convected time derivative	(Pa·s^{-1})
K_1, λ_{WM}	extensional viscosity parameters of the mWM model	(s)
$\underline{\underline{c}}^{(i)}$	recoverable Finger tensor	(1)
$I^{(i)}_{1,\underline{\underline{c}}^{(i)}}, I^{(i)}_{2,\underline{\underline{c}}^{(i)}}$	first invariant Finger recoverable tensor	(1)
$\underline{\underline{\delta}}$	unit tensor	(1)
$b_L^{(i)}$	the dissipation term of the Leonov model	(s^{-1})

$W_L^{(i)}$	elastic potential in the Leonov model	(Pa)
$\underline{\underline{e}}_p^{(i)}$	irreversible rate of strain of Leonov model	(s^{-1})
$\beta_L^{(i)}, n_L^{(i)}$	non-linear parameters of Leonov model	(1)
$\xi_L^{(i)}$, $\upsilon^{(i)}$	dissipation parameters of the Leonov model	(1)
$\overset{\circ}{\underline{\underline{c}}}{}^{(i)}$	corotational (Jaumann) time derivative $\underline{\underline{c}}^{(i)}$	(s^{-1})
R	radius of the capillary	(m)
$\tau_{xy,corr}$	corrected shear stress	(Pa)
s, k	power-law constants for extensional flow	(1)
m_p, n	power-law constants for shear flow	(1)
$\Delta p_{\mathrm{entr,E}}$	entrance pressure drop due to elongational flow (Table 10)	(Pa)
β_G	geometry subtending angle	(°)
R_{b}	barrel radius	(m)
D_{bds}	Strain die barrel diameter	(m)
L_{sd}	length of Strain die barrel	(m)
p_{ref}	reference pressure on the calibration device	(Pa)
p_{trans}	the calibrated pressure identified by the rheometer	(Pa)
Tq	torque	(N.m)
Ω	rotational speed (plate and shaft)	(s^{-1})
L_d	distance between drums	(m)
E_{a}	flow activation energy	(J·mol^{-1})
D_p	parallel plate diameter	(m)
a_T	temperature shift factor	(1)
p_1, p_2, p_3, p_4	pressures from the individual transducer of the Strain die	(Pa)
T_{Die}	Strain die temperature	(°C)

p_{right}	pressure identified by the transducer on orifice die	(Pa)
p_{left}	pressure identified by the transducer on long capillary die	(Pa)
G'	storage modulus	(Pa)
G''	loss modulus	(Pa)
η^*	complex viscosity	(Pa·s)
a_{k}	shift factor	(1)
R^2	correlation coefficient	(1)

List of abbreviations:

LVE	Linear Viscoelastic Envelope
RME	Rheometric Melt Extensional
MTR	Münstedt Tensile Rheometer
CaBER	Capillary Breakup Extensional Rheometry
FSR	Filament Stretching
CRD	Counter-Rotating Drums
MERA	Meissner Extensional Rheometry Accessory
SER	Sentmanat Extensional Rheometer
EVF	Extensional Viscosity Fixture
CSER	Cross-Slot Extensional Rheometer
FEM	Finite Element Method
K-BKZ	Kaye-Bernstein-Kearsley-Zapas model
PTT	Phan-Thien-Tanner model
CE	Constitutive equations
GNF	Generalized Newtonian fluid model
mGNF	modified Generalized Newtonian fluid model
WM	White-Metzner model
mWM	modified White-Metzner model

FCO	Forced Convection Oven (Ares G2)
SW	Software
LAOS	Long Amplitude Oscillation Shear
DMA	Dynamic Mechanical Analysis
SAOS	Small Amplitude Oscillation Shear
TTS	Time-Temperature superposition
RMSE	Root Mean Squared Error

Polymer abbreviations:

PS	Polystyrene
LDPE	Low Density Polyethylene
PP	Polypropylene
LLDPE	Linear Low Density Polyethylene
mLLDPE	metallocene Linear Low Density Polyethylene
HDPE	High Density Polyethylene
PA 6.6	Polyamide (Nylon)
PET	Polyethyleneterephthalate

LIST OF FIGURES

LIST OF TABLES

APPENDICES

Appendix P I: Material datasheet of used LDPE PG 7008

Appendix P II: Technical datasheet of Rosand RH10 capillary rheometer

Appendix P III: Technical drawings of used standard orifice dies (D = 2 mm and D = 3 mm)

Appendix P IV: Assembly drawing Strain die with parts list

Appendix P V: Technical datasheets of used pressure transducers

Appendix P VI: Calibration curves of used pressure transducers

Appendix P VII: Technical datasheet of Ares G2 rotational rheometer

Appendix P VIII: Sample script defined for middle range

*All appendices of this thesis are located outside of this document, in the attached file, and on CD-ROM.